Characterizing the convective boundary layer with wind-profiling and scanning Doppler lidar

Christiane Anabell Duscha

Thesis for the degree of Philosophiae Doctor (PhD)
University of Bergen, Norway
2024

UNIVERSITY OF BERGEN

Characterizing the convective boundary layer with wind-profiling and scanning Doppler lidar

Christiane Anabell Duscha

Thesis for the degree of Philosophiae Doctor (PhD)
at the University of Bergen

Date of defense: 22.04.2024

Year: 2024

Title: Characterizing the convective boundary layer with wind-profiling and scanning Doppler lidar

Name: Christiane Anabell Duscha

Print: Skipnes Kommunikasjon / University of Bergen

Scientific environment

This study is carried out at the Geophysical Institute, University of Bergen, the Bergen Offshore Wind Centre and the Bjerknes Centre for Climate Research. The work has been supported by the Research Council of Norway through the Offshore Boundary-Layer Observatory (OBLO) infrastructure (grant nr. 227777). I have been enrolled in the Research School on Changing Climates in the Coupled Earth Systems (CHESS).

OBLO

Offshore Boundary Layer Observatory
Norwegian Infrastructure for
Offshore Wind Energy Research run by

UNIVERSITY OF BERGEN
Geophysical Institute

UNIVERSITY OF BERGEN
Bergen Offshore Wind Centre

CHESS

BJERKNES CENTRE
for Climate Research

Acknowledgements

First of all, I would like to thank my main supervisor Joachim Reuder for the continuous support with valuable input and discussions almost every week and if needed at even higher frequencies during the whole period of my PhD project. Thanks for letting me follow my own research interests and encourage me to organize and realize my own field campaigns, as well as the gLidar research project. Also, thank you for always connecting me with other scientists at multiple institutions, that provide me with a large research network and allowed me to contribute in several additional projects and publications. Thanks goes also to my second supervisor, Mostafa Bakhoday Paskyabi, who, on many occasions, guided me through complicated, technical difficulties and provided me with valuable material and ideas to approach these problems.

Further I want to thank my colleagues and friends at the Geophysical Institute and the Bergen Offshore Wind Centre for the great atmosphere, the discussions, the social get-togethers, the after-work volleyball sessions, and company you provided throughout the period of my PhD project. Here, thanks goes in particular to my office mates over the years: Stephan Kral, Pablo Saavedra, Omar El Guernaoui, Martin Flügge, Priscila Orozco, and Shokoufeh Malekmohammadi, with special thanks to Kjersti Konstali, who helped me with the translation of the thesis' abstract to Norwegian, and Mauro Ghirardelli, for the fishing sessions, the provision of amazing food, and that he welcomed me to stay at his place, whenever I visited Bergen, after moving to the other side of Norway.

I want to thank, Anak Bhandari for the countless occasions where he helped me with configuring, repairing, and installing the instruments in the field and Tor Olaf Kristensen for input and lecturing about electrical engineering and the design and instructions to build the remote access cabinets for the gLidar project. For initially introducing me to the function and operation of the profiling lidar instrumentation, I want to thank Andrew Seidl. Thanks also goes to the large number of colleagues that contributed to the success of the field campaigns, as well as to all my co-authors for their valuable contribution to the published manuscripts.

For their hospitality and the (board) game session during my time in Bergen, I would like to thank Stephen and Ariadne Outten. Thank you, Jenny and Behnood Sjåstad, for the amazing company, the 17th of May celebrations, and countless jam sessions with Norwegian gammeldans. I would further like to thank Dag Hellesund and Kristine Petersen, for being the most amazing landlords while living in Bergen and Juraj Pálenik for the all the rememberable sailing adventures, as well as for the motivation and dedication to initiate and collaborate on the gLidar project, including the organization and execution of several field campaigns, and the CHESS summer school on land-atmosphere interaction processes and convection.

Thanks also goes to Thomas Spengler, who was essential to the initialisation, planning, and realization of the field campaigns and the CHESS summer school connected to the gLidar project. At this point, I would also like to thank the glider and skydiving plane pilots, as well as the people and the institutions that provided their properties for field campaigns in Voss and at Vaksinen and Starmoen Airport: Olaf Undeland, Anders Skorve Skarpeid, the Store Ringheim Hotel, the Os Aero Klubb and the Ole Reistad Center. Further, I want to thank Tore Birkeland, who showed me around Voss and helped me to get in contact with the locals.

Thanks to my family and friends in Germany, in particular to my parents for supporting my decision to start a PhD in Norway, visiting me in Bergen and always welcoming me, when I was travelling back. And finally, thank you Marvin, for always having my back, may it be emergency proof-reading, spelling and grammar editing of an article review, or looking after our daughter, so I was able to work on this thesis, but most importantly, for making this whole time in Bergen so enjoyable!

Christiane Duscha
January 16, 2024

> "My life amounts to no more than one drop in a limitless ocean. Yet what is any ocean, but a multitude of drops?"
>
> *David Mitchell, Cloud Atlas*

Abstract

Convection strongly impacts the structure and evolution of the atmospheric boundary layer. Yet, the characteristic temporal and spatial scales of the convective circulation are challenging to capture with the conventional meteorological measurement setup and instrumentation. As a consequence, atmospheric convection is still under-sampled. This dissertation and the three included papers introduce two approaches for observing the convective flow field and its evolution, using profiling and dual-scanning lidar techniques above the ocean, and over complex and flat terrain on land. These flow field observations are utilized to extract fundamental convection characteristics, as for example, the horizontal and vertical dimensions, and velocities of the convective updraft and downdraft. In combination with complementing meteorological measurements, this allows the investigation of the interaction of those characteristics with other processes in the convective boundary layer (CBL).

The focus of Paper I is on identifying the resolvable range of turbulent and organized eddies in the marine CBL by ship-based profiling lidar observations, that are exposed to ship motion. Paper I evaluates the impact of the ship motion and the applied motion correction on the statistics and spectra of the lidar observations. In addition to this evaluation, the dissertation includes an assessment of the utilized motion correction algorithm applied to data that are acquired during a controlled-motion experiment. The results of Paper I indicate, that convective scales can be resolved with the evaluated profiling lidar setup, given a sufficient horizontal background flow velocity.

Corresponding convective structures, under prevailing cold air outbreak conditions, are analysed in Paper II. The study applies spectral coherence and phase analysis to the lidar-observed flow field, extracting characteristics of organized convection, namely coherent structures. The short-term evolution of the structure sizes and velocity amplitudes is sensitive to the surface layer stratification and wind shear. The largest structures are observed for conditions, where the buoyancy production marginally dominates the shear production of turbulence. On the long-term, these large scale structures strongly contribute to the overturning and deepening of the marine CBL.

Complementary to the ship-based, profiling lidar approach over the ocean, Paper III explores the capability of land-based, dual-scanning lidars to sample convection. The study introduces an advanced filtering and a temporal interpolation approach, that substantially enhance the lidar data for convection sampling. Here, the shape and evolution, and interaction of the observed convective structures with other boundary-layer processes were mainly impacted by the differences in the evaluated measurement locations, i.e. flat versus complex terrain, and inland versus close vicinity to the sea.

The dissertation follows up on the findings of Paper III, presenting first results of the convective flow field retrieval achieved with the Eulerian, dual-scanning lidar approach collocated with a Lagrangian approach using gliders to sample key parameters from inside the convective updraft, i.e. velocity, temperature and humidity. For the presented case, the Eulerian and Lagrangian approaches complement each other, yielding detailed information about the lower and upper part of the convective structure, respectively.

Sammendrag

Konveksjon har stor innvirkning på strukturen og utviklingen av det atmosfæriske grenselaget. Det er imidlertid utfordrende å måle de karakteristiske lengde- og tidsskalaene ved hjelp av konvensjonelle meteorologiske metoder. Derfor er konveksjon fortsatt ikke godt nok observert. Denne avhandlingen og de tre artiklene som inngår i den, presenterer to metoder for å observere det konvektive strømningsfeltet ved hjelp av forskjellige lidar-baserte målemetoder, både over hav og flatt og komplekst terreng over land. Disse målingene av strømningsfeltet kan brukes til å trekke ut grunnleggende konvektive egenskaper, som for eksempel karakteristiske høyde- og lengdeskalaer, samt vertikale hastigheter. Å kombinere dette med supplerende meteorologiske målinger muliggjør undersøkelsen av samspillet mellom disse egenskapene og andre prosesser i det konvektive grenselaget.

I artikkel I identifiserer vi de oppløselige skalaene til turbulente og organiserte virvler i det marine konvektive grenselaget fra vindprofiler tatt med lidar på et skip i bevegelse. Artikkel I evaluerer påvirkningen av skipsbevegelsen og bevegelseskorreksjon på lidarobservasjonenes statistikk og spekter. I tillegg inkluderer avhandlingen en evaluering av bevegelseskorreksjonsalgoritmen på et datasett innhentet under et kontrollert eksperiment med bevegelse. Resultatene fra artikkel I viser at dersom bakgrunnshastigheten er tilstrekkelig kan de konvektive skalaene bli oppløst med en profilerende lidar.

Tilsvarende konvektive strukturer under et kaldluftsutbrudd er analysert i artikkel II. Studien anvender spektral koherens- og faseanalyse på det konvektive strømningsfeltet fra lidarobservasjoner for å studere karakteristikkene til koherente strukturer i organisert konveksjon. Utviklingen av strukturstørrelser og hastighet på korte tidsskalaer er følsomme for overflatelagets lagdeling og vindskjær. De største strukturene blir observert under forhold der oppdriftsproduksjonen marginalt overgår skjærsproduksjonen av turbulens. Over lange tidsskalaer bidrar disse storskala strukturene til omvelting og at det marine konvektive grenselaget blir dypere.

Artikkel III utforsker muligheten til å bruke to landbaserte lidar systemer i dual-scanning oppsett for å måle konveksjon. Studien introduserer en avansert filtrering og en interpolasjonsmetode i tid som forbedrer lidardataene vesentlig for å måle konveksjon. Observasjonene viser at formen og utviklingen til de konvektive strukturene, samt samspillet mellom disse strukturene og andre prosesser i det atmosfæriske grenselaget, hovedsakelig blir påvirket av variasjoner i lokasjon, f.eks. flatt kontra komplekst terreng, eller innlandet kontra kysten.

Avhandlingen følger opp funnene i artikkel III, og presenterer de første resultatene av det konvektive strømningsfeltet funnet ved hjelp av en euleriansk tilnærming ved bruk av dual-scanning lidar og en lagransk tilnærming som tar i bruk glidere for å måle nøkkelparametrer fra konveksjon, slik som hastighet, temperatur og fuktighet. For det presenterte tilfellet utfyller den eulerianske og lagranske tilnærmingen hverandre og gir detaljert informasjon om henholdsvis de nedre og øvre delene av de konvektive strukturene.

Outline and Scientific contribution

This thesis consists of an introductory part and three scientific papers. Chapter 1 gives an introduction to the thesis. Objectives and research questions are introduced in chapter 2. Further, chapter 3 gives an overview over the scientific background. The methods are presented in chapter 4. A summary and the common theme that links each of the three papers is given in chapter 5. Further, some additional, complementing material is presented in chapter 6. Finally, a conclusion and outlook to the thesis are given in chapter 7. The papers I, II, and III included in this thesis are:

I *Duscha et al.* (2020):
Christiane Duscha, Mostafa Bakhoday Paskyabi and Joachim Reuder, (2020) *Statistic and Coherence Response of Ship-based Lidar Observations to Motion Compensation*, Journal of Physics: Conference Series *1669/01*, doi:10.1088/1742-6596/1669/1/012020

II *Duscha et al.* (2022):
Christiane Duscha, Christopher Barrell, Ian A. Renfrew, Ian M. Brooks, Harald Sodemann and Joachim Reuder, (2022) *A Ship-Based Characterization of Coherent Boundary-Layer Structures Over the Lifecycle of a Marine Cold-Air Outbreak*, Boundary-Layer Meteorology *183/355-380*, doi:10.1007/s10546-022-00692-y

III *Duscha et al.* (2023):
Christiane Duscha, Juraj Pálenik, Thomas Spengler, Joachim Reuder, (2023) *Observing atmospheric convection with dual-scanning lidars*, Atmospheric Measurement Techniques *16/5103-5123*
doi:10.5194/amt-16-5103-2023

Additional contributions to publications:

i *Renfrew et al.* (2019): The Iceland Greenland Seas Project

ii *Renfrew et al.* (2020): An evaluation of surface meteorology and fluxes over the Iceland and Greenland Seas in ERA5 reanalysis: The impact of sea ice distribution

iii *Cheynet et al.* (2021): The COTUR project: Remote sensing of offshore turbulence for wind energy application

iv *Henkies et al.* (2023): The Arctic Fjord breeze: characteristics of a combined sea breeze and valley wind in a Svalbard fjord valley

v *Reuder et al.* (in prep): OBLEX-F1: An Extensive Observational Effort for Offshore Wind Energy Research with Emphasis on Atmospheric Measurements

vi *Malekmohammadi et al.* (in prep): Controlled-motion test of lidar wind profilers

Contents

1 Introduction

The convective boundary layer (CBL) is dominated by buoyancy-driven turbulence generation (*Stull*, 1988), where larger turbulent eddies typically organize into distinct convective structures (*Young*, 1988a). Such convective structures strongly contribute to the deepening of the boundary layer, the overturning of i.e. heat, moisture, momentum, and energy, as well as the formation of clouds, severe thunderstorms, and precipitation (*Stull*, 1988; *Emanuel*, 1994). These processes that are inherent to convection are further important for the transport of aerosols and pollutants (*Kunkel et al.*, 1977; *Melfi et al.*, 1985), the interplay with gust fronts, convergence lines, and cold pools (*Jeevanjee and Romps*, 2015; *Liu et al.*, 2023), the impact on flight safety at airports (*Ito et al.*, 2020; *Wan et al.*, 2021), the loads on wind turbines (*Kumer et al.*, 2016; *Lu et al.*, 2019) or bridges (*Wang et al.*, 2018), the interaction with wind turbine wakes (*Zhang et al.*, 2013), and local urban ventilation (*de Foy et al.*, 2006), to name some examples. However, sufficiently characterizing this complex and dynamic, three-dimensional atmospheric phenomenon, that extends both horizontally, and vertically throughout the depth of the CBL is challenging with conventional meteorological instrumentation and setups, including most ground-based in situ measurement networks and profiling techniques (*Geerts et al.*, 2018), particularly in remote locations, i.e. offshore or in complex, inaccessible terrain.

Profiles of wind, temperature and humidity from meteorological masts (see e.g *LeMone*, 1973; *Kaimal et al.*, 1982) are restricted to the lowest few hundred or less meters of the CBL, while convection usually reaches considerably higher. Also, large mast are difficult or very costly to erect and move and are rarely installed offshore, with only few exceptions, such as the FINO-1 platform in the North Sea (*Fischer*, 2006). Radiosondes are more mobile than masts and reach much higher, but provide only a single profile with a time resolution that is restricted by the number of launches (e.g. *Furevik and Haakenstad*, 2012; *Vömel and Fujiwara*, 2021). A single profile is not capable to capture the convective structure as a whole, including both the updraft and downdraft pattern, as well as horizontal convergence or divergence of the flow. Measurements from tethered balloons or kites (e.g. *Kaimal et al.*, 1976) usually provide profiles of higher resolution than radiosondes, yet their use is restricted to certain meteorological condition and usually their operation is not automatized, limiting the measurements to special observing periods. Possibly the most prominent and detailed measurements of the CBL in the past are achieved by aircraft studies (e.g. *LeMone*, 1976; *Kaimal et al.*, 1982; *Young*, 1988b; *Brümmer*, 1996; *Hartmann et al.*, 1997; *Cieszelski*, 1998; *Renfrew and Moore*, 1999; *Cook and Renfrew*, 2015; *Brilouet et al.*, 2017; *Adler et al.*, 2019). Aircraft-based measurements are capable to obtain snapshots of the convective circulation throughout the CBL, yet their temporal and spatial coverage is limited by the flight duration and trajectory. As a consequence, the dynamic, three-dimensional characteristics of convection remain under-sampled by conventional meteorological approaches in terms of required spatio-temporal resolution and long-term coverage.

Active and passive remote sensing can provide corresponding observations and has consequently the potential to fill this observational gap, on the condition that observational strategies are optimized to derive convection characteristics. Here, the structure and evolution of the convective circulation, hence the three-dimensional velocity field, is of major interest. Therefore, this dissertation explores the capability of wind-profiling and scanning lidar (Light Detection and Ranging) observations to obtain insight into the convective dynamics, that can complement estimates of CBL characteristics provided by conventional meteorological measurements and other remote sensing techniques.

Lidar systems have become increasingly relevant for wind profiling (e.g. *Werner*, 2005; *Calhoun et al.*, 2006) and sampling of the multi-dimensional wind field (e.g. *Newsom et al.*, 2005, 2008; *Stawiarski et al.*, 2013; *Vasiljević et al.*, 2017; *Whiteman et al.*, 2018; *Wildmann et al.*, 2018; *Haid et al.*, 2020; *Adler et al.*, 2020, 2021). Driven by the demand for cost efficient and mobile profile observations of the three-dimensional wind speed components by the wind energy industry, Doppler lidar systems have become comparably lightweight and affordable.This development in lidar technology has enabled the possibility for more advanced setups in remote locations, e.g. offshore (e.g. *Peña et al.*, 2009), and particularly on moving platforms, such as buoys (e.g. *Gutiérrez-Antuñano et al.*, 2017; *Viselli et al.*, 2019; *Kelberlau et al.*, 2020) and ships (e.g. *Wolken-Möhlmann et al.*, 2014; *Achtert et al.*, 2015; *Gottschall et al.*, 2017, 2018; *Zentek et al.*, 2018). Such installations are, however, exposed to platform motion, and require compensating measures, that are either included in the installation and actively compensate the motion (e.g. *Achtert et al.*, 2015), or are part of a post-processing procedure (e.g. *Wolken-Möhlmann et al.*, 2014; *Kelberlau et al.*, 2020). As lidars provide first and foremost a one dimensional perspective (literally), achieving profiles or cross-sections of the three-dimensional wind with Doppler lidars requires the application of scan patterns that are subject to certain assumptions (i.e. profiling lidars assume horizontal homogeneity of the flow). Here, some limitations appear for the utility of the lidar observations, i.e. small scale turbulence of the three wind components can not be resolved simultaneously by the standard lidar profiling technique and also the more advanced scanning techniques are limited to observe turbulence (*Sathe et al.*, 2011; *Sathe and Mann*, 2013). Even though convective structures are on the large scale end of the turbulent velocity spectrum, the ability of lidar to sufficiently capture the three-dimensional structure of the convective circulation is only sparsly studied and not yet utilized to its full potential.

In the past, lidars have demonstrated their capabilities to obtain the trace of convective updrafts from aerosol-backscatter (e.g. *Kunkel et al.*, 1977; *Melfi et al.*, 1985; *Atlas et al.*, 1986) and the gradient of the backscatter is commonly used to estimate the depth of the CBL (*Wilczak et al.*, 1996; *White et al.*, 1999; *Hägeli et al.*, 2000; *Martucci et al.*, 2007; *Emeis et al.*, 2008). Further, vertically pointing lidar observations are utilized to study the integral length scales, turbulence statistics, and spectra of vertical velocity in the CBL (*Lothon et al.*, 2006, 2009; *Adler et al.*, 2019). These approaches rely on the presence of advection and the existence of rather stationary convective structures, such that Taylor's Hypothesis of frozen turbulence can be applied (see e.g. *Han et al.*, 2019), yielding a time series of convective structures that pass the lidar observational volume. In the absence of advection, a time series of at least two-dimensional cross-sections is required to capture the evolution of the entire convective circulation. Several studies identified the presence of convective structures as convergence and divergence pattern in the horizontal velocity field. *Yoshino* (2019) utilized horizontal scans of a single lidar that, however, only provided a one-dimensional velocity estimate and required additional simulations to confirm the convective patterns. *Newsom et al.* (2005), *Iwai et al.* (2008), and *Adler et al.* (2020) identified convective structures based on the horizontal velocity vector retrieved within a plane of horizontally overlapping dual-lidar observations, that also allowed to obtain vertical velocity estimates based on continuity. Here, only *Iwai et al.* (2008) provides vertical velocity estimates for multiple altitudes. However, the time required to achieve this three-dimensional representation of the convection exceeds the typically expected evolution period of the convective structures. Further, vertical cross-sections from coplanar lidar observations, documenting the convective circulation, are obtained by *Röhner and Träumner* (2013), who, however do not make use of the cross-section, but constrain the analysis to one dimension.

As a consequence to the shortcomings of earlier lidar approaches, the focus of this dissertation is on investigating and optimizing the setup, scan procedure and processing of profiling and scanning lidar systems for the characterization of convective circulation in marine environments and over land. The three published papers, this dissertation is based on, assemble the major scientific implications of the utility of these lidar systems, respectively. The papers are presented in chronological order, mirroring the scientific focus and progression of the dissertation over time. Here, the papers I and II address the capability of profiling lidars in a marine environment utilizing a ship-based lidar installation. Paper I focuses on the technical realisation, hence the lidar capabilities to successfully sample convection from a moving platform and data processing procedures, that are further evaluated in section 6.1. Paper II presents and investigates lidar observations of the convective flow and corresponding estimates of convective properties in the marine atmospheric boundary layer. This profiling lidar approach to sample convection is, however, limited to cases of strong and consistent advection with a horizontally homogeneous heat source at the surface. Such conditions are common over the ocean, e.g. during CAO events, yet sparsely found over land. To capture the typical land-based convection, a different approach based on dual-scanning lidars was selected. The knowledge acquired during the work on papers I and II contributed to and inspired the design of the lidar deployment in three field campaigns. Paper III introduces both the technical background, documenting the data processing procedures, and presents an estimate and analysis of the convective flow field captured during two of the three field campaigns that had very similar scanning dual-lidar setups. Following up on Paper III, section 6.2 presents the setup and some first results from the third field campaign, which featured a more advanced lidar installation and complementing meteorological measurements.

2 Objective and Reseach Questions

The primary objective of this dissertation is to investigate and quantify the potential, and the limitations of profiling and scanning lidars to deepen our understanding of the dynamic characteristics of atmospheric convection. Here, the individual studies focus on assessing the different lidar types and the respective requirements to characterize convection in different meteorological settings, guiding the following research questions (RC):

1. What are the limitations of each lidar type and have these lidars the reqired capabilities for effective convection research, despite the identified limitations?
    (a) What are the limitations of moving, motion-impacted profiling lidars to characterize convection in the marine atmospheric boundary layer?
    (b) What are the limitations of dual-scanning lidars to characterize convection in flat and complex terrain?
2. How can the lidar setup and lidar data processing be optimized to mitigate the identified limitations and achieve high quality data for the characterization of convection?
3. What are the advantages of profiling and scanning lidars over conventional meteorological instrumentation and measurement setups to sample convection?
4. Which convective properties can be extracted from profiling and scanning lidar observations?
5. How does atmospheric convection interact with other boundary-layer processes and parameters?
    (a) How does convection manifest for different background conditions (ocean vs. land, different initial conditions, topography etc.)?
    (b) What is the impact of convective structures of different sizes and strength on boundary-layer growth, overturning, and development of stability?

Paper I addresses RC-1.a and RC-2. Paper II addresses RC-1.a, RC-3, RC-4, RC-5.a and RC-5.b. Finally, Paper III addresses RC-1.b, RC-2, RC-3, RC-4 and RC-5.a. A resolution to and further perspectives on RC-1, RC-2, and RC-3 are presented in Sect. 7.1, and Sect. 7.2 addresses RC-3, RC-4 and RC-5.

3 Background

3.1 Convection

Thermal convection describes the buoyancy-driven vertical motion of a fluid against stabilizing effects, i.e. viscosity, or gravitation (*Bergé and Dubois*, 1984). Convection is an important process in the atmosphere, but also in fluids physics in general. First experimental studies on thermal convection were performed by Henri Bérnard (*Bénard*, 1900). Then, Lord Rayleigh (*Rayleigh*, 1916) presented a first theoretical approach to explain Bénards observations. *Bergé and Dubois* (1984) summarized the findings of Bénard and Rayleigh and explained the physics and dynamics of "Rayleigh-Bénard" convection, utilized here to explain the general conditions required for the initialization of convection:

Rayleigh-Bénard convection is one of the simplest forms of convection. Generally, it is described by the motion of an isotropic fluid, with temperature-independent properties except for density (Boussinesq approximation), that is confined by two rigid plates of good thermal conductivity above and below. A requirement for the onset of Rayleigh-Bénard convection in any fluid is the presence of a vertical temperature, and hence vertical density gradient. Yet, in equilibrium, where the temperature and density gradients are horizontally homogeneous, there will be no forcing on the fluid particles and hence no onset of convective motion. Only an additional local perturbation in temperature (and density) can force the onset of convection. The required strength of this perturbation is dependent on the Rayleigh-number:

$$Ra = \frac{\tau_\nu}{\tau_C} \tag{3.1}$$

which describes the ratio of diffusive time scale to convective time scale of the perturbation, where τ_ν is the diffusive relaxation time (s), τ_C is the convective time scale (s). The condition for the onset of convective motion, independent of the fluid, is that Ra exceeds a critical value ($Ra_c = 1707$), which ensures that convective transport is much faster than diffusive transport in the fluid. (*Bergé and Dubois*, 1984)

The onset of the convection, more specifically the location of the perturbation determines the convective motion pattern. During equilibrium conditions, in the idealised fluid setup with a heated plate as the lower boundary and a cooled plate as the upper boundary (see Fig. 3.1), upward motion has the same probability as downward motion. In this idealised case, convection can therefore start with an upward motion due to perturbation (local decrease in density) at the bottom or a downward motion due to perturbation (local increase of density) at the top of the domain (bifurcation). In an experimental setup, small imperfections and lateral boundaries decide the branch of the bifurcation. After the onset, a circulating pattern with both updraft and downdraft evolves. The evolution of the pattern is dependent on the Prandtl-number of the fluid:

$$Pr = \frac{\tau_{th}}{\tau_\nu} \tag{3.2}$$

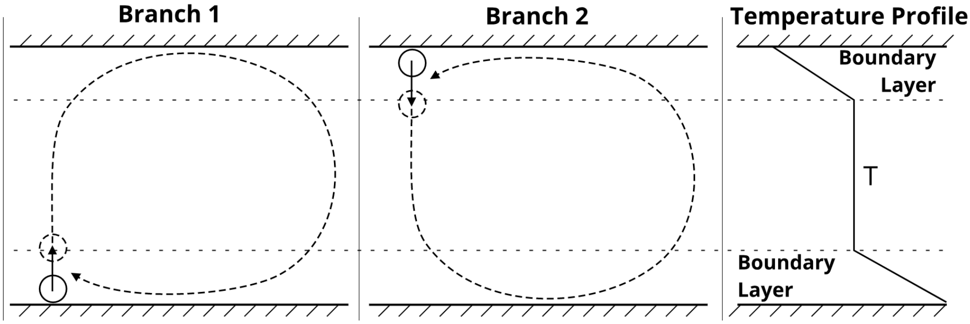

Figure 3.1: Bifurcation of the onset of convective motion in an idealised setup between two rigid plates, where the bottom plate is heated and the top plate is cooled. Left: Branch 1 corresponds to temperature (density) perturbation in the bottom boundary layer, initializing the convective circulation with an updraft. Middle: Branch 2 corresponds to temperature (density) perturbation in the top boundary layer, initializing the convective circulation with a downdraft. Right: Idialized temperature profile between the two rigid plates. (Based on Bergé and Dubois, 1984, adapted from Figure 22)

which describes the ratio of momentum diffusivity and thermal diffusivity, where τ_{th} is the thermal relaxation time (s). For large Pr (buoyant forcing), momentum diffuses faster than temperature and the velocity perturbations follow the temperature perturbations. For small Pr (inertial forcing), the temperature perturbation relaxes faster than the velocity perturbation, that may persist even after the temperature perturbation vanished. (*Bergé and Dubois*, 1984)

In contrast to the idealised case, fluid properties, such as the viscosity are dependent on the fluid temperature (non-Boussinesq convection). Viscosity increases with decreasing temperature at the upper boundary, yielding smaller Ra. Hence upward motions at the onset of convection are usually favoured. The typical hexagonal shape[1] of "Rayleigh-Bénard" convection or convective "rolls" which form in the presence of high Pr numbers, can be attributed to non-Boussinesq convection (*Bergé and Dubois*, 1984). These convective structures are highly organized and usually studied in laboratory experiments, but similar organization of the convective circulation may also occur in the atmosphere (see Sect. 3.2 and *Cieszelski*, 1998). The eventual organization of the convective circulation patterns in the atmosphere is strongly dependent on the initial conditions of the flow and a small perturbation of these initial conditions may change the resulting flow field completely. This property of atmospheric convection was demonstrated by *Lorenz* (1963), who discovered deterministic chaos while numerically solving a simplified mathematical system initially outlined by *Saltzman* (1962) used to describe atmospheric convection.

In the atmosphere, convection may be initialised by a density perturbation, that results from a locally increased buoyant forcing due to surface heterogeneities, yet also inertial forcing (e.g. lifting over mountain, shear turbulence generated by change in surface roughness, convergence lines, or a cold-pool gust front) may

---

[1] A famous example of the remnant of Rayleigh-Bénard convection in lava is the stone formation "giants causeway" that features "frozen", hexagonal Rayleigh-Bénard structures

cause the onset of convective circulation (e.g. *Jeevanjee and Romps*, 2015; *Liu et al.*, 2023). The acceleration and maintenance of velocities of the atmospheric convective circulation mainly result from the balance between archimedian buoyancy, B, and the gradient of the pressure perturbation, $\partial_z p'_s$, (see Fig. 3.2) that is created as a reaction from the environment to the acceleration of the buoyant parcels (*Jeevanjee and Romps*, 2016). The effective buoyancy, β, that combines the balance of the accelerating forces B and $\partial_z p'_s$, of an air parcel decreases with increasing aspect ratio D/H (D: diameter, H: height) of the convective updraft. Further, β decreases with time, as the convection develops internal circulation, causing inertial forces to gain importance, and entrains environmental air. Eventually, drag forces are expected to cancel the buoyant accelerations yielding a terminal updraft velocity. Convection with bubble characteristics, as well as thermal[2] characteristics can solve the balance of the convective forces, yet each results in different terminal updraft velocity profiles and hence has different implications for the transport in the CBL.(*Jeevanjee and Romps*, 2016)

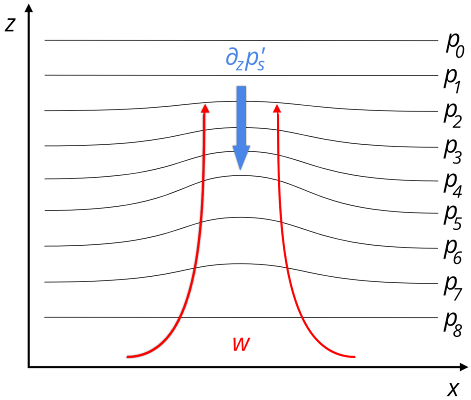

Figure 3.2: Vertical acceleration due to archimedian buoyancy, B, pushes up the pressure contours, creating a non-hydrostatic pressure anomaly, p'_s. The resulting gradient of the pressure perturbation, $\partial_z p'_s$, works against the vertical velocity acceleration forces of B.

3.2 The convective atmospheric boundary layer

In the atmosphere of our planet, convection is most prominent in the boundary layer. A detailed introduction on this lowest part of the atmosphere, which is directly impacted by the planet's surface, including the CBL state and evolution, is given by *Stull* (1988):

The CBL is characterized by buoyancy dominated turbulence generation, where larger buoyancy-driven eddies can take the form of convective plumes, thermals, or bubbles (e.g. *Young*, 1988a). Both over land and over the ocean, three layers of distinct characteristics with respect to the vertical behavior of the mean atmospheric parameters, i.e., temperature, humidity and wind, can be de-

---

[2] here: continuous stream of convective air

fined throughout the depth of the CBL: the surface layer, the mixed layer and the entrainment zone (see Figure 3.3).

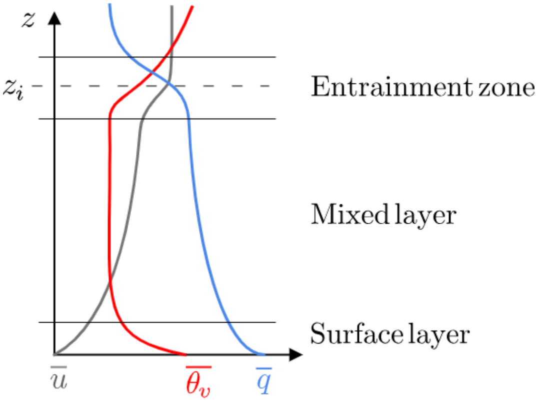

Figure 3.3: Mean Structure of the CBL characteristics: mean temperature, humidity and wind in the surface layer (5%–10% of CBL depth, z_i), the mixed layer (35%–80% of z_i), and the entrainment zone (10%–60% of z_i). Based on Stull (1988), Figure 11.1

The surface layer is characterized by large vertical gradients of temperature and humidity, that are decreasing with height, and strong wind shear. Here, passing surface layer plumes, that are of the order of the surface layer depth (≈ 100 m), superimpose a gustiness on the instantaneous wind profile (*Stull*, 1988). The horizontal extent of these plumes covers less than half of the area in the surface layer (e.g. *Wilczak and Tillman*, 1980), where they merge and eventually form larger diameter thermals in the mixed layer (*Kaimal et al.*, 1976).

Convective thermals (or bubbles) are responsible for the major transport of heat, moisture, and momentum, etc., from the bottom to the top of the CBL, z_i, where updrafts commonly feature vertical velocities between 1 m s^{-1} and 2 m s^{-1} (*Stull*, 1988), yet also convective core velocities of 5 m s^{-1} or higher have been reported (e.g. *May and Rajopadhyaya*, 1999; *Pálenik et al.*, 2021). In addition to the enhanced vertical mixing, lateral entrainment mixes environmental air into the sides of the convective updraft by small eddies, while the updraft core usually stays undiluted. Horizontal transport is strongest in the convergence zone under the thermals and in the divergence zone above. The horizontal extent of the thermals' circulation, that commonly consist of strong narrow updrafts and gentle wide downdrafts, is usually larger than z_i (e.g. *Young*, 1988a; *Stull*, 1988; *Cieszelski*, 1998). Throughout the mixed layer, the number of well-defined updrafts decreases with altitude, indicating that not all succeed to rise to the top. As the updraft diameter usually increases with altitude, a merging of individual updrafts is also a plausible explanation (e.g. *Williams*, 1993; *Renfrew and Moore*, 1999).

The convective updraft often picks up aerosols or pollutants at the surface. During the first hours after the convective onset, these particles make good tracers of the thermal updraft in, e.g., lidar observations (e.g. *Kunkel et al.*, 1977; *Melfi et al.*, 1985; *Atlas et al.*, 1986, and see Fig. 3.4). Past observations with aerosol lidar suggested that convection is mostly resembled by thermal columns that persist for some time, rather than bubbles (*Kunkel et al.*, 1977). Yet, without complementing velocity observations, there is no ruling out the possibility that traces of aerosols or pollutants remain even after the convective updraft has passed. Eventually, usually around noon, the particles become uniformly mixed

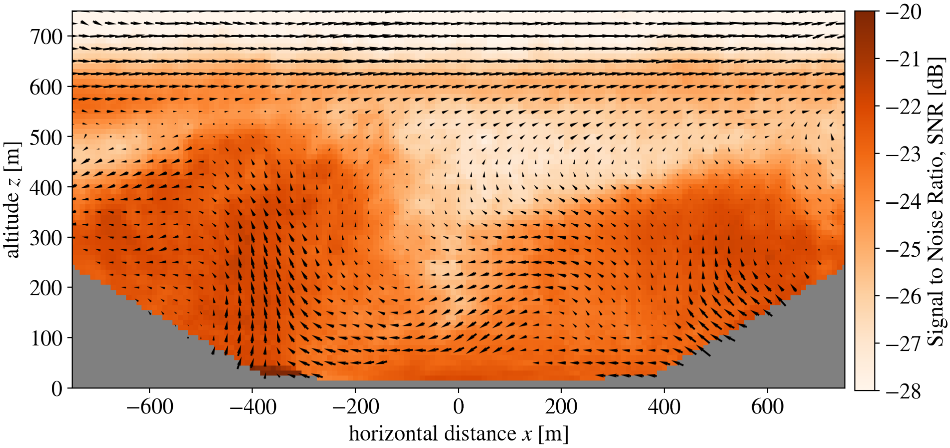

Figure 3.4: Dual-lidar observation of signal to noise ratio (SNR) and retrieved velocity field in a vertical cross-section, above Vaksinen Airport, Os, Norway on 2021-05-28 at 9 UTC (see Paper III). Increased SNR is an indicator for increased aerosol content: Aerosols are transported into higher altitudes by the convective updrafts. Here, the boundary-layer depth, the boundary to the free atmosphere (stronger, persistent wind velocity and low aerosol content), follows the shape of the thermals (highest extent above updraft).

throughout the convective boundary layer and can not be used as clear tracers anymore.

The extensive convectively-driven vertical mixing results in nearly constant mean characteristics of temperature, humidity and even wind with height (see Fig. 3.3). However, when observing instantaneous profiles, these variables are not quite as uniform with height as the overturning of the mixed layer requires some time. The convective time scale of the typical thermal to circulate between surface and top of the mixed layer is in the order of 10 to 20 min, which is the time required to observe the mixed layer equilibrium characteristics sketched in Figure 3.3. (*Stull*, 1988)

The top of the convective mixed layer, z_i, is close to the center of the entrainment zone, where the capping inversion is strongest and the vertical heat flux is most negative. Here, an undiluted air parcel, which rises from the surface, e.g. in the core of a convective updraft, first becomes neutrally buoyant. Hence, an observation of the potential surface temperature and profile can be used to estimate z_i applying the "parcel method" introduced by *Holzworth* (1964) (see also "Convective Boundary-Layer Depth", Section 3.1.1 of Paper II). In nature, convective updrafts usually do not stop at, but tend to overshoot the capping inversion due to their inertial momentum, which they gained due to their buoyant acceleration in the mixed layer. These overshooting updrafts encapture less turbulent, free-atmosphere air and sink back down into the mixed layer. This vertical, "one-way" entrainment, that dominates the entrainment zone, is a mechanical process that deepens the mixed layer. (*Stull*, 1988)

The evolution of the convective boundary layer, is often depicted analogously to the mixed layer growth. Over land, diurnally returning warming of the surface in the morning usually initialises this growth. Here, the usually strong nocturnal stable layer is tough to penetrate for the initial plumes and boundary layer growth is slow at first. By late morning, however, the top of the mixed layer transitions into the residual layer[3] base and the convective updrafts are now unhindered to rise up to the capping inversion (see Fig. 3.5). Over the ocean, the growth of a mixed layer is often initiated by cold air advection over the warm ocean surface, which directly sets on rapid upwards motion and deepening of the mixed layer up to the capping inversion, with increasing fetch (e.g. *Brümmer*, 1996). During such cold air advection, the combined surface heating and strong winds can cause the convection to organize in horizontal helical circulations, known as horizontal roll vortices or rolls (observed e.g. by *LeMone*, 1973; *Atlas et al.*, 1986; *Hartmann et al.*, 1997; *Renfrew and Moore*, 1999; *Brilouet et al.*, 2017). These vortices appear as pairs of clockwise and counterclockwise helices, aligned almost parallel to the average wind direction. In the present of sufficient moisture, cloud streets may form above the updraft regions. As these rolls progress over the ocean, they gradually transform into a cellular pattern and eventually mesoscale cellular convection, often featuring honeycomb-like cloud patterns (*Atkinson and Zhang*, 1996). These cellular patterns bear a striking resemblance to laboratory Rayleigh-Bénard convection cells (see *Cieszelski*, 1998, and Sect. 3.1).

When convective updrafts reach as high as the capping inversion, the mixed layer growth decreases and mechanical deepening by one-way entrainment of free-atmosphere air is the main driver for further deepening of the mixed layer, both over land and over the ocean. Close to sun set over land, or as cold air advection ceases over the ocean, respectively, the temperature gradient in the surface layer neutralizes, or even becomes stably stratified, while the last weak bubbles in the upper mixed layer may still cause entrainment at the mixed layer top (*Stull*, 1988). Then, generation of convective motion decreases and inertial forcing of convective turbulence can not longer be maintained against dissipation (*Nieuwstadt and Brost*, 1986).

3.3 Boundary-layer parameters, measurements, and observations

3.3.1 Basic atmospheric variables

In order to describe the evolution and the processes in the boundary layer it is first and foremost important to measure the basic meteorological parameters. Among these, one of the longest and most extensively measured variables, especially of interest to us humans, is the air temperature, T. Air temperature is a measure of average kinetic energy of the molecular motion of atmospheric gases. The unit of T is Kelvin [K], where 0 K corresponds to the state of no molecular motion and 273.15 K to the triple point of water, for example. In situ measurements of T are prone to errors from exposure to solar radiation or insufficient ventilation. To decrease these errors, temperature sensors are often used with radiation shields. Some sensors are additionally ventilated or positioned to optimize natural ventilation by utilizing the atmospheric flow. Historically, temperature measurement

---

[3] the remainder of a convective boundary layer from the day before, mostly relevant for the land-based dirunal cycle

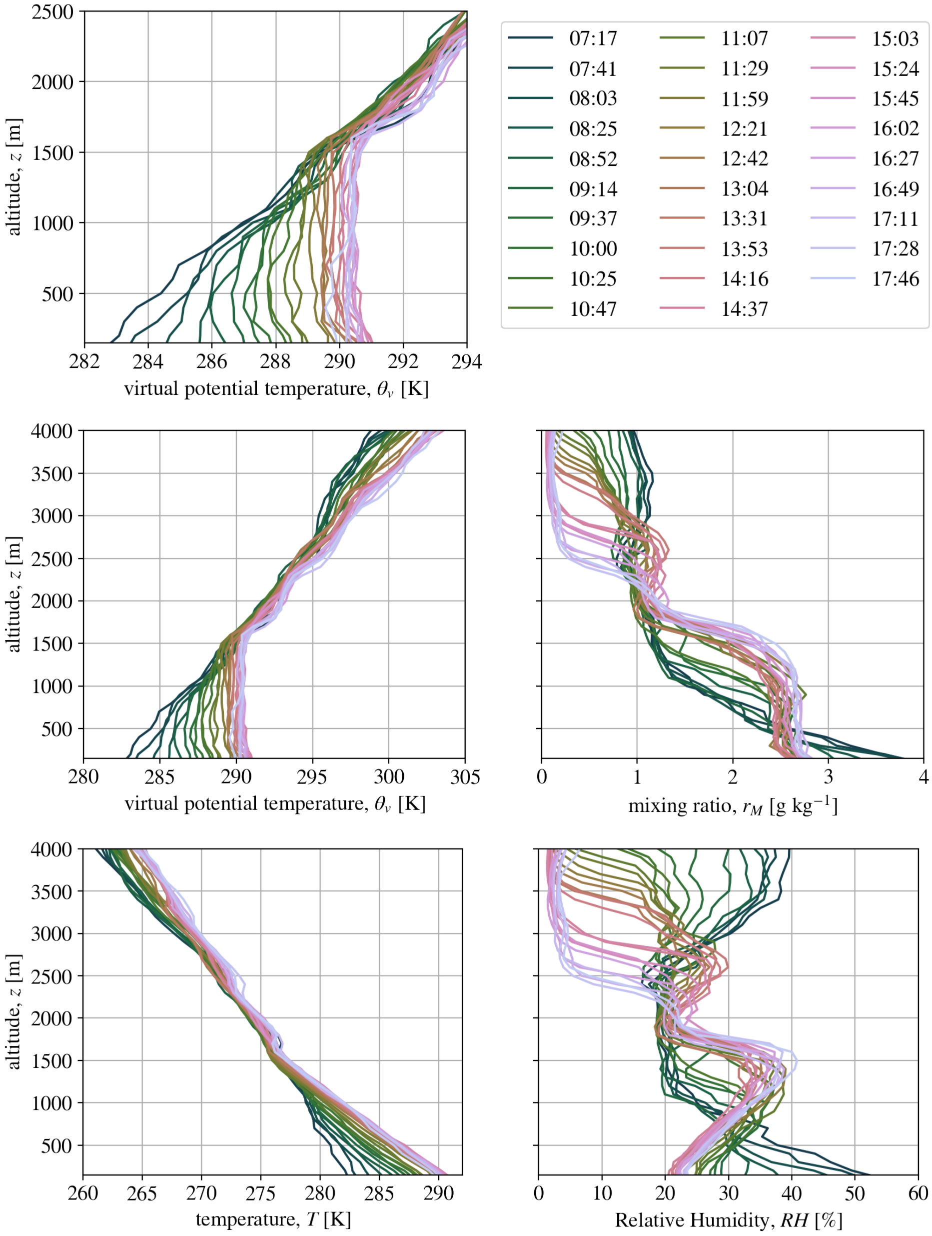

Figure 3.5: Temporal evolution of atmospheric variables in and above the CBL: virtual potential temperature profile, $\theta_v(z)$, with focus on the boundary layer (top left), and $\theta_v(z)$ up to 4 km (center left), mixing ratio, $r_M(z)$, up to 4 km (center right), temperature profile, $T(z)$, up to 4 km (bottom left), and relative humidity profile, $RH(z)$, up to 4 km (bottom right) in Voss, Norway over the course of 2022-05-16 (timestamp corresponds to start of profile [UTC]) measured by an iMet-XQ2 sensor attached to a skydiving plane (see Sect. 6.2).

relied on the expansion of liquids or solids (e.g. mercury thermometer), while nowadays resistance thermometers or sensors that rely on the speed of sound are almost exclusively used for atmospheric measurements. The Sonic anemometer (see Sect. 3.3.2), for example, can measure T based on the latter, acoustic principle. (*Foken and Bange*, 2021a)

Temperature sensors are frequently coupled with humidity sensors. This joint use of sensors is often used to correct and hence ensure the accuracy of the humidity measurements. Humidity describes the amount of water vapour present within the mixure of atmospheric gases. Various parameters are used to define the humidity of air (e.g. relative humidity, RH [%]; absolute humidity, a [kg m^{-3}]; dew point, T_d [°C]; mixing ratio, r_M [kg kg^{-1}]; specific humidity, q [kg kg^{-1}]; water vapour pressure, e [hPa]), where each parameter can be related to the other measures of humidity on the basis of e. In the past, humidity was obtained by a large variety of sensors and also today, still several methodologies to measure humidity are used: psychometric and capacitive sensors, as well as dew point and optical measurements. These sensors rely on thermodynamic principles, absorption of radiation, and material properties, respectively. (*Sonntag et al.*, 2021)

Though temperature and humidity have a greater direct impact on our human perception of the state of the boundary layer, atmospheric pressure, p, is probably the most important atmospheric parameter for weather prediction and many other atmospheric parameters are pressure dependent. Liquid and aneroid barometers, as well as hypsometers are historically used pressure sensors, while today electronic (capacitive), silicone-based barometers are the standard instruments for measuring p. Atmospheric pressure (measured in hectopascal [hPa]) refers to the force applied by the weight of the atmosphere, due to gravitational pull on the air molecules, per unit area. By implication, the pressure decreases with increasing altitude. The effect of this change in pressure on temperature (and humidity) is, for example, relevant to the formulation of the potential temperature, θ, and virtual (moist) potential temperature, θ_v:

$$\theta = T\left(\frac{P_0}{P}\right)^{R/c_p} \tag{3.3a}$$

$$\theta_v = \theta(1 + 0.61 r_M) \tag{3.3b}$$

where θ (or θ_v) describes the temperature value of a dry (or moist) air parcel if it were brought adiabatically to a reference pressure level, p_0, typically set at sea level ($p_0 \approx 1000\,\text{hPa}$). $R/c_p = 0.286$, where R is the gas constant and c_p the specific heat capacity of air, respectively. (*Torri et al.*, 2021)

Other relevant parameters in the atmospheric boundary layer are precipitation, measured e.g. by rain gauges, or disdrometers (*Cauteruccio et al.*, 2021), as well as shortwave radiation, measured by e.g. pyranometers and pyrheliometers, or longwave radiation measured by e.g. pyrgeometers (*Behrens*, 2021). The atmospheric parameter ”wind” combines the most important variables to describe the convective flow field and will therefore be introduced separately in the subsequent section.

3.3.2 Wind measurements

In contrast to the scalar variables introduced above, wind is a three-dimensional vector, (u, v, w). The horizontal wind, (u, v) is often depicted in polar coordinates, separated into wind speed, ws $[\mathrm{m\,s^{-1}}]$, and wind direction, wd $[°]$. When averaging ws and wd, it is required to transform to vector coordinates first, then perform averaging on the vector (u, v) and transform the averaged vector components $(\overline{u}, \overline{v})$ back to ws and wd using the following equations:

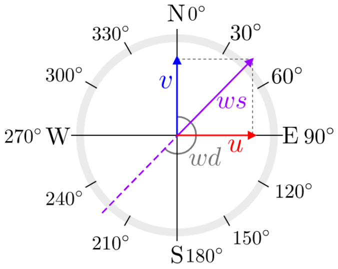

$$u = -ws \cdot sin(wd) \tag{3.4a}$$

$$v = -ws \cdot cos(wd) \tag{3.4b}$$

$$ws = \sqrt{u^2 + v^2} \tag{3.4c}$$

$$wd = \frac{180}{\pi} atan2(-u, -v) \tag{3.4d}$$

Note that in meteorology, wd is defined as the angle where the wind is coming from, hence the use of ”–” in Eq. 3.4a, b, d. Further, the arguments u and v in $atan2$ (Eq. 3.4d) may need to be switched around, depending on the utilized software[4].

Most prominent in situ wind sensors, such as mechanical cup anemometers or propeller anemometers measure ws with complementing measurements of wd obtained by wind vanes. Sonic anemometers, another often used wind sensor technique, measures the three- dimensional wind vector. Since sonic anemometers have a very high sampling frequency in the order of 10 to 100 Hz, they are often used for direct measurements of turbulence and turbulent fluxes by the eddy-covariance technique (*Lee et al.*, 2005). Figure 3.6 displays the wind sensors, used in the field campaigns presented in this dissertation. Other wind sensors, such as hot-wire anemometers, or Pitot tubes, are rather used in wind tunnels and not as commonly for atmospheric measurements, with one exception of the latter for the use on aircrafts. (*Foken and Bange*, 2021b)

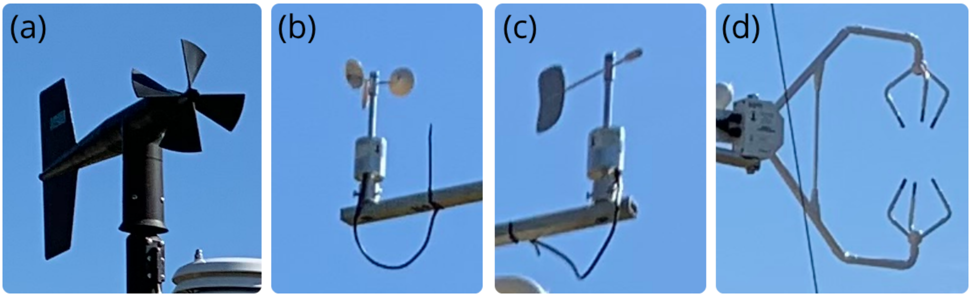

Figure 3.6: Propeller anemometer with wind vane (a), cup anemometer (b) used in combination with a separate wind vane (c), and Sonic anemometer (d)

---

[4] Here and all following uses of $atan2$: The order $atan2(-u, -v)$ in Eq. 3.4d is e.g. applicable for $numpy.arctan2$ of the $numpy$ package in python version 3.9.12

3.3.3 Boundary layer profiling

Sampling the characteristics of the boundary layer through a single-point measurement can neither represent the entire depth of the boundary layer nor capture the changes occurring across its layers (Sect. 3.2). A widely used method to measure a profile of atmospheric variables involves installing in situ sensors, as introduced in Sections 3.3.1 and 3.3.2, at different altitudes on a meteorological mast. The largest of these masts can be up to several hundereds of m high, providing a good coverage of the surface layer and the lower part of the convective mixed layer. Covering the whole convective boundary layer up to the entrainment zone is, however, unrealistic with such masts, both in terms of cost and structural engineering. After the initial installation, such tall masts are also rather immobile. (*Kolle et al.*, 2021)

Using airborne platforms is a viable alternative method to profile the entire depth of the convective boundary layer. One of the most prominent examples is the use of radiosonde soundings. In this method, a lightweight and compact system, typically equipped with sensors for temperature, humidity, pressure, and GNSS (Global Navigation Satellite System), is attached to a balloon filled with buoyant gas (Helium in modern usage or Hydrogen in the past). This balloon, released from the surface, is typically prepared to rise at an average rate of $5\,\mathrm{m\,s^{-1}}$. While ascending, the radiosonde repeatedly transmits collected atmospheric data and position to a ground-based receiving station. An estimate of horizontal wind speed and direction is estimated utilizing the changing coordinates obtained from GNSS. As the balloon ascends, its diameter expands due to the decrease in pressure with altitude, eventually bursting at altitudes typically ranging between 10 kilometers and 30 kilometers. During the descent, the radiosonde also gathers and relays atmospheric measurements. However, these measurements are generally considered less reliable than the ascending data and are not used extensively. If the radiosonde's touch down is over land, it may be recovered and reused. Unfortunately, many radiosondes get lost after use, causing expenses and environmental pollution. (*Vömel and Fujiwara*, 2021)

Similar to the radiosonde in terms of sensors and communication are dropsondes and tethersondes. Dropsondes are released from aircrafts and equipped with a parachute. Starting at the release altitude, atmospheric data is collected during the sonde's descend. A single, but also multiple tethersondes can be operated at different distances along the line of a thethered baloon. Vertical positioning is controlled by a ground-based winch and the range of the tether usually covers the depth of the boundary layer. In contrast to radiosondes, tethersondes are often equipped with cup or propeller anemometers and wind vanes to sample wind speed and direction. Since the tether poses danger to aviation, profiles are usually restricted to approximately 1000 m and measurements need to be monitored by an operator. There is also a rather strict operational limit, in the order of $10\,\mathrm{m\,s^{-1}}$, with respect to ambient wind speed. (*Vömel and Fujiwara*, 2021)

Another airborne approach that should be mentioned here, is the mounting of atmospheric sensor systems to unmanned aircraft (*Bange et al.*, 2021), as i.e. applied for the "Small Unmanned Meteorological Observer", SUMO project (*Reuder et al.*, 2009) and the "Sonic Anemometer on a MUlti-Rotor drone for Atmospheric turbulence Investigations", SAMURAI project (*Ghirardelli et al.*, 2023), as well as manned aircraft, e.g. motor planes, sailplanes, or paragliders. The latter, manned aircraft approach, will be discussed in greater detail in Section 6.2.

Observing the atmospheric profile without the need for physical extending structures or airborne installations is possible through the remote sensing technique. Remote Sensing utilizes either passive observations or active emissions of waves to retrieve information about the vertical structure of the atmosphere. Passive microwave radiometers, for example, observe the cumulative thermal emission of atmospheric gases (such as water vapor and oxygen) along their antenna path as "brightness temperature", T_B. More specifically, these gases absorb and emit at frequencies, corresponding to characteristic absorption lines in the microwave spectral range, that the radiometer receives at various frequency channels or bands. Different atmospheric gases exhibit different opacities to distinct frequencies within these channels. Through the Inversion technique (see e.g. *Rodgers*, 2000), it is possible to reconstruct the atmospheric profile of temperature and humidity – depending on the utilized channels – that resulted in the observed T_B. Microwave radiometers have a comparable long range (extending the boundary layer depth), with scanning techniques optimised for boundary layer profiling and provide time series of atmospheric profiles. Yet, in comparison to the single in situ profiles achieved by e.g. radiosondes, the profiles observed with radiometers are coarser and often smoothed, potentially underestimating the strengths of temperature or humidity inversions. (*Crewell et al.*, 2021)

Further relevant boundary-layer profiling based on the remote sensing is the sodar (Sonic Detection and Ranging) and RASS (Radio Acoustic Sounding System) technique. Sodar RASS is a combined system capable of measuring wind, turbulence, and temperature profiles in the boundary layer. The sodar actively sends out acoustic signals in the form of sound pulses. The sound pulses travel upward and are reflected by wind speed fluctuations aloft. The time the pulses require for a round trip back to the sodar (return time) are used to determine wind speed and direction at various altitudes based on the Doppler frequency shift of the returned signals (see Sect. 3.3.4 for further details). RASS combines the acoustic signal of sound waves with electromagnetic radio waves. Both sound and radio waves are affected by temperature: As the temperature varies with altitude, the radio waves encounter different refractive indices, while the speed of sound is directly affected by temperature. Following either the acoustic or radio signal, enables the determination of the other. Here, the return time also gives information about the origin altitude of the signal. (*Emeis*, 2021)

Boundary-layer profiling using radio waves, typically finds application with the radar (Radio Detection and Ranging). This active remote sensing technique is most prominent for sampling precipitation and clouds, based on the radar reflectivity returns of the respective precipitation or cloud particles. Yet, also the usage of radar for wind profiling is a common application. These radar wind profilers operate at wavelengths that are scattered at fluctuations in the refractive index of particle-free clear air (*Lehmann and Brown*, 2021). The wind retrieval is based on a similar concept as the sodar: the Doppler effect. The usage of this effect for wind observations is probably most characteristic for the lidar, the major remote sensing instrument applied and evaluated in this dissertation.

3.3.4 Doppler wind lidar

The invention of the laser by Theodore Maiman in 1960 quickly led to the development of lidar measurement techniques. Amongst backscatter lidar for aerosol and cloud detection (e.g. *Kunkel et al.*, 1977; *Chepfer et al.*, 2008), Raman lidar for water-vapour and temperature profiling (e.g. *Behrendt et al.*, 2002), and water vapour differential absorbtion lidar (e.g. *Wulfmeyer*, 1998), a new method for wind sampling was invented: the Doppler wind lidar. (*Reitebuch and Hardesty*, 2021)

Sampling the wind with Doppler wind lidar offers several advantages over conventional meteorological instrumentation (see Sect. 3.3.2). As a remote sensing technique, Doppler wind lidar allows the observation of wind speed without disturbing the atmospheric flow. Also, the observations can cover a substantial vertical and spatial extent of the atmospheric boundary layer, while the instrument samples at a relatively high frequency, typically in the order of 1 Hz. In particular the relevance of Doppler wind lidars in wind energy has accelerated the development of small, commercially available wind lidar systems. State-of-the-art Doppler wind lidars are usually ground-based, commonly used for wind energy site assessment and research (e.g. *Emeis et al.*, 2007; *Mikkelsen*, 2014; *Krutova et al.*, 2022), airport surveillance and safety (e.g. *Köpp et al.*, 2004; *Inokuchi et al.*, 2009), as well as research of the atmospheric dynamics (i.e. in complex terrain by a multitude of lidars during the Perdigão campaign, documented by by *Fernando et al.*, 2019), but can be operated from various platforms, including ships (*Gottschall et al.*, 2017, 2018; *Wolken-Möhlmann et al.*, 2014; *Achtert et al.*, 2015), aircrafts (*Rahm and Smalikho*, 2008; *Kavaya et al.*, 2014; *Witschas et al.*, 2017, 2020), and even from satellite (*Kanitz et al.*, 2019), to name some examples.

As the name suggests, the Doppler wind lidar makes use of the Doppler effect to measure atmospheric wind velocity. The Doppler effect describes a shift in frequency (or wavelength), that occurs when the source of the wave and an observer are in relative motion to each other. When using a Doppler wind lidar, this effect occurs twice, because the lidar is both actively emitting (source) and receiving (observer) the laser beam. Here, the light wave from the emitting laser source, with the frequency, f_0, is interacting with a moving particle (e.g., aerosol or cloud particle), being first sensed by the moving particle (observer) and then re-emitted (source) with the frequency, f_2, to be observed again by the lidar. The Doppler frequency shift, Δf,

$$\Delta f = f_2 - f_0 = 2 \cdot f_0 \frac{v_p}{c} \tag{3.5}$$

is determined by the speed of the moving particle, v_p, relative to the speed of light, c. The laser of conventionally used Doppler wind lidars usually emits at infrared wavelengths between $1.55\,\mu$m ($f_0 = 193$ THz) and $2.02\,\mu$m ($f_0 = 148$ THz), for which a frequency shift of $\Delta f = 1.29$ MHz, or $\Delta f = 0.99$ MHz, would correspond to $v = 1\,\mathrm{m\,s^{-1}}$, respectively. (*Reitebuch and Hardesty*, 2021)

During a sample interval, the lidar beam interacts not only with one, but with multiple particles within a certain atmospheric volume, each possessing its own velocity (see Fig. 3.7). This collective of particle velocities represents the wind velocity with added small-scale, random (turbulent) motion. Hence, the

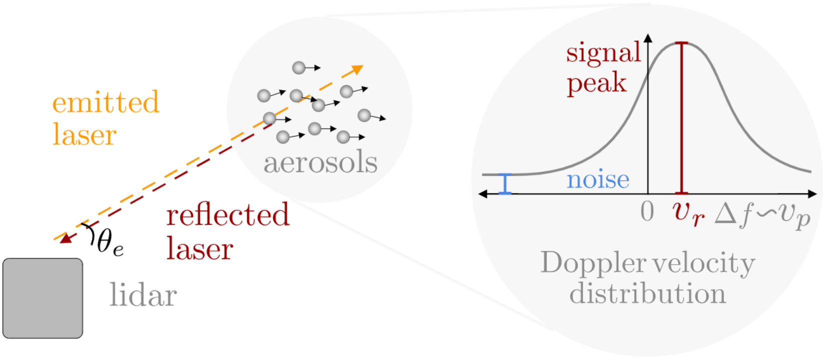

Figure 3.7: Schematic of the Doppler wind lidar measurement principle. Left: Lidar beam interacts with aerosol particles, that are moved by the average wind and local turbulence. Right: Idealised distribution of aerosol Doppler velocities over the lidar volume and sampling interval based on the frequency shift between emitted and returned laser signal.

lidar receives a distribution of Doppler frequency shifts (Doppler broadening) in the signals returning from the bulk of particles, with a peak at the Doppler frequency shift distribution, that is a measure of the wind velocity, averaged over the measured volume and sampling interval. The width of the Doppler frequency shift distribution (or Doppler velocity distribution, see Fig. 3.7) is a measure for the turbulent motion, superimposed on the average wind velocity.

The velocity peak observed by the lidar is the velocity of the wind, projected onto the Line-of-Sight (LOS) or "viewing direction", of the instruments laser. The direction of the LOS is usually defined in polar coordinates using elevation angle, θ_e, or zenith angle, θ_z=|90 - θ_e|, azimuth angle, α, and range, r (see Fig. 3.8). The velocity, that is measured along the LOS of the laser beam is called radial velocity, v_r, and is connected to the Cartesian wind speed components, u, v, and w as follows:

$$v_r(r,\alpha,\theta_z) = u(r)\, sin\,\alpha\ sin\,\theta_z\ +\ v(r)\, cos\,\alpha\ sin\,\theta_z\ + w(r)\, cos\,\theta_z \tag{3.6a}$$

$$v_r(r,\alpha,\theta_e) = u(r)\, sin\,\alpha\ cos\,\theta_e\ +\ v(r)\, cos\,\alpha\ cos\,\theta_e\ + w(r)\, sin\,\theta_e \tag{3.6b}$$

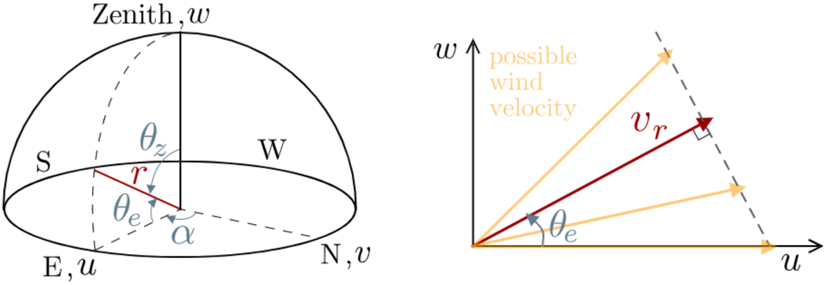

Figure 3.8: Polar coordinates (left): azimuth angle, α, elevation angle, θ_e, or zenith angle, θ_z and range, r. Radial velocity projection (right) in a vertical plane along the horizontal x-axis (u and w coordinates). All combinations of u and w along the gray striped line, that is perpendicular to the lidar's beam orientation, would result in the indicated radial velocity.

In addition to v_r, the variable "Signal-to-Noise Ratio", SNR, can be derived from the lidar observations, on the basis of the intensity of the velocity peak in relation to the noise intensity of the relevant spectral bandwidth (see Fig. 3.7). The SNR can be used as a measure for the density of aerosols in the boundary layer and for detection of clouds.

There are two main types of Doppler wind lidar technologies used today: the pulsed lidar and the continuous wave (CW) lidar. Over the past decades, the majority of technological advancements have been linked with long-range pulsed lidar systems (see Figure 3.9). Pulsed lidars can observe v_r simultaneously at multiple ranges, maintaining a constant range resolution even as the range increases. However, pulsed lidars encounter limitations in measuring at short distances. Typically the first distance at which v_r is measured is located at fifty to several hundred meters away from the lidar. CW lidar systems, on the other hand, focus solely on a single range. Within the first tens of meters, CW lidar exhibit high precision, with a range resolution in the order of centimeters. Nevertheless, their range resolution decreases considerably with increasing distance from the lidar and their range is typically limited to approximately 100 meters. The CW lidar finds applications in scenarios requiring high precision at short ranges, a niche not covered by the pulsed lidar, such as complementing observations in the lowest levels of the wind profile.

Figure 3.9: Left: profiling WindCubeV2 lidar installed on the research vessel Kristine Bonnevie during the 2019 cruise in Masfjord, Norway. Right: scanning WindCube100S lidar installed on Vaksinen airport, Os, Norway during the gLidar campaign 2021.

The range ($r = ct/2$) of a volume, where the laser beam of a lidar system (both pulsed and CW) interacts with aerosol or cloud particles, is determined by the time, t, the light wave travels between being emitted by the lidar, being scattered and re-emitted by the particle, and being picked up again by the lidar receiver. As the name suggest, pulsed Doppler wind lidar emit laser pulses of up to a few hundred ns pulse length, τ, with some pause in between the pulses. Here, the range resolution $\Delta r = c\tau/2$, is determined analogously to r, being proportional to the pulse length.

The Doppler wind lidars utilized in the studies included in this dissertation are almost exclusively pulsed lidars, with the two most prominent systems displayed in Figure 3.9: a profiling (WindCubeV2) and a scanning (WindCube100S) lidar, manufactured by Leosphere, a now Vaisaila owned company. The WindCubeV2 (Offshore) is a relatively short ranged ($r_{max} = 300\,\mathrm{m}$) wind profiler, that is equipped with an inertial motion unit (IMU) and a differential global positioning system (GPS) to sample high frequency information on the instrument attitude and motion. The comparably small size (ca. 55 cm wide, deep, and high, respectively) and low weight (ca. 55 kg) make the WindCubeV2 lidar system easy to install on and operate from moving platforms, such as buoys or ships. Here, the internal motion record enables corrections for motion induced observational errors (see Sect. 4.1.3). Nonetheless, the WindCubeV2 is restricted to a single scan pattern, which can primarily be used to retrieve the three-dimensional wind profile at several ranges, here altitudes above the instrument (see Sect. 4.1.1). The WindCube100S is substantially larger (ca. 1 m wide, deep, and high, respectively) and heavier (ca. 230 kg), yet comes with a considerably more powerful laser, with maximum ranges of a few kilometers, and the possibility to program flexible scan patterns (see Sect. 4.2.1) for various applications.

4 Methodology

4.1 Profiling lidar

4.1.1 Retrieval of the wind profile utilizing pulsed lidars

To obtain a profile of the tree-dimensional wind speed vector, $\mathbf{u} = (u,\ v,\ w)$ pulsed lidars generally use a scanning technique called "doppler beam swinging" (DBS). During a single DBS scan the lidar beam (constant $\theta_z > 0$) is subsequently oriented in four different $\alpha = (0°,\ 90°,\ 180°,\ 270°)$, with each beam rotated by 90° in comparison to the subsequent beam. For the WinCubeV2, the profiling lidar, that is most relevant to the studies included in this dissertation $\theta_z = 28°$, yielding a separation distance between opposing beams that is equal to the altitude. In contrast to the WindCubeV1, this newer, second generation of profiling WindCube lidars utilizes a fifth vertical oriented beam ($\theta_z = 0°$). Here, the range gates of the four vertically titled beams are programmed to be situated at the same altitude as the range gates of the vertical pointing beam. For pulsed lidars, measurements of v_r are obtained at all range gates simultaneously along a single beam, until the beam is rotated to the next position (α, θ_z), where another set of v_r is obtained at all range gates. The DBS cycle (see Fig. 4.1) is continuously repeated, with a return period of 3.8 s for the WindcubeV2.

The retrieval of $\mathbf{u}(z)$ requires the observation of at least three independent $v_r(z)$, to construct an equation system based on Eq. 3.6. With any additional observation of $v_r(z)$ included into the equation system, it becomes over-constrained.

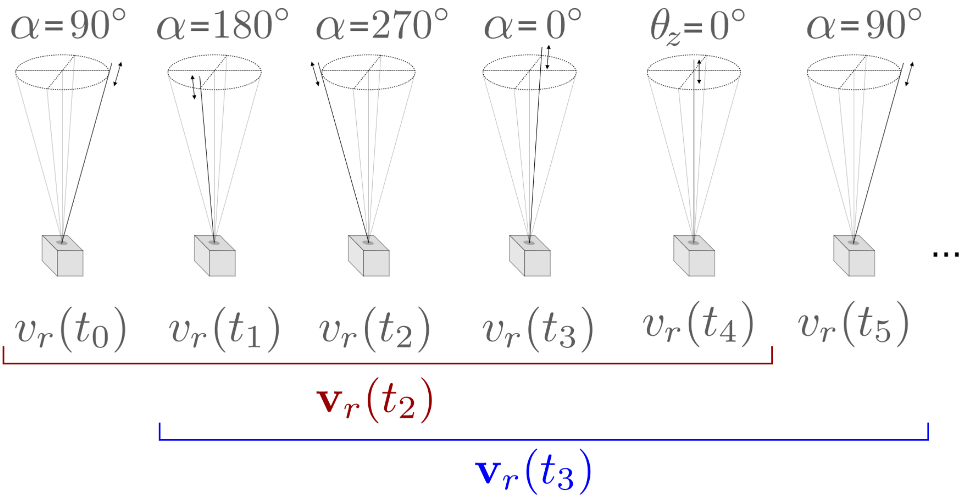

Figure 4.1: DBS scan cycle and corresponding construction of time dependent $\mathbf{v_r}$ *with the same time resolution as the continuous series of observed* v_r *values. Time step of* $\mathbf{v_r}$ *corresponds to the time step of the central utilized* v_r *value.*

Typically, $\mathbf{u}$ at a certain altitude, z, is retrieved on the basis of five[1] $v_r(z)$ corresponding to observations of a complete DBS cycle of the WindcubeV2 (see Fig. 4.1). The resulting equation system can be written as follows:

$$\mathbf{v_r} = \mathbf{N}\mathbf{u} \tag{4.1}$$

and an example for $\mathbf{v_r}$ and $\mathbf{N}$ is constructed corresponding to $\mathbf{v_r}(t_2)$ displayed in Fig. 4.1 (red highlight):

$$\mathbf{v_r} = \begin{pmatrix} v_r(\alpha\ =\ 90^\circ) \\ v_r(\alpha\ = 180^\circ) \\ v_r(\alpha\ = 270^\circ) \\ v_r(\alpha\ =\ \ 0^\circ) \\ v_r(\theta_z =\ \ 0^\circ) \end{pmatrix} \quad \mathbf{N} = \begin{pmatrix} sin(\theta_z) & 0 & cos(\theta_z) \\ 0 & sin(\theta_z) & cos(\theta_z) \\ -sin(\theta_z) & 0 & cos(\theta_z) \\ 0 & -sin(\theta_z) & cos(\theta_z) \\ 0 & 0 & 1 \end{pmatrix}$$

It is common to retrieve a time series of $\mathbf{u}$ with the same temporal resolution as the original v_r observations. To achieve this, the DBS scan is perceived as a continuous series. Here, each new $\mathbf{v_r}$ is constructed from the last four v_r observations used in the preceding retrieval time step and the next v_r time step in line (see Fig. 4.1). It should be noted, however, that the resulting estimate of $\mathbf{u}$ is still strongly dependent on the preceding time step (80% of v_r values are reused) and that this has a rolling-average effect on the retrieved series, an effect visible in the velocity spectra that is also discussed in Paper I.

To finally retrieve u, v, and w, the equation system defined in Eq. 4.1, needs to be solved $\mathbf{u}$. In the case of the example $\mathbf{v_r}$ and $\mathbf{N}$, that that is based on v_r from only five beams can be solved analytically, as also documented in Paper I,

$$u = \frac{v_r(\alpha =\ 90^\circ) - v_r(\alpha = 270^\circ)}{2 \cdot sin(\theta_z)} \tag{4.2a}$$

$$v = \frac{v_r(\alpha =\ \ 0^\circ) - v_r(\alpha = 180^\circ)}{2 \cdot sin(\theta_z)} \tag{4.2b}$$

$$w = v_r(\theta_z = 0^\circ) \tag{4.2c}$$

provided the beam that is oriented to geographic north corresponds to $\alpha = 0^\circ$. However, such analytical solution is rather unflexible, e.g., in case data from one beam is missing, if more than one DBS cycle is used for the retrieval, or if motion correction should be applied simultaneously to the retrieval. Therefore, the retrieval of $\mathbf{u}$ utilized in the studies included in this dissertation follow a more general applicable approach to define the equation system (Eq. 4.1)

$$\mathbf{v_r} = \begin{pmatrix} v_r(\alpha_1, \theta_{z,1}) \\ v_r(\alpha_2, \theta_{z,2}) \\ . \\ . \\ v_r(\alpha_n, \theta_{z,n}) \end{pmatrix} \quad \mathbf{N} = \begin{pmatrix} sin(\alpha_1)\, sin(\theta_{z,1}) & cos(\alpha_1)\, sin(\theta_{z,1}) & cos(\theta_{z,1}) \\ sin(\alpha_2)\, sin(\theta_{z,2}) & cos(\alpha_2)\, sin(\theta_{z,2}) & cos(\theta_{z,2}) \\ . & . & . \\ . & . & . \\ sin(\alpha_n)\, sin(\theta_{z,n}) & cos(\alpha_n)\, sin(\theta_{z,n}) & cos(\theta_{z,n}) \end{pmatrix}$$

where n corresponds to the number of utilized v_r values. A general solution of $\mathbf{u}$ for Eq. 4.1 is achieved by using the method of Least-squares (e.g. *Lai et al.*, 1978):

$$\hat{\mathbf{u}} = (\mathbf{N}^T\mathbf{N})^{-1}\mathbf{N}^T\mathbf{v_r} \tag{4.3}$$

where $\hat{\mathbf{u}}$ is the best estimate of $\mathbf{u}$.

---

[1] four $v_r(z)$ observations for the WindcubeV1

4.1.2 Motion impact on profiling lidar observations

In the case of an installation on a moving platform, e.g., a buoy or a ship, the profiling lidar is exposed to motion. This motion has six degrees of freedom, corresponding to rotational motion (pitch, φ; roll, ϕ; and yaw, ψ) around, as well as translatory motion (surge, sway, and heave) along the x, y, and z-axis, respectively (see Fig. 4.2). The motion impacts the observed v_r values and also the retrieved $\mathbf{\hat{u}}$ inherits this motion impact, if only the basic retrieval (Eq. 4.2 or Eq. 4.3) is applied.

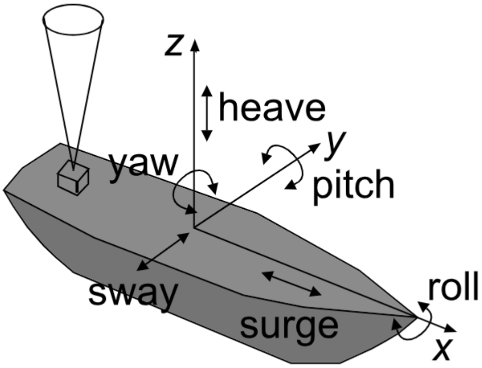

Figure 4.2: Six degrees of motion displacement, that a profiling lidar experiences on a vessel: Angular motion displacements (roll, ϕ, pitch, φ, and yaw ψ) around the x, y, and z axes and translatory motion displacements (surge, sway, and heave) along the x, y, and z axes.

The effect of rotational and translatory motion on the observed v_r values is displayed in Figure 4.3 for a one-dimensional example that only uses the u component (here, $v = 0$ and $w = 0$). In the absence of motion the u component is projected onto the LOS of the lidar beam, corresponding to θ_z, based on Eq. 3.6:

$$v_r = u\,sin(\theta_z) \tag{4.4}$$

If the beam is, however, tilted due to rotational motion (Fig. 4.3a), the orientation of the beam is altered (here, by φ) and hence also the projection of the observed radial velocity, $v_{r,o}$, changes to

$$v_{r,o} = u\,sin(\theta_z + \varphi) \tag{4.5}$$

Applying a basic retrieval to $v_{r,o}$, that still assumes that the beam is oriented with θ_z, results a different estimate, $\hat{u}$, than u.

If the lidar does not experience any rotational motion, but translatory motion, u_t, (Fig. 4.3b),

$$v_{r,o} = u\,sin(\theta_z) + u_t\,sin(\theta_z) = v_r + v_{r,t} \tag{4.6}$$

the retrieved velocity would differ from u by the amount of u_t:

$$\hat{u} = u + u_t \tag{4.7}$$

As the lidar on a moving platform is usually exposed to a combination of rotational and translatory movement (Fig. 4.3c), the observed $v_{r,o}$ can be described by:

$$v_{r,o} = u\,sin(\theta_z + \varphi) + u_t\,sin(\theta_z + \varphi) \tag{4.8}$$

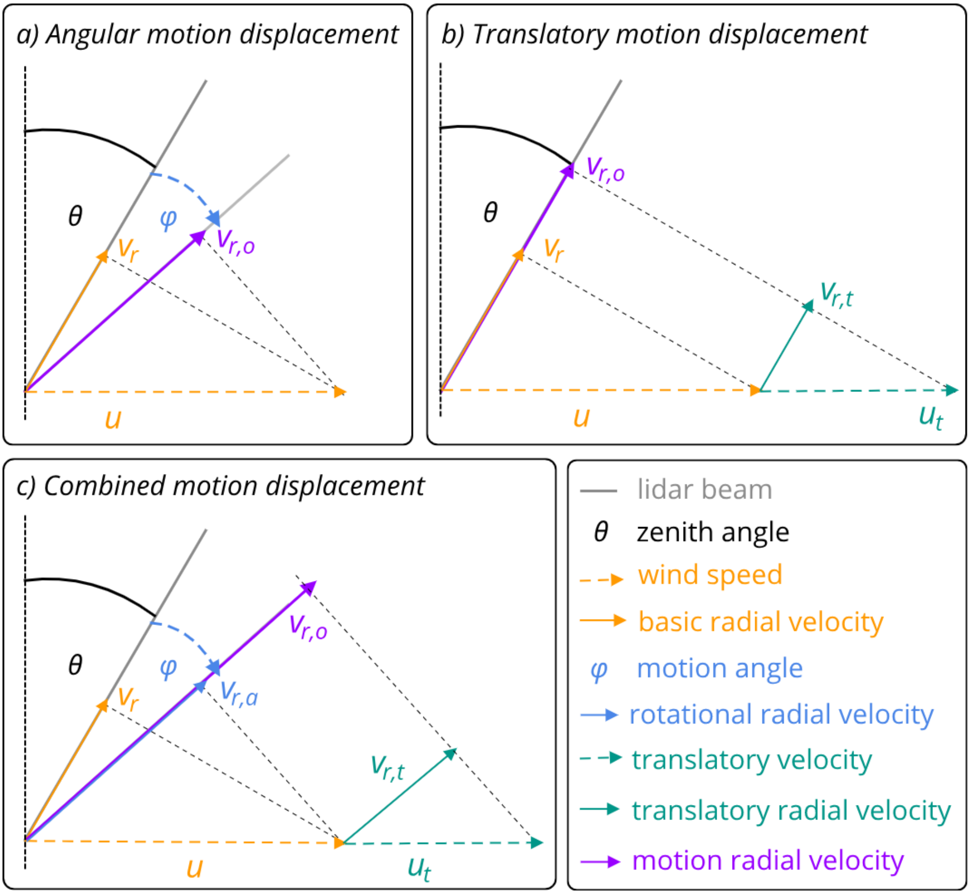

Figure 4.3: Motion impact on the radial velocity observation by a) angular motion displacement, b) translatory motion displacement, and c) combined motion displacement.

4.1.3 Motion correction of profiling lidar

If the lidar system is exposed to motion, the basic retrieval (Eq. 4.2 or Eq. 4.3) will result in an incorrect estimate of $\hat{u}$. Hence, the observations from such lidar installations need to be corrected, to remove the motion impact. A requirement for the application of motion correction is the measurement of the rotational and translatory motions. These measurements need to be precisely synchronised with and preferably of higher temporal resolution than the lidar observations. Such measurements are usually obtained by GPS and IMU, that combines gyroscopes and accelerometers to retrieve angular motion and velocities. The main lidar wind profiler utilized on moving platforms for campaigns relevant to this dissertation was the offshore version of the WindCubeV2. This lidar system includes an IMU system, combined with a differential GPS that obtains rotational and translatory motions, synchronised to the v_r observations, at a frequency of 10 Hz.

Motion correction can be applied to $\hat{\mathbf{u}}$ utilizing the measurements of the translatory velocity vector, $\mathbf{u_t}$, and the rotation matrix, $\mathbf{R}$, that specifies the rotation by the angular motion:

$$\mathbf{\hat{u}_c} = \mathbf{R}^{-1}\mathbf{\hat{u}} - \mathbf{u_t} \tag{4.9}$$

where $\mathbf{\hat{u}_c}$ is the motion corrected $\mathbf{\hat{u}}$ and $\mathbf{R}$ is constructed from multiplication of the rotation matrices $\mathbf{R}_x$, $\mathbf{R}_y$ and $\mathbf{R}_z$, that describe the rotational motion around the x, y, and z, respectively (*Edson et al.*, 1998).

$$\mathbf{R}_x = \begin{pmatrix} 1 & 0 & 0 \\ 0 & cos\phi & sin\phi \\ 0 & -sin\phi & cos\phi \end{pmatrix} \; \mathbf{R}_y = \begin{pmatrix} cos\varphi & 0 & -sin\varphi \\ 0 & 1 & 0 \\ sin\varphi & 0 & cos\varphi \end{pmatrix} \; \mathbf{R}_z = \begin{pmatrix} cos\psi & sin\psi & 0 \\ -sin\psi & cos\psi & 0 \\ 0 & 0 & 1 \end{pmatrix}$$

Estimating the radial velocity for the example case discussed in Sect. 4.1.2 ($u > 0$, $v = 0$, $w = 0$, $\varphi > 0$), on the basis of $\mathbf{R} = \mathbf{R}_y$ results:

$$v_{r,o} = u\,(sin\theta_z\, cos\varphi + cos\theta_z\, sin\varphi) \tag{4.10}$$

which resembles the expanded trigonometric form of Eq. 4.5 and confirms the validity to apply $\mathbf{R}$ for motion correction.

However, if angular motion is present around more than one of the principal axis (x, y, and z), the order of applied rotations influences the resultant $\mathbf{R}$, because the initial rotation will transform the two remaining axes, and so on. The discrepancy between the various angle systems, denoted as $\mathbf{R}i, j, k = \mathbf{R}_i \cdot (\mathbf{R}_j \cdot \mathbf{R}_k)$ is proportionate to the square of the rotation angle (*Thwaites*, 1995). To minimize the error of $\mathbf{\hat{u}_c}$, the multiplication of the rotation matrices is ordered, starting from the rotation around the axis corresponding to the smallest motion angle for each retrieval time step.

The basic approach for motion correction (Eq. 4.9) has the advantage that it can be applied to $\mathbf{\hat{u}}$, that is usually already processed by the computer that is integrated in the lidar system. However, the retrieved values correspond to an average (Sect. 4.1.1 and see Fig. 4.1), typically over the v_r observations from five beams. The basic approach will therefore apply motion correction that is of the decreased temporal resolution that corresponds to the averaging intervals. Yet, motion impacts each v_r observation individually and typically varies at higher frequencies than the return frequency of the averaging interval. Hence, to achieve a more accurate correction of the motion impact, the correction should be applied directly to the individual v_r observation, before any form of retrieval is applied.

To correct for translatory motion upfront, the wind retrieval, $\mathbf{u_t}$ needs to be transformed to the rotated coordinate system of the lidar, using $\mathbf{R}$ (that corresponds to the same time step as $\mathbf{u_t}$ and $\mathbf{u}$), and projected on to the LOS of each of the lidar beams using $\mathbf{N}$:

$$\mathbf{v_{r,t}} = \mathbf{N} \cdot (\mathbf{R} \cdot \mathbf{u_t}) \tag{4.11}$$

Then the v_r observations can be corrected by subtracting $\mathbf{v_{r,t}}$.

$$\mathbf{v_{r,c}} = \mathbf{v_r} - \mathbf{v_{r,t}} \tag{4.12}$$

Similar to Eq. 4.1, but including the motion impact, this translatory-motion corrected, radial velocity vector, $\mathbf{v_{r,c}}$, can be derived on the basis of $\mathbf{u}$ and $\mathbf{N}$, utilizing $\mathbf{R}$ to comprise the rotational motion impact.

$$\mathbf{v_{rc}} = (\mathbf{N} \cdot \mathbf{R}^T) \cdot \mathbf{u} \tag{4.13}$$

This equation system can be solved analogous to Eq. 4.3, using a least squares approach:

$$\mathbf{\hat{u}_c} = [(\mathbf{R} \cdot \mathbf{N})^T (\mathbf{R} \cdot \mathbf{N})]^{-1} \cdot (\mathbf{R} \cdot \mathbf{N})^T \cdot \mathbf{v_{r,c}} \tag{4.14}$$

It should be noted, that here, rotational-motion correction is applied during the retrieval, yet the entries in $\mathbf{R}$ (Eq. 4.13 and 4.14) still correspond to only a single time step within the return period of the DBS cycle, while translatory-motion correction is applied each time step of the DBS cycle. Motion impacted lidar data that is presented in the studies of this dissertation is corrected, using this second approach that applies translatory-motion correction before and rotational-motion correction during the wind speed retrieval. The corresponding code is made available within the python package *oblopy*[2].

4.2 Scanning lidar

4.2.1 Scan patterns

The simplest scan setting used by the scanning lidar is the "fixed LOS". Here, the scanning lidar obtaines a time series of v_r, while the scanner head is oriented towards a fixed set of α and θ_e. Usually, all points within the upper hemisphere (α between 0° and 360°; θ_e between 0° and 90°) and even some negative θ_e can be covered. The fixed LOS is, for example, used to obtain vertical velocity profiles with $\theta_e = 90°$ (e.g. *Lothon et al.*, 2006, 2009; *Adler et al.*, 2019). With information on wind direction, also a sequence of horizontal LOS ($\theta_e = 0°$) fixed to $\alpha = wd$ is applicable (e.g. *Cheynet et al.*, 2021). Finally, fixed LOS also find application in hard target alignment (see Sect. 4.2.4).

Similar to the profiling lidar (see Sect.4.1.1), also the scanning lidar can apply a DBS scanning pattern, that is a sequence of five single fixed LOS observations. In contrast to the profiling lidar, however, the scanning lidar must physically rotate its scanner head to change between the different fixed LOS orientations. The rotation of the scanner head takes considerably longer than the change in beam orientation for the profiling lidar. Hence, the order of the sequential beam orientations is optimised for the scanning lidar to take up as little time as possible. Still, one cycle of a typical DBS scan performed by a scanning WindCube-100S lidar takes approximately 11 s. In order to keep the separation distance comparably-small, θ_z is usually chosen to be considerably smaller (θ_z=15°) than for the profiling lidar, as the scanning lidar has a much larger range. As a consequence, the impact of the vertical wind speed component in the wind retrieval is increased. To estimate the three-dimensional wind speed from DBS observations obtained by the scanning lidar, the same retrieval algorithm as for the profiling lidar (Sect.4.1.1) can be applied.

In contrast to obtaining observations with a sequence of fixed LOS, the scanning lidar can also obtain observations while changing the beam's orientation. The plan position indicator (PPI) is one example of this sampling technique. Here, θ_e is kept constant, while α changes continuously with a certain angular speed

---

[2] author: Christiane Duscha, first published: 9. April 2021, url: `https://pypi.org/project/oblopy/`, last accessed: 17. November 2023

v_a ($^\circ\,\mathrm{s}^{-1}$). For each range gate, the v_r observation is derived from the bulk of particle velocities sampled during a selected integration time τ_i [s]. Consequently, the result is a velocity composite over a certain angular range $\Delta a = v_a \cdot \tau_i$ [°]. A full PPI scan corresponds to complete rotation from $\alpha = 0^\circ$ to $\alpha = 359^\circ$ (e.g. *Yoshino*, 2019), but also PPI scans with smaller azimuth sectors are commonly used (e.g. *Alcayaga*, 2020; *Krutova et al.*, 2022). A typical application for PPI is the observation of horizontal velocities with a "bird's eye" view using small θ_e, i.e., to observe wind turbine wakes (*Krutova et al.*, 2022). A special form of the PPI with large θ_e is the velocity azimuth display, VAD, that is used for wind profiling.

Similar to the PPI scan, the Range Height Indicator (RHI) scan uses a continuous sampling technique. Here, α is kept constant, while θ_e continuously changes with v_a. A full RHI scan corresponds to the realization of a cross-section or vertical slice, starting horizontally from θ_e=0°, over the zenith (θ_e=90°) until pointing horizontally again (θ_e=180°). The RHI scan provides information about the vertical structure of the atmosphere and is often applied to document the flow field in complex terrain (e.g. *Fernando et al.*, 2019; *Haid et al.*, 2020). Here, in particular the observations of SNR provide insight about the boundary-layer depth (see Paper III). Regions of the RHI scan with near horizontal pointing beams, up to approximately 30° elevation ($\theta_e < 30^\circ$ or $\theta_e > 150^\circ$), can provide a relatively good estimate of the horizontal, plane-parallel flow that is projected to the chosen α, while observations close to the zenith are representative for the vertical velocity component. To achieve estimates of horizontal, plane-parallel and vertical velocities throughout the cross-section, a more advanced approach is needed, requiring the use of at least two coordinated lidars (see Sect 4.2.2).

4.2.2 Coplanar dual-lidar retrieval

Combining the observations of multiple scanning lidars in a plane enables the estimate of at least two of the three wind speed components at several points in space and time. Such an estimate can be achieved by overlapping the scanned areas of at least two lidars (see e.g. *Newsom et al.*, 2005, 2008; *Stawiarski et al.*, 2013; *Adler et al.*, 2019; *Haid et al.*, 2020). The retrieval of the velocity components in the overlap region of the lidar scans can be set up similar to the DBS retrieval. Here, one velocity component can be dropped from Eq. 3.6 during the set up of the equation system for the two dimensional plane:

$$v_{r,RHI} = u_p\, cos(\theta_e) + w\, sin(\theta_e) \tag{4.15a}$$

$$v_{r,PPI} = \ u\, sin(\alpha) \ + v\, cos(\alpha) \tag{4.15b}$$

with Eq. 4.15a applicable for overlapping RHI scans and Eq. 4.15b for overlapping PPI scans. Here, it should be noted, that the u-component, u_p, of the overlapping RHI scans does not necessarily correspond to the u-component in the terrestrial frame, but to the horizontal velocity, projected on to the azimuth orientation of the RHI cross-section. Based on Eq. 4.15 the LOS-transition matrices are defined as follows:

$$\mathbf{N}_{RHI} = \begin{pmatrix} cos(\theta_{e,1}) & 0 & sin(\theta_{e,1}) \\ cos(\theta_{e,2}) & 0 & sin(\theta_{e,2}) \\ . & . & . \\ . & . & . \\ cos(\theta_{e,n}) & 0 & sin(\theta_{e,n}) \end{pmatrix} \quad \mathbf{N}_{PPI} = \begin{pmatrix} sin(\alpha_1) & cos(\alpha_1) & 0 \\ sin(\alpha_2) & cos(\alpha_2) & 0 \\ . & . & . \\ . & . & . \\ sin(\alpha_n) & cos(\alpha_n) & 0 \end{pmatrix}$$

The matrix format of Eq. 4.15a and b:

$$\mathbf{v}_{r,RHI} = \mathbf{N}_{RHI} \cdot \mathbf{u_p} \tag{4.16a}$$

$$\mathbf{v}_{r,PPI} = \mathbf{N}_{PPI} \cdot \mathbf{u} \tag{4.16b}$$

with $\mathbf{u_p} = (u_p, 0, w)$. Eq. 4.16 can be solved on a cartesian grid analogously to Eq. 4.3 using the method of least-squares (see *Cherukuru et al.*, 2015). Here, the respective radial velocity vectors, $\mathbf{v}_{r,RHI}$ and $\mathbf{v}_{r,PPI}$, contain all v_r observations from both lidars within a certain radius from the cartesian retrieval point (see Paper III for more detailed information).

The coplanar, scanning lidar approach is often used to estimate the horizontal wind speed components from two overlapping PPI scans, i.e. to estimate the flow in and around a wind farm (e.g. *Vollmer et al.*, 2015), or evaluate coherent structures in the horizontal wind field (e.g. *Newsom et al.*, 2008; *Stawiarski et al.*, 2015; *Träumner et al.*, 2015; *Adler et al.*, 2020). Yet, in this dissertation the vertical structure of the atmospheric velocities and, hence, the overlapping RHI scans are more relevant. Figure 4.4 shows the angular differences and the time differences of two perfectly synchronized RHI scans (see also *Stawiarski et al.*, 2013). Even

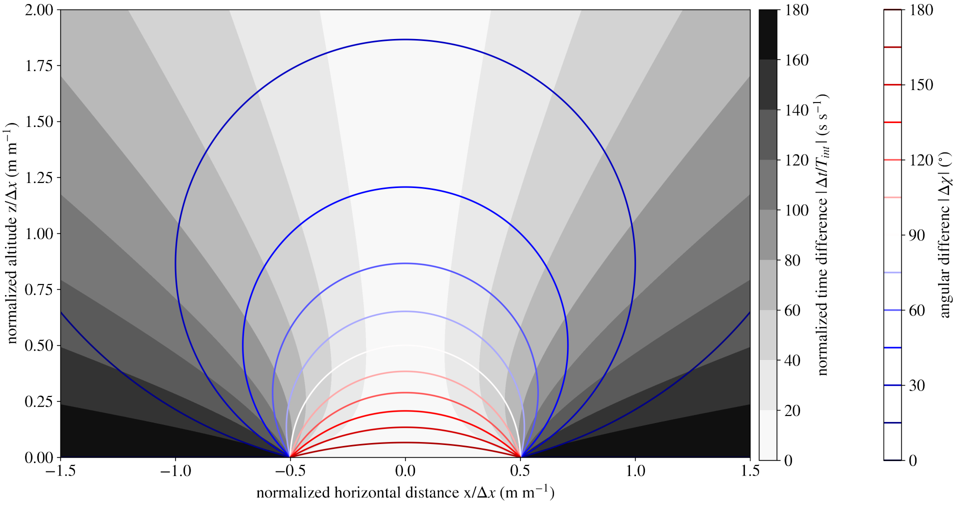

Figure 4.4: Estimates of the time difference Δt, normalized by the integration time T_int, as well as angle, $\Delta\chi$, between the two lidar beams at each point (x, z) normalized by the horizontal separation distance, Δx, of the lidars in the coplanar RHI cross-section. The two lidars are situated at (-0.5,0) and (0.5,0), respectively.

for perfectly synchronised scans, the observations only match in time above the center between the two lidars. Towards the sides, the time difference increases substantially (Fig. 4.4). If temporal interpolation is applied and instantaneous RHI scans are achieved (see Sect. 4.2.3 and Paper III), perfect synchronisation of the RHI scans is not necessary. Instead, time synchronisation of the lidars is utterly important, to ensure correct matching of the observations in each point of the coplanar cross-section.

A major source for error in the coplanar retrieval is miss-alignment of the lidars in the terrestrial reference frame. This error can be minimized by using a hard-target alignment approach (See Sect. 4.2.4). Any retrieval error is amplified by the factor $1/\sin^2(\Delta\chi)$, with $\Delta\chi$ being the angle between the two intersecting lidar beams (*Stawiarski et al.*, 2013), that is largest for points where the beams of the lidars are oriented parallel or near parallel to one another and smallest for $\Delta\chi = 90°$. The minimum error amplification is only achieved for a small section between the lidars and increases both towards the lower altitudes between the lidars as well as above and to the sides (see Fig. 4.4). The positions of these lidars should be separated by a sufficiently large distance, such that the respective α (for overlapping PPI scans), or θ_e (for overlapping RHI scans) are different by at least 30° ($150° > |\Delta\chi| > 30°$) in the same points within the area of interest. Because the data corresponding to the area of larges error amplification is not valuable, the dual-scanning lidars installed during campaigns relevant to this dissertation were programmed to scan only a partial RHI, reducing also the maximum time difference in between the scans, with maximum angular range between $\theta_e = 0°$ and $\theta_e = 150°$, or $\theta_e = 30°$ and $\theta_e = 180°$, respectively.

4.2.3 Data processing

The v_r data observed by lidars tend to be noisy in the case of low SNR, usually caused by low airborne particle content. Further, v_r observations of continuous scans (RHI and PPI) can feature erroneous "streak" patterns, namely range folded ambiguities, that result from incorrect range and velocity allocation of the lidar beam that interacts with distant objects, such as clouds (*Bonin and Brewer*, 2017). Finally, also obstacles in the LOS of the lidar beam cause erroneous patterns in the observed velocity field. Such errors in the v_r observations propagate and amplify in the dual-lidar retrieval (Sect. 4.2.2), if not filtered beforehand. A common approach to remove noise from the v_r observation, is to apply a filter to the data that removes all v_r observations that are below a certain SNR threshold. However, conservative SNR thresholds, that ensure a thorough noise filtering, typically also discard a comparably large amount of correct v_r data, when low SNR conditions are present. To overcome this disadvantage, the utility of a more advanced approach to filter the scanning lidar observations is applied in this dissertation. The approach utilizes the Density-Based Spacial Clustering of Applications with Noise (DBSCAN) approach[3] (*Ester et al.*, 1996) to separate noise, and erroneous features from correct data, successfully applied to scanning lidar observations by *Alcayaga* (2020). The approach takes advantage of the fact, that correct data points are typically organized into clusters in the scatter of v_r against

---

[3] Here the implementation of DBSCAN in the "scipy" python package (*Virtanen et al.*, 2020) was utilized

SNR, while noise or erroneous features usually are not clustered (see Paper III). For each scan, the DBSCAN approach identifies clusters in the v_r–SNR space, that includes all points that are within a density radius, ϵ, from each other, where ϵ contains at least a minimum number of points, n_{sample}. These points are the "core points" of the cluster. All points, that are within ϵ from the core points are also considered part of the cluster, even though there is less than n_{sample} points within ϵ from these "reachable points". All points not reachable with ϵ from the core points of a cluster in the v_r–SNR space are considered noise. The v_r values identified as noise by the DBSCAN filter are removed from the dataset.

The filtering and the associated gaps in the dataset demand for a gap-filling procedure. The necessity to eliminate the time lag within the dual-lidar cross-section (see Fig. 4.4) promotes the usage of temporal interpolation as a gap-filling procedure. Here, each v_r value in the polar coordinate system (r, θ), or (r, α) of the respective RHI, or PPI scan is interpolated linearly in time to the same point in space of a subsequent scan with available v_r observation. Here, the interpolated time series of each of these spacial points is stored for discrete points in time, that is of the same time resolution as the observations of each angle in the lidar scan. Hence, the result of this temporal interpolation is a series of instantaneous, gap-filled lidar scans. The improvement of these instantaneous scans compared to the originally obtained scan resolution is evaluated in Paper III. Further, the instantaneous scans from dual-scanning lidars, that match in time are further used in the coplanar retrieval (Sect. 4.2.2).

4.2.4 Hard target allignment

During the installation of a scanning lidar in the field, achieving exact alignment between the scanning lidar's internal orientation and the terrestrial reference frame, where the 0° beam aligns with North, is challenging and usually some initial misalignment remains. Typically, the scanning lidar does not provide yaw observations, hence a crucial step is to estimate the lidar's orientation relative to the terrestrial reference frame, that can be achieved by the hard target approach. Here, an isolated and comparably narrow hard target, such as a building, tree, or pole, in free LOS of the lidar, but in some distance to be beyond the first range gate of the lidar, is found or installed. Then, the geographical coordinates longitude, lon, and latitude, lat, of both the lidar and the hard target are precisely measured. This information on geo-location can be used to estimate the azimuth (α) from the lidar to the hard target in the terrestrial reference frame.

$$\alpha = atan2(a, b) \tag{4.17}$$

with

$$a = sin(\Delta lon) \cdot cos(lat_2) \tag{4.18a}$$

$$b = cos(lat_1) \cdot sin(lat_2) - sin(lat_1) \cdot cos(lat_2) \cdot cos(\Delta lon) \tag{4.18b}$$

$$\Delta lon = lon_2 - lon_1 \tag{4.18c}$$

$$\Delta lat = lat_2 - lat_1 \tag{4.18d}$$

Also the exact distance, d, between lidar and target can be estimated on the basis of the geo-location:

$$d = 2 \cdot R \cdot atan2(\sqrt{\gamma}, \sqrt{1-\gamma}) \tag{4.19}$$

with

$$\gamma = sin\left(\frac{\Delta lat}{2}\right)^2 + cos(lat_1) \cdot cos(lat_2) \cdot sin\left(\frac{\Delta lon}{2}\right)^2 \tag{4.20}$$

Here, a larger d compensates for errors in α, that are caused by inaccuracies in the measurement of the geo-locations.

To identify the relative angle, $\hat{\alpha}$, of the hard target to the lidar in the lidar's reference frame, a PPI scan with low angular resolution and a 10° to 20° angular coverage is initiated in the direction of the hard target. During these scans, the hard target appears as a distinctive peak in the lidar's carrier-to-noise ratio[4] (CNR) signal at the corresponding d and $\hat{\alpha}$. After identifying the approximate $\hat{\alpha}$, a new scan is set up with increased angular resolution (ca. one measurement every 0.1°) and smaller angular coverage (ca. 5°) centered around the preliminary estimate of $\hat{\alpha}$. This approach allows for a refined identification of the CNR peak and the logging of more detailed information on the $\hat{\alpha}$. To confirm the estimate of $\hat{\alpha}$, a fixed LOS series can be initiated, with the lidar's beam oriented directly towards $\hat{\alpha}$ and checked for increased CNR corresponding to d. Figure 4.5 shows an example of a hard target in LOS of the lidar and the corresponding peak in CNR as displayed by the visual interface of the lidar software.

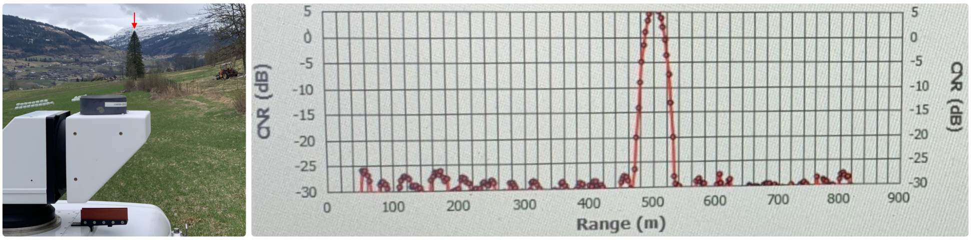

Figure 4.5: Left: Example of a tree ("Norbert") that was used as a hard target in the gLidar campaign in Voss, Norway, in April 2022. Right: CNR displayed in the visual interface of the WindCube-100S user software during the process of a hard target alignment.

With the detailed information on α and $\hat{\alpha}$, the offset between the two can be adjusted in the lidar's software, by rotating the lidar's reference frame by this offset. To ensure ongoing alignment of the lidar's orientation with the terrestrial reference frame, the PPI and fixed LOS scans are repeated daily. Any physical or electronic drifting of the lidar's orientation can be addressed directly in the field by correcting the offset in the lidar's software, or needs to be accounted for in post-processing and error estimates.

---

[4] Term used for signal-to-noise ratio, SNR, by the WindCube lidar series, manufactured by Leosphere

4.3 Characterization of convection

After retrieving the velocity components of the atmospheric flow, either contained in a time series of velocity profiles (profiling lidar), or within a series of two-dimensional vertical cross-sections (dual-scanning lidar), the next step is to identify the velocity patterns that are associated with atmospheric convection. Here, the data is evaluated for the characteristic circulating structure of convection, with areas dominated by vertical velocity: the updraft (convective core) and the downdraft, that are linked by a compensating horizontal flow. At lower altitudes, the convective circulation is dominated by horizontal convergence and entrainment into the updraft, while horizontal divergence dominates at the top of the updraft (see Sect. 3.2).

4.3.1 Spectral Coherence and Phase Analysis

Based on the characteristics of the convective circulation that are listed above, the along wind, cross-wind, and and vertical velocity fluctuations, u', v', and w', of such circulation are cross-correlated with a phase shift, $\Delta\rho_{ij} = \pm\pi/2$ (see Fig. 4.6), where i and j are placeholders for u' and w', or v' and w', respectively. Here, the sign of $\Delta\rho_{ij}$ depends on the direction of the horizontal component series (convergence or divergence).

A measure of cross-correlation and phase at certain frequencies or wavelengths are the coherence spectrum, Co_{ij}, and phase spectrum, ρ_{ij}, of horizontal and vertical velocity fluctuations. These measures can provide the information required to identify the presence and dimensions of convective circulation patterns, that occur periodically in the atmospheric flow field, and that are advected to the li-

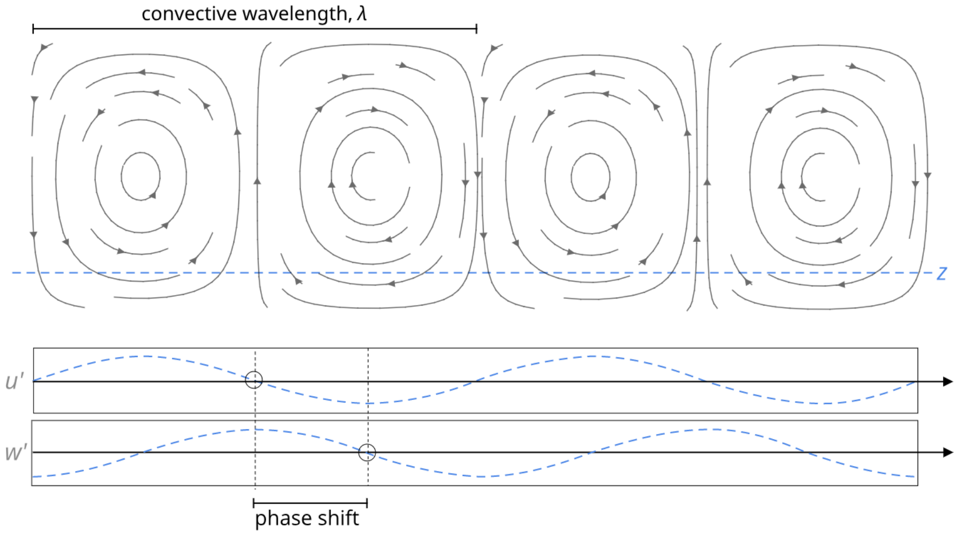

Figure 4.6: Side view of a convective circulation advected over the lidar by the mean wind (top) and corresponding horizontal (here u') and vertical velocity components at an altitude z in the lower part of the circulation (bottom). Adapted from Paper II (Figure 3).

dar's position (profiling lidar). The coherence and phase spectrum are estimated on the basis of the cross-covariance spectrum of i and j, G_{ij} its complex conjugate G^T_{ij}, and the respective auto-correlation spectra of i and j, G_{ii} and G_{jj} (*Emery and Thomson*, 2001):

$$Co_{ij} = \frac{G_{ij} \cdot G^T_{ij}}{G_{ii} \cdot G_{jj}} \tag{4.21a}$$

$$\rho_{ij} = \mathrm{atan2}[\mathrm{Im(G_{ij})}, \mathrm{Re(G_{ij})}]. \tag{4.21b}$$

A spike in Co_{ij} at a certain wavelength, λ, that indicates a sufficiently strong cross-correlation of horizontal and vertical velocity fluctuations ($Co_{ij}(\lambda)$ close to 1, or at least larger than 0.7), combined with a $\rho_{ij}(\lambda)$ within a 5° window around $\pm\pi/2$ are the necessary and sufficient conditions for the presence of a coherent convective circulation with horizontal size λ (based on *Hartmann et al.*, 1997). A more detailed documentation of the coherence approach to identify and characterize organised convection, as well as the correspondingly required processing of profiling lidar data is included in Paper II.

4.3.2 Single convective structure analysis

In particular over land, convection is rarely organised into structures of similar λ, nor advected over the lidar. As application of the spectral coherence and and phase approach requires these characteristics, a different approach is needed to characterize single convective structures.

The horizontal and vertical velocity field, $u_p(x,z)$ and $w(x,z)$ of the coplanar retrieval (Sect. 4.2.2) can be used to identify the presence and location of a convective circulation, in particular of the convective updraft. The conditions for the presence of a convective updraft is that the w, averaged over the lowest part (lowest 100 m to 300 m) of the circulation exceeds 0.5 m s^{-1}, while the horizontal derivative of u_p, the divergence, $\Delta u_p/\Delta x$, is negative (converging flow). The horizontal distance, at which the two conditions are fulfilled defines the initial updraft width. The point of largest convergence defines the triggering location for the convective updraft. The streamline, that originates from this location, describes the core of the convective updraft, which should be followed to investigate the change in w with altitude. Paper III illustrates this approach with an example case.

5 Introduction to the papers

Paper I: Statistic and Coherence Response of Ship-based Lidar Observations to Motion Compensation

Christiane Duscha, Mostafa Bakhoday Paskyabi, Joachim Reuder (2020),
Journal of Physics Conference Series, 1669/01

Ship-based, profiling lidar installations have been part of several field campaigns planned and conducted before and during the PhD period. These installations yield a large basis of wind observations to analyze in the remote, usually undersampled marine atmospheric boundary layer.

Paper I investigates the impact of ship motion on the profiling lidar observations and to which degree a standard motion correction can improve these observations. Emphasis is on investigating which temporal scales are unaffected by motion or sufficiently captured after motion correction, yielding insight into which atmospheric flow properties can be resolved by ship-based lidar observations, i.e. turbulence, convective structures, or solely the large scale wind.

A big disadvantage of ship-based lidars, if not installed on a motion-compensating platform (see *Achtert et al.*, 2015) is that the lidar is exposed to the motion of the vessel. Both the direct observations (radial velocity), as well as the retrieval of the three-dimensional wind are corrupted by the ship's motion (see Sect. 4.1.2). Paper I evaluates the error, utilizing basic statistical metrics, and investigates the impact of motion on the velocity and coherence spectra.

A simple, commonly used motion compensation is applied to the lidar observations (see Sect. 4.1.3). Further, the mean properties of the wind profile are compared against measurements from radiosondes, which notably are less reliable close to the vessel, estimating the statistical error metrics "bias" (systematic error) and "standard deviation error" (random error). While the bias is comparable (small) for the retrieval based on the motion-corrected and original lidar data, the random error between radiosonde and lidar profiles is substantially improved by the motion correction.

Further, histograms of the corrected and uncorrected horizontal velocity component, as well as a respective difference histogram, reveal that angular motions account mainly for smaller fluctuations between $\pm 2\,\mathrm{m\,s^{-1}}$, while translatory movement ($\sim$ship speed) causes the largest deviations (up to $8\,\mathrm{m\,s^{-1}}$). The horizontal translatory movement causes the largest impact on the total velocity, but changes at a much lower frequency than angular motion or the heave motion and is therefore much easier to correct. The vertical velocity histogram, on the other hand is mainly affected by angular and heave motion. Here motion correction achieves to shift the uncorrected peak at $0.5\,\mathrm{m\,s^{-1}}$ caused by persistent tilting of the instrument to $0.0\,\mathrm{m\,s^{-1}}$ after correction. Additionally, motion correction achieves a narrowing of the vertical velocity peak, which can be accounted to the reduction of high-frequency angular and heave displacement.

The velocity spectra of uncorrected and motion-corrected wind velocity retrievals are also compared. These spectra reveal the general limitations of the DBS scanning pattern, namely a rolling average effect, as radial velocity observations are used several times to retrieve consecutive time steps of the velocity vector (see Figure 4.1), and cross-contamination effects. Here, the vertical velocity spectrum is, in particular, affected by ship motion and motion correction. The spectral energy peak caused by heave motion is substantially reduced for the corrected spectrum. But for frequencies larger than the Nyquist frequency of the corresponding DBS scanning cycle (ca. $2 \cdot \frac{1}{3.8}$ s^{-1}), motion compensation causes the corrected spectrum to follow the heave spectrum more closely than the uncorrected spectrum.

Because the ship-based campaign unfortunately lacks high-frequency reference data to validate the spectra, this effect was further investigated using the metrics "coherence", "co-coherence" and "phase". Coherence of the vertical velocity retrievals at different altitudes decreases with increasing vertical separation distances and frequency, as expected for natural turbulence and eddies, but suddenly increases again for frequencies, where motion impact gains importance. At high frequencies, the motion correction overcompensates, in particular, in the frequency range larger than the Nyquist frequency, confirming the hypothesis, that the rolling average effect amplifies the motion-induced error that simple motion correction can not remove. Here, the retrieval principle does not allow to resolve oscillations caused by motion, and motion correction introduces artificial oscillations on the corrected series.

Main finding and link to Paper II

Ship-based, profiling lidar can be considered to study (turbulent) eddies that correspond to frequencies lower than the resonance frequency of the vessel, and frequencies lower than those affected by the measurement principle (DBS) of the lidar. While the majority of turbulent eddies exceed this frequency threshold, the majority of convectively driven eddies in the marine atmosphere boundary layer fall into the frequency range which is not corrupted by the ship's motion. Even though, the study presented in Paper I was initially motivated to provide an estimate of the performance of ship-based profiling lidars for offshore wind energy applications, this finding changed the focus of the PhD project to investigate convective structures in more detail.

The data evaluated in Paper I already contained several periods with strong convective conditions. Here, the convection above the ocean was triggered by advection of air that is colder than the ocean's surface. During such cold air outbreak conditions, the convective eddies move with the mean wind and frequency can be related to scale. This effect enabled the evaluation of convection from the time series of a ship-based lidar wind profile in the marine atmospheric boundary layer, which is discussed in Paper II.

Paper II: A Ship-Based Characterization of Coherent Boundary-Layer Structures Over the Lifecycle of a Marine Cold-Air Outbreak

Christiane Duscha, Christopher Barrell, Ian A. Renfrew, Ian M. Brooks, Harald Sodemann, Joachim Reuder (2022),
Boundary-Layer Meteorology, 183/355-380

Paper II demonstrates the capability of the profiling lidar to sample organised convective structures in the marine atmospheric boundary layer. Here, ship-based lidar observations during a cold air outbreak, a strongly convective atmospheric event, are presented. The main focus of the paper is on identifying characteristic properties of the convective structures based on the flow field sampled by the lidar, i.e., horizontal length scales, and vertical and horizontal velocity amplitudes. Those characteristics are linked to properties of the marine atmospheric boundary layer, obtained by complementing in situ and remote sensing observations operated from the ship, such as boundary-layer depth, surface heat fluxes, and stability estimates, to achieve an understanding of their interplay.

The methodology to identify the convective properties utilizes the comparably strong and consistent advection during cold air outbreak conditions. This enables the profiling lidar to yield observations of the two-dimensional flow field along the apparent wind, assuming the convective eddy does not change while advected over the ship (Taylor Hypothesis). Estimates of the coherence and phase spectra between vertical and along-wind speed fluctuations indicate the presence of periodically returning (coherent) structures in the flow field (see Sect. 4.3.1). As concluded from Paper I, motion, and lidar measurement principle only affect turbulent eddies of comparably short temporal and spatial scales, while motion correction successfully removes the motion impact at scales relevant to convection.

Accepting the coherent structures only within certain coherence and phase thresholds (as suggested by *Hartmann et al.*, 1997), limits the evaluated structures to convective origin. Paper II demonstrates this methodology in the form of an example snapshot of the flow field captured by the lidar. The flow field clearly features a convective circulation pattern with individual convective cells of comparable structure wavelength. This organisation of the convective flow field is also evident in the coherence spectrum by a peak, that is within the defined phase thresholds at the corresponding wavelength. Based on a satellite snapshot of the same situations, only a fraction of the convective thermals initiated at the surface and obtained by the lidar manifests as clouds.

The analysis of the coherent structure length and velocity scale statistics throughout the life-cycle of a cold air outbreak further reveals, that not even all convective thermals extend throughout the whole lidar range. Further, the structure characteristics align with those typically expected for cellular convection. Here, the ratio of horizontal and vertical scale (anisotrophy) increases with increasing structure size and velocity, respectively. The coherent convective structures mainly feature comparably wide and weak downdrafts, as well as comparably narrow and strong updrafts. For the large coherent structures, the size and horizontal velocity amplitude greatly exceed the vertical counterparts.

Paper II investigates the interplay of structure characteristics on short temporal scales, utilizing heat maps of the structure scale and boundary-layer parameter occurrences. Long time scales, on the other hand, are interpreted on the basis of a time series over the life-cycle of the cold air outbreak. Short-term variations in the structures' characteristics are found to be primarily influenced by the near-surface stratification and the fetch. Under unstable, buoyancy-driven turbulence conditions, small-scale structures dominate. However, these structures are relatively weak and contribute minimally to the mixing and overturning of the MABL. As the importance of shear-generated turbulence (neutral stratification) increases, the size and strength of coherent structures also increase. Larger coherent structures become more prominent as the convective boundary-layer depth increases. The ratio between the median horizontal structure size and the boundary-layer depth is approximately 2, consistent with the median ratio between the along-wind and vertical velocity amplitudes of the coherent structures. The largest coherent structures are predominant under weakly unstable, buoyancy-dominated conditions and conditions equally balanced between buoyancy and shear-generated turbulence. The observed turbulent heat fluxes are partly driven by small-scale and non-coherent turbulence, and organized large-scale convective overturning by coherent structures occurs mainly on long time scales.

Main finding and link to Paper III

The ship-based, profiling lidar installation yields a detailed picture of the convective flow-field, which enables the identification of characteristic properties of the convective circulation. The evaluation of these convective properties allow an advanced interpretation of the MABL processes, which are usually only studied on the basis of conventionally observed boundary-layer parameters. The paper discusses the interplay of coherent (convective) structures with the boundary-layer parameters, highlighting their role in building up and maintaining the overturning of the boundary layer.

In-situ profiling of temperature, humidity, and updraft velocity from the inside of the convective updraft, carried out by voluntary observing pilots (VOP) of paraglider, hang glider, and sailplane, can extend the conventionally observed convective boundary-layer parameters by a Lagrangian perspective. Such observations are part of the PhD project of Juraj Pálenik in Visualisation (Department of Informatics, University of Bergen). After scientific exchange through local seminars, collaboration was the natural next step. Combining convective flow field observations of comparable detail, as provided by the profiling lidar installation presented in Paper II, with observations of the convection sampled by the VOP, was the objective to further enhance our understanding of the processes connected to thermal convection. In contrast to the marine convection studied in Paper II, the land-based convection studied by VOP is mostly stationary and hence not accompanied by strong advection, required for Taylor's Hypothesis to apply to the convective eddies. Consequently, the convective flow field can not be estimated on the basis of a single profiling lidar as utilized in Paper II. Instead, Paper III explores the approach to combine two scanning lidar systems to achieve convective flow field observations of sufficient coverage and detail in space and time.

Paper III: Observing atmospheric convection with dual-scanning lidars

Christiane Duscha, Juraj Pálenik, Thomas Spengler, and Joachim Reuder (2023), Atmospheric Measurement Techniques, 16/5103–5123

Paper III evaluates the ability of dual-scanning lidars to sufficiently capture the flow field corresponding to daytime atmospheric convection over land. During the years 2021 and 2022 we planned and carried out three field campaigns, that featured dual-lidar set-ups in order to achieve and optimize such observations. Paper III presents the analysis of observations from dual-lidar installations during two of the three field campaigns, that were along the runway of two Norwegian airports as a proof-of-concept. Here, the study is intended as a stepping stone towards more advanced convection analysis during the remaining extensive field campaign, which collocates the lidar setup and retrieval with additional profiles of temperature and humidity, obtained by VOP. The main strategy carried out in all three campaigns were overlapping scans of vertical planes between two lidars which were installed at several hundred meter distance from each other. The information from the overlap of both scans were used to retrieve flow fields of the orthogonal wind components (plane- parallel and vertical).

The focus of the study presented in Paper III was to explore different processing procedures and scan configurations to improve the final velocity retrieval such that convective flow fields were sufficiently captured in space and time. To improve the data quality of the rather noisy and partly erroneous radial velocity observations, the capabilities of an advanced filtering approach are evaluated. This filter successfully separates clusters of reasonable radial velocity data from noise and erroneous features and proves to be indispensable for further data processing. Further, the convective flow field rapidly evolves even during a single lidar-scan of the vertical plane. Here, the maximum velocity error, which is due to the individual time lag at each point within the plane, estimated over the course of a convective day increases with increasing convective activity. Applying temporal interpolation to match the timing of each spacial point in the scans of the two lidars substantially reduces the velocity error and hence the temporal undersampling error, which is the radial velocity error that is amplified in the dual-lidar retrieval. Additionally, temporal interpolation enables the use of instantaneous scans and therefore increases the temporal resolution of the retrieval.

The study presents one case of the convective flow field retrieval for each of the two utilized field campaigns, featuring one clear-sky and one cloud-topped case. For the clear-sky case, the lidars were run with different scan configurations, specifically different angular resolutions and integration times. Here, all angular resolutions provide sufficient spatial resolution in the retrieved flow field to capture details of convective circulation. Hence, there is no disadvantage to prioritize an increased temporal resolution over angular resolution for monitoring changes in the convective circulation over time. The ability of the dual-lidar setup and retrieval to capture the evolution of the convective circulation is evaluated for the cloud-topped case. Here, only one scan configuration is used for the whole evaluated case, providing a continuous series of the scanning pattern over 50 min, opposed to only 10 min in the clear-sky case. This continuous time series of the flow field allows to successfully follow the different stages of the life-cycle of a large convective circulation from onset to break-down. The retrieval is fit to capture mainly the dry part of the convection, which is invisible to the bare eye, as the reliability of the lidar observations and of the retrieval decreases rapidly within the cloud.

Though different in location and background conditions, both case studies featured convection that spanned, increased, or maintained the depth of the boundary layer, demonstrating their important role for the overturning of heat, moisture, momentum, and energy. Further, the retrieved flow field allowed for identification of secondary parameters, such as the origin, depth, width, and strength of the convective updraft and their evolution in time and space.

Main Finding and further work

The dual-lidar retrieval, when combined with an advanced clustering filter and temporal interpolation for gap-filling, yields sufficient estimates of the convective flow field in space and time for further processing, e.g. by comparison and further processing with in situ profiles of temperature and humidity obtained by VOP in the vicinity.

Such a collocation of lidars and VOP was achieved in one of the field campaigns that took place in Voss, Norway from April to June 2022. Here, we installed three lidars, yielding three vertically intersecting scanning cross-sections. These cross-sections were located in a major flight areal for gliders and in the vicinity of the local airport where an aircraft for skydivers that launched approximately every 20 min. During convective days, we equipped the skydiving plane and a paraglider each with a mobile temperature and humidity sensor to sample background profiles and profiles from inside the convective updrafts, respectively. The next step is to identify matching or representative convective thermals or bubbles in the lidar retrievals and paraglider measurements. By combining the estimates of characteristic convective velocities, temperature, or humidity with the background profiles, we can investigate some of the processes which shape the development, evolution, and structure of atmospheric convection.

6 Complementing field campaigns and material

6.1 Controlled motion experiment in Grimstad, Norway

The performance of the motion correction algorithm applied to the ship-based lidar observation, that was introduced in Section 4.1.3 and utilized to correct ship-based lidar data presented in Paper I and II, was evaluated with a controlled-motion lidar dataset. This dataset was collected during an experiment on the Adger University campus in Grimstad, Norway in August 2011, that included the setup of a pulsed profiling Lidar (WindCubeV1) on a motion platform and a reference lidar of the same type (see Fig. 6.1). The setup additionally included two profiling CW lidars of the type Zephir300 (manufactured by ZX Lidars, United Kingdom), also with one lidar installed on the motion platform and one reference lidar. This type of profiling lidar utilizes a different scanning and retrieval technique. As a consequence, these CW lidars also require a different motion correction algorithm (see e.g *Kelberlau et al.*, 2020), than the one utilized for the pulsed lidars. This Section will focus on the evaluation of the motion correction algorithm presented in this dissertation (Sect. 4.1.3). A more extensive analysis of the controlled motion lidar dataset will be presented in *Malekmohammadi et al.* (in prep).

Figure 6.1: Setup of lidars on motion platform and the reference lidars in 5 m horizontal and 3 m vertical distance on the ground at the Grimstad campus of the University of Adger, Norway. Picture imported from the experiment report (Hellevang et al., 2012)

During the experiment, single and combined translatory and rotational motion, as well as complex motion patterns (e.g. simulating waves during a storm) were applied to the motion platform and the lidar installed on top. In addition there were some periods without motion, that could be used as a baseline to identify the random error between the two lidars due to individual instrument specific differences, their separation distance, and different timing of their beam orientation[1].

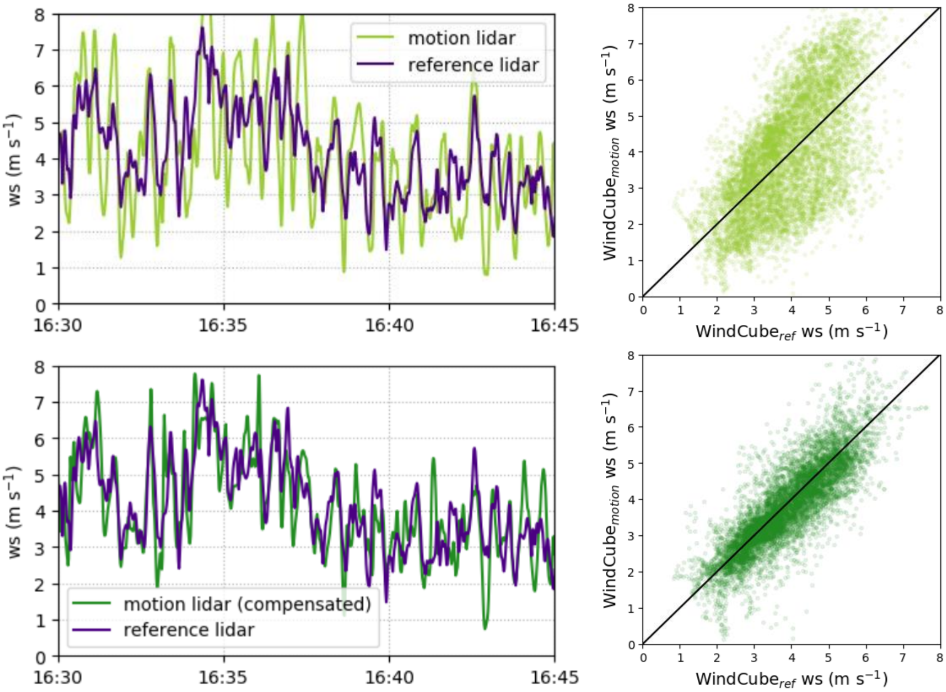

Figure 6.2: Left top: 15 min example ws time series obtained by reference lidar and the lidar on the motion platform that is exposed to sinusoidal pitch motion with $\varphi_A = 2 \cdot 15°$. *Left bottom: The same ws time series obtained by reference lidar as above, but with corrected motion lidar time series. Right top: Scatter of reference time series and motion lidar time series corresponding to the complete motion test case of sinusoidal pitch motion with* $\varphi_A = 2 \cdot 15°$ *(3 hours duration). Right bottom: Scatter of reference time series and corrected motion lidar time series corresponding to the same complete motion test case as above*

Figure 6.2 shows the horizontal wind speed data obtained from the motion lidar and processed with the correction algorithm in comparison with the data observed by the reference lidar, respectively for a case of simple sinusoidal pitch movement with an amplitude of $\varphi_A = 2 \cdot 15°$. The impact of this simple angular motion on the retrieved ws is clearly visible in the displayed comparison of the example reference and motion time series and in particular in the scatter of the

---

[1] The WindcubeV1 utilizes a rotating mirror to distribute the beam in the four (perpendicular) directions (no vertical beam). The orientation at startup depends on the orientation when the lidar was shutdown. Synchronising beam orientation of the two lidars is not guaranteed at startup

two series for the whole angular motion case (see Fig. 6.2). Figure 6.3 documents the correlation, R, the standard deviation, σ, and the standard deviation error[2], σ_e, corresponding to the horizontal wind speed and the vertical velocity series of the pitch test case displayed in Fig. 6.2, as well as two single translatory motion cases: a heave motion case with an amplitude of 0.4 m, and a surge motion case with an amplitude of 0.4 m.

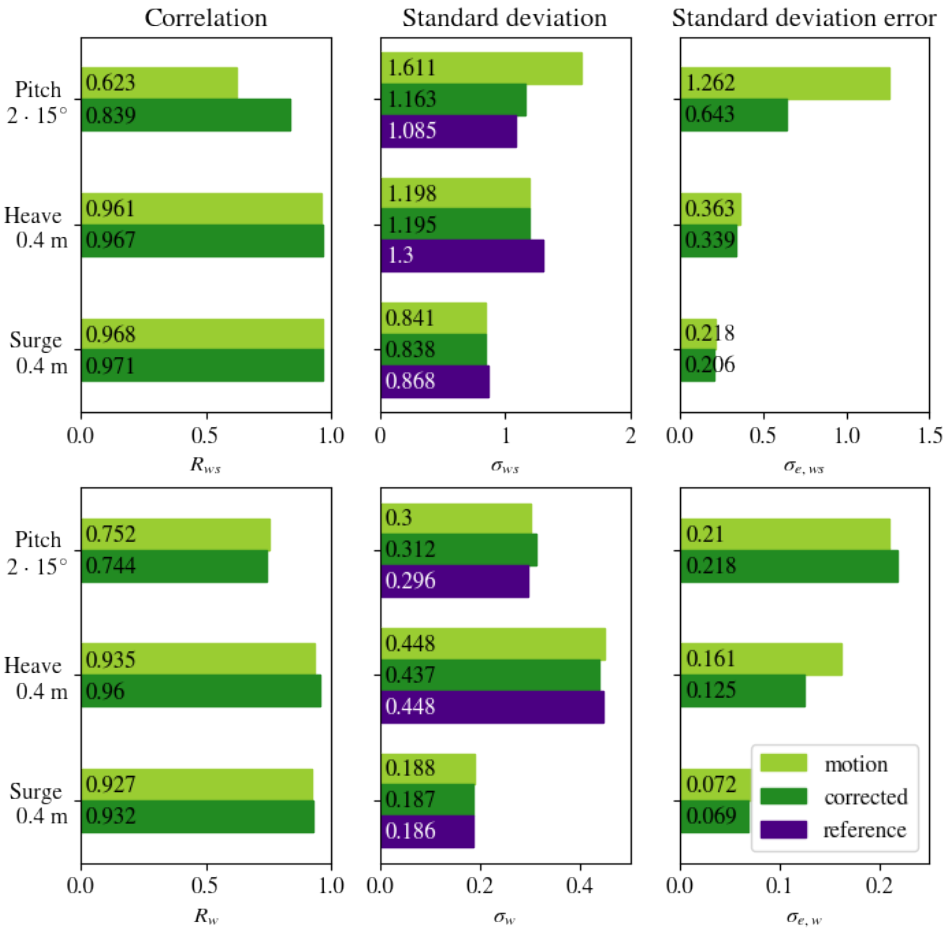

Figure 6.3: Statistics of reference lidar time series compared to motion lidar, and corrected motion lidar time series for three test cases: pitch motion, heave motion, surge motion. Left top: Correlation between reference ws series and motion ws series (lime) and corrected motion ws series (dark green). Left bottom: Same as above but for w component. Middle top: standard deviation of motion ws series (lime), corrected motion ws series (dark green), and reference ws series (purple). Middle bottom: Same as above but for w component. Right top: Standard deviation error between reference ws series and motion ws series (lime) and corrected motion ws series (dark green). Right bottom: Same as above but for w component.

---

[2] The standard deviation applied to time series resulting from subtraction of the motion time series from the reference time series

For the pitch motion test case, σ_{ws} of the motion series is substantially increased compared to σ_{ws} of the reference lidar series and $R_{ws} = 0.623$ between the motion and reference series is relatively low (Fig. 6.3). After applying the correction algorithm to the pitch motion series, $R_{ws} = 0.839$ is substantially increased and σ_{ws} of the corrected series is much closer to σ_{ws} of the reference series. For the vertical velocity component, R_w of the corrected series is slightly decreased in comparison to the uncorrected series and also $\sigma_{e,w}$ of the corrected series is marginally increased (see Fig. 6.3). The utilized motion correction algorithm (see Sect. 4.1.3) updates the applied rotation matrices only once per scan cycle, possibly causing the observed decline in quality of the corrected w series. Still, this decline in quality is negligible in comparison to the relative and absolute improvements of the pitch-motion correction in the ws series.

An improvement of the ws estimate with motion correction was also achieved for two example cases with translatory (heave and surge) motion, each with an amplitude of 0.4 m (see Fig. 6.3). Yet, in comparison to the rotational motion case discussed above, the motion impact is small, evident from the comparably large R_{ws} and small $\sigma_{e,ws}$ between the reference series and the motion and motion-corrected series, respectively. Unfortunately, the motion platform is restricted to maximum translatory amplitudes of 0.4 m, that yields only this relatively small motion impact. As expected, the heave case shows the largest relative improvement due to motion correction for the w component. Even for the surge case the w component series improved slightly after motion correction.

Except for the ws series of the pitch case, the standard deviations of the reference, motion-impacted and motion-corrected series do not differ very strongly from one another. For the translatory example cases, σ_{ws} corresponding to the reference lidar even exceeds the motion-impacted and motion-corrected counterpart. Here, the baseline cases confirmed (no shown) that the remaining random error between reference and respective motion-impacted, or motion-corrected series is predominantly caused by the separation distance of the lidars, the absent synchronisation of beam orientation, and individual sampling errors of each of the lidars. The controlled motion experiment indicates that the motion correction algorithm applied on the moving lidar obsevations can provide a representation of the wind field that is comparable to the observations by a static lidar system.

6.2 GLidar – Campaign in Voss, Norway

Gliders (e.g. paragliders, sailplanes, and hang gliders) are small manned aerial vehicles that use the convective updraft in the boundary layer to gain altitude above ground. Each glider is equipped with a device to monitor its trajectory through the atmosphere. In addition to information on the position and attitude of the glider, this trajectory data can be used to estimate the convective updraft velocity, given the characteristic sink rate of the glider (see *Pálenik et al.*, 2021). During the course of a convective day a large quantity of gliders potentially fly within the same or within a multitude of convective thermals or bubbles, yielding a large sample of convective updraft velocities throughout the boundary layer in an area. One hot-spot for glider activity is the area around Vossevangen, a small town in the Voss municipality in Norway.

Additionally measured background profiles of the atmospheric state variables (in particular temperature and humidity), yield the possibility to investigate the mechanisms responsible for the sampled vertical velocity profiles. However, the interplay and impact of the unknown variables, i.e. the virtual temperature (density) anomaly, the aspect ratio of the updraft, or the drag acting on the ascending air, is manifold. The inter-dependencies of these parameters can, for example, be investigated with the interactive visualisation tool *IsoTrotter*, introduced in *Pálenik et al.* (2021) that incorporates a model to solve the convective vertical velocity equation. Here, reducing the degree of free variables improves the certainty about the prevailing atmospheric mechanism substantially (e.g. by identifying the predominant convection characteristic: bubble or thermal, see Sect. 3.1).

Obtaining the evolution of the convective flow field enables the possibility to gain an estimate of the updrafts aspect ratios and the characteristic form (bubble or thermal). Utilizing a setup of multiple lidars with overlapping co-planar RHI scans (see Fig. 6.4) can achieve time series of such observations of the convective flow field. The flow field retrieval approach and how it can be optimized for observing convection is presented in Paper III.

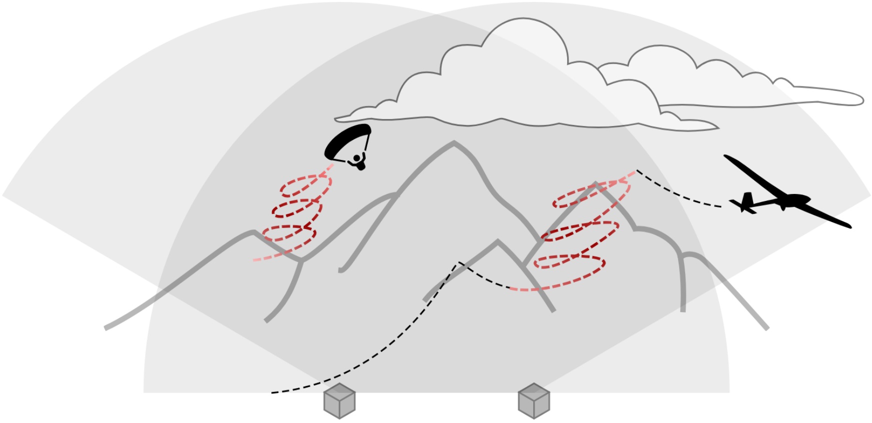

Figure 6.4: Visualisation of the gLidar Project: A schematic dual-lidar scanning cross-section in complex terrain co-located with measurements provided by voluntary observing glider pilots

Project Outline : gLidar

The **gLidar** Project aims to collocate and combine Lagrangian measurements gathered by **gliders** and Eulerian **lidar** observations to enhance the sampling capacity and understanding of convection in the atmospheric boundary layer.

From 29. April 2022 until 07. June 2022 we installed three scanning Wind-Cube 100S lidars with overlapping cross-sections in north-south orientation (”eastern cross-section” between lidar-34 and lidar-40) and near east-west orientation (”southern cross-section” between lidar-37 and lidar-40) approximately parallel to the southern and eastern slopes, as well as one cross-section (”slope cross-section” between lidar-34 and lidar-37) spanning partly over the slopes of Mount Hangur, in Voss, Norway (see Fig. 6.5). Close to the top of Mount Hangur is an official take-off point for paragliders and hang gliders that makes the area a hot-spot for flight activity. This yields an extensive potential for sampling the convection triggered in the region both by the gliders and the lidars.

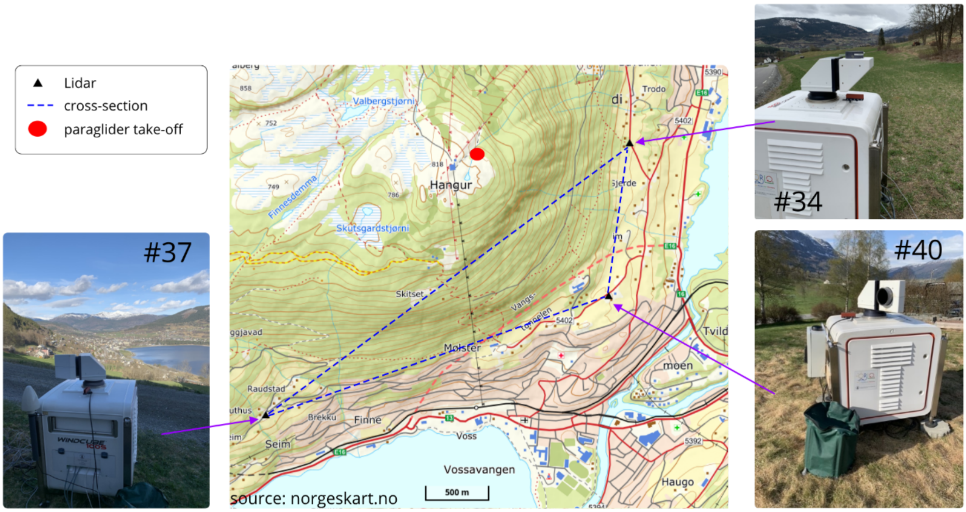

Figure 6.5: Map of the triangular setup of the lidar instrumentation (with pictures) along the southern and eastern slopes of Mount Hangur in Voss, Norway and the location of glider take-off point on top of the mountain.

For the eastern and southern cross-section, the lidars had free LOS to one another, yielding a sufficient overlap at most altitudes. Scans to achieve these cross-sections were scheduled throughout the campaign. Here, the two outer lidars (lidar-34 and lidar-37) performed continuous scans towards lidar-40, while lidar-40 switched between LOS towards lidar-34 and lidar-37 for each new scan. As the LOS between lidar-34 and lidar-37 was partially blocked by the mountain (slopes of 30° and 18°, respectively), the overlap of the lidar scans was limited, in particular at lower altitudes. The slope cross-section was therefore only applied during special observing periods in June 2022.

In order to achieve a sufficiently large overlap, at least for the eastern and southern cross-sections, the setup of the lidars required a distance of at least one kilometer between the individual instruments. Interconnecting the lidars on a single network with a physical link, e.g., a long ethernet cable was therefore no option. Hence, we developed and build a remote access solution inside a cabinet for each lidar (see Fig. 6.6), to interconnect, synchronise and remotely monitor their observations.

Each utilized cabinet includes an industrial router (RUTX11, Teltonika, Lithuania) with an antenna for mobile network, wifi, bluetooth and GPS, as well as a small computer with a linux operating system (Raspberry Pi 4B[3]), corresponding power sources, and a fuse. The router is connected to the internet via mobile SIM network subscription, and also creates a local network, which includes the lidar and the linux computer. The latter is set up as a local server to which data is streamed from the lidar via File Transfer Protocol (FTP). This data is synchronised to an online webserver with resources provided by the Norwegian Research and Education Cloud, NREC[4], once every 15 minutes using the unix command ”rsync”. The linux computer can be accessed remotely (via ssh or Teamviewer) and used to operate the lidar with the Leosphere API[5]

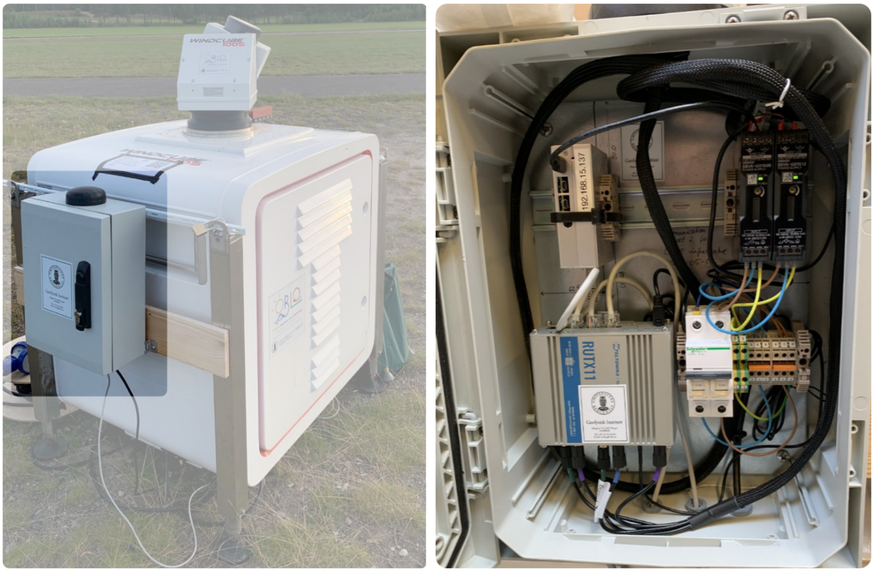

Figure 6.6: Right: Remote access cabinet mounted to a lidar. Left: cabinet interior

As discussed in Paper III, to ensure a good quality of the dual-lidar retrieval, a reliable time synchronisation is essential. From earlier field deployment of the lidars, we experienced that the internal, GPS-based time synchronisation was insufficient. While connected to the remote access cabinet, time synchronisation of the lidars was achieved by Network Time Protocol (NTP) instead of GPS.

---

[3] `https://www.raspberrypi.com/products/raspberry-pi-4-model-b/`, last access: 2024-01-05

[4] `https://www.nrec.no/`, last access: 2023-11-09

[5] `https://leosphere.github.io/LeosphereAPI/`, last access: 2023-11-09

The setup location of the lidars in Voss added an additional advantage to the dense paragliding activity: the possibility to attach a sensor that measures temperature, humidity, pressure, geo-location, and altitude to a small motorized airplane that carries skydivers up to 4000 m altitude and higher (see Fig. 6.7). This installation yielded in situ background profiles of temperature and humidity in substantially higher temporal resolution, with one profile per 20 min to 30 min (time elapsed for ascent and descent of the plane) and closer proximity than

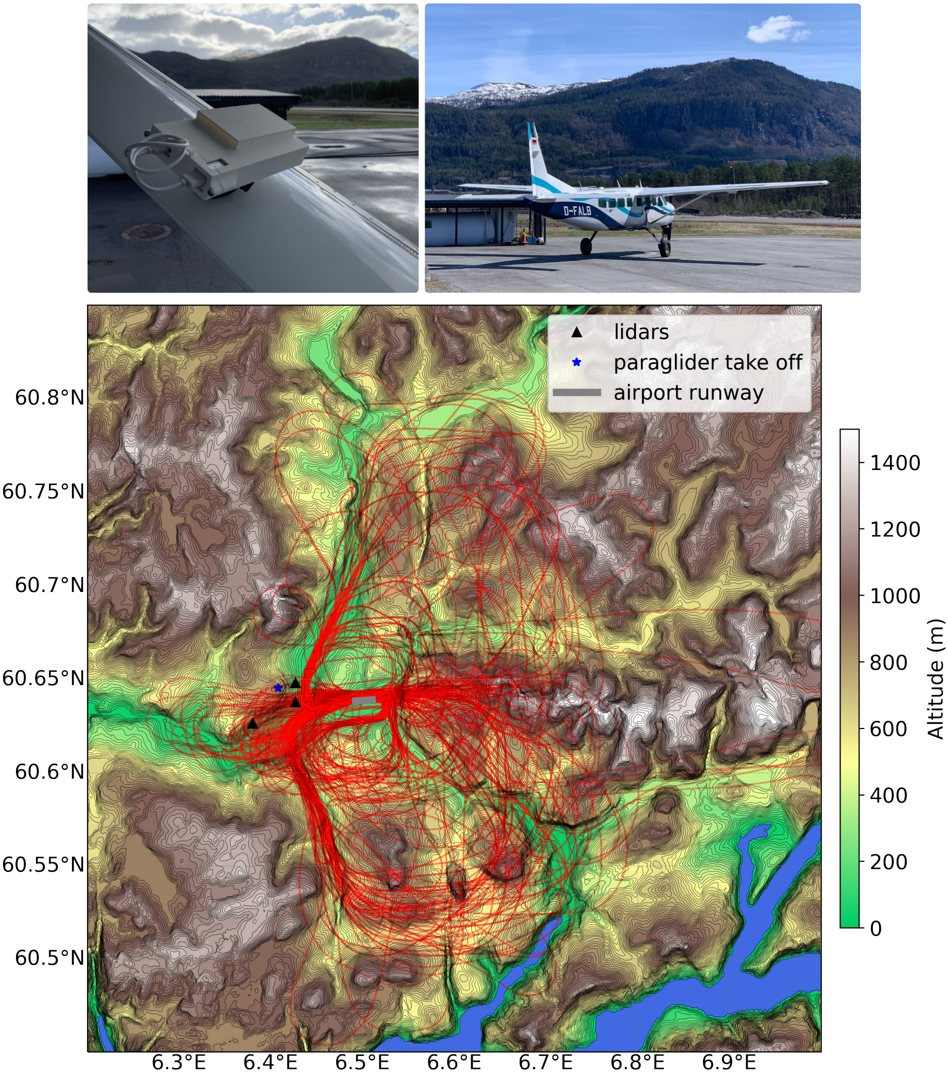

Figure 6.7: Top left: iMet sensor with radiation shield, mounted to wing of skydiving plane. Top right: the skydiving plane. Bottom: Enlarged map of the Voss region (elevation data by de Ferranti and Hormann, 2022) and with skydiving plane flight tracks (representative footprint area for the background profiles) and locations of lidars and paragliding take off in relation.

achieved by officially launched radiosondes (usually twice per day, at 200 km distance to Voss). Figure 3.5 shows an example of an extensive profile time series obtained with the skydiving plane on 16 May 2022.

The iMet[6] sensor, used for measuring the background profiles, experienced substantial measurement errors, due to the great velocity of the skydiving plane, in particular during the descent. The source of the error was twofold: (1) An incorrect altitude allocation due to a time lag of the sensor, visible as a "loop" at the top of the combined ascent and descent profile; (2) An increase of temperature, as air compresses[7] due to the skydiving planes velocity inside the box, installed around the sensor to shield it from radiation. At highest speed of the plane (≈ 100 m s^{-1}) during the descent this temperature error exceeds 5 K. Both error sources could be compensated in post processing (see *Pálenik*, 2022), such that profiles of ascent and descent align (e.g. the profiles displayed in Fig. 3.5 are corrected).

To gain an estimate of temperature and humidity anomalies within the convective updraft compared to the background profiles, we also equipped some paragliders with iMet sensors, as often as possible. The utilized sensors and radiation shielding are identical in construction to those used on the skydiving plane. However, the speed of the paraglider is much smaller than the skydiving plane, such that the time lag and compression errors are negligible. The paraglider equipped with the additional sensors attempted to find updrafts and fly as close to the lidar cross sections as possible (see. Fig. 6.8)

Figure 6.8: Left: Paraglider equipped with iMet sensor flys close to lidar-sampled cross-sections. Right: Voluntary observing paraglider pilot Juraj Pálenik after flight with iMet sensor (mounted to helmet).

---

[6] https://www.intermetsystems.com/products/imet-xq2-uav-sensor/, last access: 2024-01-05

[7] The effect of increased pressure and corresponding adiabatic temperature increase was confirmed with a computational fluid dynamics simulation (CFD) of the flow through the model of the radiation shielding box (see https://glidar-project.github.io/pg/2022/08/26/cfd/, last access: 2023-11-08)

First Results

A first analysis of the data collected by paragliders, lidars, and skydiving plane yielded some interesting insights. In particular over the course of 16th May 2022, the paragliding activity was dense and featured several paragliding flights with an iMet sensor. Figure 6.9 shows the cumulative number of points (vertical velocity measurements) provided by the bulk of paragliders per area within the proximity of the triangular lidar setup and three selected flights, each within a convective updraft, with iMet sensors. During the 16th May 2022, also the iMet sensor that was attached to the skydiving plane provided more than 10 hours of measurements (see Fig. 3.5).

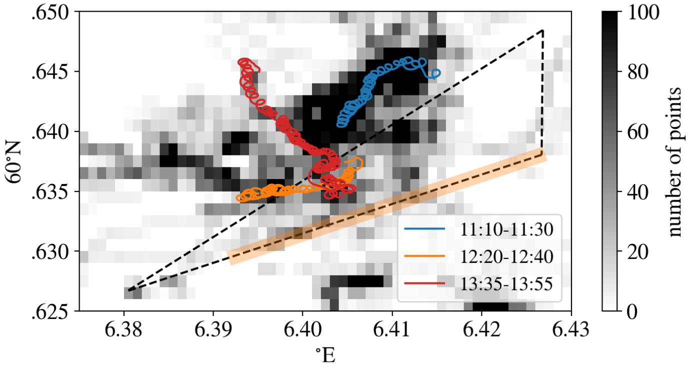

Figure 6.9: Density of aerial paragliding activity, displayed as number of paragliding measurement points per area (0.001°)^2 and trajectory of three selected paraglider flights equipped with iMet sensor (colored lines) on 2022-05-16 within the proximity of the triangular lidar setup (striped black lines). The highlighted area (orange) corresponds to the part of the southern lidar cross-section displayed in Figure 6.12

Figure 6.10 documents the evolution of the convective boundary layer observed by paragliders, lidars and skydiving plane during 16th May 2022. Here, a time series of z_i (center of capping inversion, see section 3.2) is extracted on the basis of the θ_v profiles obtained by the iMet, mounted to the skydiving plane (see estimation of convective boundary layer depth in Paper II). The first z_i values, estimated around 7 UTC, suggest the initial presence of a shallow nocturnal boundary layer. The increased SNR between the surface and 500 m, that predominates until z_i increases (approximately 8 UTC) can be attributed to a nocturnal layer of fog (see increased near-surface r_M, Fig. 3.5). Between 8 UTC and 13 UTC, a rapid growth of the convective boundary layer is indicated by an increase in z_i. Simultaneously, the SNR is increased between the surface and $z \approx z_i$, compared to the free atmosphere above z_i. This indicates the presence of vertical transport and enrichment of aerosols by the convective circulation up to the capping inversion.

The first paraglider began to fly and utilize the convective updraft to gain altitude after 10 UTC. The highest vertical velocity reached within the bulk of the paragliders, $w_{pg,max}$, is marked at the corresponding altitude in Fig. 6.10 for 10 minute intervals. During the period of rapid boundary layer growth, the

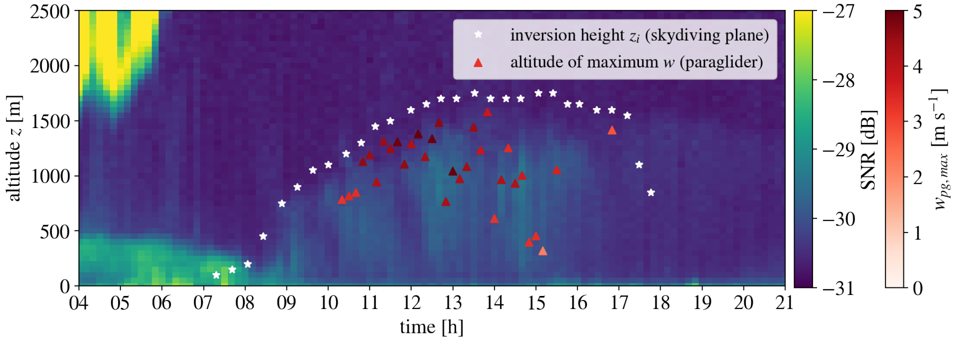

Figure 6.10: Evolution of the convective boundary layer on 16th May 2022: Time series of lidar observed SNR (10 minute time average and spacial average over 100 m height bins of all RHI scans of the three lidars) as indicator of cloud, fog, or aerosol particles; height time series of the center of the capping inversion (z_i), estimated on the basis of θ_v background profiles, obtained by the iMet sensor installed on the skydiving plane; and time series of the altitude that corresponds to the maximum vertical velocity observed by all paragliders within a 10 min interval.

altitude of $w_{pg,max}$ is located below, but near z_i, indicating that the convective updraft accelerates almost until z_i with largest $w_{pg,max}$ between 11 UTC and 14 UTC. The three paraglider flights that are equipped with iMet sensors are selected from this period (see Fig. 6.9). Their $w_{pg,max}(z)$ is shown in Figure 6.11 in comparison to the distribution of $w_{pg}(z)$ of all paraglider flights during 16th May 2022.

During all three selected flights, the glider pilot captures the convective updraft between 700 m and 800 m altitude, that is slightly below the altitude of the

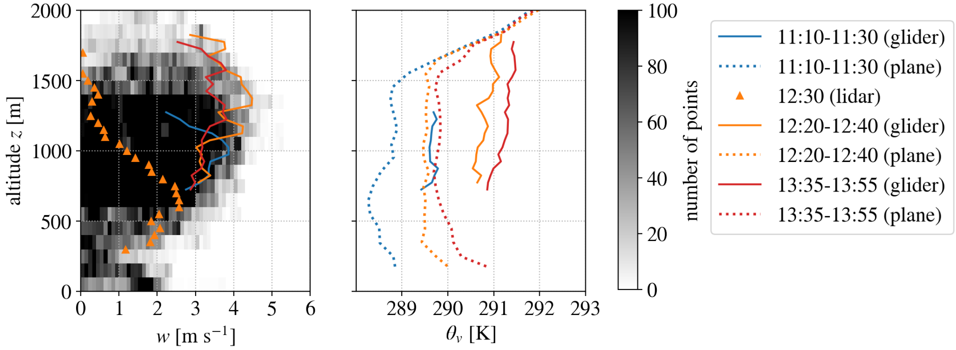

Figure 6.11: Left: Distribution (number of $w_{pg}(z)$ measurements per 100 m altitude and 0.1 m s^{-1} vertical velocity bin) of vertical velocity obtained during all paraglider flights on 16th May 2022 in the Voss area and $w_{pg,max}(z)$ of three selected paraglider flights equipped with iMet sensors, as well as $w_{max}(z)$ extracted from the flow field of a lidar retrieval. Right: Profiles of θ_v, obtained from the inside of a convective thermal by an iMet that was attached to a paraglider and background profile of θ_v, obtained by an iMet installed on the skydiving plane for three periods on 16th May 2022

paragliding take-off spot on top of Mount Hangur ($z \approx 800\,\mathrm{m}$). The glider pilot stays within the first selected convective updraft (11:10 - 11:30 UTC) only up to $z = 1300\,\mathrm{m}$ (Fig. 6.11) with a peak velocity of almost $4\,\mathrm{m\,s^{-1}}$ around $z = 1000\,\mathrm{m}$. During the flight, the paraglider drifts, indicating a tilt of the convective updraft in north-easterly direction, following a similar track as a large number of other paragliders during that day (Fig. 6.9). The virtual potential temperature measured within the sampled range of the updraft is approximately 1 K warmer than the background θ_v. Here, an extrapolation of the updraft's θ_v profile intersects the capping inversion of the background profile approximately 300 m above the altitude, where the glider pilot left the updraft (Fig. 6.11).

About an hour later, during the subsequent selected flight (12:20 - 12:40), the glider pilot reaches $w_{pg,max}(z)$ between $3\,\mathrm{m\,s^{-1}}$ and $4.5\,\mathrm{m\,s^{-1}}$ (with the peak in $w_{pg,max}$ around $z = 1400\,\mathrm{m}$), that are close to the maximum observed w_{pg} of all paragliders (Fig. 6.11). Here, $\theta_v(z)$ within the convective updraft is approximately 1 K to 1.5 K larger than the background $\theta_v(z)$, and touches the capping inversion at $z \approx 1800\,\mathrm{m}$. Even though the paraglider left the convective updraft at that point, the velocity of the updraft was still around $3\,\mathrm{m\,s^{-1}}$, likely causing the updraft to overshoot the capping inversion.

Simultaneously to this paraglider flight, at 12:30, the horizontal and vertical flow field retrieval from the southern dual-lidar cross-section showed clear evidence of a convective circulation (see Fig. 6.12). The observed convective circulation spans a horizontal distance of approximately 1200 m. Here, the negative component of the horizontal velocity component (flow towards east) in the lower convergence zone and upper divergence zone is larger than the corresponding positive horizontal velocity component (flow towards west). This causes the updraft to be tilted toward east, a feature also visible in the horizontal drift of the track of the corresponding paragliding flight (Fig. 6.9). The updraft captured by the lidar retrieval (Fig. 6.12) extends up to $z \approx 1200\,\mathrm{m}$, while divergence of the flow and subsidence connected to the convective circulation is still evident up to $z \approx 1700\,\mathrm{m}$, comparable to the extend of the convection that was simultaneously

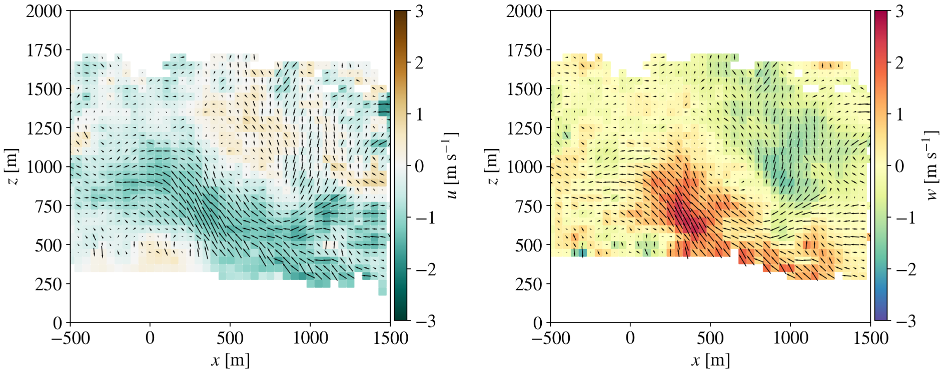

Figure 6.12: Retrieved flow field of the southern dual-lidar cross-section with an overlay of the convective circulation on 16th May 2022, 12:30 UTC. Left: Retrieval of the horizontal velocity component. Right: Retrieval of the vertical velocity component

sampled by the paraglider. Hence, vertical extent of the convective circulation exceeds its horizontal extent, yielding an aspect ratio (width over height) smaller than 1. At lower altitudes up to approximately $z = 600\,\mathrm{m}$, the maximum updraft velocity within the lidar cross-section follows the maximum values of the w_{pg} distribution profile provided by the bulk of paragliders during that day (Fig. 6.11). Between 600 m and 700 m altitude, the maximum w profile of the retrieved lidar cross-section reaches it's peak at $w \approx 2.6\,\mathrm{m\,s^{-1}}$, decreasing again at higher altitudes. Here, the convective updraft, that was mapped by the lidar retrieval, either exits the lidar cross-section due to a horizontal tilt of the convective circulation relative to the lidar cross section (see Fig. 6.9 and Fig. 6.12) at higher altitudes, or has bubble characteristics with the convective bubble located close to the surface at the evaluated time step. A combination of these two effects is also possible. In either case, the relative position of the displayed lidar cross-section and paraglider track (12:20-12:40 UTC) suggest, that the updraft that was mapped by the paraglider can be interpreted as a complementing sample of the upper part of the convective circulation, observed by the dual-lidar (see Fig. 6.9).

After 13 UTC, the change in z_i negligible, keeping a value around 1700 m until suddenly dropping after 17 UTC (Fig. 6.10). During this period (13 -17 UTC), the altitude corresponding to $w_{pg,max}$ varies much stronger than during the preceding period of boundary-layer growth, indicating less favourable convective conditions for paragliding. The last displayed paraglider flight with an iMet sensor took place at the beginning of this period (between 13:35 UTC and 13:55 UTC). The altitude range and virtual potential temperature anomaly of this flight is similar to the flight with iMet approximately one hour earlier. The corresponding $w_{pg,max}$ is, however, smaller at almost every altitude and the paraglider does not reach the altitude at which θ_v within the convective updraft intersects the capping inversion. Also, the drift of the paraglider's track changed compared to the preceding flights displayed, indicating a tilt of the convective updraft in south-easterly direction (Fig. 6.9). The drop of z_i after 17 UTC that is accompanied by a decrease in SNR and ceasing paraglider activity (Fig. 3.5), indicates the termination of convection activity and a possible change of air masses due to advection.

7 Conclusions and Outlook

7.1 Potential and limitations to observe atmospheric convection

7.1.1 Profiling lidars

Profiling lidars are limited to a one-dimensional view in space along the vertical axis. In order to observe convection with a profile time series some requirements need to be met, which are not necessarily in the hand of the lidar operator. The setup requires a comparably consistent horizontal movement of the convective structures relative to the lidar system. The speed of this relative movement must be sufficiently large to capture individual convective structures within their life-cycle (Taylor hypothesis of frozen turbulence) while being small enough to capture the convective circulation in sufficient detail. Such conditions are limited to certain convective events in the atmospheric boundary layer. Paper I and II showed that marine CAOs with cellular convective structures provide the required background flow conditions for a ship-based profiling lidar investigation. The interpretation of convective structures is mostly limited to convective characteristics, that change along the mean wind direction. Typical ship velocity[1] is of the same order as the average flow velocity. Hence, in contrast to stationary installations, as e.g. on a buoy, the ship-based setup allows for some modulation of the speed and direction of structure movement relative to the lidar (apparent wind). This opens up the possibility to study convective structures, such as roll vortices, that need to be characterized perpendicular to the mean wind direction, along the cross-wind axis of the atmospheric flow. Still, a ship-based lidar installation comes with its own limitations.

A critical limitation of the lidar installation on a ship is the exposure of the lidar to ship motion, that substantially impacts the lidar observations (see Sect. 4.1.2 and 6.1). In particular at high frequencies, that correspond to small structure wavelengths, the averaging effect of the lidar measurement principle (DBS scan) complicates the removal of the motion impact. For frequencies that correspond to a time resolution that exceeds the time allocated for one DBS scan cycle, the application of motion correction corrupts the observations even more. Due to the motion impact, the relevant velocities of convective structure movement relative to the lidar limits the characterization of the convective circulation to horizontal scales of a few hundreds of m or larger. Yet, also the separation distance of the lidar beams in the DBS scan limits the size of detectable structures to horizontal diameters of comparable size. The smallest relevant convective structures that are expected to be present in the CBL are surface layer plumes with horizontal dimensions in the order of the surface layer depth, that corresponds to the lowest hundreds of m for the observed boundary layer depths. Generally, the motion correction approach improves the lidar observations, in particular at lower frequencies, that are most relevant for the convective structure characteriza-

---

[1] A comparable lidar installation on a much faster platform, i.e. an aircraft, would exceed the maximum velocity condition, yielding insufficient detail of smaller scale convective structures

tion. Hence, despite the limitations inherent to insufficient motion compensation and lidar measurement principle, the ship-based lidar setup is able to characterize the majority of relevant convective structures and provide sufficient temporal coverage in the marine CAO context.

A specific shortcoming of the profiling lidar type (WindcubeV2) that was used in the studies connected to Paper I and Paper II is the limited vertical coverage. The WindcubeV2 lidar provides measurements exclusively up to 300 m above the instrument, limiting the characterization of the convective structures to the lower segment of convective overturning circulation, mainly confined to the surface layer. Such limitation of the vertical range of the lidar observations is comparable to the range limitation of meteorological masts. Still, a mast of such dimensions is hardly feasible in the observational settings in the marine atmospheric boundary layer, that provide the conditions required for the applied analysis technique (Sect. 4.3.1) and in contrast to masts, the lidar does not disturb the atmospheric flow. To cover the entire convective overturning circulation, a long-range lidar profiler with a smaller cone angle (θ_z) should be utilized, either instead, or alongside with the short-range profiling lidar. Yet, even with a smaller θ_z, limitations of detectable structure size emerge at longer ranges, where the separation distance between beams may exceed some of the relevant horizontal scales of convection.

In the future, the reliability of the ship-based lidar observations should be improved at higher frequencies for a more accurate turbulence characterization within the convective circulation, i.e., for applications with faster relative horizontal structure movement and smaller separation distance. Such an improvement could, for example, be achieved with the implementation and evaluation of a beam-wise rotational motion correction, as theoretically derived in appendix A. In addition, the elimination of the moving average effect in the velocity spectra (DBS scanning technique) needs to be addressed, e.g., by applying a theoretical fit to the velocity spectra, using the anchor points at the Nyquist frequency of the scan cycle and of the radial velocity time resolution, respectively. Another approach to improve the basis of convection and turbulence investigation could be to include an additional long-range, vertically pointing lidar on a motion compensating platform into the setup, yielding a higher resolved and improved series of vertical velocity.

7.1.2 Dual scanning lidars

Since profiling lidars are limited in capturing convection characteristics unless there is adequate movement of convective structures relative to the lidar, observing convection in a two-dimensional plane with dual-scanning lidars is advantageous, for example, in low wind conditions. Yet, also this approach has some limitations, in particular because it is restricted to two dimensions in space, while convection is a three-dimensional phenomenon. Consequently, there is no guarantee that the core of a convective structure is appropriately mapped within a two-dimensional plane. The velocities within the observed slice through the convective structure can be smaller compared to a perfect slice through the core. In addition, convective structures are not always symmetrical around their vertical axis. Horizontal flow can tilt the convective structure, and even in low wind conditions, convective structures may not rise vertically but with a considerable tilt by following the terrain. Optimally, the dual-lidar cross-section should be oriented parallel to the circulations' predominant tilt direction, hence along the mean wind, or along the slope of the terrain. Another possibility could be to install the dual-lidar plane orthogonal to the predominant tilt direction and apply a tilt to the scanned cross-section. Yet, such tilted cross-sections are more complicated to achieve with continuous scans, since both θ_e and α need to change simultaneously. Also, a distinction between horizontal and vertical velocity components would be limited and the tilt of the cross-section would need to be adjusted to the structure's tilt correspondingly. An alternative approach would be to install a grid of dual-scanning lidars, with multiple dual-lidar planes in cross-and along wind orientation, to fully map the three-dimensional structure of the convective circulation.

Another limiting factor for the use of dual-scanning lidar, experienced in the field, was the availability of airborne particles (i.e. aerosols). Often, longer periods ($>1\,\mathrm{d}$) with precipitation events were followed by several days of extremely low SNR ($\approx -30\,\mathrm{dB}$) despite the presence of convective conditions, estimated from complementing flux and profiling measurements. Even though it was possible to recover a substantial amount of v_r data using the DBSCAN approach and gap-filling using temporal interpolation (see Sect. 4.2.3). The recovered v_r data was primarily at closer distances to the lidar, while larger distances still suffered from substantial data loss. This yielded a reduced overlap with sufficient data availability for dual-lidar wind speed retrieval, in particular for increased separation distance between the two lidars. Still, in a controlled setup, i.e., along the runway of an airport, and for conditions with a sufficient amount of airborne particles, even a single dual-lidar setup is well suited to capture and resolve the evolution of convective structures of multiple scales in space and time. Here, the minimum size of detectable structures is mainly dependent on the range gate width, while the maximum size is limited by the separation distance between the lidars and their maximum range.

7.2 Interplay of convective processes and boundary-layer evolution

7.2.1 Marine observations during a cold air outbreak

The spectral coherence and phase analysis (see Sect. 4.3.1) of the vertical wind and along wind speed fluctuations retrieved from ship-based, profiling lidar observations (see Sect. 4.1) yielded detailed insight into coherent convective structures in the MABL. Throughout the lifecycle of the evaluated marine CAO event, convective structures in the atmospheric flow field provide a strong coherent signal. The profiling lidar estimates are independent of cloud formation and able to provide more detailed observations in space than satellites. Here, the lidar estimates yield additional information of the structures' dynamics, i.e., that the detected coherent structures during the evaluated CAO featured strong and narrow updrafts and wide and comparably weak downdrafts. Further, the ship-based lidar installation provides a better temporal coverage than aircraft-based measurements. Still, the interpretation of the interplay of convection and other boundary-layer processes strongly benefits from complementing observations from, e.g., satellite or aircraft. In fact, to interpret the convective characteristics estimated from the lidar observations in the boundary layer context, at least complementing ship-based boundary-layer observations, as available for the study presented in Paper II, are essential.

Here, the Richardson number, that describes the predominating source of turbulence generation, and the surface-layer stratification has a direct and most notable impact on the size, strength and proportions (isotropic vs anisotropic) of coherent convective structures. The largest coherent convective structures, that are responsible for the overturning of the boundary layer and hence achieve the most effective vertical transport, are present for conditions, where turbulence generation is weakly buoyancy-dominated, or balanced between buoyancy and shear. Over the life-cycle of the CAO, buoyancy dominated regimes, that feature strong unstable stratification in the surface layer, are predominated by the small scale convective structures in the altitude range covered by the lidar observations. Here, a decoupling of surface layer and mixed layer above is possible, and a long-range lidar profiler could yield improved insight with respect to the predominating convective structures and atmospheric processes (decoupling versus merging) in the mixed layer. In shear-dominated regimes, that correspond to neutral or even weakly stable stratification in the surface layer, larger scale convection is suppressed, and consequently no, or only small scale coherent structures, are detectable in the atmospheric flow field.

The growth of the boundary-layer depth is closely linked to the evolution in horizontal structure scale. Initially, smaller and weaker convective structures push up the boundary layer. Here, boundary-layer depth and horizontal size of these structures are of comparable size (aspect ratio ≈ 2). The convective structures increase both horizontally and vertically as the boundary layer increases, maintaining a near constant aspect ratio. After the boundary layer growth, and the related increase in vertical coherent structures size and velocity, declines at some point, the coherent structures continue to increase in horizontal size, yielding an increasing aspect ratio and anisotropy of the structures with time. In contrast to periods of elevated boundary-layer growth, the corresponding overturning circulation by convective structures is able to compensate the enrichment of near-surface moisture and heat, that is driven by turbulent fluxes during periods where the boundary-layer growth stagnates.

In the surface layer up to approximately 150 m altitude ($\approx 0.1\, z_i$), plumes with horizontal scales between 400 m and 1 km predominate. At higher altitudes in the mixed layer (≥ 170 m) the horizontal scale of these smaller coherent structures approximately doubled (1 km to 2 km scale) compared the scale of the surface layer plumes. Smaller structures are found to feature weaker vertical velocities and consequently do not always provide the necessary momentum to penetrate into the mixed layer. Further, of the mixed layer convection, not all observed convective structures (between 170 m and 300 m altitude) extend through the whole mixed layer and manifest as clouds[2] at the top of the MABL. Only the convective structures with horizontal scales, that are two to three times the boundary layer depth

---

[2] The cloud estimate is based on complementing satellite observations

or larger, penetrate the whole boundary layer and contribute to the convective over-turning and deepening of the CBL.

The investigated convective structures only represent highly organised convection, that periodically reoccurs in the flow (see Sect. 4.21). Yet, in particular the largest scale convective structures, do not necessarily follow this periodic behaviour as a pattern of such structures possibly evolves and changes during the period required for the structures to pass over the lidar. To detect and include non-coherent convection into the evaluation, a different methodology is needed. A possibility is to apply a wavelet analysis to the series of velocity fluctuations to identify the temporal evolution of both coherent and irregular convective structures in the flow (see e.g *Barthlott et al.*, 2007). Here, the challenge is to distinguish convective from non-convective structures, due to the lack of the phase information.

7.2.2 Land-based observations in flat and complex terrain

The analysis of the convective velocity field retrieved from the dual-lidar observations (see Sect. 4.2.2) revealed a multitude of valuable insights into land-based convection in flat and complex terrain. For instance, surface heterogeneities strongly impacted the location at which convection was triggered and convective structures tended to maintain a similar triggering region over their life-cycle. During the two cases, presented in Paper III, the region of horizontal convergence around the lower part of the updraft was much clearer defined than the region of divergence around the upper part. In the case observed at Vaksinen airport, the updrafts were rather narrow and featured well defined cores, that originated as continuous streams at the surface (thermal characteristics). In the divergence region, towards the top of the convective circulation, however, clusters of increased updraft velocity detached (bubble characteristics). Here, the individual convective structures modulated the boundary layer depth horizontally, being slightly deeper above the updraft. The case observed at Starmoen airport featured a narrow updraft core that was attached to the surface and that widened with increasing altitude in the initial phase of the convection. Interestingly, the convective flow, confined by streamlines, maintained approximately the same width throughout the boundary-layer depth. Here, the vertical velocity cluster (updraft) detached (bubble character) at a later stage in the evolution of the convective circulation. This event initialised the break down of circulation, as buoyant forcing decreased and only inertia maintained the circulation against back-pressure (see Fig. 3.2) and drag forces.

Despite similar forcing by incoming short-wave and long-wave radiation and resulting similar turbulent heat fluxes, the two case studies evaluated in Paper III result in a different evolution of the convective circulation and the boundary layer parameters. The largest differences observed between the cases were the boundary-layer depth and the near-surface flux Richardson number. In contrast to the observations in the MABL, the case with buoyancy dominated turbulence generation (Starmoen airport) featured larger convective structures and a deeper boundary layer than the case where turbulence was approximately balanced between buoyancy and shear (Vaksinen airport). Still, in both cases the evaluated convective structures spanned the entire boundary layer and featured similar maximum updraft velocities (between $2\,\mathrm{m\,s^{-1}}$ and $3\,\mathrm{m\,s^{-1}}$). Mainly the differences in geography and terrain were postulated to be responsible for the different responses to the forcing mechanisms.

The site corresponding to the shallow boundary-layer case (Vaksinen airport) is located in close vicinity to the North Sea and in rather complex terrain with peaks around 300 m. Here, accumulation of cold air in the studied valley system possibly caused a nocturnal low-level temperature inversion. Further, cold air advection from sea possibly created an internal boundary layer, that contributed to the maintenance of the inversion and increased horizontal velocity (shear) in the free atmosphere, that is too strong to penetrate by the vertical velocities of the observed convection. The site corresponding to the deeper boundary layer and convection (Starmoen airport), on the other hand, is located further inland and in rather flat terrain. Here, a deeper residual layer remained from the proceeding day presumably with a weaker capping inversion and weaker wind shear to free atmosphere aloft. However, to confirm this hypothesis without doubt, additional profile series of temperature that complement the lidar estimates are required and should be included in future setups.

Results presented for collocated observations sampled by dual-scanning lidars, and sensors installed on paragliders and a skydiving plane in the Voss area (see Sect. 6.4), provided first insights into the potential of such complementing profiles for studying atmospheric convection in complex terrain. Here, the dual-lidar installation was able to capture and resolve the lower part of a convective circulation, while paraglider data contributed complementing information about the updraft velocity and virtual potential temperature anomaly in the upper part of the convective updraft. During the growth of the convective boundary layer, maximum updraft velocities of up to $4.5\,\mathrm{m\,s^{-1}}$ were obtained just below the capping inversion. Here, virtual potential temperature anomalies between 1 K and 1.5 K were measured inside the updraft. Despite the considerably large updraft velocities and virtual potential temperature anomalies, the boundary-layer growth was capped at approximately 1800 m, opposed to a boundary-layer depth above 2000 m in the cloud-topped case at Starmoen Airport. In contrast to the cases evaluated in Paper III, the convective structures were considerably tilted and their aspect ratio was comparably smaller. For the latter, it should be noted, that evaluation in the Voss case was focused on the period of boundary-layer growth, in contrast to evaluation of a convective circulation in the fully developed convective boundary layer. Already from the selection of these three cases of convection it can be confirmed, that the interplay of convection and boundary-layer processes is complex and the number of different mechanisms is manifold.

7.3 Further perspective

The profiling and dual-scanning lidar approaches evaluated in this dissertation yield promising insight into the structure and dynamics of convection. They constitute a very promising proof-of-concept and open up for new pathways to overcome the still existent observational gaps in CBL research. Here, more lidar installations with similar or improved strategies to observe convection, combined with conventional meteorological observations and new approaches, such as the highly resolved background temperature and humidity profiles and profiles from within the convective updraft as tested during the gLidar campaign in Voss (Sect. 6.2), are required. These observations need to be based on longer observational periods and need to cover a larger variety of geographical and meteorological background conditions. Corresponding long term lidar installations can in the future provide robust and representative statistics on convective key parameters that will further deepen our understanding of atmospheric convection and its relation to atmospheric boundary-layer processes. In combination with Large Eddy Simulations, that require high-resolution observations both for the initialization of the model runs and their validation, this will also provide considerable potential for a future improvement of the boundary layer and convection parameterization schemes in the numerical weather prediction and climate models.

Bibliography

Achtert, P., I. M. Brooks, B. J. Brooks, B. I. Moat, J. Prytherch, P. O. G. Persson, and M. Tjernström (2015), Measurement of wind profiles by motion-stabilised ship-borne Doppler lidar, *Atmospheric Measurement Techniques*, *8*(11), 4993–5007, doi:10.5194/amt-8-4993-2015. 2, 18, 37

Adler, B., O. Kiseleva, N. Kalthoff, and A. Wieser (2019), Comparison of Convective Boundary Layer Characteristics from Aircraft and Wind Lidar Observations, *Journal of Atmospheric and Oceanic Technology*, *36*(7), 1381 – 1399, doi:10.1175/JTECH-D-18-0118.1. 1, 2, 28, 29

Adler, B., N. Kalthoff, and O. Kiseleva (2020), Detection of structures in the horizontal wind field over complex terrain using coplanar Doppler lidar scans, *Meteorologische Zeitschrift*, *29*(6), 467–481, doi:10.1127/metz/2020/1031. 2, 3, 30

Adler, B., A. Gohm, N. Kalthoff, N. Babi, U. Corsmeier, M. Lehner, M. W. Rotach, M. Haid, P. Markmann, E. Gast, G. Tsaknakis, and G. Georgoussis (2021), CROSSINN: A Field Experiment to Study the Three-Dimensional Flow Structure in the Inn Valley, Austria, *Bulletin of the American Meteorological Society*, *102*(1), E38 – E60, doi:10.1175/BAMS-D-19-0283.1. 2

Alcayaga, L. (2020), Filtering of pulsed lidar data using spatial information and a clustering algorithm, *Atmospheric Measurement Techniques*, *13*(11), 6237–6254, doi:10.5194/amt-13-6237-2020. 29, 31

Atkinson, B. W., and J. Zhang, Wu (1996), Mesoscale shallow convection in the atmosphere, *Reviews of Geophysics*, *34*(4), 403–431, doi:10.1029/96RG02623. 12

Atlas, D., B. Walter, S.-H. Chou, and P. J. Sheu (1986), The Structure of the Unstable Marine Boundary Layer Viewed by Lidar and Aircraft Observations, *Journal of the Atmospheric Sciences*, *43*(13), 1301–1318, doi:10.1175/1520-0469(1986)043<1301:TSOTUM>2.0.CO;2. 2, 10, 12

Bange, J., J. Reuder, and A. Platis (2021), Unmanned Aircraft Systems, in *Springer Handbook of Atmospheric Measurements*, edited by T. Foken, pp. 1331–1349, Springer International Publishing, Cham, doi:10.1007/978-3-030-52171-4_49. 16

Barthlott, C., P. Drobinski, C. Fesquet, T. Dubos, and C. Pietras (2007), Long-term study of coherent structures in the atmospheric surface layer, *Boundary-Layer Meteorology*, *125*, 1–24, doi:10.1007/s10546-007-9190-9. 61

Behrendt, A., T. Nakamura, M. Onishi, R. Baumgart, and T. Tsuda (2002), Combined Raman lidar for the measurement of atmospheric temperature, water vapor, particle extinction coefficient, and particle backscatter coefficient, *Appl. Opt.*, *41*(36), 7657–7666, doi:10.1364/AO.41.007657. 18

Behrens, K. (2021), Radiation Sensors, in *Springer Handbook of Atmospheric Measurements*, edited by T. Foken, pp. 297–357, Springer International Publishing, Cham, doi:10.1007/978-3-030-52171-4_11. 14

Bénard, H. (1900), Étude expérimentale des courants de convection dans une nappe liquide. Régime permanent: tourbillons cellulaires, *Journal of Physics: Theories and Applications*, *9*(1), 513–524. 7

Bergé, P., and M. Dubois (1984), Rayleigh-bénard convection, *Contemporary Physics*, *25*(6), 535–582, doi:10.1080/00107518408210730. 7, 8

Bonin, T. A., and A. W. Brewer (2017), Detection of Range-Folded Returns in Doppler Lidar Observations, *IEEE Geoscience and Remote Sensing Letters*, *14*(4), 514–518, doi:10.1109/LGRS.2017.2652360. 31

Brilouet, P.-E., P. Durand, and G. Canut (2017), The marine atmospheric boundary layer under strong wind conditions: Organized turbulence structure and flux estimates by airborne measurements, *Journal of Geophysical Research: Atmospheres*, *122*(4), 2115–2130, doi:10.1002/2016JD025960. 1, 12

Brümmer, B. (1996), Boundary-layer modification in wintertime cold-air outbreaks from the Arctic sea ice, *Boundary-Layer Meteorology*, *80*, 109125, doi: 10.1007/BF00119014. 1, 12

Calhoun, R., R. Heap, M. Princevac, R. Newsom, H. Fernando, and D. Ligon (2006), Virtual Towers Using Coherent Doppler Lidar during the Joint Urban 2003 Dispersion Experiment, *Journal of Applied Meteorology and Climatology*, *45*(8), 1116 – 1126, doi:10.1175/JAM2391.1. 2

Cauteruccio, A., M. Colli, M. Stagnaro, L. G. Lanza, and E. Vuerich (2021), Insitu Precipitation Measurements, in *Springer Handbook of Atmospheric Measurements*, edited by T. Foken, pp. 359–400, Springer International Publishing, Cham, doi:10.1007/978-3-030-52171-4_12. 14

Chepfer, H., S. Bony, D. Winker, M. Chiriaco, J.-L. Dufresne, and G. Sèze (2008), Use of CALIPSO lidar observations to evaluate the cloudiness simulated by a climate model, *Geophysical Research Letters*, *35*(15), doi:10.1029/2008GL034207. 18

Cherukuru, N. W., R. Calhoun, M. Lehner, S. W. Hoch, and C. D. Whiteman (2015), Instrument configuration for dual-Doppler lidar coplanar scans: METCRAX II, *Journal of Applied Remote Sensing*, *9*(1), 096,090, doi:10.1117/1.JRS.9.096090. 30

Cheynet, E., M. Flügge, J. Reuder, J. B. Jakobsen, Y. Heggelund, B. Svardal, P. Saavedra Garfias, C. Obhrai, N. Daniotti, J. Berge, C. Duscha, N. Wildmann, I. H. Onarheim, and M. Godvik (2021), The COTUR project: remote sensing of offshore turbulence for wind energy application, *Atmospheric Measurement Techniques*, *14*(9), 6137–6157, doi:10.5194/amt-14-6137-2021. ix, 28

Cieszelski, R. (1998), A Case Study of Rayleigh-Bénard Convection with Clouds, *Boundary-Layer Meteorology*, *88*(2), 211–237, doi:10.1023/A:1001145803614. 1, 8, 10, 12

Cook, P., and I. Renfrew (2015), Aircraft-based observations of air-sea turbulent fluxes around the British Isles: Observations of Air-Sea Fluxes, *Quarterly Journal of the Royal Meteorological Society*, *141*, doi:10.1002/qj.2345. 1

Crewell, S., M. Wendisch, and U. Löhnert (2021), Passive Solar and Microwave Spectral Radiometers, in *Springer Handbook of Atmospheric Measurements*, edited by T. Foken, pp. 821–840, Springer International Publishing, Cham, doi:10.1007/978-3-030-52171-4_29. 17

de Ferranti, J., and C. Hormann (2022), Digital elevation data, http://viewfinderpanoramas.org/dem3.html (last access: 2023-11-15). 50

de Foy, B., J. R. Varela, L. T. Molina, and M. J. Molina (2006), Rapid ventilation of the Mexico City basin and regional fate of the urban plume, *Atmospheric Chemistry and Physics*, *6*(8), 2321–2335, doi:10.5194/acp-6-2321-2006. 1

Duscha, C., M. B. Paskyabi, and J. Reuder (2020), Statistic and Coherence Response of Ship-based Lidar Observations to Motion Compensation, *Journal of Physics: Conference Series*, *1669*, 012,020, doi:10.1088/1742-6596/1669/1/012020. ix

Duscha, C., C. Barrell, I. A. Renfrew, I. M. Brooks, H. Sodemann, and J. Reuder (2022), A Ship-Based Characterization of Coherent Boundary-Layer Structures Over the Lifecycle of a Marine Cold-Air Outbreak, *Boundary-Layer Meteorology*, *183*, 355–380, doi:10.1007/s10546-022-00692-y. ix

Duscha, C., J. Pálenik, T. Spengler, and J. Reuder (2023), Observing atmospheric convection with dual-scanning lidars, *Atmospheric Measurement Techniques*, *16*(21), 5103–5123, doi:10.5194/amt-16-5103-2023. ix

Edson, J., A. A. Hinton, K. Prada, J. Hare, and C. Fairall (1998), Direct Covariance Flux Estimates from Mobile Platforms at Sea, *Journal of Atmospheric and Oceanic Technology*, *15*, 547–562, doi:10.1175/1520-0426(1998)015<0547:DCFEFM>2.0.CO;2. 27

Emanuel, K. A. (1994), *Atmospheric convection*, Oxford University Press, New York, ISBN: 9780195066302. 1

Emeis, S. (2021), Sodar and RASS, in *Springer Handbook of Atmospheric Measurements*, edited by T. Foken, pp. 661–681, Springer International Publishing, Cham, doi:10.1007/978-3-030-52171-4_23. 17

Emeis, S., M. Harris, and R. M. Banta (2007), Boundary-layer anemometry by optical remote sensing for wind energy applications, *Meteorologische Zeitschrift*, *16*(4), 337–347, doi:10.1127/0941-2948/2007/0225. 18

Emeis, S., K. Schäfer, and C. Münkel (2008), Surface-based remote sensing of the mixing-layer height a review, *Meteorologische Zeitschrift*, *17*(5), 621–630, doi:10.1127/0941-2948/2008/0312. 2

Emery, W. J., and R. E. Thomson (2001), Data Analysis Methods in Physical Oceanography - Time-series Analysis Methods, chap. 5, pp. 371–567, Elsevier Science, doi:10.1016/B978-044450756-3/50006-X. 35

Ester, M., H.-P. Kriegel, J. Sander, and X. Xu (1996), A density-based algorithm for discovering clusters in large spatial databases with noise, pp. 226–231, AAAI Press, Proceedings of the Second International Conference on Knowledge Discovery and Data Mining (KDD-96). ISBN 1-57735-004-9. 31

Fernando, H. J. S., J. Mann, J. M. L. M. Palma, J. K. Lundquist, R. J. Barthelmie, M. Belo-Pereira, W. O. J. Brown, F. K. Chow, T. Gerz, C. M. Hocut, P. M. Klein, L. S. Leo, J. C. Matos, S. P. Oncley, S. C. Pryor, L. Bariteau, T. M. Bell, N. Bodini, M. B. Carney, M. S. Courtney, E. D. Creegan, R. Dimitrova, S. Gomes, M. Hagen, J. O. Hyde, S. Kigle, R. Krishnamurthy, J. C. Lopes, L. Mazzaro, J. M. T. Neher, R. Menke, P. Murphy, L. Oswald, S. Otarola-Bustos, A. K. Pattantyus, C. V. Rodrigues, A. Schady, N. Sirin, S. Spuler, E. Svensson, J. Tomaszewski, D. D. Turner, L. van Veen, N. Vasiljevi, D. Vassallo, S. Voss, N. Wildmann, and Y. Wang (2019), The Perdigão: Peering into Microscale Details of Mountain Winds, *Bulletin of the American Meteorological Society*, *100*(5), 799 – 819, doi:10.1175/BAMS-D-17-0227.1. 18, 29

Fischer, G. (2006), Installation and Operation of the Research Platform FINO1 in the North Sea, in *Offshore Wind Energy: Research on Environmental Impacts*, edited by J. Köller, J. Köppel, and W. Peters, pp. 237–253, Springer Berlin Heidelberg, Berlin, Heidelberg, doi:10.1007/978-3-540-34677-7_15. 1

Foken, T., and J. Bange (2021a), Temperature Sensors, in *Springer Handbook of Atmospheric Measurements*, edited by T. Foken, pp. 183–208, Springer International Publishing, Cham, doi:10.1007/978-3-030-52171-4_7. 14

Foken, T., and J. Bange (2021b), Wind Sensors, in *Springer Handbook of Atmospheric Measurements*, edited by T. Foken, pp. 243–272, Springer International Publishing, Cham, doi:10.1007/978-3-030-52171-4_9. 15

Furevik, B. R., and H. Haakenstad (2012), Near-surface marine wind profiles from rawinsonde and NORA10 hindcast, *Journal of Geophysical Research: Atmospheres*, *117*(D23), doi:10.1029/2012JD018523. 1

Geerts, B., D. J. Raymond, V. Grubii, C. A. Davis, M. C. Barth, A. Detwiler, P. M. Klein, W.-C. Lee, P. M. Markowski, G. L. Mullendore, and J. A. Moore (2018), Recommendations for In Situ and Remote Sensing Capabilities in Atmospheric Convection and Turbulence, *Bulletin of the American Meteorological Society*, *99*(12), 2463 – 2470, doi:10.1175/BAMS-D-17-0310.1. 1

Ghirardelli, M., S. T. Kral, N. C. Müller, R. Hann, E. Cheynet, and J. Reuder (2023), Flow Structure around a Multicopter Drone: A Computational Fluid

Dynamics Analysis for Sensor Placement Considerations, *Drones*, *7*(7), doi:10.3390/drones7070467. 17

Gottschall, J., B. Gribben, D. Stein, and I. Würth (2017), Floating lidar as an advanced offshore wind speed measurement technique: current technology status and gap analysis in regard to full maturity, *WIREs Energy and Environment*, *6*(5), e250, doi:10.1002/wene.250. 2, 18

Gottschall, J., E. Catalano, M. Dörenkämper, and B. Witha (2018), The NEWA Ferry Lidar Experiment: Measuring Mesoscale Winds in the Southern Baltic Sea, *Remote Sensing*, *10*(10), doi:10.3390/rs10101620. 2, 18

Gutiérrez-Antuñano, M. A., J. Tiana-Alsina, and F. Rocadenbosch (2017), Performance evaluation of a floating lidar buoy in nearshore conditions, *Wind Energy*, *20*(10), 1711–1726, doi:10.1002/we.2118. 2

Haid, M., A. Gohm, L. Umek, H. C. Ward, T. Muschinski, L. Lehner, and M. W. Rotach (2020), Foehncold pool interactions in the Inn Valley during PIANO IOP2, *Quarterly Journal of the Royal Meteorological Society*, *146*(728), 1232–1263, doi:10.1002/qj.3735. 2, 29

Han, G., G. Wang, and X. Zheng (2019), Applicability of Taylors Hypothesis for Estimating the Mean Streamwise Length Scale of Large-Scale Structures in the Near-Neutral Atmospheric Surface Layer, *Boundary-Layer Meteorology*, *172*, 215–237, doi:10.1007/s10546-019-00446-3. 2

Hartmann, J., C. Kottmeier, and S. Raasch (1997), Roll Vortices and Boundary-Layer Development during a Cold Air Outbreak, *Boundary-Layer Meteorology*, *84*, 4565, doi:10.1023/A:1000392931768. 1, 12, 35, 39

Hellevang, J. O., S. H. Stavland, I. Øyvind Sand, and J. Reuder (2012), Lidar Motion Test: Grimstad 2011 - Setup and results, CMR Instrumentation, Report for Fugro OCEANOR. 43

Henkies, M., V. Høyland, Knut, A. Shestov, C. Duscha, and A. Sjöblom (2023), The Arctic Fjord Breeze: Characteristics of a Combined Sea Breeze and Valley Wind in a Svalbard Fjord Valley, *Boundary-Layer Meteorology*, doi:10.1007/s10546-023-00840-y. ix

Holzworth, G. C. (1964), Estimates of mean maximum mixing depths in the contiguous united states, *Monthly Weather Review*, *92*(5), 235 – 242, doi:10.1175/1520-0493(1964)092<0235:EOMMMD>2.3.CO;2. 11

Hägeli, P., D. G. Steyn, and K. B. Strawbridge (2000), Spatial And Temporal Variability Of Mixed-Layer Depth And Entrainment Zone Thickness, *Boundary-Layer Meteorology*, *97*, 47–71, doi:10.1023/A:1002790424133. 2

Inokuchi, H., H. Tanaka, and T. Ando (2009), Development of an Onboard Doppler Lidar for Flight Safety, *Journal of Aircraft*, *46*(4), 1411–1415, doi:10.2514/1.41738. 18

Ito, J., H. Niino, and K. Yoshino (2020), Large Eddy Simulation on Horizontal Convective Rolls that Caused an Aircraft Accident during its Landing at Narita Airport, *Geophysical Research Letters*, *47*(6), doi:10.1029/2020GL086999. 1

Iwai, H., S. Ishii, N. Tsunematsu, K. Mizutani, Y. Murayama, T. Itabe, I. Yamada, N. Matayoshi, D. Matsushima, S. Weiming, T. Yamazaki, and T. Iwasaki (2008), Dual-Doppler lidar observation of horizontal convective rolls and near-surface streaks, *Geophysical Research Letters*, *35*(14), doi:10.1029/2008GL034571. 3

Jeevanjee, N., and D. M. Romps (2015), Effective Buoyancy, Inertial Pressure, and the Mechanical Generation of Boundary Layer Mass Flux by Cold Pools, *Journal of the Atmospheric Sciences*, *72*(8), 3199 – 3213, doi:10.1175/JAS-D-14-0349.1. 1, 9

Jeevanjee, N., and D. M. Romps (2016), Effective buoyancy at the surface and aloft, *Quarterly Journal of the Royal Meteorological Society*, *142*(695), 811–820, doi:10.1002/qj.2683. 9

Kaimal, J. C., J. C. Wyngaard, D. A. Haugen, O. R. Coté, Y. Izumi, S. J. Caughey, and C. J. Readings (1976), Turbulence Structure in the Convective Boundary Layer, *Journal of Atmospheric Sciences*, *33*(11), 2152 – 2169, doi:10.1175/1520-0469(1976)033<2152:TSITCB>2.0.CO;2. 1, 10

Kaimal, J. C., R. A. Eversole, D. H. Lenschow, B. B. Stankov, P. H. Kahn, and J. A. Businger (1982), Spectral Characteristics of the Convective Boundary Layer Over Uneven Terrain, *Journal of Atmospheric Sciences*, *39*(5), 1098 – 1114, doi:10.1175/1520-0469(1982)039<1098:SCOTCB>2.0.CO;2. 1

Kanitz, T., J. Lochard, J. Marshall, P. McGoldrick, O. Lecrenier, P. Bravetti, O. Reitebuch, M. Rennie, D. Wernham, and A. Elfving (2019), Aeolus first light: first glimpse, in *International Conference on Space Optics ICSO 2018*, vol. 11180, edited by Z. Sodnik, N. Karafolas, and B. Cugny, p. 111801R, International Society for Optics and Photonics, SPIE, doi:10.1117/12.2535982. 18

Kavaya, M. J., J. Y. Beyon, G. J. Koch, M. Petros, P. J. Petzar, U. N. Singh, B. C. Trieu, and J. Yu (2014), The Doppler Aerosol Wind (DAWN) Airborne, Wind-Profiling Coherent-Detection Lidar System: Overview and Preliminary Flight Results, *Journal of Atmospheric and Oceanic Technology*, *31*(4), 826 – 842, doi:10.1175/JTECH-D-12-00274.1. 18

Kelberlau, F., V. Neshaug, L. Lønseth, T. Bracchi, and J. Mann (2020), Taking the Motion out of Floating Lidar: Turbulence Intensity Estimates with a Continuous-Wave Wind Lidar, *Remote Sensing*, *12*(5), doi:10.3390/rs12050898. 2, 43

Kolle, O., N. Kalthoff, C. Kottmeier, and J. W. Munger (2021), Ground-Based Platforms, in *Springer Handbook of Atmospheric Measurements*, edited by T. Foken, pp. 155–182, Springer International Publishing, Cham, doi:10.1007/978-3-030-52171-4_6. 16

Krutova, M., M. Bakhoday-Paskyabi, J. Reuder, and F. G. Nielsen (2022), Development of an automatic thresholding method for wake meandering studies and its application to the data set from scanning wind lidar, *Wind Energy Science*, *7*(2), 849–873, doi:10.5194/wes-7-849-2022. 18, 29

Kumer, V.-M., J. Reuder, M. Dorninger, R. Zauner, and V. Grubisic (2016), Turbulent kinetic energy estimates from profiling wind LiDAR measurements and their potential for wind energy applications, *Renewable Energy*, *99*, 898 – 910, doi:10.1016/j.renene.2016.07.014. 1

Kunkel, K. E., E. W. Eloranta, and S. T. Shipley (1977), Lidar Observations of the Convective Boundary Layer, *Journal of Applied Meteorology and Climatology*, *16*(12), 1306 – 1311, doi:10.1175/1520-0450(1977)016<1306:LOOTCB>2.0.CO;2. 1, 2, 10, 18

Köpp, F., S. Rahm, and I. Smalikho (2004), Characterization of Aircraft Wake Vortices by 2-m Pulsed Doppler Lidar, *Journal of Atmospheric and Oceanic Technology*, *21*(2), 194 – 206, doi:10.1175/1520-0426(2004)021<0194:COAWVB>2.0.CO;2. 18

Lai, T. L., H. Robbins, and C. Z. Wei (1978), Strong consistency of least squares estimates in multiple regression, *Proceedings of the National Academy of Sciences*, *75*(7), 3034–3036, doi:10.1073/pnas.75.7.3034. 24

Lee, X., W. Massman, and B. Law (2005), *Handbook of Micrometeorology - A Guide for Surface Flux Measurement and Analysis*, 1, Springer Dordrecht, doi:10.1007/1-4020-2265-4. 15

Lehmann, V., and W. Brown (2021), Radar Wind Profiler, in *Springer Handbook of Atmospheric Measurements*, edited by T. Foken, pp. 901–933, Springer International Publishing, Cham, doi:10.1007/978-3-030-52171-4_31. 17

LeMone, M. A. (1973), The Structure and Dynamics of Horizontal Roll Vortices in the Planetary Boundary Layer, *Journal of the Atmospheric Sciences*, *30*(6), 1077–1091, doi:10.1175/1520-0469(1973)030<1077:TSADOH>2.0.CO;2. 1, 12

LeMone, M. A. (1976), Modulation of Turbulence Energy by Longitudinal Rolls in an Unstable Planetary Boundary Layer, *Journal of the Atmospheric Sciences*, *33*(7), 1308–1320, doi:10.1175/1520-0469(1976)033<1308:MOTEBL>2.0.CO;2. 1

Liu, H., Z. Meng, Y. Zhu, and Y. Huang (2023), Convection Initiation Associated with a Boundary Layer Convergence Line over a Real-World Sharp Vegetation-Contrast Area, *Monthly Weather Review*, *151*(5), 1189 – 1212, doi:10.1175/MWR-D-22-0083.1. 1, 9

Lorenz, E. N. (1963), Deterministic Nonperiodic Flow, *Journal of Atmospheric Sciences*, *20*(2), 130 – 141, doi:10.1175/1520-0469(1963)020<0130:DNF>2.0.CO;2. 8

Lothon, M., D. Lenschow, and S. Mayor (2006), Coherence and Scale of Vertical Velocity in the Convective Boundary Layer from a Doppler Lidar, *Boundary-Layer Meteorology*, *121*, 521536, doi:10.1007/s10546-006-9077-1. 2, 28

Lothon, M., D. Lenschow, and S. Mayor (2009), Doppler Lidar Measurements of Vertical Velocity Spectra in the Convective Planetary Boundary Layer, *Boundary-Layer Meteorology*, *132*(1573-1472), 205–226, doi:10.1007/s10546-009-9398-y. 2, 28

Lu, N.-Y., P. Hawbecker, S. Basu, and L. Manuel (2019), On Wind Turbine Loads During Thunderstorm Downbursts in Contrasting Atmospheric Stability Regimes, *Energies*, *12*(14), doi:10.3390/en12142773. 1

Malekmohammadi, S., A. D. Jenkins, C. Duscha, F. Kelberlau, J. Gottschall, and J. Reuder (in prep), Controlled-motion test of lidar wind profilers, *Atmospheric Measurement Techniques*. ix, 43

Martucci, G., R. Matthey, V. Mitev, and H. Richner (2007), Comparison between Backscatter Lidar and Radiosonde Measurements of the Diurnal and Nocturnal Stratification in the Lower Troposphere, *Journal of Atmospheric and Oceanic Technology*, *24*(7), 1231 – 1244, doi:10.1175/JTECH2036.1. 2

May, P. T., and D. K. Rajopadhyaya (1999), Vertical Velocity Characteristics of Deep Convection over Darwin, Australia, *Monthly Weather Review*, *127*(6), 1056 – 1071, doi:10.1175/1520-0493(1999)127<1056:VVCODC>2.0.CO;2. 10

Melfi, S. H., J. D. Spinhirne, S.-H. Chou, and S. P. Palm (1985), Lidar Observations of Vertically Organized Convection in the Planetary Boundary Layer over the Ocean, *Journal of Applied Meteorology and Climatology*, *24*(8), 806 – 821, doi:10.1175/1520-0450(1985)024<0806:LOOVOC>2.0.CO;2. 1, 2, 10

Mikkelsen, T. (2014), Lidar-based Research and Innovation at DTU Wind Energy a Review, *Journal of Physics: Conference Series*, *524*(1), doi:10.1088/1742-6596/524/1/012007. 18

Newsom, R., R. Calhoun, and D. Ligon (2008), Linearly Organized Turbulence Structures Observed Over a Suburban Area by Dual-Doppler Lidar, *Boundary-Layer Meteorology*, *127*, 111130, doi:10.1007/s10546-007-9243-0. 2, 29, 30

Newsom, R. K., D. Ligon, R. Calhoun, R. Heap, E. Cregan, and M. Princevac (2005), Retrieval of microscale wind and temperature fields from single-and dual-Doppler lidar data, *Journal of Applied Meteorology and Climatology*, *44*(9), 1324–1345, doi:10.1175/JAM2280.1. 2, 3, 29

Nieuwstadt, F. T. M., and R. A. Brost (1986), The Decay of Convective Turbulence, *Journal of Atmospheric Sciences*, *43*(6), 532 – 546, doi:10.1175/1520-0469(1986)043<0532:TDOCT>2.0.CO;2. 12

Peña, A., C. B. Hasager, S.-E. Gryning, M. Courtney, I. Antoniou, and T. Mikkelsen (2009), Offshore wind profiling using light detection and ranging measurements, *Wind Energy*, *12*(2), 105–124, doi:10.1002/we.283. 2

Pálenik, J. (2022), gLidar project website, https://glidar-project.github.io/ (last access: 2023-01-25). 51

Pálenik, J., T. Spengler, and H. Hauser (2021), IsoTrotter: Visually Guided Empirical Modelling of Atmospheric Convection, *IEEE Transactions on Visualization and Computer Graphics*, *27*(2), 775–784, doi:10.1109/TVCG.2020.3030389. 10, 47

Rahm, S., and I. Smalikho (2008), Aircraft Wake Vortex Measurement with Airborne Coherent Doppler Lidar, *Journal of Aircraft*, *45*(4), 1148–1155, doi: 10.2514/1.32896. 18

Rayleigh, L. (1916), LIX. On convection currents in a horizontal layer of fluid, when the higher temperature is on the under side , *The London, Edinburgh, and Dublin Philosophical Magazine and Journal of Science*, *32*(192), 529–546, doi:10.1080/14786441608635602. 7

Reitebuch, O., and R. M. Hardesty (2021), Doppler Wind Lidar, in *Springer Handbook of Atmospheric Measurements*, edited by T. Foken, pp. 759–797, Springer International Publishing, Cham, doi:10.1007/978-3-030-52171-4_27. 18

Renfrew, I. A., and G. W. K. Moore (1999), An Extreme Cold-Air Outbreak over the Labrador Sea: Roll Vortices and AirSea Interaction, *Monthly Weather Review*, *127*(10), 2379–2394, doi:10.1175/1520-0493(1999)127<2379:AECAOO>2.0.CO;2. 1, 10, 12

Renfrew, I. A., R. S. Pickart, K. Våge, G. W. K. Moore, T. J. Bracegirdle, A. D. Elvidge, E. Jeansson, T. Lachlan-Cope, L. T. McRaven, L. Papritz, J. Reuder, H. Sodemann, A. Terpstra, S. Waterman, H. Valdimarsson, A. Weiss, M. Almansi, F. Bahr, A. Brakstad, C. Barrell, J. K. Brooke, B. J. Brooks, I. M. Brooks, M. E. Brooks, E. M. Bruvik, C. Duscha, I. Fer, H. M. Golid, M. Hallerstig, I. Hessevik, J. Huang, L. Houghton, S. Jónsson, M. Jonassen, K. Jackson, K. Kvalsund, E. W. Kolstad, K. Konstali, J. Kristiansen, R. Ladkin, P. Lin, A. Macrander, A. Mitchell, H. Olafsson, A. Pacini, C. Payne, B. Palmason, M. D. Pérez-Hernández, A. K. Peterson, G. N. Petersen, M. N. Pisareva, J. O. Pope, A. Seidl, S. Semper, D. Sergeev, S. Skjelsvik, H. Søiland, D. Smith, M. A. Spall, T. Spengler, A. Touzeau, G. Tupper, Y. Weng, K. D. Williams, X. Yang, and S. Zhou (2019), The Iceland Greenland Seas Project, *Bulletin of the American Meteorological Society*, *100*(9), 1795–1817, doi:10.1175/BAMS-D-18-0217.1. ix

Renfrew, I. A., C. Barrell, A. D. Elvidge, J. K. Brooke, C. Duscha, J. C. King, J. Kristiansen, T. L. Cope, G. W. K. Moore, R. S. Pickart, J. Reuder, I. Sandu, D. Sergeev, A. Terpstra, K. Våge, and A. Weiss (2020), An evaluation of surface meteorology and fluxes over the Iceland and Greenland Seas in ERA5 reanalysis: the impact of sea ice distribution, *Quarterly Journal of the Royal Meteorological Society.* ix

Reuder, J., P. Brisset, M. M. Jonassen, and S. Mayer (2009), The Small Unmanned Meteorological Observer SUMO: A new tool for atmospheric boundary layer research, *Meteorologische Zeitschrift*, *18*(2), 141–147, doi:10.1127/0941-2948/2009/0363. 16

Reuder, J., M. Flügge, M. B. Paskyabi, E. Cheynet, C. Duscha, S. T. Kral, P. S. Garfias, I. Fer, B. Svardal, R. Frühmann, J. B. Jakobsen, D. Wagner, A. Fligg, A. Külpmann, L. von Bremen, J. Gottschall, M. Kreklau, J. Hahn, O. Outzen, K. Herklotz, and B. Gellatly (in prep), OBLEX-F1: An Extensive Observational Effort for Offshore Wind Energy Research with Emphasis on Atmospheric Measurements, *Wind Energy Science*. ix

Rodgers, C. D. (2000), *Inverse methods for atmospheric sounding: theory and practice*, vol. 2, World scientific, ISBN: 9789810227401. 17

Röhner, L., and K. Träumner (2013), Aspects of Convective Boundary Layer Turbulence Measured by a Dual-Doppler Lidar System, *Journal of Atmospheric and Oceanic Technology*, *30*(9), 2132 – 2142, doi:10.1175/JTECH-D-12-00193.1. 3

Saltzman, B. (1962), Finite Amplitude Free Convection as an Initial Value ProblemI, *Journal of Atmospheric Sciences*, *19*(4), 329 – 341, doi:10.1175/1520-0469(1962)019<0329:FAFCAA>2.0.CO;2. 8

Sathe, A., and J. Mann (2013), A review of turbulence measurements using ground-based wind lidars, *Atmospheric Measurement Techniques*, *6*(11), 3147–3167, doi:10.5194/amt-6-3147-2013. 2

Sathe, A., J. Mann, J. Gottschall, and M. S. Courtney (2011), Can Wind Lidars Measure Turbulence?, *Journal of Atmospheric and Oceanic Technology*, *28*(7), 853–868, doi:10.1175/JTECH-D-10-05004.1. 2

Sonntag, D., T. Foken, H. Vömel, and O. Hellmuth (2021), Humidity Sensors, in *Springer Handbook of Atmospheric Measurements*, edited by T. Foken, pp. 209–241, Springer International Publishing, Cham, doi:10.1007/978-3-030-52171-4_8. 14

Stawiarski, C., K. Träumner, C. Knigge, and R. Calhoun (2013), Scopes and Challenges of Dual-Doppler Lidar Wind Measurements – An Error Analysis, *Journal of Atmospheric and Oceanic Technology*, *30*(9), 2044 – 2062, doi:10.1175/JTECH-D-12-00244.1. 2, 29, 30, 31

Stawiarski, C., K. Träumner, C. Kottmeier, C. Knigge, and S. Raasch (2015), Assessment of Surface-Layer Coherent Structure Detection in Dual-Doppler Lidar Data Based on Virtual Measurements, *Boundary-Layer Meteorology*, *156*(1573-1472), 371–393, doi:10.1007/s10546-015-0039-3. 30

Stull, R. B. (1988), Convective Mixed Layer, in *An Introduction to Boundary Layer Meteorology*, edited by R. B. Stull, pp. 441–497, Springer Netherlands, Dordrecht, doi:10.1007/978-94-009-3027-8_11, ISBN:978-94-009-3027-8. 1, 9, 10, 11, 12

Thwaites, F. T. (1995), Development of an acoustic vorticity meter to measure shear in ocean-boundary layers, Ph.D. thesis, Massachusetts Institute of Technology and Woods Hole Oceanographic Institution, doi:10.1575/1912/1576. 27

Torri, A., T. Foken, and J. Bange (2021), Pressure Sensors, in *Springer Handbook of Atmospheric Measurements*, edited by T. Foken, pp. 273–295, Springer International Publishing, Cham, doi:10.1007/978-3-030-52171-4_10. 14

Träumner, K., T. Damian, C. Stawiarski, and A. Wieser (2015), Turbulent Structures and Coherence in the Atmospheric Surface Layer, *Boundary-Layer Meteorology*, *154*(1), 1–25, doi:10.1007/s10546-014-9967-6. 30

Vasiljević, N., J. M. L. M. Palma, N. Angelou, J. Carlos Matos, R. Menke, G. Lea, J. Mann, M. Courtney, L. Frölen Ribeiro, and V. M. M. G. C. Gomes (2017), Perdigão 2015: methodology for atmospheric multi-Doppler lidar experiments, *Atmospheric Measurement Techniques*, *10*(9), 3463–3483, doi:10.5194/amt-10-3463-2017. 2

Virtanen, P., R. Gommers, T. E. Oliphant, M. Haberland, T. Reddy, D. Cournapeau, E. Burovski, P. Peterson, W. Weckesser, J. Bright, S. J. van der Walt, M. Brett, J. Wilson, K. J. Millman, N. Mayorov, A. R. J. Nelson, E. Jones, R. Kern, E. Larson, C. J. Carey, İ. Polat, Y. Feng, E. W. Moore, J. VanderPlas, D. Laxalde, J. Perktold, R. Cimrman, I. Henriksen, E. A. Quintero, C. R. Harris, A. M. Archibald, A. H. Ribeiro, F. Pedregosa, P. van Mulbregt, and SciPy 1.0 Contributors (2020), SciPy 1.0: Fundamental Algorithms for Scientific Computing in Python, *Nature Methods*, *17*, 261–272, doi:10.1038/s41592-019-0686-2. 31

Viselli, A., M. Filippelli, N. Pettigrew, H. Dagher, and N. Faessler (2019), Validation of the first LiDAR wind resource assessment buoy system offshore the Northeast United States, *Wind Energy*, *22*(11), 1548–1562, doi:10.1002/we.2387. 2

Vollmer, L., M. van Dooren, D. Trabucchi, J. Schneemann, G. Steinfeld, B. Witha, J. Trujillo, and M. Kühn (2015), First comparison of LES of an offshore wind turbine wake with dual-Doppler lidar measurements in a German offshore wind farm, *Journal of Physics: Conference Series*, *625*(1), 012,001, doi:10.1088/1742-6596/625/1/012001. 30

Vömel, H., and M. Fujiwara (2021), Aerological Measurements, in *Springer Handbook of Atmospheric Measurements*, edited by T. Foken, pp. 1247–1280, Springer International Publishing, Cham, doi:10.1007/978-3-030-52171-4_46. 1, 16

Wan, Z., X. Liu, and C. Xu (2021), Multi-source observations and high-resolution numerical model applied on the analysis of a severe convective weather affecting the airport, *Meteorological Applications*, *28*(4), e2012, doi:10.1002/met.2012. 1

Wang, J., E. Cheynet, J. Þór Snæbjörnsson, and J. B. Jakobsen (2018), Coupled aerodynamic and hydrodynamic response of a long span bridge suspended from floating towers, *Journal of Wind Engineering and Industrial Aerodynamics*, *177*, 19–31, doi:10.1016/j.jweia.2018.03.024. 1

Werner, C. (2005), Doppler Wind Lidar, in *Lidar: Range-Resolved Optical Remote Sensing of the Atmosphere*, edited by C. Weitkamp, pp. 325–354, Springer, New York, NY, doi:10.1007/0-387-25101-4_12, ISBN: 978-0-387-25101-1. 2

White, A. B., C. J. Senff, and R. M. Banta (1999), A Comparison of Mixing Depths Observed by Ground-Based Wind Profilers and an Airborne Lidar, *Journal of Atmospheric and Oceanic Technology*, *16*(5), 584 – 590, doi:10.1175/1520-0426(1999)016<0584:ACOMDO>2.0.CO;2. 2

Whiteman, C. D., M. Lehner, S. W. Hoch, B. Adler, N. Kalthoff, R. Vogt, I. Feigenwinter, T. Haiden, and M. O. G. Hills (2018), The Nocturnal Evolution of Atmospheric Structure in a Basin as a Larger-Scale Katabatic Flow Is Lifted over Its Rim, *Journal of Applied Meteorology and Climatology*, *57*(4), 969 – 989, doi:10.1175/JAMC-D-17-0156.1. 2

Wilczak, J., E. Gossard, W. Neff, and W. Eberhard (1996), Ground-Based Remote Sensing of the Atmospheric Boundary Layer: 25 Years of Progress, *Boundary-Layer Meteorology*, *78*, 321–349, doi:10.1007/BF00120940. 2

Wilczak, J. M., and J. E. Tillman (1980), The Three-Dimensional Structure of Convection in the Atmospheric Surface Layer, *Journal of Atmospheric Sciences*, *37*(11), 2424 – 2443, doi:10.1175/1520-0469(1980)037<2424:TTDSOC>2.0.CO; 2. 10

Wildmann, N., S. Kigle, and T. Gerz (2018), Coplanar lidar measurement of a single wind energy converter wake in distinct atmospheric stability regimes at the Perdigão 2017 experiment, *Journal of Physics: Conference Series*, *1037*(5), 052,006, doi:10.1088/1742-6596/1037/5/052006. 2

Williams, J. M., A. G.and Hacker (1993), Interactions between coherent eddies in the lower convective boundary layer, *Boundary-Layer Meteorology*, *64*(1573-1472), 55–74. 10

Witschas, B., S. Rahm, A. Dörnbrack, J. Wagner, and M. Rapp (2017), Airborne Wind Lidar Measurements of Vertical and Horizontal Winds for the Investigation of Orographically Induced Gravity Waves, *Journal of Atmospheric and Oceanic Technology*, *34*(6), 1371 – 1386, doi:10.1175/JTECH-D-17-0021.1. 18

Witschas, B., C. Lemmerz, A. Geiß, O. Lux, U. Marksteiner, S. Rahm, O. Reitebuch, and F. Weiler (2020), First validation of Aeolus wind observations by airborne Doppler wind lidar measurements, *Atmospheric Measurement Techniques*, *13*(5), 2381–2396, doi:10.5194/amt-13-2381-2020. 18

Wolken-Möhlmann, G., J. Gottschall, and B. Lange (2014), First Verification Test and Wake Measurement Results Using a SHIP-LIDAR System, *Energy Procedia*, *53*, 146–155, doi:10.1016/j.egypro.2014.07.223, EERA DeepWind' 2014, 11th Deep Sea Offshore Wind R&D Conference. 2, 18

Wulfmeyer, V. (1998), Ground-based differential absorption lidar for water-vapor and temperature profiling: development and specifications of a high-performance laser transmitter, *Appl. Opt.*, *37*(18), 3804–3824, doi:10.1364/AO.37.003804. 18

Yoshino, K. (2019), Low-Level Wind Shear Induced by Horizontal Roll Vortices at Narita International Airport, Japan, *Journal of the Meteorological Society of Japan. Ser. II*, *97*(2), 403–421, doi:10.2151/jmsj.2019-023. 3, 29

Young, G. S. (1988a), Convection in the atmospheric boundary layer, *Earth-Science Reviews*, *25*(3), 179–198, doi:10.1016/0012-8252(88)90020-7. 1, 9, 10

Young, G. S. (1988b), Turbulence Structure of the Convective Boundary Layer. Part I. Variability of Normalized Turbulence Statistics, *Journal of the Atmospheric Sciences*, *45*(4), 719–726, doi:10.1175/1520-0469(1988)045<0719:TSOTCB>2.0.CO;2. 1

Zentek, R., S. H. E. Kohnemann, and G. Heinemann (2018), Analysis of the performance of a ship-borne scanning wind lidar in the Arctic and Antarctic, *Atmospheric Measurement Techniques*, *11*(10), 5781–5795, doi:10.5194/amt-11-5781-2018. 2

Zhang, W., C. D. Markfort, and F. Porté-Agel (2013), Wind-Turbine Wakes in a Convective Boundary Layer: A Wind-Tunnel Study, *Boundary-Layer Meteorology*, *146*(1573-1472), 161–179, doi:10.1007/s10546-012-9751-4. 1

Paper I

Statistic and Coherence Response of Ship-based Lidar Observations to Motion Compensation

Christiane Duscha, Mostafa Bakhoday Paskyabi, Joachim Reuder

Journal of Physics: Conference Series, **1669/01** (2020)
https://dx.doi.org/10.1088/1742-6596/1669/1/012020

EERA DeepWind'2020 IOP Publishing
Journal of Physics: Conference Series **1669** (2020) 012020 doi:10.1088/1742-6596/1669/1/012020

Statistic and Coherence Response of Ship-based Lidar Observations to Motion Compensation

Christiane Duscha[1], **Mostafa Bakhoday Paskyabi**[1], **Joachim Reuder**[1]
[1]Geophysical Institute, Bergen Offshore Wind Center, University of Bergen and Bjerknes Centre for Climate Research, Postbox 7803, 5020 Bergen, Norway

E-mail: `christiane.duscha@uib.no`

Abstract. Ship-based profiling Lidar systems experience a strong influence of rotational and translational motion on beam direction and hence the line-of-sight velocity. This motion error is inherited by the retrieved 3-dimensional wind vector and is especially visible in the velocity spectra and cross-spectra of velocities at different measurement heights (coherence). Applying motion compensation on the line-of-sight velocity observations was found to have a strong impact on the statistical properties of the retrieved wind vector and successfully improved the corresponding velocity distributions. The impact of motion correction on the spectra of the horizontal wind speed components was found to be neglectable. The Lidar measurement principle, in particular the effect of cross-contamination at higher frequencies, was found to have a larger impact in shaping the horizontal spectra than motion correction. Vertical velocity spectra were strongly affected by ship motion and the motion correction was only partly successful. Precisely, this effect was present at frequencies larger than the resonance frequency of the ship.

1. Introduction

The rotor diameter of state-of-the-art and future planned offshore wind turbines is increasing rapidly, now already exceeding 200 m. Nowadays, most wind power production and turbine load estimates are mainly based on the extrapolation of mean wind characteristics from lower levels, utilizing either the simple wind shear exponent approach or the more advanced Monin-Obukhov similarity theory (MOST)[1]. However, these methods are only applicable within the surface layer, i.e. the lowest part of the atmospheric boundary layer, and in addition only under certain stability conditions [2]. Yet, at the length scale of these new wind turbines, it is not given that these assumptions are valid over the whole rotor diameter. It was found, that assimilating atmospheric observations, such as wind shear, turbulence and atmospheric stability significantly improves both the quality of power production and risk estimates from physical models as well as from statistical models, which are based on machine learning [3].

Unfortunately, the availability of the corresponding marine boundary layer observations is still sparse. Only few platforms featuring meteorological masts (e.g. the FINO platforms in the North and Baltic Sea [4]) or buoy mounted Lidars [5] are installed today. A novel approach to gain detailed observations of wind speed profiles over a larger spacial extend was presented by Gottschall et al. 2018 [6]. They utilized a profiling Lidar on a ferry route over the baltic sea to sample different wind and boundary layer parameters in order to validate the New European Wind Atlas (NEWA) [7]. Similar and accessible ferry infrastructures exist in many coastal regions interesting for offshore wind exploration. In the future, these might be utilized as a network of mobile wind profile observatories, when equipped with profiling Lidar.

Platforms at sea, e.g. buoys, are exposed to the transfer of momentum from the underlying wave field, causing the platform and the installed Lidar system to move. Here, six degrees of freedom have to be considered, namely the rotational motions around the three main axes, defined as *pitch*, *roll* and *yaw*, and the translational motion along those axes defined as *heave*, *sway* and *surge*. Additional translational motion is generated, if the lidar is installed on a ship for example. Both, wave induced and ship induced motion, influences thus the observation of a ship mounted Lidar.

The following study evaluates the potential of ship-based Lidar installations, with focus on the impact of motion and motion compensation on the Lidar observations. The manuscript is structured as follows. Section 2 describes the measurement campaign, the instrumentation and its limitations used in this study. Section 3 introduces the measurement and retrieval principle, the motion correction algorithm and the data analysis methodology. The main results on statistical, spectral and coherence impact of motion compensation are presented and discussed in Section 4, followed by some concluding remarks in Section 5.

2. Measurements and Instrumentation

2.1. Campaign

The data evaluated in this study originates from the Wincube V2 Lidar observations (see Section 2.2) during the Iceland Greenland Seas Project [8]. During the 7 weeks of the campaign (Feb-Mar 2018), the Lidar was installed on deck (stern side) of the NATO Research Vessel *Alliance*. For the period of the Lidar deployment, the *Alliance* travelled the Iceland and Greenland Seas area, featuring a large range of wind, wave and atmospheric stability conditions. The main part of the cruise was performed at large distance to shore and is therefore representative for offshore conditions. A great advantage of this campaign was the extensive availability of an additional remote sensing and in situ observations. Specifically important boundary layer variables at different heights, such as temperature, humidity and wind were obtained from Radiosonde launches (in situ). This enabled the classification of the data, for example by stability conditions as well as a validation of the remote sensing observations.

2.2. Windcube V2 Lidar Wind Profiler

The Windcube V2 system, manufactured by *Leosphere*, consists of two main parts: a pulsed doppler Lidar and an Inertial Motion Unit (IMU). The pulsed doppler Lidar performs a four beam doppler beam swinging (DBS) scanning pattern (0°, 90°, 180°, 270°) that includes an additional vertical beam (V). A whole cycle of 5 beams corresponds to a duration of approximately 3.8 s (0.72 s for each DBS and 0.97 s for the vertical beam). Along each beam, or line-of-sight (LOS), the Lidar measures radial velocities ($\overrightarrow{v_r}$), obtained from doppler shift of the back-scattered Lidar signal. The three dimensional wind vector $\overrightarrow{u}$ can be retrieved by combining subsequent measurements of $\overrightarrow{v_r}$ (see Section 3.1). The wind vector is obtained at twelve range gates between 40 m and 290 m, with a gate width of 20 m between the lower levels and 30 m between the four highest levels.

When installed on a moving platform at sea (e.g. a ship), the IMU integrated within the Windcube V2 system can be used to obtain motion angles, motion velocities and translational horizontal velocity of the instrument. These parameters are retrieved from internal processing with a frequency of 10Hz. Motions cause the Lidar to observe $\overrightarrow{v_r}$ in a moving coordinate system, that is rotated relative to the earths coordinate system. A basic retrieval (see Section 3.1) in the earths coordinate system, based on this modified $\overrightarrow{v_r}$ will yield incorrect results of three dimensional wind speed. Angular displacement causes exchange of absolute velocity between the different wind speed components. Motion velocities modulate the wind speed components along the same axis. Finally, translational motions cause a modulation of the horizontal wind speed, depending on the platform heading relative to the wind direction.

2.3. Instrument Limitations with regard to Turbulence

In this study, we will eventually evaluate the impact of motion compensation on the velocity spectra of the wind components, retrieved from Lidar observations. However, general limitations of doppler swinging and profiling Lidar, which are not in motion must be recalled first. In the past, Sathe et. al 2011 [9] found that these kind of Lidar do not perform well in observing turbulence by evaluating 2nd order statistics. Comparisons of Lidar and Sonic spectra (e.g. [10], [11]) found only poor agreement when a certain frequency range was exceeded. Keberlau and Mann 2019 [12] evaluated the main causes for this erroneous spectral behaviour. They concluded that cross-contamination of the horizontal velocity components due to large separation distances of the beams is the dominant source for errors, that is visible in the spectrum. They identified resonance frequencies for eddies corresponding to $2/n$ times the size of the spacial separation distance between the beams ($n = 1, 2, ...$). Secondary sources of contamination were identified from time averaging effects: beams in one complete scanning pattern are used multiple times during the retrieval (see Section 3.1). Retrieved values are therefore not independent from one another, causing a "running mean" effect at frequencies larger than the sampling frequency of the complete scan ($\sim$ 3.8s). Additionally, the LOS averaging effect can influence the spectrum and is mainly present at higher frequencies.

3. Methodology

3.1. Lidar Measurement Principle and Basic Retrieval

In its inertial state (no motion), radial velocities measured by the Lidar can be linked to the 3D wind speed vector $\overrightarrow{u}$ following [13] (adjusted for Windcube V2 system):

$$v_r(\theta,\varphi) = u \cdot \sin(\varphi)\sin(\theta) + \mathrm{v} \cdot \cos(\varphi)\sin(\theta) + \mathrm{w} \cdot \cos(\theta) \tag{1}$$

with φ as the azimuth angle and θ as the cone angle of the DBS pattern ($\theta = 28°$). Setting in φ and θ corresponding to the five beams of $\overrightarrow{v_r}$ yields an equation system, that can be solved analytically for $\overrightarrow{u} = (u, v, w)$:

$$u = \frac{v_r(28°, 90°) - v_r(28°, 270°)}{2 \cdot \sin(\theta = 28°)} \qquad v = \frac{v_r(28°, 0°) - v_r(28°, 180°)}{2 \cdot \sin(\theta = 28°)} \qquad w = v_r(\theta = 0°) \tag{2}$$

It should be noted, that unlike the conventional meteorological definition, w is negative defined for upwards directed velocities within the Windcube V2 coordinate system.

3.2. Lidar Motion Compensation

In order to gain motion independent observations of the wind vector, it is possible to apply motion correction to the observations of the Windcube V2 system. The challenge is to compensate for the complex interaction between rotation of the platform's coordinate system and translational and heave motion.

In this study, two simple motion correction methods, introduced by Wolken-Möhlmann et al. 2014 [14], are tested. The computational cheaper method of the two applies motion correction to the retrieved wind vector $\overrightarrow{u_r}$ (see Section 3.1). Here, $\overrightarrow{u_r}$ is rotated corresponding to the motion angles, utilizing the inverse rotation matrix $\mathbf{R}^{-1}$ (for details on $\mathbf{R}$ and its limitations see [15]) and the ship velocity vector $\overrightarrow{u_{ship}}$ is simply subtracted. A disadvantage of this method is, however, that motion correction due to angular displacement and translational and heave motion are decoupled. Additionally, the retrieved wind vector will always be dependent on the

radial velocity observations corresponding to different time steps. Hence, the choice of time step corresponding to the motion data (10Hz resolution) will not sufficiently cover all utilized radial velocity observations ($\sim$ 3.8s).
A possible approach for improvement is to apply the motion correction already on $\overrightarrow{v_r}$ or "pre-retrieval" (also see [14]). A shortcoming of this method is, however, a higher computational cost. For this method, $\overrightarrow{u_{ship}}$ is projected on to the vector along the LOS of each of the Lidar beams. This vector is then subtracted from $\overrightarrow{v_r}$. The resulting motion velocity compensated radial velocity vector $\overrightarrow{v_{rc}}$ can be expressed in terms of the rotated (utilizing $\mathbf{R}$) and LOS projected, three dimensional wind vector. The resulting equation system is, however, not as trivial to solve, as the one introduced in Section 3.1. In order to solve this equation system, linear regression, based on a least squares approach is utilized, following [16].

3.3. Statistic, Spectral and Coherence Analysis

To evaluate the overall quality of the corrected wind speed profile series, it is compared (consistency check) to in situ wind speed measurements that are obtained from 86 Radiosonde ascents, over the course of the cruise at the different Lidar levels. Here, two common error metrics between Lidar and Radisonde data are used: the systematic error (BIAS) and the random or standard deviation error (SDE).
To evaluate the impact of motions on the statistics of Lidar wind observations, a histogram (distribution) of horizontal wind speed and vertical wind speed are created, both for corrected and original series. For more insight on the specific impact of motion velocity on the horizontal wind, an additional histogram of the difference between the corrected and the original horizontal wind speed is estimated, which is conditioned by present and non-present ship translational movement.
For the spectral analysis, the energy spectra of the three wind components, rotated in wind direction (along wind u, cross wind v and vertical wind w) at one level are investigated. Additionally, the cross-correlation spectra between observations of the Lidar at different levels and vertical motion velocity (heave) are evaluated in terms of corresponding coherent modes at specific frequencies. The coherence estimates are constructed from the cross spectral density G_{xy} (and its complex conjugate G'_{xy}), which is the Fourier transform of the cross-covariance function between the variables x and y [17] (x and y are for example series of velocity observed at two different Lidar levels). The coherence estimates are calculated following [17]:

Coherence estimate C:

$$C_{xy} = \frac{G_{xy} \cdot G'_{xy}}{G_{xx} \cdot G_{yy}} \tag{3}$$

real part of Co-Coherence estimate Co (coincident spectrum):

$$Co_{xy} = \mathrm{Re}\left(\frac{\mathrm{G_{xy}}}{\sqrt{\mathrm{G_{xx}} \cdot \mathrm{G_{yy}}}}\right) \tag{4}$$

imaginary part of Co-Coherence estimate iCo (quadrature spectrum):

$$iCo_{xy} = \mathrm{Im}\left(\frac{\mathrm{G_{xy}}}{\sqrt{\mathrm{G_{xx}} \cdot \mathrm{G_{yy}}}}\right) \tag{5}$$

phase ρ:

$$\rho = \mathrm{atan2}\left(\mathrm{Im}(\mathrm{G_{xy}}), \mathrm{Re}(\mathrm{G_{xy}})\right) \tag{6}$$

The coincident spectrum determines the contributions to the correlation of x and y at different frequencies, that are ”in phase” (phase: 0° or 180°), while the quadrature spectrum determines those, that are ”out of phase” (phase: ± 90°) [17].

For analysis, the spectra corresponding to the three velocity components are each combined as a composite of discrete fast Fourier transformation of several time series slices of 30 min length. Each time slice is shifted by 1 min to the proceeding one, over a period of 6 h. Composites of coherence and corresponding estimates (compare Equations 3-6) are estimated in a similar way. A time period of maximum data availability, stationary wind and motion signal was chosen for the spectral analysis of this study. The requirements for stationary were achieved for periods where the statistical properties, in particular mean μ and standard deviation σ, of the evaluated series were independent of absolute time [17], utilizing thresholds for μ and σ of 0.1 m/s and 0.1°, respectively.

4. Results and Discussion

The following Subsections will evaluate and discuss the impact of motion compensation from three points of view: statistical, spectral and from coherent modes. In the process of analysis it was found that distributions, spectra and coherence are similar for the two motion correction approaches introduced in Section 3.2 in almost all evaluated cases. Hence, in order to increase the readability, results from both approaches are only shown and discussed, in case they differ significantly. Otherwise, only the method that applies motion correction ”pre”-retrieval is shown.

4.1. Lidar Profile Assessment

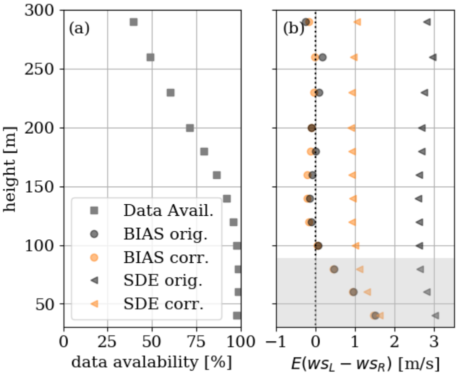

Figure 1. Lidar data availability with height over whole series (a) and Error estimates E (BIAS and SDE) between the horizontal wind speed of Lidar (ws_L) and Radiosonde (ws_R) from original and corrected series (b).

First, the quality of the Lidar observations is evaluated in terms of data availability [%] at each level, displayed in Figure 1a. In the lowest levels (up to 100m), the data availability is very close to 100% for the whole campaign (excluding harbour time). However, at higher levels, a decreasing trend of $\overrightarrow{u}$ data availability with increasing Lidar level can be recognised. With decreasing data availability, also reliability decreases and gaps in the series reduce the quality of spectral analysis.

Before determining the consistency of the evaluated Lidar dataset with independent Radiosonde measurements, we need to discuss the limitations such a comparison implies. Previous studies (e.g. [18]) found that Radiosonde measurements of the horizontal wind speed do not agree well with Lidar observations close to the surface, due to inertia effects during the acceleration and oscillatory motion of the Radiosonde. This superimposed motion naturally reduces the reliability and accuracy of the Radiosonde measurements close to the ground. However, there is no standardized cut-off height for Radiosonde measurements, as inertia and oscillatory effects are dependent on the environmental conditions during release. Lidar observations do not experience such inertial forcing and were in general found to perform well independent of height in comparison to met masts (see e.g. [19]). Flow distortion around the research vessel, however, evidently influences wind speed observations [20]. This can potentially enhance the inertia effect on the Radiosondes, but also modify the wind field observed by the Lidar at the lowest levels close to the ship.

Direct comparison of the independent datasets displayed in Figure 1b, indeed confirms the observations of previous studies. The systematic differences between Lidar and Radiosonde wind speed are most dominant at the lowest levels. In case of the evaluated campaign, these differences vanish around 100 m for both, the corrected and the original Lidar dataset. In order to avoid potential criticism of "cherry picking" and to make this relevant information available for further deployments, we choose to display the whole profile assessment, but added a shading at the height levels that are critical for the Radiosonde measurements. Still, the strong consistency between Lidar and Radiosonde ws at higher levels, despite the decreased data availability of Lidar data comparable to lower levels, give strong confidence in the Lidar observations.

Even though the systematic differences are very similar between original and corrected ws, a clear improvement of the corrected ws compared to the original ws can be observed in terms of the random differences.

4.2. Statistical Analysis

The original and motion corrected distributions of horizontal and vertical wind speed at the Lidar level corresponding to 100 m are displayed in Figure 2. This level was chosen, because the most robust results in combined data availability and consistency (Section 4.1) were found at that level.

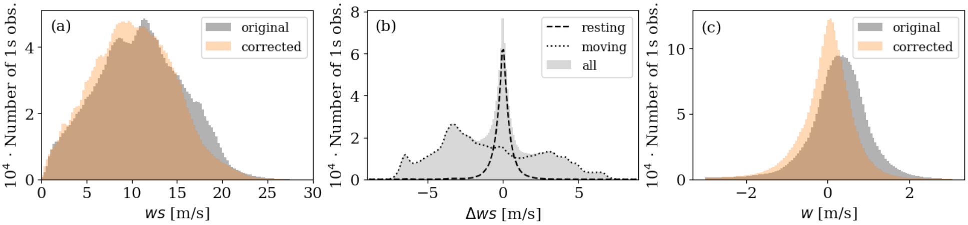

Figure 2. Distribution of original and corrected horizontal wind speed ws (a), distribution of difference between original and corrected horizontal wind speed Δws, conditioned by resting and moving ship (b) and distribution of original and corrected vertical wind speed w distribution.

The distribution of corrected ws (0.25 m/s bin width), shown in Figure 2.a, implies an overall reduction in the amount of observations at higher ws values (between 15 and 20 m/s) in comparison to the original distribution. The amount of observations at lower ws values (between 0 and 15 m/s), on the other hand is increased for almost every bin in this velocity range. The largest impact on the horizontal velocity is expected from ship translational movement (see Section 2.2). If this assumption applies, the adjustment of the ws distribution towards lower ws values after motion correction suggest that the ship was sailing against the mean wind for a longer part of the campaign, or at a higher speed than with the wind.

The distribution of the difference between original and corrected series ($\Delta ws = ws_{corrected} - ws_{original}$) is shown in Figure 2.b. From this distribution (0.1 m/s bin width) a more detailed insight into the cause of adjustment of corrected compared to original ws distribution can be gained. This distribution is conditioned by cases, where the ship was in translational movement and cases, where it was resting at a certain point in space. A distribution of absolute ship speed is shown in Figure 3. As *surge* and *sway* are still larger than zero during periods of rest, translational movement is defined as $u_{ship} > 0.25$ m/s.

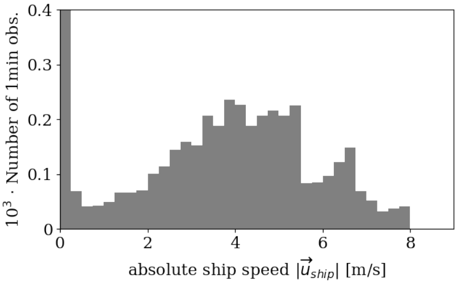

Figure 3. Distribution of 1 min resolution absolute ship speed $|\overrightarrow{u_{ship}}|$

The Δws distribution shows a distinct peak around 0 m/s. For resting conditions ($u_{ship} <$ 0.25 m/s) this peak is almost perfectly mapped. Here, maximum and minimum velocity differences vary only around ±2 m/s.
A comparably small portion ($\Delta ws > |0.25 m/s|$) of the distribution (resting conditions) can be accounted to the angular motion, meaning a transfer of horizontal velocity to the vertical velocity and vice versa (see Section 3.2). The influence of angular motion on the horizontal wind speed is therefore small in comparison to the overall observed wind speed values. For translational movement conditions ($u_{ship} >$ 0.25 m/s), the peak is barely recognisable. For this condition the distribution ranges between -8 m/s to 8 m/s, which is approximately the maximum speed the ship reached within the observation period. This confirms the above formulated hypothesis: ship translational movement can be identified as the dominant motion impact on the originally obtained ws. The amount of negative Δws exceeds the amount of positive Δws. This confirms, that the ship was dominantly sailing against the wind during the evaluated campaign.
For the vertical velocity distributions, which are displayed in Figure 2c, a distinct shift from the original ($\sim$ 0.5 m/s) to the corrected ($\sim$ 0 m/s) peak velocity value can be observed. The peak additionally narrows after motion compensation. A hypothesis to explain the shift is the dominant presence of a static angular displacement of the Lidar beams. Such an angular displacement causes parts of the horizontal wind speed to be mis-interpreted as vertical velocity and vice versa (see Section 2.2). A reason for displacement could for example be due to imperfectly leveling during installation or a change in ship listing angle over the course of the campaign, e.g. caused by a change in weight distribution by fuel consumption. The hypothesis behind the narrowing of the peak is the successful removal of artificial variance due to a combination of ship angular motion, *heave* motion and non-linear transfer of velocity from the horizontal wind speed components.

4.3. Spectral Analysis

The statistical analysis (Section 4.2) was able to give insight to mean features caused by motion compensation. How and at which frequencies motion compensation is of dominant influence, can on the other hand, be evaluated from original and corrected energy spectra of the three wind components. Figure 4 shows the spectra of those three wind speed components (as defined in Section 3.3) for corrected and original series at the 100 m level. For each spectrum, the frequency range from $1.3{\cdot}10^{-1}$Hz (Nyquist frequency corresponding to one complete scan) and larger frequencies is shaded in grey. At this range, time averaging ("running mean") effects in combination with cross-contamination effects were found to be dominant (see Section 2.3). These effects are visible in all three wind components, but especially in the u and v spectra (Figure 4a & b), in form of a drop in spectral energy at frequencies slightly larger than $1.3{\cdot}10^{-1}$Hz.
Only minor differences between original and corrected spectra of u and v (Figure 4a & b) can be recognised. There is for example slightly less energy in the corrected u and v spectra at the lowest frequencies. A potential explanation for this is the removal of periodic ship movement present during the evaluated period (movement in between periods of resting). Additionally, the corrected v spectrum (Figure 4b) improves slightly in comparison to the original spectrum with respect to the -5/3 slope, characteristic for the inertial subrange of turbulence.

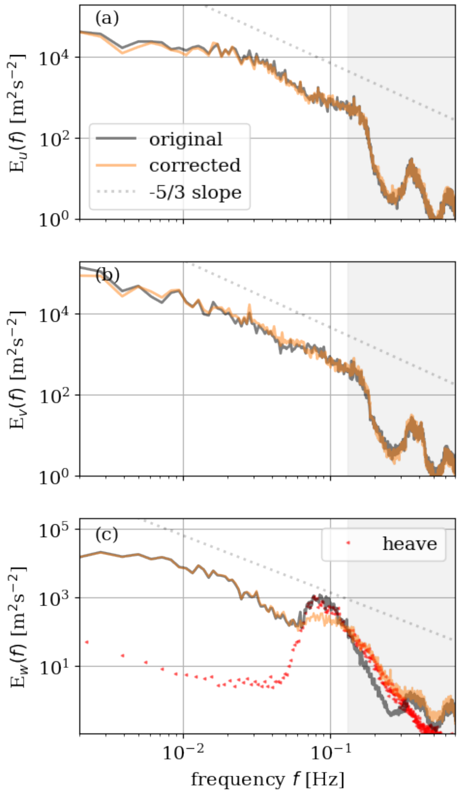

Figure 4. Original and corrected frequency (f) dependent energy spectrum $E_u(f)$ of the along wind component u (a), $E_v(f)$ of the cross-wind component v (b), $E_w(f)$ of the vertical wind speed component w (c). The vertical spectra are accompanied heave spectrum. The grey shading indicates the frequency range which exceeds the Nyquist frequency (∼0.13Hz).

Unfortunately, no in situ measurements of turbulence are available to confirm, that the inertial subrange really is present at this frequency range for the evaluated situation. In contrast to the v spectra (Figure 4b), the slope of both the original and corrected u spectra (Figure 4a) deviates from the -5/3 slope. As this deviation increases with increasing level height and therefore increasing separation distance (see Appendix Figure A1), the cross-contamination effect is most likely responsible for the deviation in slope from the inertial subrange.

In case of the vertical component, the spectra were found to differ in between the retrieval methods introduced in Section 3.2. Both corrected and original spectra of the two retrieval methods are displayed in the Appendix Figure A2. One major difference to point out between the two methods: the spectra corresponding to the "basic" retrieval were found to fit better with the -5/3 slope of the inertial subrange than the "pre"-retrieval method.

In contrast to the u and v spectra, the impact of motion compensation can be identified clearly, when evaluating the w energy spectra, shown in Figure 4c. One advantage in the analysis of the w spectra is, that we also can display *heave* in the same coordinate system (here plotted in red), as it has the same unit $[m/s]$ and direction (z) as w. *Heave* motion results from the ship oscillations, which are forced by the underlying wave field. These oscillations amplify close to the natural frequency specific to the ship. A peak in *heave* spectrum can therefore be related to the resonance frequency of ship and wave field.

A clear peak at $8 \cdot 10^{-2}$Hz can be identified in the original w spectrum, shown in Figure 4c. This peak is maximal at the same frequency and is of similar magnitude as the peak in *heave* spectrum (Figure 4c). However, at frequencies larger than $1.3{\cdot}10^{-1}$Hz, the slope of the original w spectrum is steeper than the slope of the *heave* spectrum. The peak is also observed for the corrected w spectrum, yet it is reduced in comparison to the original w spectrum between $6{\cdot}10^{-2}$Hz and $1.3{\cdot}10^{-1}$Hz. For $f > 1.3{\cdot}10^{-1}$Hz, on the other hand, the spectral energy of the corrected spectrum is increased. At this frequency range it is of similar magnitude and slope as the *heave* spectrum. A hypothesis to explain this behaviour is, that the oscillations caused by motion can not be resolved at this frequency range by the Lidar measurement principle (Section 3.1). If this hypothesis is true, motion compensation possibly caused a transfer of energy, which is conserved in the motion measurement, artificially to the spectral energy of corrected w. This hypothesis is evaluated utilizing coherence estimates and coherent modes in the following subsection.

4.4. Coherence Analysis

Original and corrected estimates of spectral coherence, real and imaginary part of the co-coherence and the phase between series of w at different Lidar levels are, together with *heave*, displayed in Figure 5. These estimates are in the following utilized to identify coherent modes at specific frequencies, with focus on motion impact.

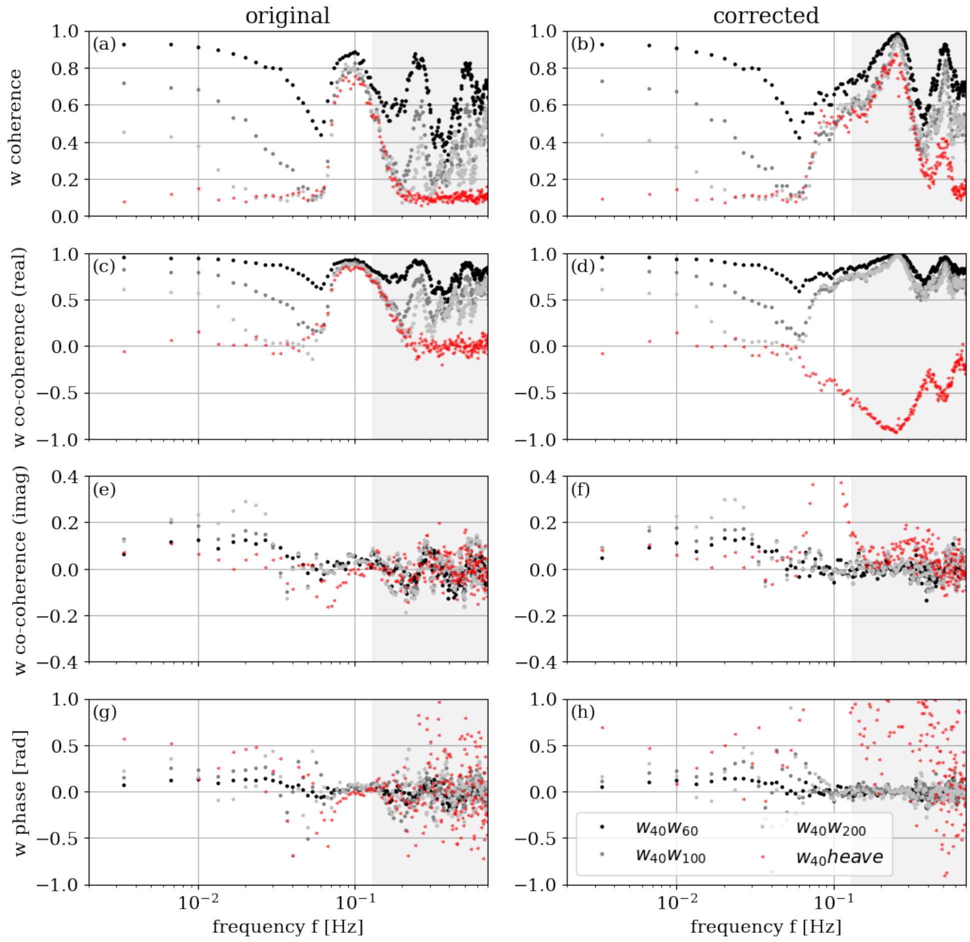

Figure 5. Coherence estimates from cross spectral density estimates of vertical velocity w_iw_j between different Lidar levels ($i = 40m$ and $j = [60m, 100m, 200m]$) and *heave*. Coherence $C_{w_iw_j}$ and $C_{w_i,heave}$ of original w (a) and corrected w (b), real co-coherence $Co_{w_iw_j}$ and $Co_{w_i,heave}$ of original w (c) and corrected w (d), imaginary co-coherence $iCo_{w_iw_j}$ and $iCo_{w_i,heave}$ of original w (e) and corrected w (f) and phase $\rho_{w_iw_j}$ and $\rho_{w_i,heave}$ of original w (g) and corrected w (h).

A turbulent eddy of a specific size s_E ($\sim f$) will be recognised at two different points in space (correlation), if their separation distance is smaller than s_E. Hence, in theory, the spectral coherence of w at two different levels is expected to overall decrease with frequency and vertical separation distance.

From the original spectral coherence estimate shown in Figure 5a, a coherent mode ($6{\cdot}10^{-2}$ Hz< f <$2{\cdot}10^{-1}$ Hz) can be identified for all coherence estimates of w_iw_j at two different levels i and j. The maximum of the coherent mode can be identified around 10^{-1}Hz. At a frequency around $6{\cdot}10^{-2}$Hz, the spectral coherence of w_iw_j ($j = 100m$ and $j = 200m$) decreases to minimal values, then both coherence estimates increase rapidly (to ~ 0.8) and in the same manner, matching the spectral coherence between w and *heave*. This implies that spectral coherence (correlation) at this frequency range is mainly caused by ship motion (around the resonance frequency). At higher frequencies (f >$2{\cdot}10^{-1}$Hz) the coherent modes can be identified in between w at different levels, but not with *heave*. For this frequency range, the increased spectral coherence between w at different levels is potentially connected to the limitations in the measurement and retrieval principle in combination with cross-contamination at the resonance frequencies (Section 2.3).

Similar, and even more distinct peaks were also identified from coherence estimates of a Lidar, which was installed on a fixed platform. The w coherence estimate from a measurement corresponding to this fixed period is shown in Figure 6.

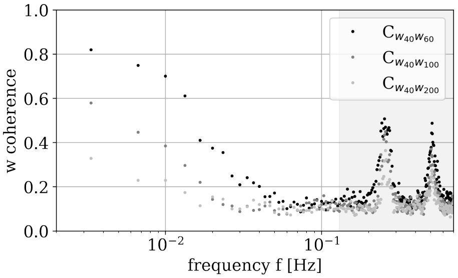

Figure 6. Spectral coherence between different levels of observations from a Lidar installed on a fixed platform (no motion)

For all frequencies of the coherent mode, the real part of the original spectral co-coherence (Figure 5c), is positive (correlated). For frequencies around maximum correlation ($\sim$ 10^{-1}Hz), the imaginary part of the co-coherence (Fig. 5e) is very close to zero. This implies, that the w series in not only strongly correlated with *heave* and in between the levels for the frequency range of the coherent mode, but also also in phase (phase mode), as shown in Figure 5g.

The spectral coherence corresponding to the corrected w series at different levels and with *heave* is shown Figure 5b. In comparison to the original coherent mode with *heave* (Fig. 5a), the corrected coherent mode with *heave* is present over a larger frequency range and at higher frequencies. Within the frequency range of the original coherent mode, the corrected coherent mode is reduced in magnitude. Yet, real corrected spectral co-coherence (Figure 5d) is negative (anti-correlated) and the imaginary corrected spectral co-coherence (Figure 5f) is strongly increased and therefore out of phase (anti-phase mode) at this frequency range (Figure 5h). This implies that the motion correction potentially overcompensates and introduces opposing and out of phase oscillations to the w series. At frequencies larger than the Nyquist frequency (grey shaded), cross-correlation with *heave* and corrected spectral coherence in between the levels increases (Figure 5b). From the real part of the corrected spectral co-coherence (Figure 5d) it can be observed, that the motion correction causes w and *heave* to be anti-correlated as well. Especially for frequencies > $1.3{\cdot}10^{-1}$Hz the anti-correlation corresponding to the corrected coherent mode (Figure 5d) is strongly increased in comparison to the original coherent mode (Figure 5c). This supports the hypothesis formulated in Section 4.3: At this frequency range the Lidar observations are not able to resolve oscillations connected to ship motion and motion correction introduces artificial oscillation on the corrected w series.

5. Conclusions and Outlook

Motion correction has a strong impact on mean horizontal and vertical wind speed and was found to be able to adjust the analysed series towards more realistic distributions. The impact of motion on spectra of horizontal wind speed components, is found to be small in comparison to limitations caused by the measurement principle, in particular due to cross-contamination. In contrast, the vertical velocity spectrum was found to be strongly impacted by motion contamination. Motion correction is only partly successful. It even causes the series (and spectrum) to be more complicated to separate in a realistic and an erroneous part. On basis of these findings, it is not recommended to utilize a time resolution finer than the time the Lidar system requires for one complete scanning cycle (∼3.8 s), even though it can be provided. Specifically for the vertical component, an even smaller part of the spectrum should be considered, depending on the natural frequency of the ship, the Lidar is installed on. In this case, it is recommended to utilize the w component, which is only retrieved from the vertical beam ("basic"), as it is less contaminated by cross-contamination, inherited from the horizontal components.

In order to gain information on turbulence, there exists the possibility to replace the unresolvable part of the velocity spectra by a theoretical formulation (e.g. the Kaimal spectrum [21]), if it is possible to identify the inertial subrange[1]. Here additional information on stability can for example be used to achieve more realistic spectra. Improved turbulence estimates such as turbulent kinetic energy (TKE) and turbulence intensity can be acquired from integrating the adjusted spectra.

There are also other approaches to correct for motion in turbulence estimates. In order to remove motion impact on momentum flux estimates, Rieder and Smith 1998 [23] suggested a method which utilizes the cross-correlation spectra between velocity components and motion estimates to directly correct cross-correlation spectra between two of the velocity components (momentum flux).

References

[1] Monin, A. S. and A. M. Obukhov, 1954, Basic laws of turbulent mixing in the atmosphere near the ground, Tr. Akad. Nauk SSSR Geofiz. Inst 24 (151), 163-187.

[2] Gryning, S.-E., Batchvarova E., Brümmer B., Jørgensen H., and Larsen S., 2007, On the extension of the wind profile over homogeneous terrain beyond the surface boundary layer, Boundary-Layer Meteorol., 124(2), 251-268, doi:10.1007/s10546-007-9166-9.

[3] Optis M. and J. Perr-Sauer, 2019, The importance of atmospheric turbulence and stability in machine-learning models of wind farm power production, Renewable and Sustainable Energy Reviews, Volume 112, Pages 27-41, ISSN 1364-0321, doi:10.1016/j.rser.2019.05.031.

[4] Fischer G., 2006, Installation and Operation of the Research Platform FINO 1 in the North Sea In: Köller J., Köppel J., Peters W. (eds), Offshore Wind Energy. Springer, Berlin, Heidelberg, doi:10.1007/978-3-540-34677-7-15.

[5] Gottschall, J., Gribben B., Stein D., and Würth I., 2017, Floating lidar as an advanced offshore wind speed measurement technique: current technology status and gap analysis in regard to full maturity, Wiley Interdisciplinary Reviews: Energy and Environment, 6(5), e250, doi:10.1002/wene.250.

[6] Gottschall J., Catalano E., Dörenkämper M. and B. Witha, 2018, The NEWA Ferry Lidar Experiment: Measuring Mesoscale Winds in the Southern Baltic Sea. Remote Sensing, 10 (10), 1620, doi:10.3390/rs10101620.

[7] Karagali, I., Hahmann A. N., Badger M., Hasager C., and Mann J., 2018, Offshore New European Wind Atlas, Journal of Physics: Conference Series, 1037, 052007, doi:10.1088/1742-6596/1037/5/052007.

[8] Renfrew, I. A. et al. , 2019, The Iceland Greenland Seas Project, Bulletin of the American Meteorological Society, Volume 100, Number 9, Pages 1795-1817, https://doi.org/10.1175/BAMS-D-18-0217.1

---

[1] It should be noted that not only motion and cross-contamination effects can contaminate the inertial subrange. Also random waves (wave-induced motions) can modify the slope of the inertial subrange, even for frequencies far from the wave peak [22]

[9] Sathe, A., J. Mann, J. Gottschall, and M.S. Courtney, 2011: Can Wind Lidars Measure Turbulence?. J. Atmos. Oceanic Technol., 28, 853–868, https://doi.org/10.1175/JTECH-D-10-05004.1

[10] Canadillas, B., Bégué, A. and T. Neumann, 2010: Comparison of turbulence spectra derived from LiDAR and sonic measurements at the offshore platform FINO1. 10th German Wind Energy Conference (DEWEK 2010), No. Dewek

[11] Kumer,V. M., Reuder J., Dorninger, M., Zauner, R. and V. Grubisic, 2016, Turbulent kinetic energy estimates from profiling wind LiDAR measurements and their potential for wind energy applications. Renewable Energy, 99, 898 - 910, https://doi.org/10.1016/j.renene.2016.07.014

[12] Kelberlau, F. and Mann, J., 2019, Cross-contamination effect on turbulence spectra from Doppler beam swinging wind lidar, Wind Energ. Sci. Discuss., https://doi.org/10.5194/wes-2019-71, in review

[13] Weitkamp, C., 2005, Lidar: Range-Resolved Optical Remote Sensing of the Atmosphere, Springer Series in Optical Sciences, Vol. 102, Springer, New York, NY, USA

[14] Wolken-Möhlmann, G., Gottschall, J. and Lange, B., 2014, First Verification Test and Wake Measurement Results Using a SHIP-LIDAR System. Energy Procedia. 53. https://doi.org/10.1016/j.egypro.2014.07.223 .

[15] Thwaites, F. T. 1995, Developement of an acoustic vorticity meter to measure shear in Ocean-Boundary Layers, Massachusetts Institute of Technology, https://doi.org/10.1575/1912/1576.

[16] Lai, T. L., Robbins, H. and Wei, C. Z., 1978, Strong consistency of least squares estimates in multiple regression, Proceedings of the National Academy of Science, Volume 75, Pages 3034–3036, ISSN 0027-8424, https://doi.org/10.1073/pnas.75.7.3034.

[17] Emery, W. J. and Thomson, R. E., 2001, Data Analysis Methods in Physical Oceanography, Chapter 5 - Time-series Analysis Methods, Elsevier Science, Pages 371-567, ISBN 9780444507563, https://doi.org/10.1016/B978-044450756-3/50006-X.

[18] Kumer V.M., Reuder J. and Furevik B. R. 2014, A Comparison of LiDAR and Radiosonde Wind Measurements, Energy Procedia,Volume 53, Pages 214-220, ISSN 1876-6102, https://doi.org/10.1016/j.egypro.2014.07.230.

[19] Westerhellweg, A., Canadillas, B., Beeken, A. and Neumann, T., 2010, One year of LiDAR measurements at FINO1-Platform: Comparison and verification to met-mast data, 10th German Wind Energy Conference DEWEK 2010

[20] Yelland, M. J. and Moat, B. I. and Pascal, R. W. and Berry, D. I., 2002, CFD Model Estimates of the Airflow Distortion over Research Ships and the Impact on Momentum Flux Measurements. Journal of Atmospheric and Oceanic Technology, 19, 1477-1499,https://doi.org/10.1175/1520-0426(2002)019¡1477:CMEOTA¿2.0.CO;2

[21] Kaimal, J.C., Wyngaard, J.C., Izumi, Y. and Coté, O.R. (1972), Spectral characteristics of surface-layer turbulence. Q.J.R. Meteorol. Soc., 98: 563-589. doi:10.1002/qj.49709841707.

[22] Lumley, J.L., Terray, E.A., 1983, Kinematics of turbulence convected by a random wave field., J Phys Oceanogr 13:2000–2007

[23] Rieder, K. F. and Smith, J. A. 1998, Removing wave effects from the wind stress vector, J. Geophys. Res., 103(C1), 1363– 1374, doi:10.1029/97JC02571.

A. Appendix: Figures

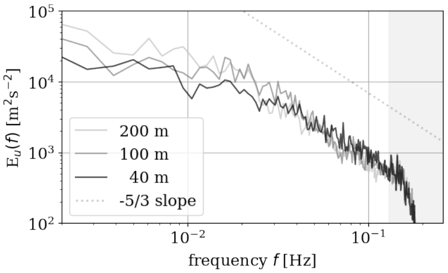

Figure A1. Along wind (u) energy spectra corresponding to different Lidar level

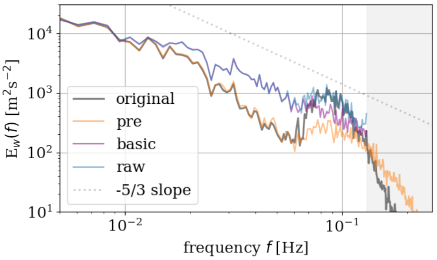

Figure A2. Vertical velocity (w) spectra, corresponding to different retrieval and motion correction appoaches

Paper II

A Ship-Based Characterization of Coherent Boundary-Layer Structures Over the Lifecycle of a Marine Cold-Air Outbreak

Christiane Duscha, Christopher Barrell, Ian A. Renfrew, Ian M. Brooks,
Harald Sodemann, Joachim Reuder

Boundary-Layer Meteorology, **183/355-380** (2022)
https://doi.org/10.1007/s10546-022-00692-y

Boundary-Layer Meteorology (2022) 183:355–380
https://doi.org/10.1007/s10546-022-00692-y

RESEARCH ARTICLE

A Ship-Based Characterization of Coherent Boundary-Layer Structures Over the Lifecycle of a Marine Cold-Air Outbreak

Christiane Duscha[1] · **Christopher Barrell**[2] · **Ian A. Renfrew**[2] ·
Ian M. Brooks[3] · **Harald Sodemann**[4] · **Joachim Reuder**[1]

Received: 8 February 2021 / Accepted: 22 January 2022 / Published online: 24 March 2022

Abstract

Convective coherent structures shape the atmospheric boundary layer over the lifecycle of marine cold-air outbreaks (CAOs). Aircraft measurements have been used to characterize such structures in past CAOs. Yet, aircraft case studies are limited to snapshots of a few hours and do not capture how coherent structures, and the associated boundary-layer characteristics, change over the CAO time scale, which can be on the order of several days. We present a novel ship-based approach to determine the evolution of the coherent-structure characteristics, based on profiling lidar observations. Over the lifecycle of a multi-day CAO we show how these structures interact with boundary-layer characteristics, simultaneously obtained by a multi-sensor set-up. Observations are taken during the Iceland Greenland Seas Project's wintertime cruise in February and March 2018. For the evaluated CAO event, we successfully identify cellular coherent structures of varying size in the order of 4×10^2 m to 10^4 m and velocity amplitudes of up to 0.5 m s^{-1} in the vertical and 1 m s^{-1} in the horizontal. The structures' characteristics are sensitive to the near-surface stability and the Richardson number. We observe the largest coherent structures most frequently for conditions when turbulence generation is weakly buoyancy dominated. Structures of increasing size contribute efficiently to the overturning of the boundary layer and are linked to the growth of the convective boundary-layer depth. The new approach provides robust statistics for organized convection, which would be easy to extend by additional observations during convective events from vessels of opportunity operating in relevant areas.

Keywords Cold-air outbreak · Convective coherent structures · Iceland–Greenland sea · Lidar wind profiling

---

✉ Christiane Duscha
christiane.duscha@uib.no

[1] Geophysical Institute, Bergen Offshore Wind Center and Bjerknes Centre for Climate Research, University of Bergen, Post box 7803, 5020 Bergen, Norway

[2] School of Environmental Sciences, University of East Anglia, Norwich, UK

[3] School of Earth and Environment, University of Leeds, Leeds, UK

[4] Geophysical Institute and Bjerknes Centre for Climate Research, University of Bergen, Bergen, Norway

1 Introduction

Large temperature differences between the atmosphere and ocean typically develop due to the advection of cold air over a warmer ocean surface. This process is often referred to as a marine cold-air outbreak (CAO). The elevated turbulent fluxes of sensible and latent heat initiated by the large air–sea temperature contrast can easily reach several hundreds of $\mathrm{W\,m^{-2}}$, or, in extreme cases, even exceed $1000\,\mathrm{W\,m^{-2}}$ (Grossman and Betts 1990). Organized convective structures contribute an essential part to these compensating fluxes. Detailed statistical sampling of the parameters necessary to characterize these structures is still sparse in the relevant regions. During the Iceland–Greenland Seas Project (IGP) in February and March 2018 we observed several CAO events from aboard the *NRV Alliance* (Renfrew et al. 2019). For one of these CAOs we investigate the impact of organized convective-structure development on the evolution of the instabilities and the turbulent fluxes.

The heat fluxes during CAOs typically result in significant boundary-layer warming and moistening (e.g., Papritz and Spengler 2017). Further, Papritz and Sodemann (2018) found that CAOs create an intense local water cycle, with rapid turnover of water vapour associated with a distinct signature in the stable water isotope composition (Thurnherr et al. 2020). The warming and moistening of the atmosphere occurs at the expense of ocean surface-layer cooling and salinification, important drivers for the formation of dense water and thus important for the global ocean circulation (Buckley and Marshall 2016). The turbulent heat fluxes into the atmospheric boundary layer also play an important role for the maturing of polar lows responsible for high-impact weather conditions in the Nordic Seas and the adjacent coasts (e.g., Føre et al. 2011). Consequently, regional weather as well as the global climate system are directly affected by elevated turbulent heat fluxes during CAOs.

Organized convection, which results in coherent structures in the wind, temperature, and moisture fields, was found to contribute an essential part to these turbulent heat fluxes (e.g., LeMone 1973; Chou and Ferguson 1991; Brilouet et al. 2020). Mesoscale shallow convection patterns, such as roll vortices, open cellular convection, and closed cellular convection, are generally affiliated with marine CAO events (Atkinson and Zhang 1996). Even though these mesoscale structures have received major attention in the past, small-scale cellular structures, comparable to cellular Rayleigh–Bénard convection, studied in laboratory experiments, are also important in the convective marine atmospheric boundary layer (MABL) (Cieszelski 1998). Mesoscale convection often manifests in the form of organized cloud patterns clearly seen in satellite images. However, characterizing small-scale convection requires more detailed observations of the meteorological variables, such as wind speed and direction, in the MABL.

Previous case studies of marine CAOs have identified coherent-structure characteristics from research aircraft measurements (Atlas et al. 1986; Chang and Braham 1991; Brümmer 1996; Hartmann et al. 1997; Cieszelski 1998; Renfrew and Moore 1999; Cook and Renfrew 2015; Brilouet et al. 2017). These studies determined coherent-structure characteristics, such as along and across wind asymmetries, the wavelength and aspect ratio of roll vortices, and snapshots of the turbulence characteristics throughout the MABL. Yet research flights only have a few hours to sample. Thus, the estimated characteristics of coherent structures are averages over short periods, and the evolution of coherent structures in time remains poorly sampled. Hence, achieving detailed statistical sampling of coherent structures during CAO conditions is an important goal of this study.

Here, we utilize ship-based observations from the Iceland and Greenland Seas region, obtained by a multi-sensor set-up during the IGP campaign. A distinct CAO case forms the basis of our study. We sampled profiles of the core MABL variables, such as temperature, humidity, precipitation, and wind with three remote-sensing instruments: a passive microwave radiometer, a micro rain radar, and a wind-profiling Doppler lidar. The resulting observations provide improved temporal and vertical resolutions compared to those provided by aircraft measurements. Brooks et al. (2017) demonstrate the large potential of such multi-sensor and ship-based MABL estimates, utilizing a similar set of remote-sensing instrumentation. Nonetheless, the sampling of coherent structures remains challenging with the available instrumentation and from aboard a ship exposed to wave motion. Here, we use motion-compensated lidar observations to identify coherent structures and investigate their temporal development. Such an improved statistical sampling of the coherent structures over the lifecycle of CAOs directly contributes to the overall goal of the IGP mission. The project aims to identify and characterize the exact atmospheric mechanisms, including the impact of coherent structures, involved in the high-latitude water mass transformations. In this study, we provide the methodology to estimate the coherent-structure characteristics from observations over the lifecycle of a CAO, evaluate the inter-dependency of the structures' characteristics, and evaluate the processes which link the structure evolution to the respective boundary-layer characteristics.

2 The Iceland and Greenland Seas' Cruise

We focus on the ship-based part of the IGP campaign, which lasted 43 days, starting on 6 February and terminating on 21 March 2018 in Reykjavik, Iceland. For an overview of the entire IGP campaign as well as the major atmospheric and oceanic events over the corresponding observational period we refer the reader to Renfrew et al. (2019). The cruise on the *NRV Alliance* covered an area of the Iceland and southern Greenland Seas. Over the course of the cruise, Renfrew et al. (2019) identified several marine CAOs, of which we study one in more detail. Figure 1 shows a map of the study area relevant to the IGP cruise (Fig. 1a) and a close up of the area relevant to the ship track corresponding to the evaluated CAO event from 28 February to 3 March (Fig. 1b). Also displayed are radiosonde launches along the track, as well as the sea-surface temperature, SST, and the sea-ice cover averaged over the evaluated CAO period.

2.1 Ship-Based Observations

Time series of air temperature, T_a; relative humidity, RH; pressure, P; wind speed, ws; and wind direction, wd, were sampled with a 1-min time resolution by three automatic weather stations, situated on the bow mast of the *NRV Alliance* at $\approx$ 15 m above sea level. Also, the sea-surface temperature was measured continuously at the bow of the ship using a digital oceanographic thermometer (SBE 38, Sea-Bird Scientific, Bellevue, USA). The data are fully quality controlled (see Renfrew et al. 2021) and time series of measurements are combined and made available by Barrell and Renfrew (2020) in the Centre for Environmental Data Analysis (CEDA) archive.

In addition to the instruments permanently installed on the ship we installed several sensors to obtain a wider range of variables and, in particular, atmospheric profiles of T_a, RH, the three-dimensional wind vector, $\mathbf{u}$, and precipitation properties, in particular the terminal or fall velocity of precipitating particles, v_t. These instruments included a Doppler wind-profiling lidar (WindCube V2 Offshore 8.66, Leosphere, Orsay, France), a micro rain radar

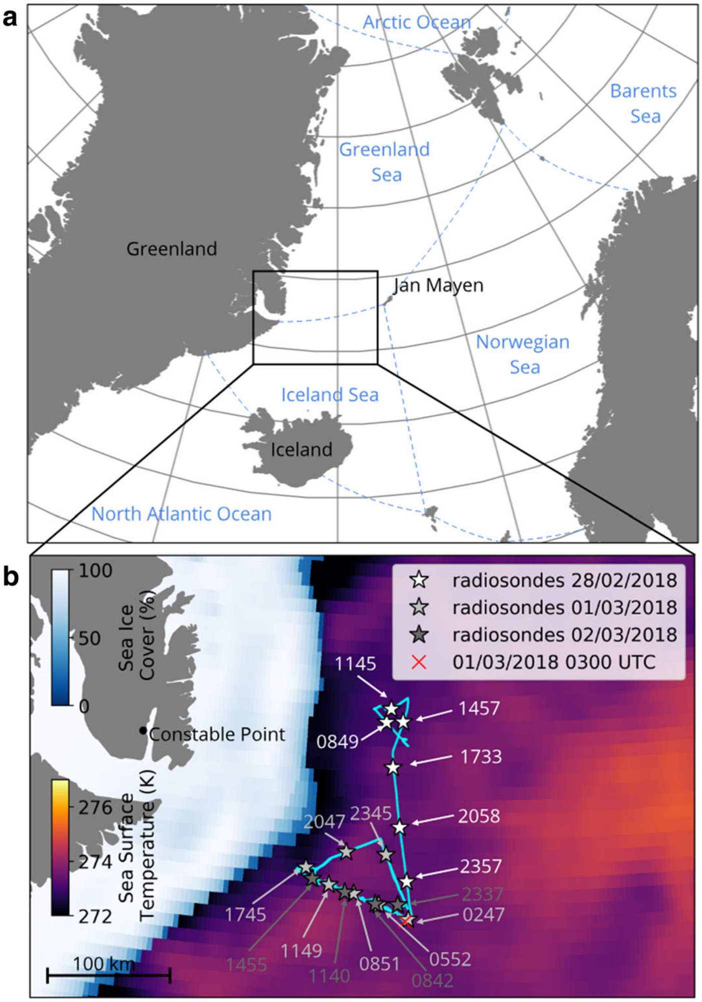

Fig. 1 **a** Overview of the area relevant to the IGP cruise and **b** close-up of the study area in the Greenland and Iceland Seas relevant to the CAO event from 28 February to 3 March, the corresponding track of the *NRV Alliance* as well as the corresponding average *SST*, and sea-ice cover from the GHRSST satellite product. Locations and time (UTC) of the ship corresponding to radiosonde launches are indicated along the track. The red cross marks the location of the ship during the example situation discussed in Sect. 4. (Color figure online)

(MRR-2, Metek, Elmshorn, Germany), a cavity ring-down spectrometer (L2140-i Ser. No. HIDS2254, Picarro Inc, Sunnyvale, USA) for stable water isotope analysis, and a passive microwave radiometer (RPG-HATPRO-G4, Radiometer Physics GmbH, Meckenheim, Germany). The radiometer was situated on a single axis motion-correction table, following Achtert et al. (2015), to compensate for the roll motion of the ship and minimize motion errors during boundary-layer scans. Ship motion was removed during post-processing from the lidar observations, as described by Duscha et al. (2020). Radar retrievals were re-processed to improve the data for snow-dominated precipitation (Maahn and Kollias 2012). Figure 2 shows the location of the instrumentation during the IGP cruise. The lidar, the radiometer,

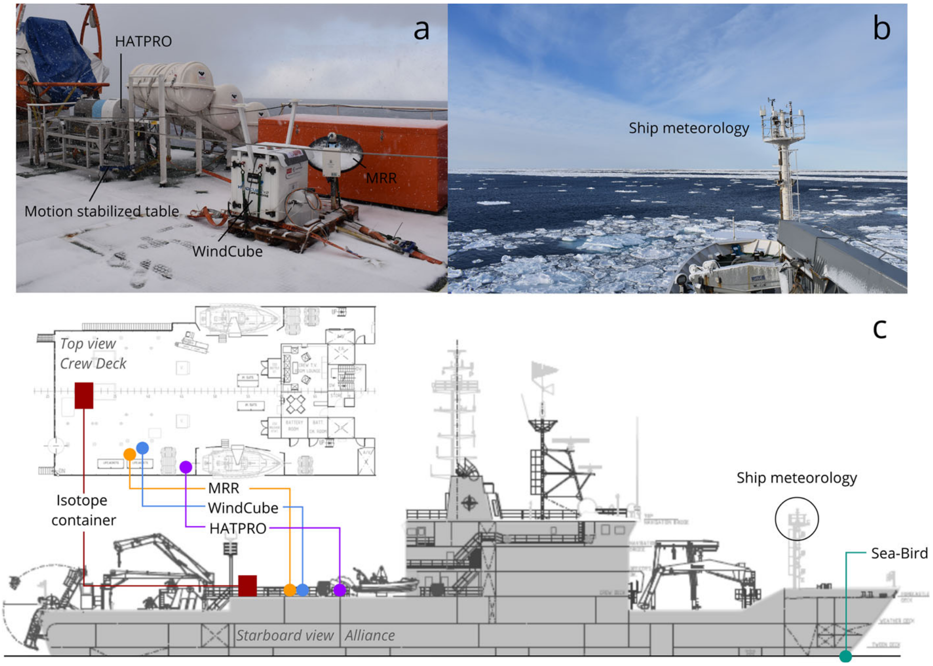

Fig. 2 Set-up of instrumentation utilized during the IGP campaign on the *NRV Alliance*. **a** Photos of the remote sensing equipment and **b** photos of the meteorology sensors on the bow mast. **c** Schematics of the *NRV Alliance* looking down and in cross-section (CMRE 2017), with the marked instrument locations: radar (orange), lidar (blue), radiometer (purple), isotope container (red), ship's in situ meteorology (black circle), and the Sea-Bird Scientific digital oceanographic thermometer (green). (Color figure online)

and the radar were placed on the starboard side of the crew deck ≈ 10 m above sea level and the spectrometer was operated from the isotope container. Radiosondes (RS41, Vaisala, Vantaa, Finland) were launched from the ship at least every 24 h with high-frequency launches throughout intensive observational periods. During the first 24 h of the evaluated CAO event, for example, radiosondes were launched every 3 h. Further specifications of the profiling instruments, in particular the vertical range (m above the respective instrument) and the vertical and temporal resolution, are summarized in Table 1.

2.2 Satellite Observations

We extract the spatial distribution of SST and sea-ice cover over the course of the IGP cruise displayed in Fig. 1b, as well as a series of SST along the track of the *NRV Alliance*, from the GHRSST satellite product (JPL 2015). The dataset provides daily values at $0.1^\circ \times 0.1^\circ$ spatial resolution. In addition, infrared and visible satellite images were collected and stored for a predefined domain in real time for the IGP field campaign by the Natural Environment Research Council Earth Observation Data Acquisition and Analysis Service. The images are available up to 35 times per day with a resolution of 500 m.We utilize one of these satellite images to display and evaluate the cloud situation, corresponding to the time and location marked by the red cross in Fig. 1b (see Sect. 4). The image used here is from the MODIS instrument aboard the NASA Aqua satellite.

Table 1 Specification of the profiling instruments operated from the *NRV Alliance* during the IGP campaign

Instrument	Variables		Resolution		Dataset
(Identifier)	Direct	Retrieval	Time	Range	Reference
Lidar (WindCube)	$\mathbf{v}_r$ (m s^{-1})	$\mathbf{u}$ (m s^{-1})	0.26 Hz (every 3.8 s)	20 m (40–200 m) 30 m (200–290 m)	Duscha (2020)
Radiometer (HATPRO)	T_b (K)	T_a (K) RH (%)	1.67×10^{-3} Hz (every 10 min)	Discretized to 10 m (0–3 km)	Brooks (2019a)
Radar (MRR)	v_t (m s^{-1}) Z_e (dBZ)		0.1 Hz (every 10 s)	75 m (75–2325 m)	Sodemann (2021)
Radiosonde (RS41)	T_a (K) RH (%) z (m)	P (hPa) ws (m s^{-1}) wd (°)	1 Hz (every 1 s)	5 m (up to 20000 m)	Brooks (2019b)

Documentation of the main evaluated variables (measured and retrieved), the temporal and vertical resolution of the instruments, and the reference to the data in the CEDA database. The vertical resolution is documented as range resolution, valid for a certain range (in brackets) above the respective instrument. The variables are defined in the text, with the exception of the radial velocity vector, $\mathbf{v}_r$, the brightness temperature, T_b, and the radar reflectivity, Z_e, directly observed by the remote-sensing instruments

3 Methodology

3.1 Boundary-Layer Diagnostics

Based on the variables obtained from the ship-installed and ship-launched instrumentation, we estimate several diagnostics that characterize the structure of the MABL. Many of these diagnostics require a profile of potential temperature, $\theta(z)$, which we estimate from $T(z)$, and $p(z)$, obtained by the radiometer and the radiosondes, respectively. We also calculate the local lapse rate, $\Delta\theta/\Delta z$, using $\Delta z = 100$ m, with the respective level, z, in the centre. We estimate $\Delta\theta/\Delta z$ in overlapping intervals every 10 m, starting at $z = 50$ m above sea level.

3.1.1 Convective Boundary-Layer Depth

The MABL is the layer of the atmosphere that is directly impacted by ocean surface fluxes. It is hence characterized by the presence of mechanically and thermally generated turbulence. During marine CAO events a convective boundary layer develops. In this case the maximum depth of the turbulent convective motion, initiated at the sea surface, predominantly determines the depth of the mixed layer and hence the depth of the MABL. Utilizing the parcel method (Holzworth 1964), we determine the convective boundary-layer depth, h_b. The method relies on the principle of adiabatically following an air parcel from the sea surface, where $\theta = \theta_{SST}$, to its height of neutral buoyancy. The level that precedes the first instance of $\theta(z_j) - \theta_{SST} \geq 0$ K, so the level z_{j-1}, is defined as h_b

$$h_b = z_{j-1}|_{(\theta(z_j)-\theta_{SST})\geq 0\ K}.$$

The parcel method has been found to work well for convective conditions (Seibert et al. 2000). Additionally, Collaud Coen et al. (2014) found very good agreement of the convective boundary-layer depth between radiometer and radiosonde estimates, utilizing the parcel method. The uncertainty of h_b, in particular for the radiometer, was found to be most sensitive to the accuracy in the measurement of sea-surface temperature, which is within ±0.5 K

(Collaud Coen et al. 2014). The value of h_b additionally serves as a measure of the potential maximum vertical extent of convective structures.

3.1.2 Gradient Richardson Number

Even though convective conditions usually predominate during marine CAOs, we still expect wind shear to have a strong influence on turbulence generation. To evaluate the dominant source of near-surface turbulence, we estimate the discretized, near-surface gradient Richardson number, Ri_g (e.g., Stull 1988)

$$Ri_g = \frac{g}{\theta} \frac{\Delta\theta/\Delta \mathrm{z}}{\left[(\Delta u/\Delta z)^2 + (\Delta v/\Delta z)^2\right]},$$

with g being the the acceleration due to gravity. Here, we estimate Ri_g, centred at $z = 100$ m above sea level, utilizing lidar observations of u and v at 50 m and 150 m above sea level in order to estimate the corresponding velocity gradients. We average the lidar estimates over 10 min to match the time resolution of the radiometer estimates of $\theta(z)$ and the lapse rate between 50 m and 150 m above sea level.

3.1.3 Updraft and Downdraft Velocities

To evaluate the strength of the near-surface turbulent circulation, we estimate the maximum updraft and downdraft velocity, $w^{\uparrow}_{\max}$ and $w^{\downarrow}_{\max}$, from lidar observations of the vertical velocity component, w. We evaluate the positive and negative w as two separate time series, using absolute values. For both the updraft and downdraft series we estimate the value of maximum velocity over the whole lidar altitude range at each timestep. We average the resulting series of maximum updraft and downdraft velocities over a 10-min interval to again match the time resolution of the radiometer.

3.1.4 Stable Water Isotope Composition

Cold-air outbreak events feature large humidity gradients and high wind speeds, which lead to intense evaporation from the sea surface (e.g., Papritz and Pfahl 2016). Under such conditions, the stable water isotopes $H_2^{18}O$ and HDO (deuterium-enriched water) carry a specific signature in the evaporating vapour. We use this isotopic signature here as an integrating process tracer. More specifically, in intense evaporation conditions, the comparably higher diffusion speed of the HDO molecules compared to $H_2^{18}O$ molecules leads to relatively high values (>15 ‰) of the secondary isotope parameter d-excess (d) defined as

$$d = \delta D - 8\,\delta^{18}O,$$

where δD and $\delta^{18}O$ denote the deuterium and oxygen-18 abundance in the water vapour relative to VSMOW (Vienna Standard Mean Ocean Water, e.g., Dansgaard 1964). Generally, d in water vapour is close to 10 ‰ on a global average, and tends towards lower values as ambient conditions approach saturation (e.g., Pfahl and Sodemann 2014). The particular use of the parameter d in the context of this study is its ability to integrate over the evaporation history and mixing processes of water vapour in an airmass along its trajectory. Within a CAO, the local, high d signal from intense evaporation can be moderated by convective overturning of the MABL that transports comparably dry air with low d vapour, originating from heights dominated by condensation or from outside of the CAO to the surface. The isotope data are available in the CEDA archive (Sodemann and Weng 2022).

3.1.5 Fetch

Apart from the temporal evolution, the ship-based observations also describe a spatial evolution of the boundary-layer parameters, as the ship moves. This spatial evolution can be quantified by the fetch, f (km), the distance to the sea-ice edge, following the trajectory of the wind. Here, we estimate the fetch on the basis of the sea-ice edge from the GHRSST sea ice product and the locally observed wd, which is varied by $\pm 5^\circ$ to achieve an uncertainty estimate.

3.1.6 Surface Heat Fluxes

Turbulent sensible and latent heat fluxes, Q_H and Q_L, are a measure of the local energy transport of heat and moisture between the ocean and the atmosphere due to turbulent atmospheric motion. We determine these surface fluxes from the ship's meteorological observations (see Barrell and Renfrew 2020; Renfrew et al. 2021) using the well-established COARE 3.0 bulk flux algorithm (Fairall et al. 2003).

3.2 Coherent Structures

During CAO conditions, convective structures are superimposed on to the mean wind speed, $\overline{ws}$. For this study, we rely on the assumption that these structures are stationary, or "frozen", when sampled (i.e., Taylor's hypothesis). Also, the presence of advection or movement of the ship is a requirement to capture the convective signal with the lidar. Relative to the ship, convective structures are transported by the mean apparent wind speed, $\overline{ws_a}$, which results from the sum of $\mathbf{u}$ and the ship's translational velocity vector, $\mathbf{u}_{ship}$. We apply a rolling average for $\overline{ws}$ and $\overline{ws_a}$ (local Taylor hypothesis). We chose a rolling average of 1 h, as it captures the synoptic and the diurnal variations in the flow, but filters variations due to convective structures $\leq O$ (10^4 m) for the range of apparent wind velocity scales of O (10 m s^{-1}), obtained during the CAO event. The coherent signal of convection needs to be evaluated along the mean apparent wind direction, $\overline{wd_a}$. So we rotate $\mathbf{u}$ into $\overline{wd_a}$ and subtract $\overline{ws}$ from the rotated u component to obtain the along-wind, cross-wind, and vertical velocity fluctuations, u', v', and w', respectively.

$$\begin{pmatrix} u' \\ v' \\ w' \end{pmatrix} = \begin{pmatrix} \cos(\overline{wd_a}) & \sin(\overline{wd_a}) & 0 \\ -\sin(\overline{wd_a}) & \cos(\overline{wd_a}) & 0 \\ 0 & 0 & 1 \end{pmatrix} \begin{pmatrix} u \\ v \\ w \end{pmatrix} - \begin{pmatrix} \overline{ws} \\ 0 \\ 0 \end{pmatrix}$$

The series of the velocity fluctuations u', v', and w' enable an estimate of the dynamic and spatial properties of coherent structures in the flow.

3.2.1 Cellular Structures

For a set of idealized convective cells, Fig. 3 illustrates how $u'(t)$ and $w'(t)$ would be observed by the ship-based lidar set-up at two altitude ranges, z_1 and z_2. In this idealized case, $u'(t)$ and $w'(t)$ oscillate with the same period, T_{cell}. At both displayed levels, the two series are cross-correlated, but have a phase shift $\Delta\rho_{u'w'} = \pm \pi/2$ ($\pm 90^\circ$). The sign of $\Delta\rho_{u'w'}$ is reversed for the upper and lower part of the cell. This is the case because the sign of $w'(t)$ is conserved over the depth of the cell (lines overlap), while $u'(t)$ switches sign from the

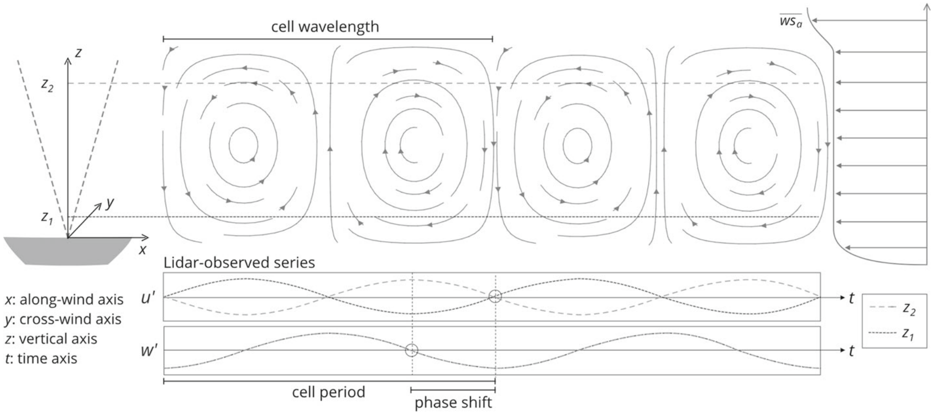

Fig. 3 Schematic of the method utilized to observe cellular coherent structures with the ship-based lidar set-up. The top panel illustrates a cross-section through convective cells, along the mean apparent wind speed $\overline{ws_a}$. The bottom panels show the series of $u'(t)$ and $w'(t)$ the ship-based lidar observes at two levels, z_1 and z_2, when these cells are advected over the ship with $\overline{ws_a}$

lower to the upper part of the cell. The wavelength of the advected cell is proportional to the lidar-observed period ($\lambda_{cell} \propto T_{cell}\overline{ws_a}$).

Figure 3 displays only the two-dimensional, observational perspective from the ship-based lidar of a phenomenon that is three-dimensional in reality. In the idealized case, the convective cells are horizontally isotropic. Consider the case that the centre of such an isotropic cell is advected over the ship with $\overline{ws_a}$. Here, the amplitude, u'_A, of the observed u' is maximal, while the amplitude, v'_A, of the observed v' is zero. Now consider the case that a cell is advected over the ship at a certain distance to its centre. Here, we expect to observe a contribution of the cellular circulation to v'_A. In contrast to the u' series, which is phase-shifted to w' by $\pm\pi/2$ (Fig. 3), the corresponding v' series is instead anti-correlated to w', hence phase-shifted by π. The ratio between v'_A and u'_A increases if the cell is sampled at an increasing distance to its center and this ratio can even exceed 1. Yet, the absolute values of u'_A and v'_A decrease towards the cell's edges rendering the coherent signal less reliable. Only if the cell passes the ship at approximately half the distance between its centre and edge is v'_A expected to yield a considerable coherent signal. Thus, in contrast to u', the evaluation of v' is only reliable if a comparably narrow segment of the subsequent cells passes over the ship. This narrow segment is more likely to be missed by our set-up, compared to the larger segment relevant to the analysis of u'. Therefore, we focus our investigation on the estimation of the coherent signal between u' and w' to identify cellular coherent structures with the ship-based set-up.

3.2.2 Spectral Analysis

Based on the assumptions presented above, a measure of cross-correlation between the series of u' and w', and a corresponding estimate of the phase shift for a range of periods or wavelengths can provide information about the presence of convective structures in the flow, including their respective T_{cell} and λ_{cell}. The coherence spectrum $Co_{u'w'}$ is a measure for normalized cross-correlation between u' and w' (Emery and Thomson 2001)

$$Co_{u'w'} = \frac{G_{u'w'} \cdot G^T_{u'w'}}{G_{u'u'} \cdot G_{w'w'}},$$

where $G_{u'w'}$ is the cross-covariance spectrum of u' and w', and $G^{T}_{u'w'}$ its complex conjugate. Further, $G_{u'u'}$ and $G_{w'w'}$ are the auto-correlation spectra of u' and w', respectively. The $Co_{u'w'}$ takes on values between 0 and 1, where 0 implies that u' and w' are not correlated, while 1 implies that u' and w' are correlated for a certain period or wavelength. If coherent structures are present in the flow, we expect to detect a spike in the $Co_{u'w'}$ at T_{cell} or λ_{cell}, respectively. A spike in the $Co_{u'w'}$ is the necessary condition for the presence of coherent structures. The corresponding sufficient condition is the presence of a phase shift of $\pm\pi/2$ between u' and w' at the spike in the $Co_{u'w'}$ (see Sect. 3.2.1). The phase spectrum $\rho_{u'w'}$ is defined as follows (Emery and Thomson 2001)

$$\rho_{u'w'} = \mathrm{atan2}[\mathrm{Im}(\mathrm{G_{u'w'}}), \mathrm{Re}(\mathrm{G_{u'w'}})].$$

With $Co_{u'w'}$ and $\rho_{u'w'}$ we can identify if coherent structures are superimposed on to the mean flow and estimate their horizontal length scale, $L_{h,c}$, along $\overline{wd_a}$.

3.2.3 The Coherent Length Scale

We found that the periodicity of the convective structures is sensitive to temporal changes in $\overline{ws_a}$, which can cause corresponding spikes in the frequency dependent $Co_{u'w'}$ to widen and reduce in maximum value. A reliable interpretation of convection in the time domain is therefore not given (Lohse and Xia 2010). Hence, we convert both $u'(t)$ and $w'(t)$, from a time to a space dependent series, $u'(x)$ and $w'(x)$, using an approach based on the local Taylor hypothesis (see Pinton and Labbé 1994). We construct the space index, x (m), which describes the increasing distance covered along $\overline{wd_a}$, by multiplying the timestep $\Delta t = 3.8$ s of the lidar observations with $\overline{ws_a}(t)$ (m s^{-1}) and integrate over t,

$$x(t) = \sum_{0}^{t} \Delta t \, \overline{ws_a}(t).$$

We then rearrange the resulting $u'(x)$ and $w'(x)$ series to an equidistant grid. We chose a grid resolution of 50 m, to avoid aliasing effects at scales of O (10^2 m). We then split the series into a number of independent segments to capture the evolution of coherent structures. For a robust spectral analysis, the evaluated segment should contain at least five to ten cycles of the convective circulation. The length of the chosen segment should therefore be at least five times longer than the maximum coherent length scale of interest. For increasing scales the assumption of stationarity is less likely to be applicable and the application of the local Taylor hypothesis limits the maximum detectable structures to O (10^4 m). We utilize the u' and the w' series in segments of 100 km length to estimate $Co_{u'w'}(\lambda)$ and $\rho_{u'w'}(\lambda)$. Here, each segment overlaps the next evaluated segment by 90 km, to ensure the detection of the large structures, which only persist at a constant scale for a limited number of consecutive structures throughout the observations. For each segment, this yields $Co_{u'w'}(\lambda)$ and $\rho_{u'w'}(\lambda)$ for a range of λ between 10^2 m (Nyquist) and 2×10^4 m (five cycles over 100 km). However, the coherent signal in the lidar observations can be attenuated by ship-motion, the post-processing procedure applied to the lidar data to remove the ship-motion signal, and the lidar measurement principle. For the maximum observed $\overline{ws_a} \approx 20$ m s^{-1} this limits the detectable structures to $L_{h,c} > 400$ m along $\overline{wd_a}$. Even though coherent structures with $L_{h,c} < 400$ m likely occur in the flow, it is difficult to detect them with the utilized set-up. Such scales will thus be under-represented in the structure statistics. For the range of obtained $\overline{ws_a}$, we expect to achieve robust coherent-structure statistics for $L_{h,c}$ between 4×10^2 m and 2×10^4 m.

Each $L_{h,c}$ can be traced back to a certain time interval, as x is a function of t. We can thereby estimate the temporal fraction of the CAO that is occupied by coherent structures of a certain $L_{h,c}$. We estimate this temporal fraction relative to the whole duration of the CAO period. Integrating this relative time fraction over the duration of the whole CAO period results in the occurrence (%) of the respective $L_{h,c}$. If a coherent-structure pattern of respective $L_{h,c}$ would persist throughout the whole CAO period, it would correspond to a 100 % occurrence. The temporal occurrence of each $L_{h,c}$ can be estimated for any given time interval of the CAO. Here, we use 10-min intervals, to match the resolution of the boundary-layer parameters. Note, for each $Co_{u'w'}(\lambda)$ and $\rho_{u'w'}(\lambda)$, it is possible to identify several coherent circulation patterns of different scales, coexisting in the flow field. Consequently, each evaluated segment is not limited to only a single length scale, $L_{h,c}$, but can host a multitude of them and their occurrences need to be interpreted independently. To identify the respective $L_{h,c}$, which correspond to coherent structures, we first need to define thresholds for $Co_{u'w'}(\lambda)$ and $\rho_{u'w'}(\lambda)$, which are representative for real convective circulation in the atmospheric flow.

3.2.4 Thresholds for Atmospheric Convection

Convective circulation in the atmosphere deviates from the ideal case displayed in Fig. 3. We neither expect $u'(x)$ and $w'(x)$ to be perfectly correlated nor phase shifted. We need to define thresholds for $Co_{u'w'}$ and $\rho_{u'w'}$ that ensure that we correctly identify convective structures in the flow. A spectral analysis of horizontal and vertical velocity fluctuations by Hartmann et al. (1997) yielded a maximum coherence ≈ 0.9 when sampling organized convection during CAO conditions. Hartmann et al. (1997) sampled the velocity fluctuations along an aircraft track, perpendicular to the convective circulation, hence with a similar perspective as for one altitude displayed in Fig. 3. Here, coherence was generally smaller than 0.7, at scales that did not correspond to convective motion. Also, Hartmann et al. (1997) found the phase shift to be very close to the theoretical value of $\pm\pi/2$. Orienting on the thresholds defined by Hartmann et al. (1997), we select all λ as corresponding $L_{h,c}$ (Sect. 3.2.2), for which the following criteria apply

$$\begin{aligned} Co_{u'w'}(\lambda) &> 0.7, \\ 85^\circ < |\rho_{u'w'}(\lambda)| &< 95^\circ. \end{aligned}$$

These thresholds ensure an exclusive detection of atmospheric convective structures with high confidence.

3.2.5 Strength of the Convective Circulation

In addition to the auto and cross-correlation spectra, we estimate the amplitude spectra of u', v', and w'. Hence, each identified coherent structure can be linked to its corresponding horizontal and vertical velocity amplitudes, $u'_A(L_{h,c})$, $v'_A(L_{h,c})$, and $w'_A(L_{h,c})$. It should be noted that the velocity amplitudes are conservative estimates, as they depend on which part of the structure passes over the ship. The values of u'_A and w'_A are reduced if the intersect is closer towards the structures' edges.

4 Coherent Structures During a Cold-air Outbreak

We estimate u', v', and w' from the motion-corrected and post-processed lidar observations obtained during the CAO. To demonstrate the methodology described in Sect. 3.2, we first

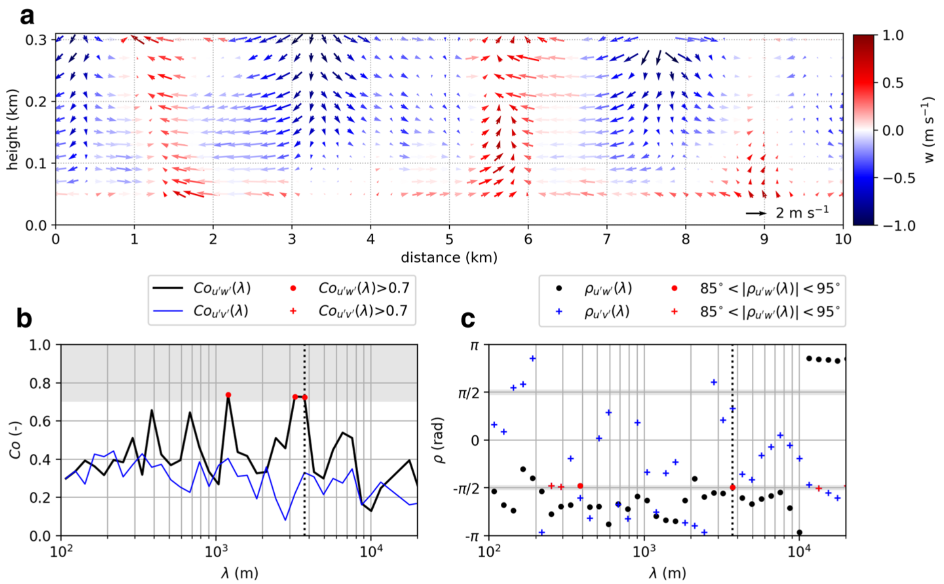

Fig. 4 **a** Snapshot of the $u'w'$ vector field retrieved from lidar observations, here displayed at an along-wind resolution of 200 m. **b** Corresponding coherence (Co) spectra and **c** phase (ρ) spectra calculated at 110 m above sea level obtained on 1 March 2018 at 0300 UTC. Grey shading highlights the range of Co and ρ where the criteria for coherent structures apply. Red markers indicate λ which fulfill the criteria in the displayed example. (Color figure online)

evaluate only a single exemplary situation. Here, we illustrate a convective situation, sampled on 1 March at 0300 UTC. Figure 4 displays the vector field of the u' and w' fluctuation, as well as the $Co_{u'w'}(\lambda)$, $Co_{v'w'}(\lambda)$, $\rho_{u'w'}(\lambda)$, and $\rho_{v'w'}(\lambda)$ spectra.

The vector field displayed in Fig. 4a is dominated by wide, diverging downdrafts which feed the comparably narrow, converging updrafts. Such proportions in the convective updraft and downdraft are typically observed for open cells, which are dynamically driven from the bottom to the top (Salesky et al. 2017). In this 10-km-wide slice, approximately three wavelengths ($L_{h,c} \approx 3 - 4$ km) of the lower part of the convective circulation pattern are represented. The convection pattern is level-consistent, except for one updraft around the 9 km mark, which does not penetrate as high. The corresponding coherence and phase spectra, estimated at 110 m above sea level, are displayed in Fig. 4b, c. The $Co_{u'w'}$ spectrum shows three instances of λ where the $Co_{u'w'}$ threshold is exceeded. As anticipated for cellular convection obtained by the ship-based lidar set-up (Sect. 3.2.1), the $Co_{v'w'}$ spectrum features smaller values than the $Co_{u'w'}$ spectrum and does not show the same distinct spikes. For the chosen example situation, the two criteria for the presence of a coherent-structure pattern defined in Sect. 3.2.4 apply for the coherence and phase spectra corresponding to the u' and w' series, $Co_{u'w'}$, and the $\rho_{u'w'}$, at $\lambda \approx 3.7$ km. Hence, the spectral analysis method (Sect. 3.2.2), which identifies a pattern of convective structures of $L_{h,c} \approx 3.7$ km, matches the visual evaluation corresponding to 3 to 4 km (Fig. 4a).

The large-scale cloud situation, obtained by the NASA Aqua polar orbiting satellite on 1 March 2018 at 0317 UTC, is shown in Fig. 5a. The satellite snapshot documents the cloud situation above the Iceland and Greenland Seas during the period relevant to the convective situation discussed above, representative for the early stage of the CAO. Surface pressure isobars and fronts from the U.K. Met Office's 0000 UTC analysis chart on 1 March were added

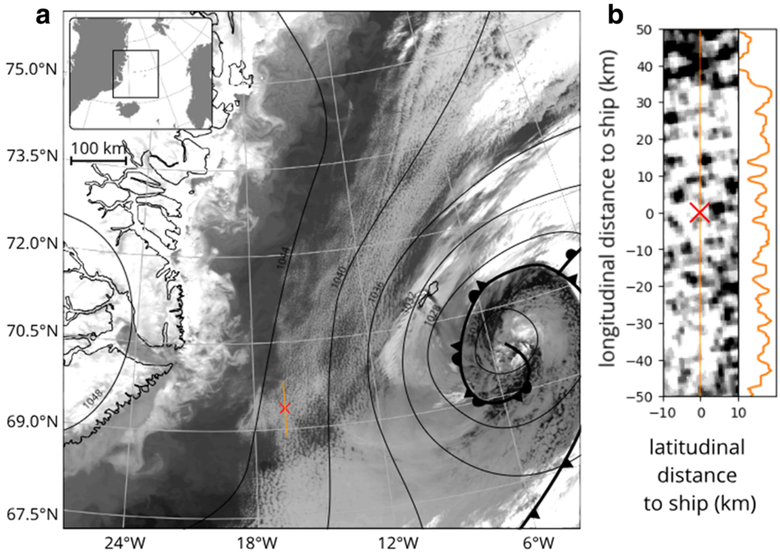

Fig. 5 **a** Observations from MODIS on the NASA Aqua satellite, representing the cloud situation for the CAO on 1 March 2018 at 0317 UTC and surface pressure isobars and fronts, corresponding to the U.K. Met Office's 0000 UTC analysis chart on 1 March 2018. **b** Close-up of the cloud pattern in the vicinity of the ship (red cross) and corresponding MODIS reflectance along the longitudinal cross-section (orange line). (Color figure online)

to document the synoptic situation. Here, the geostrophic flow is predominantly directed from north-north-east to south-south-west. Closer to the surface, the flow is expected to gain a more northerly component due to friction. This flow initiated the advection of cold and dry air from the sea-ice, which eventually initiated the onset of the CAO conditions in the Iceland and Greenland Seas region. The organization of the flow is connected to the passage of a cyclone through the area of the Iceland and Greenland Seas, a typical mechanism for the genesis of CAOs over high-latitude ocean areas (e.g., Fletcher et al. 2016). The area in the ship's vicinity, marked by a red cross in Fig. 5a (see also Fig. 1a), is covered by cellular clouds. Figure 5b shows a close-up of this cloud pattern and the corresponding reflectance in the satellite observations, along the longitudinal cross-section at ±50 km distance from the ship. Along the 100-km-long cross-section, we observe 13 single cellular clouds, which yields a corresponding cloud wavelength, $\lambda_{cloud} \approx 7.7$ km. The horizontal cloud scale is therefore approximately twice as large as the $L_{h,c}$ found from spectral analysis on 1 March at 0300 UTC of the near-surface range of the wind-profiling lidar (Fig. 4). Similar to findings presented by Renfrew and Moore (1999), this observation implies that every second convective cell, initiated near the surface and observed by the ship-based lidar (Fig. 4), manifested as a cloud, which can be identified from the satellite image (Fig. 5).

4.1 Coherent-Structure Statistics

We now apply the methodology demonstrated above over the lifecycle of the CAO event and integrate the occurrence of each identified $L_{h,c}$ over the entire evaluated period. Figure 6a shows the resulting occurrence for structures integrated over all the lidar levels. Note, individual structures that span the entire vertical lidar range are counted as one. Identified

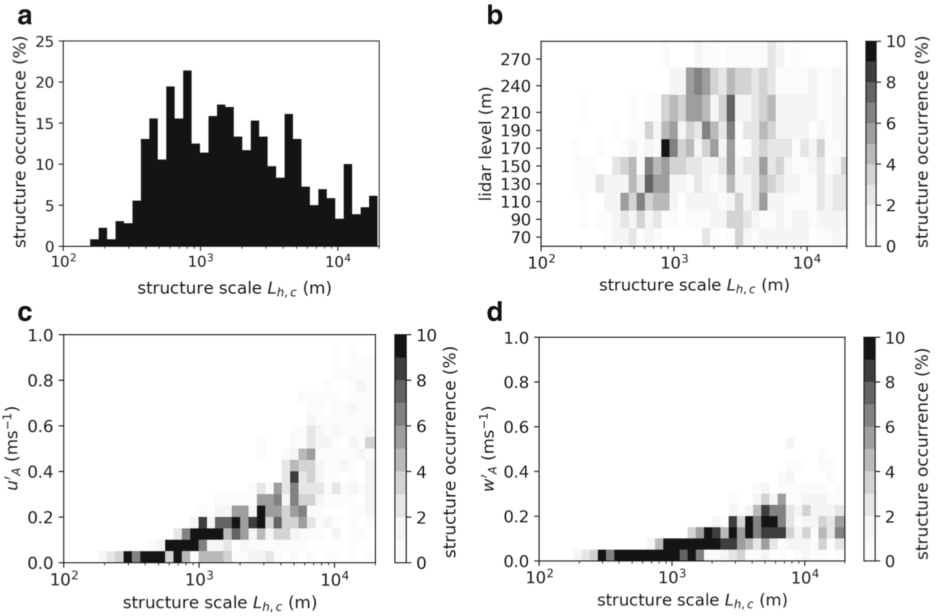

Fig. 6 Coherent-structure occurrence, displayed versus $L_{h,c}$ over the evaluated CAO period. The panels show **a** integrated $L_{h,c}$ occurrence. **b** $L_{h,c}$ occurrence per vertical lidar level. **c** $L_{h,c}$ occurrence per u'_A interval. **d** $L_{h,c}$ occurrence per w'_A interval

structures with $L_{h,c}$ between 4×10^2 m and 6×10^3 m occur frequently. This is in line with the range of scales we expect to obtain with the ship-based lidar (Sect. 3.2.3). Coherent structures with $L_{h,c} \approx 7 \times 10^2$ m are most frequently observed corresponding to $\approx 20\%$ of the evaluated CAO period (Fig. 6a). Here, the occurrences of $L_{h,c}$ at the individual lidar levels provide an interesting insight (Fig. 6b). For $L_{h,c}$ smaller than 2×10^3 m the identified $L_{h,c}$ increase with increasing lidar level, explaining the frequent $L_{h,c}$ occurrences at smaller scales (Fig. 6a). The increasing $L_{h,c}$ with height, evident in Fig. 6b, indicates that only a fraction of the individual thermals observed at the lowest lidar levels reaches up to higher altitudes. We also observed this process during the investigation of the 10-km-wide wind fluctuation field (Fig. 4). If an individual thermal does not reach as high, the distance between the updrafts increases at higher altitudes and hence causes the identified $L_{h,c}$ to increase. The formation of clouds with λ_{cloud}, identified to be twice the size of $L_{h,c}$ at comparably lower altitudes (Fig. 4, Fig. 5), follows the same mechanism at larger scales. This mechanism was also reported in past CAO studies (e.g., Atlas et al. 1986; Renfrew and Moore 1999; Cook and Renfrew 2015). With increasing structure scales, e.g. at $L_{h,c} \approx 2.5 \times 10^3$ m and $L_{h,c} \approx 5 \times 10^3$ m, individual structures span the entire lidar range more frequently throughout the CAO event (Fig. 6b). Due to the higher occurrence of smaller $L_{h,c}$, identified at lower lidar levels, the corresponding $L_{h,c}$ occurrence distribution features more distinct peaks than the occurrence of structures with the respective $L_{h,c}$ at the higher levels (Fig. 6a, b).

Figure 6c, d show the respective dependency of u'_A and w'_A on $L_{h,c}$. Small coherent structures ($L_{h,c} < 10^3$ m) contribute exclusively with small u'_A and w'_A (< 0.2 m s^{-1}), i.e. reduced turbulent mixing in the MABL. With increasing $L_{h,c}$, the corresponding u'_A and w'_A increase. The velocity amplitude u'_A exhibits a stronger increase with increasing $L_{h,c}$ than

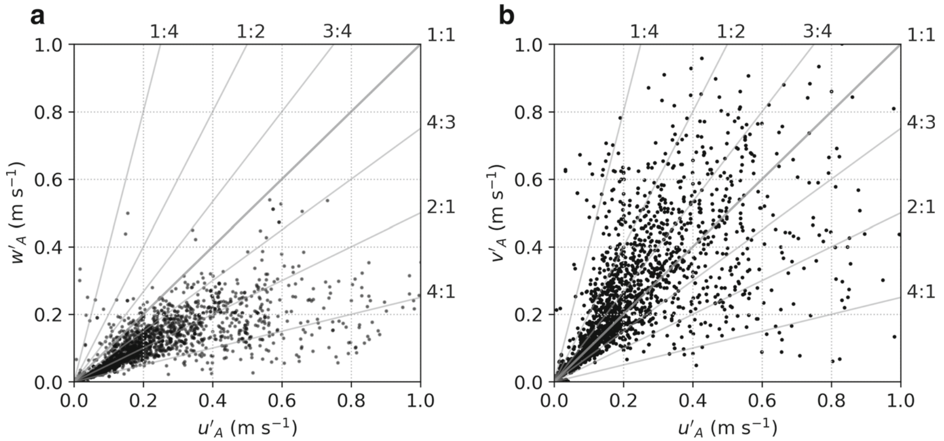

Fig. 7 Scatter of u'_A against **a** w'_A and **b** v'_A corresponding to each coherent structure identified for the whole range of $L_{h,c}$ and throughout the evaluated CAO period. Grey lines indicate the proportions between u'_A and w'_A and u'_A and v'_A, respectively

w'_A. In fact, w'_A increases only until $L_{h,c} \approx 8 \times 10^3$ m and remains at the same maximum value and velocity range for larger $L_{h,c}$. For $L_{h,c} < 8 \times 10^3$ m, u'_A is mostly two to three times as large as the corresponding w'_A. These large differences are also apparent in the scatter of u'_A against w'_A for the whole range of obtained $L_{h,c}$, which is displayed in Fig. 7a. For the evaluated CAO event, the maximum observed amplitude of the vertical overturning of the MABL is capped at approximately 0.5 m s^{-1} (Figs. 6d, 7a). The velocity amplitude, u'_A, which compensates the vertical contribution to the convective circulation along-wind, reaches much larger values of up to 1 m s^{-1} (Figs. 6c, 7a). For small coherent structures and velocity amplitudes, u'_A and w'_A scatter around the 2:1 ratio (Fig. 7a). For increasing u'_A, which also correspond to larger $L_{h,c}$ (Fig. 6c), the scatter of u'_A and w'_A is closer to the 4:1 ratio (Fig. 7a). An implication of this increasing ratio between u'_A and w'_A is that the ratio between $L_{h,c}$ and the vertical coherent-structure depth also increases from small $L_{h,c}$ to large $L_{h,c}$.

Figure 7b displays the scatter of u'_A against v'_A for the whole range of $L_{h,c}$ over the evaluated CAO period. Note, we find a similar relationship between $L_{h,c}$ and v'_A as for $L_{h,c}$ and u'_A (not shown). The scatter between u'_A and v'_A is dense about the 1:1 ratio and mainly within the 1:2 and 2:1 ratios for small u'_A and v'_A (Fig. 7b), corresponding to $L_{h,c}$, which are predominantly smaller than 2×10^3 m (Fig. 6c). A ratio close to 1 is within the range expected for horizontally isotropic cells. The velocity amplitudes, u'_A and v'_A, result from composites of several structures intersecting the ship's path at varying distance to their centre. For small $L_{h,c}$, a large number of structures resemble the corresponding coherent-structure pattern, representing average u'_A and v'_A over the different intersects (see Sect. 3.2.1). Neither u'_A nor v'_A represents the maximum strength of the structures, but rather average properties over the corresponding structure sizes. For increasing u'_A and v'_A, the spread of the scatter points increases (Fig. 7b). A relatively higher fraction of scatter points than for small u'_A or v'_A lies outside the 1:2 and 2:1 ratios, respectively. The larger spread at increasingly large velocity amplitudes corresponds to $L_{h,c}$ larger than 2×10^3 m (Fig. 6c). Here, the ship's intersection with a single large-scale structure strongly contributes to the corresponding values of u'_A and v'_A in contrast to a composite velocity amplitude of multiple small coherent structures.

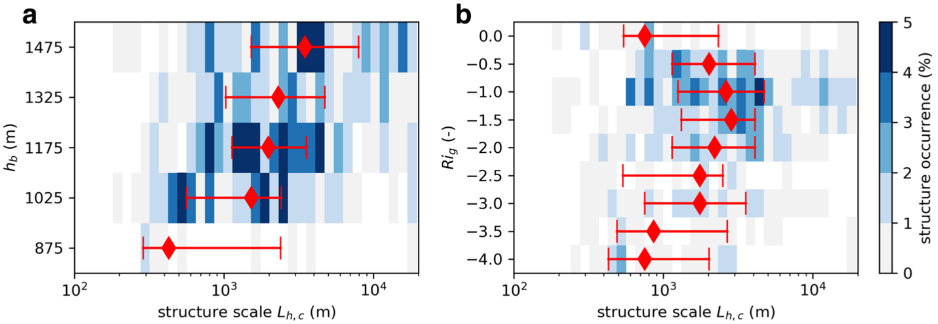

Fig. 8 Occurrence of coherent structures of respective $L_{h,c}$, corresponding to the evaluated CAO period and integrated over **a** h_b range bins of 150 m between 800 m and 1550 m, **b** Ri_g range bins of 0.5, ranging from − 4.25 to 0.25. Occurrences corresponding to structures outside of the displayed h_b and Ri_g ranges are counted to the corresponding lowest or highest range bins, respectively. For each bin of the corresponding boundary-layer parameter, the quartiles (25-percentile, median, 75-percentile) are indicated in red. The median is indicated by red diamonds and the interquartile range of $L_{h,c}$ is indicated by the horizontal red line. (Colour figure online)

We now shift the focus of the discussion from the inter dependency of the coherent-structure characteristics to their dependency on the obtained boundary-layer parameters. Each boundary-layer parameter, introduced in Sect. 3.1, is separated into bins, corresponding to their respective uncertainty range. We combine the time series of the identified $L_{h,c}$ and the time series of the boundary-layer parameters by integrating the temporal occurrence of each $L_{h,c}$ over each of the boundary-layer bin ranges. Similar to the occurrence distribution displayed in Fig. 6a, we count a $L_{h,c}$ that is simultaneously observed at several lidar levels as a single coherent-structure pattern. Hence, integrating the resulting $L_{h,c}$ occurrence distribution over the whole range of the respective boundary-layer parameter would yield the same distribution as shown in Fig. 6a. Note, an integration of the occurrences over the range of $L_{h,c}$, on the other hand will not yield the occurrence of the boundary-layer parameter, because structures of different scales can coexist in the flow field. Figure 8 displays the $L_{h,c}$ occurrences, corresponding to h_b and Ri_g, which show a noticeable dependency on $L_{h,c}$ over the course of the evaluated CAO period.

Figure 8a shows the dependency of the $L_{h,c}$ occurrences on h_b range bins. With increasing h_b, the occurrence distribution of $L_{h,c}$ shifts to larger $L_{h,c}$ values. Except for the lowest h_b bin between 800 m and 950 m, which includes only a small fraction of the $L_{h,c}$ occurrence, the median $L_{h,c}$ is in the range of $\approx 2 \times 10^3$ m to 4×10^3 m (2 to 4 km). The median $L_{h,c}$ is approximately twice as large as h_b over the range of h_b between $\approx$ 1 km and 1.5 km. We observe similar values for the ratio between u'_A and w'_A displayed in Fig. 7a. Cieszelski (1998) sampled cellular convection , which featured a very similar horizontal extent of 2 km to 3 km at a comparable convective boundary-layer depth of 1 km. Cieszelski′s observations corresponded very well with ratios between the horizontal and the vertical convective scales found in laboratory experiments of cellular Rayleigh–Bénard convection. Based on their size and ratios, we also expect the coherent structures obtained during this study to have properties which are similar to cellular Rayleigh–Bénard convection, such as their dependency on the temperature gradient in the flow.

The Richardson number Ri_g is a measure for the balance between buoyancy (temperature gradient) and shear (velocity gradient) in the boundary layer. For the evaluated CAO, we observe a distinct dependency between the $L_{h,c}$-occurrence distribution and the near-surface

Ri_g (Fig. 8b). Here, the median $L_{h,c}$ decreases with increasingly negative $Ri_g \leq -2$. This is in line with the development of Rayleigh–Bénard convection scales with increasing buoyant forcing observed in laboratory experiments (e.g., Hu et al. 1995). Figure 8b shows that the largest median $L_{h,c} \approx 3 \times 10^3$ m are present at Ri_g between -1.75 and -1.25, where the turbulence generation is weakly buoyancy dominated. For the Ri_g bin centred at -1, where the turbulence generation is equally balanced between buoyancy and shear, we observe the most frequent occurrence of coherent structures, which is consistently high over almost the whole range of $L_{h,c}$. This dense $L_{h,c}$ occurrence is both due to the frequent occurrence of Ri_g around minus 1, and due to increased multi-scale characteristics of the coherent structures for this Ri_g range bin. For $Ri_g \geq -1$, medium $L_{h,c}$ decreases with increasing Ri_g. Yet, the occurrence of $L_{h,c}$ also decreases for the more shear-dominated conditions corresponding to Ri_g values around 0. For $Ri_g \geq 0.5$ (not shown), we identify no $L_{h,c}$. This is mainly because this condition is sparsely present during the obtained CAO period. But we also do not expect to obtain coherent structures during increasingly stable conditions, for which past studies (e.g., Barthlott et al. 2007) predominantly report very small turbulent-structure scales $< 2 \times 10^2$ m in the boundary layer. Such small-scale structures are unlikely to be resolved accurately with the observations available here. Positive Ri_g correspond to comparably small $L_{h,c}$, because structures are hindered to grow to large scale, while a positive lapse rate works against the structure's expansion. Yet, large negative Ri_g also correspond to comparably small $L_{h,c}$. On the contrary to positive Ri_g, however, vertical decoupling is a key mechanism for large negative Ri_g and the strong buoyant forcing enhances the emergence of individual thermals. In the absence of the suppressing, enhancing, or vertically restricting factors, turbulence conditions, which are balanced between buoyancy and shear, favour comparably increased $L_{h,c}$.

The boundary-layer parameters, $w^{\uparrow}_{\max}$, $w^{\downarrow}_{\max}$, Q_H, Q_L, and d are not displayed in Fig. 8, as they exhibit a more complex dependency on $L_{h,c}$ than h_b and Ri_g. The parameters are obtained during evolving synoptic conditions as well as from a moving ship, which results in both a temporal and a spatial perspective of the processes that shape the coherent structures during the CAO event. In the following section, we investigate this temporal and spatial development of the boundary-layer parameters, the connected predominating processes, and their impact on the coherent-structure development.

4.2 Coherent-Structure Evolution

The final shape of the $L_{h,c}$-occurrence distribution (Fig. 6a) depends on the temporal and spatial evolution of the coherent structures identified during the evaluated CAO period. The time series of the predominating $L_{h,c}$ is now examined via Fig. 9a. Displayed are the time series of structures with respective $L_{h,c}$ which occurred most frequently throughout the CAO. Figure 9b–f shows the complementing time series of the boundary-layer parameters. Additionally, Fig. 9g depicts the general evolution of T_a, SST, and wind during the CAO and Fig. 9h shows the fetch, representative for the spatial evolution of the evaluated CAO from the ship's perspective.

We identify the first robust signal of coherent structures in the lidar observations shortly after an initial increase in h_b, d, Q_H, and Q_L (Fig. 9b, e, f). The increase of these parameters is due to the advection of cold air from the north, indicated by a drop in T_a (Fig. 9g). The fetch corresponding to these first hours of the CAO event is consistently fixed at $f \approx 250$ km (Fig. 9h). Even though near-surface instability is increased, the turbulence generation and deepening of the boundary layer to 1 km is mainly shear-driven, indicated by a Ri_g close to

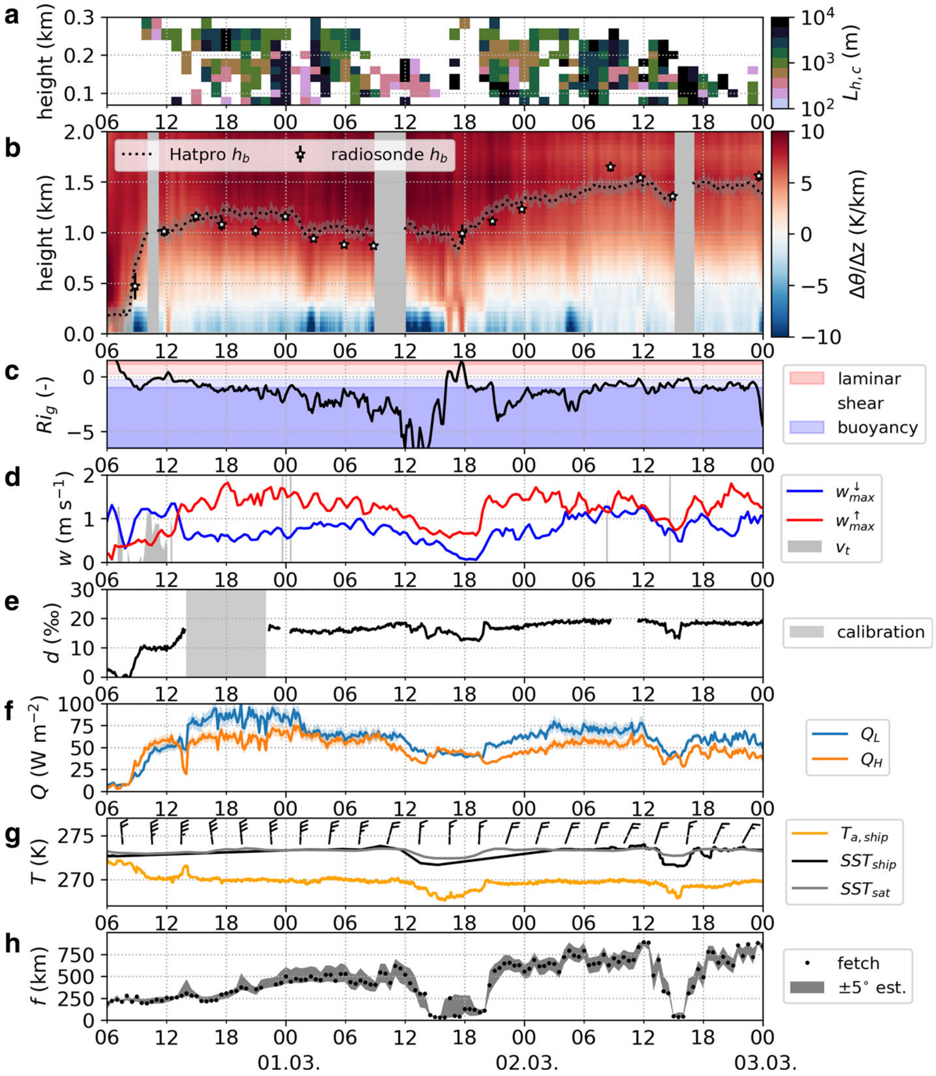

Fig. 9 Time series of various variables obtained during the CAO period. **a** Hourly, most frequent $L_{h,c}$, obtained at different lidar levels. Timesteps, at which no coherent structures were identified are left blank. **b** Lapse rate $\Delta\theta/\Delta z$ and buoyancy height h_b with corresponding uncertainty ranges from radiometer and radiosondes, with missing data marked in light grey. **c** Ri_g and indication of buoyancy-driven, shear-driven, and suppressed turbulence regime. **d** Time series of maximum velocities in up- and downdrafts. **e** Time series of d, with calibration periods shaded in grey. **f** Bulk sensible and latent heat fluxes Q_H and Q_L and corresponding uncertainty ranges. **g** Time series of T_a, SST from ship and collocated along satellite observations of SST. Also wind barbs every 3 h, pointing in direction of the wind, with long feathers = 10 knots and short feathers =5 knots. **h** Fetch, f, and corresponding $wd \pm 5°$ uncertainty range estimate. Note that 1 knot = 0.514 m s^{-1} [Ed.]. (Colour figure online)

zero (Fig. 9b, c). Remarkably, the evolution of h_b, estimated on the basis of the radiometer observation, is very close to those from the radiosonde measurements. During the first hours of the CAO, observations of small terminal velocities of precipitation ($v_t \leq 1$ m s^{-1}, Fig. 9d) indicate the presence of snow-type precipitation (Maahn and Kollias 2012). Simultaneously increased $w^{\downarrow}_{\max}$ and low $w^{\uparrow}_{\max}$ values indicate an impact of this type of precipitation on the absolute vertical velocity observations by the lidar. Because an accurate observation of w is essential to estimate $L_{h,c}$, such a long period of precipitation potentially impacts the applicability of the spectral analysis method (Sect. 3.2.2), when the velocity fluctuations are dampened by the precipitation signal. This precipitation event also marks a halt in the otherwise monotonic increase of d from 0 ‰ to $\approx$ 18 ‰ at the beginning of the CAO (Fig. 9e). As long as d increases any convective overturning of the MABL is not sufficient to compensate for the increasing relative enrichment of HDO molecules in the water vapour, due to increased evaporation in the CAO conditions. Hence, along the whole distance between the ship and the origin of the CAO air masses ($f \approx 250$ km), the evaporation process at the sea surface provides a stronger isotopic signal than the mixing by convection. Unfortunately we cannot directly evaluate the observed trends in the boundary-layer parameters (Fig. 9b–f) in the context of $L_{h,c}$ as no coherent structures could be detected during these first few hours (Fig. 9a). Assuming that precipitation does not conceal coherent-structure development, this indicates that the organization of coherent structures in the flow requires a certain spin-up time. This spin-up time is determined by the strength and speed of the cold-air advection.

From 28 February 1200 UTC, the evaluated CAO features organized convection, detectable with the spectral-analysis method introduced in Sect. 3.2. The predominating $L_{h,c}$ gradually increase from O (4×10^2 m) on 28 February 1200 UTC to O (10^4 m) on 1 March 0000 UTC and overall decrease again to O (4×10^2 m) within 1 March 1200 UTC. On this comparably long time scale of 24 h, the boundary-layer parameters, h_b, $w_{\max}$, d, and Q show a response to the overall evolution of $L_{h,c}$ (Fig. 9a–f). Yet a distinct, short-lived minimum $L_{h,c} \approx O$ (4×10^2 m) around 1 March 0200 UTC is not captured by these parameters. Here, only the near-surface instability and Ri_g (Fig. 9b, c) take increasingly negative values in correspondence. This observation confirms the sensitivity of $L_{h,c}$ to Ri_g found in the Ri_g-dependent heatmap of $L_{h,c}$ occurrences (Fig. 8b), while the other evaluated boundary-layer parameters show a less distinct relationship to $L_{h,c}$. The processes responsible for the evolution of the near-surface instability and Ri_g are therefore particularly interesting. On the short time scales, which are of interest to the evolution of Ri_g, changes in atmospheric conditions due to the ship's movement play a key role. From 28 February 1200 UTC to 1 March 0300 UTC f increases to ≈ 500 km, as the ship steamed to the south and away from the sea-ice edge (Fig 1b, Fig. 9h). Along the way, on 1 March around 0000 UTC, the rain radar detects two short precipitation events with $v_T > 2$ m s^{-1} (Fig. 9d), indicating that liquid droplets predominate during these events (see Maahn and Kollias 2012). With increasing fetch and time such precipitation events are expected to occur more frequently, as a response to the convective overturning of water vapour and cloud growth during the progressing CAO (e.g, Papritz and Sodemann 2018). Locally, evaporating precipitation can cause cooling in the near-surface layers. This can result in increased negative lapse rate and a stronger near-surface instability, which is observed when the ship moves into a location affected by precipitation. Cooling of the lower atmospheric layers can introduce vertical decoupling of the air-masses (Abel et al. 2017) and a corresponding restriction of the vertical structure scale and corresponding $L_{h,c}$, as observed on 1 March around 0200 UTC. Such decoupling is independent of the theoretical maximum vertical structure extension, represented by h_b. Except for the near-surface instability and Ri_g, none of the boundary-layer parameters respond or can be identified as cause for the decreased $L_{h,c}$ for this local, short-term mechanism.

After 1 March 0300 UTC the ship moves almost perpendicular to the wind direction and towards the sea-ice edge in the west (see Fig. 1b). Here, a second mechanism connected to the ship's movement impacts the evolution of Ri_g, $L_{h,c}$, and most of the boundary-layer parameters. The fetch decreases and temporarily reaches a minimum around 1 March 1500 UTC (Fig. 9h). For a short fetch, the internal boundary layer initiated at the sea-ice edge is expected to be comparably shallow. Here, the value of h_b is not representative of the actual boundary-layer depth because it corresponds to that of a fully developed boundary layer, which is not present for such a short fetch. Within the shallow boundary layer the near-surface temperature gradient is steeper and coherent structures are restricted in vertical extent and hence in $L_{h,c}$, corresponding to a large negative Ri_g. With decreasing f, Ri_g, and $L_{h,c}$ (Fig. 9a, b, h), the strength of the vertical circulation, $w^{\uparrow}_{\max}$ and $w^{\downarrow}_{\max}$ and the turbulent fluxes, Q_H and Q_L, are correspondingly reduced (Fig. 9d, f). Also, d temporarily decreases from ≈ 18 ‰ to a local minimum of ≈ 12 ‰ (Fig. 9e). Here, the convective overturning of the MABL by predominantly small and weak convective structures is negligible and the structures' contribution to the exchange of near-surface air-masses exposed to evaporation is expected to be small. Hence, the sharp decrease in d can mainly be linked to the short fetch, as d results from an accumulated signal of the evaporation along the distance of the air-masses' trajectory. Large changes in f close to the spatial boundary of the CAO therefore yield the strongest concurrent impact of the ship's movement on the coherent-structure and the boundary-layer characteristics and need to be taken into account, when evaluating the event from a temporal perspective.

Over the lifecycle of the CAO, the predominantly northerly wind direction gains a small easterly component (Fig. 9g). This small change in wind direction causes an overall increase of the estimated f from ≈ 250 km at the onset of the CAO event to ≈ 750 km at the end of the evaluated period, independent of the ship's movement. There are two exceptions, where the ship's movement becomes apparent in a drop of f, on 1 March from 1200 UTC to 2100 UTC, which is discussed in the preceding paragraph and on 2 March from 1200 UTC to 1800 UTC, respectively. Following the overall trend of f, we identify the largest predominating coherent structures, corresponding to $L_{h,c}$ of O (10^3 m) to O (10^4 m) more frequently towards the end of the evaluated CAO period. Also h_b increases from around 1 km in the first half to around 1.5 km in the second half of the evaluated CAO period, for which the near-surface lapse rate approaches zero. Notably, the trend identified for the overall evolution in f, the boundary-layer characteristics, and the coherent-structure characteristics is present for two periods corresponding to 1 March around 0600 UTC and 2 March around 0800 UTC. These two periods represent almost the same point in space, yet are separated by 26 h in time. Thus, temporal evolution and maturing of the CAO event impacts the evolution of the boundary-layer parameters and the corresponding coherent-structure characteristics. In contrast to the rapid changes observed for spatial changes, the temporal CAO evolution has a more moderate impact on the boundary-layer and the coherent-structure development.

For several of the boundary-layer parameters, we identify a long-term evolution, which can be linked to the coherent-structure characteristics. For periods during which we observe a coherent signal, we predominantly observe $w^{\uparrow}_{\max}$ larger or equal to $w^{\downarrow}_{\max}$ (Fig. 9d). This implies that the turbulent circulation generally features strong, but narrow updrafts and wider, but generally weaker downdrafts. Such a behaviour of the wind field is already depicted in Figure 4. Throughout the CAO, the estimated coherent vertical velocity amplitudes (Fig. 6d) correspond to approximately 10% of the sum of maximum updraft and downdraft velocities (Fig. 9d). In the presence of predominantly large-scale coherent structures, d remains mostly constant. Coherent structures are an important driver of the convective turnover of the MABL and hence work against the increase of d in the near-surface layers. During CAO conditions with large humidity gradients in the near-surface layer, a constant d implies that the enrichment of HDO due to evaporation is balanced by the convective overturning, which exchanges the air in the near-surface layer with comparably dry air from higher atmospheric levels. Here, d reaches maximum values of 18 ‰ to 20 ‰ throughout the evaluated CAO period. To maintain such moderately high values of d, in the presence of strong turnover of the MABL, a large humidity gradient is required above the water surface along the trajectory of the CAO air masses. According to the empirical relation of Pfahl and Sodemann (2014), the relative humidity above the water surface needs to be $\approx 60\%$ on average along the trajectory, when calculated with respect to the measured SST, to yield such a value of d. The humidity and temperature gradients we observe during the CAO period result in turbulent heat fluxes. In comparison to previously studied CAOs, however, the turbulent heat fluxes obtained during the evaluated CAO event are relatively weak. Yet, the heat fluxes are elevated during periods, where large-scale coherent structures predominate relative to periods where small-scale coherent structures predominate. Hence, the coherent structures and large-scale overturning of the MABL have an impact on the overall evolution of Q_H and Q_L. The variations in Q_H and Q_L are, however, less sensitive to the coherent-structure characteristics, than for example those in Ri_g. This implies that small-scale and non-coherent turbulence also has an impact on Q_H and Q_L in the CAO event evaluated here and the turbulent heat fluxes result from a complex composite of irregular turbulent structures and convectively driven coherent structures. On the long-term, large-scale coherent structures yield the largest contribution to the heat fluxes and overturning of the MABL.

5 Conclusions

We develop a novel methodology to identify coherent structures based on the velocity fluctuations in the atmospheric flow during CAO conditions. We utilize a ship-based, wind-profiling lidar, employed during the IGP campaign on board of the *NRV Alliance*. We estimate the characteristics of the convective structures, and evaluate their interplay with other boundary-layer parameters. The ship-based approach captures the long-term statistics of the structure characteristics, an advantage over aircraft observations, which are limited to relatively short observational periods. In contrast to satellite snapshots, the ship-based approach provides a dynamical perspective on convection, and is able to determine coherent structures of multiple sizes in the flow simultaneously. Furthermore, the method does not require the formation of clouds in order to identify these structures and their corresponding characteristic spatial dimension.

The evaluated ship-based and multi-sensor set-up provides a detailed insight into the major processes revolving around coherent structures and the evolution of their characteristic size and strength in the MABL. Spectral analysis of the along-wind and vertical velocity fluctuations frequently yields a strong coherent signal throughout the lifecycle of the CAO. This indicates the organization of the convection into coherent structures. Each of these structures is linked to a characteristic horizontal length scale and an along-wind, cross-wind, and vertical velocity amplitude, under the assumption that isotropic cells predominate in the flow. The structures' characteristics identified for the evaluated CAO period match the characteristics expected for cellular convection. Over the course of the CAO event, the coherent structures feature variations in horizontal size and strength, which are sensitive to the near-surface stratification and Ri_g. For unstable conditions, where turbulence generation is strongly dominated by buoyancy, small-scale structures O (4×10^2 m) predominate. These structures are comparably weak and contribute little to the turbulent mixing in the MABL. We identify these small-scale structures more frequently in the lower lidar levels, while individual large-scale structures occur over the whole lidar range. Only a fraction of the individual thermals initiated at the surface occur throughout the lidar range and an even smaller number manifest as clouds. As shear-generated turbulence increases in importance, the size and strength of the coherent structures increases. Increasing median horizontal structure size of O (10^3 m) coincides with increasing convective boundary-layer depth. The ratio between the median horizontal structure size and the boundary-layer depth is ≈ 2. This ratio coincides with the median ratio found between the along-wind and vertical velocity amplitudes of the coherent structures. Throughout the evaluated CAO event the identified coherent convective structures mainly feature comparably wide and weak downdrafts and comparably narrow and strong updrafts. The largest coherent structures predominate for weakly buoyancy dominated conditions and for conditions equally balanced between buoyancy and shear-generated turbulence. For these large coherent structures, the size and horizontal velocity amplitude greatly exceed the vertical counterparts. The efficiency of the vertical overturning of the MABL is found to be capped for structures exceeding $\approx 8 \times 10^3$ m for the evaluated CAO event. The overturning of the MABL compensates the near-surface enrichment of HDO, corresponding to the evaporation along the trajectory of CAO air-masses, yielding a maximum d between 18 ‰ and 20 ‰. Turbulent heat fluxes observed here are partly driven by small-scale and non-coherent turbulence and correspond to organized large-scale convective overturning by coherent structures only on long time scales. Short-term variations of the coherent-structure characteristics correspond almost exclusively to the near-surface stratification and Ri_g, which are mainly introduced by the ship's movement and the respective fetch.

The coherent structures discussed in this study correspond to one CAO case study obtained during the IGP campaign. The detailed observations of the velocity fluctuations provide the opportunity to further study the dynamics and direct impacts of the single or composite convective cells on the processes acting in the MABL. This can be particularly useful if additional observations of highly resolved boundary-layer processes are available. An example are the observations from additional platforms operated during IGP, such as a research aircraft, which provide overlapping observations corresponding to a few single convective structures. Investigating the observed structures in such detail will be the subject of a subsequent study. Yet to achieve statistics on coherent-structure characteristics applicable to the extensive range of CAO conditions in the Arctic, a larger observational basis is required. Such enhanced statistics on atmospheric convection during CAOs can, for example, be beneficial to model validation. Here, one should consider the utility of ship-based remote sensing, e.g., by ships of opportunity, which are operated in relevant but remote locations.

Acknowledgements This study was a part of the Iceland Greenland Seas Project. We are grateful for the constructive comments and insightful questions from the four anonymous reviewers, that helped to substantially improve the manuscript. We thank A. Seidl, A. Terpstra, S. Zou and Y. Weng for the set-up, maintenance and documentation of the ship-based instrumentation and measurements. We also thank M. Kähnert for helping with the formal editing and proofreading of the manuscript. J. Reuder acknowledges the Offshore Boundary Layer Observatory, OBLO, funded by the Research Council of Norway (NRF Grant No. 227777) for access to the WindCube V2 lidar system. H. Sodemann acknowledges the projects FARLAB (NRF Grant No. 245907) and SNOWPACE (NRF Grant No. 262710) for the stable water isotope instrumentation and measurements, respectively. The HATPRO and radiosounding system were provided by the Atmospheric Measurement and Observations Facility (AMOF) of the National Centre for Atmospheric Science (NCAS). The radiosondes were funded by the Atmospheric Forcing of the Iceland Sea project (AFIS) via the Natural Environment

Research Council (NERC) Grant NE/N009754/1, which also partly funded the contribution of I. Renfrew and C. Barrell to the study.

Funding Open access funding provided by University of Bergen (incl Haukeland University Hospital).

Appendix: Applicability to Mesoscale Convection and Roll Vortices

For the utilized ship-based lidar set-up, the presented methodology (Sect. 3.2) is restricted to estimates of $L_{h,c}$ along the apparent wind direction, $\overline{wd_a}$. For a horizontally isotropic convective cell, the estimated $L_{h,c}$ from spectral analysis directly represents its spatial extent. Yet, previous CAO studies (e.g., Atkinson and Zhang 1996; Hartmann et al. 1997; Renfrew and Moore 1999) report the presence of roll vortices, convective structures that have a much larger spatial extent along-wind than cross-wind. Due to this horizontal anisotropy, these structures need to be interpreted with care in terms of $L_{h,c}$. The longitudinal axis of rolls tends to align with a small angle, α, to the mean wind direction. This is, for example, discussed by Atkinson and Zhang (1996), and evident in large-eddy simulations by Brilouet et al. (2020). Cross-wind movement of the ship can introduce an increased α, relative to $\overline{wd_a}$. The roll circulation, v'_{roll}, perpendicular to the longitudinal roll axis, projected to u'_A and v'_A yields the following dependencies

$$\frac{u'}{v'_{roll}} = \sin(\alpha); \qquad \frac{v'}{v'_{roll}} = \cos(\alpha) \qquad \Rightarrow \qquad \frac{u'}{v'} = \tan(\alpha).$$

When rolls are present in the flow and α is small yet larger than 0° the coherent signal, obtained by the ship-based lidar, has a much larger contribution to v'_A, than to u'_A. The distribution of the ratio between u'_A and v'_A is expected to clearly shift to values close to zero. The v' series is proportional to v'_{roll}, which follows an analogous circulation with w' as illustrated in Fig. 3 in the cross-wind direction. The obtained v' for the roll case is thus phase-shifted by $\pm\pi/2$ to the corresponding w', in contrast to v' for isotropic cells. Hence, in the presence of roll vortices, one should also take $Co_{v'w'}$ and $\rho_{v'w'}$ into account as an criterion for the estimation of $L_{h,c}$. On the one hand, v' is expected to yield a much clearer coherent signal, at least for small α. On the other hand, a corresponding phase shift between v' and w', which is close to $\pm\pi/2$, provides the sufficient criterion that rolls are present in the flow. We tested this criterion for the evaluated CAO period, yet found no evidence that such anisotropic structures are present.

In the roll case, an estimate of $L_{h,c}$ using the proposed method will correspond to the wavelength, λ'_{roll}, which describes the roll wavelength, λ_{roll}, transposed to the axis of $\overline{wd_a}$

$$\frac{\lambda_{roll}}{\lambda'_{roll}} = \sin(\alpha).$$

The obtained $L_{h,c}$ for rolls will be larger than the roll extent perpendicular to the longitudinal roll axis and smaller than the extent parallel to this axis.

References

Abel SJ, Boutle IA, Waite K, Fox S, Brown PRA, Cotton R, Lloyd G, Choularton TW, Bower KN (2017) The role of precipitation in controlling the transition from stratocumulus to cumulus clouds in a northern hemisphere cold-air outbreak. J Atmos Sci 74(7):2293–2314. https://doi.org/10.1175/JAS-D-16-0362.1

Achtert P, Brooks I, Brooks B, Moat B, Prytherch J, Persson O, Tjernström M (2015) Measurement of wind profiles by motion-stabilised ship-borne Doppler lidar. Atmos Meas Tech 8:4993–5007. https://doi.org/10.5194/amt-8-4993-2015

Atkinson BW, Zhang JW (1996) Mesoscale shallow convection in the atmosphere. Rev Geophys 34(4):403–431. https://doi.org/10.1029/96RG02623

Atlas D, Walter B, Chou SH, Sheu PJ (1986) The structure of the unstable marine boundary layer viewed by lidar and aircraft observations. J Atmos Sci 43(13):1301–1318

Barrell C, Renfrew I (2020) Iceland Greenland seas Project (IGP): surface layer meteorological measurements on board the NATO research vessel Alliance. Centre for Environmental Data Analysis. https://catalogue.ceda.ac.uk/uuid/b4ba8f11459c422d84d7293b9211ccf7

Barthlott C, Drobinski P, Fesquet C, Dubos T, Pietras C (2007) Long-term study of coherent structures in the atmospheric surface layer. Boundary-Layer Meteorol 125:1–24. https://doi.org/10.1007/s10546-007-9190-9

Brilouet PE, Durand P, Canut G (2017) The marine atmospheric boundary layer under strong wind conditions: Organized turbulence structure and flux estimates by airborne measurements. J Geophys Res Atmos 122(4):2115–2130. https://doi.org/10.1002/2016JD025960

Brilouet PE, Durand P, Canut G, Fourrié N (2020) Organized turbulence in a cold-air outbreak: Evaluating a large-eddy simulation with respect to airborne measurements. Boundary-Layer Meteorol 175(1):57–91. https://doi.org/10.1007/s10546-019-00499-4

Brooks BJ (2019a) Iceland Greenland seas Project (IGP): Humidity and temperature profiles from the NCAS Humidity And Temperature PROfilers (HATPRO) scanning radiometer on board the alliance research vessel. Centre for Environ Data Anal. https://catalogue.ceda.ac.uk/uuid/35f30876a4894169bb1ebeafe1e0c447

Brooks BJ (2019b) Iceland Greenland seas Project (IGP): Upper air sounding: Profiles of temperature, pressure, humidity, wind speed and wind direction. Centre for Environmental Data Analysis. https://catalogue.ceda.ac.uk/uuid/5acca11ececb4d8283b7e633370b6751

Brooks IM, Tjernström M, Persson POG, Shupe MD, Atkinson RA, Canut G, Birch CE, Mauritsen T, Sedlar J, Brooks BJ (2017) The turbulent structure of the arctic summer boundary layer during the arctic summer cloud-ocean study. J Geophys Res Atmos 122(18):9685–9704. https://doi.org/10.1002/2017JD027234

Brümmer B (1996) Boundary-layer modification in wintertime cold-air outbreaks from the arctic sea ice. Boundary-Layer Meteorol 80:109–125. https://doi.org/10.1007/BF00119014

Buckley MW, Marshall J (2016) Observations, inferences, and mechanisms of the Atlantic Meridional Overturning Circulation: A review. Rev Geophys 54(1):5–63. https://doi.org/10.1002/2015RG000493

Chang SS, Roscoe Braham JR (1991) Observational study of a convective internal boundary layer over lake Michigan. J Atmos Sci 48(20):2265–2279

Chou SH, Ferguson MP (1991) Heat fluxes and roll circulations over the western gulf stream during an intense cold-air outbreak. Boundary-Layer Meteorol 55(3):255–281. https://doi.org/10.1007/BF00122580

Cieszelski R (1998) A case study of Rayleigh-Bénard convection with clouds. Boundary-Layer Meteorol 88(2):211–237. https://doi.org/10.1023/A:1001145803614

CMRE (2017) NRV alliance drawings. Science and technology organisation centre for maritime research and experimentation, Tech rep

Collaud Coen M, Praz C, Haefele A, Ruffieux D, Kaufmann P, Calpini B (2014) Determination and climatology of the planetary boundary layer height above the Swiss plateau by in situ and remote sensing measurements as well as by the COSMO-2 model. Atmos Chem Phys 14(23):13,205-13,221. https://doi.org/10.5194/acp-14-13205-2014

Cook P, Renfrew I (2015) Aircraft-based observations of air-sea turbulent fluxes around the British Isles: Observations of air-sea fluxes. Q J R Meteorol Soc 141:139–152. https://doi.org/10.1002/qj.2345

Dansgaard W (1964) Stable isotopes in precipitation. Tellus 16(4):436–468. https://doi.org/10.1111/j.2153-3490.1964.tb00181.x

Duscha C (2020) Iceland Greenland seas Project (IGP): three dimensional wind profile measurements from the University of Bergen Windcube V2 pulsed lidar on board the NATO research vessel Alliance. Centre Environ Data Anal. https://catalogue.ceda.ac.uk/uuid/cc93b95c264644519777aa1ab37c23c0

Duscha C, Bakhoday-Paskyabi M, Reuder J (2020) Statistic and coherence response of ship-based lidar observations to motion compensation. Journal of Physics conference series. In: Proceedings of the 17th EERA DeepWind Conference, Trondheim, Norway https://doi.org/10.1088/1742-6596/1669/1/012020

Emery WJ, Thomson RE (2001) Data analysis methods in physical oceanography - time-series analysis methods. Elsevier Science, chap 5:371–567. https://doi.org/10.1016/B978-044450756-3/50006-X

Fairall CW, Bradley EF, Hare JE, Grachev AA, Edson JB (2003) Bulk parameterization of air-sea fluxes: Updates and verification for the COARE algorithm. J Clim 16(4):571–591

Fletcher J, Mason S, Jakob C (2016) The climatology, meteorology, and boundary layer structure of marine cold air outbreaks in both hemispheres. J Clim 29(6):1999–2014. https://doi.org/10.1175/JCLI-D-15-0268.1

Føre I, Kristjánsson JE, Saetra Ø, Breivik Ø, Røsting B, Shapiro M (2011) The full life cycle of a polar low over the norwegian sea observed by three research aircraft flights. Q J R Meteorol Soc 137(660):1659–1673. https://doi.org/10.1002/qj.825

Grossman RL, Betts AK (1990) Air-sea interaction during an extreme cold air outbreak from the eastern coast of the United States. Mon Weather Rev 118(2):324–342

Hartmann J, Kottmeier C, Raasch S (1997) Roll vortices and boundary-layer development during a cold air outbreak. Boundary-Layer Meteorol 84:45–65. https://doi.org/10.1023/A:1000392931768

Holzworth GC (1964) Estimates of mean maximum mixing depths in the contiguous United States. Mon Weather Rev 92(5):235–242

Hu Y, Ecke RE, Ahlers G (1995) Time and length scales in rotating Rayleigh-Bénard convection. Phys Rev Lett 74:5040–5043. https://doi.org/10.1103/PhysRevLett.74.5040

JPL (2015) GHRSST level 4 MUR Global Foundation Sea Surface Temperature analysis (v4.1), accessed 2020-01-27. https://doi.org/10.5067/GHGMR-4FJ04

LeMone MA (1973) The structure and dynamics of horizontal roll vortices in the planetary boundary layer. J Atmos Sci 30(6):1077–1091

Lohse D, Xia KQ (2010) Small-scale properties of turbulent Rayleigh-Bénard convection. Annu Rev Fluid Mech 42(1):335–364

Maahn M, Kollias P (2012) Improved micro rain radar snow measurements using Doppler spectra post-processing. Atmos Meas Tech 5(11):2661–2673. https://doi.org/10.5194/amt-5-2661-2012

Papritz L, Pfahl S (2016) Importance of latent heating in mesocyclones for the decay of cold air outbreaks: a numerical process study from the pacific sector of the southern ocean. Mon Weather Rev 144(1):315–336. https://doi.org/10.1175/MWR-D-15-0268.1

Papritz L, Sodemann H (2018) Characterizing the local and intense water cycle during a cold air outbreak in the nordic seas. Mon Weather Rev 146(11):3567–3588. https://doi.org/10.1175/MWR-D-18-0172.1

Papritz L, Spengler T (2017) A lagrangian climatology of wintertime cold air outbreaks in the Irminger and Nordic seas and their role in shaping air-sea heat fluxes. J Clim 30(8):2717–2737. https://doi.org/10.1175/JCLI-D-16-0605.1

Pfahl S, Sodemann H (2014) What controls deuterium excess in global precipitation? Clim Past 10:771–781. https://doi.org/10.3929/ethz-b-000082937

Pinton JF, Labbé R (1994) Correction to the taylor hypothesis in swirling flows. J Phys II France 4(9):1461–1468. https://doi.org/10.1051/jp2:1994211

Renfrew IA, Moore GWK (1999) An extreme cold-air outbreak over the Labrador sea: Roll vortices and air-sea interaction. Mon Weather Rev 127(10):2379–2394

Renfrew IA, Pickart RS, Våge K, Moore GWK, Bracegirdle TJ, Elvidge AD, Jeansson E, Lachlan-Cope T, McRaven LT, Papritz L, Reuder J, Sodemann H, Terpstra A, Waterman S, Valdimarsson H, Weiss A, Almansi M, Bahr F, Brakstad A, Barrell C, Brooke JK, Brooks BJ, Brooks IM, Brooks ME, Bruvik EM, Duscha C, Fer I, Golid HM, Hallerstig M, Hessevik I, Huang J, Houghton L, Jónsson S, Jonassen M, Jackson K, Kvalsund K, Kolstad EW, Konstali K, Kristiansen J, Ladkin R, Lin P, Macrander A, Mitchell A, Olafsson H, Pacini A, Payne C, Palmason B, Pérez-Hernández MD, Peterson AK, Petersen GN, Pisareva MN, Pope JO, Seidl A, Semper S, Sergeev D, Skjelsvik S, Søiland H, Smith D, Spall MA, Spengler T, Touzeau A, Tupper G, Weng Y, Williams KD, Yang X, Zhou S (2019) The iceland greenland seas project. Bull Am Meteorol Soc 100(9):1795–1817. https://doi.org/10.1175/BAMS-D-18-0217.1

Renfrew IA, Barrell C, Elvidge AD, Brooke JK, Duscha C, King JC, Kristiansen J, Cope TL, Moore GWK, Pickart RS, Reuder J, Sandu I, Sergeev D, Terpstra A, Våge K, Weiss A (2021) An evaluation of surface meteorology and fluxes over the Iceland and Greenland seas in ERA5 reanalysis: the impact of sea ice distribution. Q J R Meteorol Soc 147(734):691–712. https://doi.org/10.1002/qj.3941

Salesky ST, Chamecki M, Bou-Zeid E (2017) On the nature of the transition between roll and cellular organization in the convective boundary layer. Boundary-Layer Meteorol 163:41–68. https://doi.org/10.1007/s10546-016-0220-3

Seibert P, Beyrich F, Gryning SE, Joffre S, Rasmussen A, Tercier P (2000) Review and intercomparison of operational methods for the determination of the mixing height. Atmos Environ 34(7):1001–1027. https://doi.org/10.1016/S1352-2310(99)00349-0

Sodemann H (2021) Iceland Greenland seas Project (IGP): precipitation measurements from the university of bergen micro rain radar (MRR2) on board the nato research vessel alliance. Centre for Environmental Data Analysis. https://catalogue.ceda.ac.uk/uuid/dc723f82939843f199fff78778d5b8d0

Sodemann H, Weng Y (2022) Iceland-Greenland Seas Project (IGP): water isotope measurements from the University of Bergen vapour isotope analyzer on board the NATO Research Vessel Alliance within SNOWPACE. NERC EDS Centre for Environmental Data Analysis, 09 March 2022. https://doi.org/10.5285/705abc2d9988444ba79e942f22219bc0

Stull RB (1988) An introduction to boundary layer meteorology. Springer, Dordrecht. https://doi.org/10.1007/978-94-009-3027-8

Thurnherr I, Hartmuth K, Jansing L, Gehring J, Boettcher M, Gorodetskaya I, Werner M, Wernli H, Aemisegger F (2020) The role of air-sea fluxes for the water vapour isotope signals in the cold and warm sectors of extratropical cyclones over the southern ocean. Weather Clim Dyn Discuss 2020:1–42. https://doi.org/10.5194/wcd-2020-46

Paper III

Observing atmospheric convection with dual-scanning lidars

Christiane Duscha, Juraj Pálenik, Thomas Spengler, Joachim Reuder
Atmospheric Measurement Techniques, **16/5103–5123** (2023)
https://doi.org/10.5194/amt-16-5103-2023

Atmos. Meas. Tech., 16, 5103–5123, 2023
https://doi.org/10.5194/amt-16-5103-2023

Atmospheric Measurement Techniques
Open Access

Observing atmospheric convection with dual-scanning lidars

Christiane Duscha[1,3], **Juraj Pálenik**[2,3], **Thomas Spengler**[3], **and Joachim Reuder**[1,3]

[1]Geophysical Institute, University of Bergen, and Bergen Offshore Wind Centre, Bergen, Norway
[2]Department of Informatics, University of Bergen, Bergen, Norway
[3]Geophysical Institute, University of Bergen, and Bjerknes Centre for Climate Research, Bergen, Norway

Correspondence: Joachim Reuder (joachim.reuder@uib.no)

Received: 10 February 2023 – Discussion started: 20 February 2023
Revised: 3 July 2023 – Accepted: 18 September 2023 – Published: 3 November 2023

Abstract. While convection is a key process in the development of the atmospheric boundary layer, conventional meteorological measurement approaches fall short in capturing the evolution of the complex dynamics of convection. To obtain deeper observational insight into convection, we assess the potential of a dual-lidar approach. We present the capability of two pre-processing procedures, an advanced clustering filter instead of a simple threshold filter and a temporal interpolation, to increase data availability and reduce errors in the individual lidar observations that would be amplified in the dual-lidar retrieval. To evaluate the optimal balance between spatial and temporal resolution to sufficiently resolve convective properties, we test a set of scan configurations. We deployed the dual-lidar setup at two Norwegian airfields in a different geographic setting and demonstrate its capabilities as a proof of concept. We present a retrieval of the convective flow field in a vertical plane above the airfield for each of these setups. The advanced data filtering and temporal interpolation approaches show an improving effect on the data availability and quality and are applied to the observations used in the dual-lidar retrieval. All tested angular resolutions captured the relevant spatial features of the convective flow field, and balance between resolutions can be shifted towards a higher temporal resolution. Based on the evaluated cases, we show that the dual-lidar approach sufficiently resolves and provides valuable insight into the dynamic properties of atmospheric convection.

1 Introduction

Convection plays a key role in the redistribution of energy, heat, moisture, momentum, and matter in the atmospheric boundary layer. Convection also contributes to the deepening of the boundary layer, the formation of convective clouds, and the generation of precipitation (Stull, 1988; Emanuel, 1994). Accurately resolving or parameterizing convection in our weather and climate models is thus of great importance. However, the adequate physical and dynamical representation of atmospheric convection in our models remains challenging (Siebesma et al., 2007; Prein et al., 2017). Conventional meteorological instrumentation usually provides in situ point measurements, profiles (meteorological masts, radiosondes, or ground-based remote sensing), or measurements along an aircraft track of limited spatiotemporal resolution and coverage. Given the complex three-dimensional and short-lived nature of convection, such conventional instrumentation setups are often unsuitable to constrain or validate convection parameterization schemes (Kunkel et al., 1977; Geerts et al., 2018). Instead, we must resort to large-eddy simulations (LESs) that resolve the three-dimensional dynamics of convection to guide such parameterizations (Brown et al., 2002; Siebesma et al., 2007). However, LESs used to constrain the convection parameterization schemes also lack sophisticated observations to be validated against. Hence, there is a demand for high-resolution and long-term observations of the multidimensional character of convection. We introduce a combined measurement and processing technique to achieve observations that cover the spatial and temporal scales necessary to resolve convection. We present and assess this novel methodology based on a dual-

Published by Copernicus Publications on behalf of the European Geosciences Union.

scanning lidar retrieval combined with an advanced filtering and a temporal interpolation approach.

Early aerosol–backscatter lidar observations demonstrated the potential of scanning lidars to capture the size and life cycle of convective thermals in the boundary layer (Kunkel et al., 1977). Lidar technology has advanced significantly since then with substantially increased spatial and temporal resolution. In addition to aerosol and cloud–particle backscatter, Doppler lidar can also obtain the wind velocity field projected onto the lidar's beam. Lidar scan configurations and setups have been developed and optimized to retrieve wind vector profiles (e.g., Werner, 2005; Calhoun et al., 2006) or even in multidimensional space when combining multiple instruments (e.g., Newsom et al., 2005, 2008; Iwai et al., 2008; Stawiarski et al., 2013; Whiteman et al., 2018; Wildmann et al., 2018; Haid et al., 2020; Adler et al., 2020, 2021).

Single profiling lidars are able to capture properties of convective structures that move over the instrument within timescales that are shorter than the life cycle of the convective structures (Duscha et al., 2022). However, these structures are mainly found in the marine boundary layer under extreme atmospheric conditions in the presence of strong advection. Over land, however, convection is often more localized and the timescale of horizontal displacements by advection is usually slower than the life cycle of the convective structures (Kunkel et al., 1977). Hence, a more advanced approach is required to sample these land-based convective structures. In our study, we propose and evaluate the potential of a dual-lidar setup that obtains the convective flow field in a vertical two-dimensional cross-section.

There have been attempts to characterize convection with such dual-Doppler lidar setups. Röhner and Träumner (2013) evaluated variance profiles of convection with a dual-lidar setup in a vertical plane. However, they only utilize certain points along two lines within this cross-section and thus do not make use of the entire plane. Iwai et al. (2008) present a retrieval of all three wind components of the convective flow field on a three-dimensional Cartesian grid using a set of overlapping near-horizontal planes of two scanning lidars and assuming continuity to retrieve the vertical wind component. The timescale to obtain one retrieval based on a full set of scans, however, exceeds the typically expected life cycle of the convective structures of interest, thereby limiting its assessment.

Motivated by the shortcomings of earlier attempts, we develop and optimize a methodology for the use of dual-scanning Doppler lidars to probe atmospheric convection. Superior to conventional meteorological instrument setups, this dual-lidar approach extends the observations of the convective boundary layer by a spatial dimension. We investigate the performance of the proposed measurement and processing technique to capture convective structures and sufficiently resolve essential characteristics of the convective flow field in space and time. We define the following criteria to achieve this goal: the dual-lidar retrieval should resolve convective circulation in sufficient detail on the Cartesian retrieval grid; the retrieval section should extend at least over one wavelength of the convective circulation such that both updraft and downdraft are captured; the retrieval of the flow field should be continuous and undisturbed by noise or erroneous features; though the emphasis is on the performance of the approach in space, it should not be at the cost of sufficient temporal resolution needed to describe the evolution of the convective circulation. We evaluate the performance of the proposed dual-lidar approach and evaluate the benefit of improved filtering and temporal interpolation of the lidar scans as a proof of concept based on two cases obtained during convective days at two small airports in Norway.

Evaluating the potential of the dual-lidar approach to accurately sample the convective flow is a part of the gLidar project (Pálenik, 2022). The project aims to enhance sampling capacity and understanding of convection by combining Eulerian (lidar) and Lagrangian observations. The latter are based on voluntary observing pilots of sailplanes, hang gliders, and paragliders, equipped with instrumentation to measure and log real-time position together with temperature, humidity, and pressure. These gliders utilize convective updrafts to gain altitude and hence also provide vertical convective velocities as well as temperature and humidity anomalies of the convective updraft. Environmental profiles outside the convective updrafts are obtained from parts of the flight track outside convective plumes or from a skydiving airplane that is also equipped with the identical sensors. The collocation of these in situ data, together with the dual-lidar retrievals, is utilized in the empirical convection model by Pálenik et al. (2021) to enhance our process understanding of convection in the atmospheric boundary layer.

2 The experiment

The data collected for this study originate from a similar experimental setup at two sites. The instrumentation installed at these two sites, the measurement strategy of the lidars, which are the main instrumentation of the setup, and the challenges, which were met during the experiment at each site, are introduced in the following sections.

2.1 The sites

We have chosen two small airports in Norway for sailplanes and small motor planes as measurement sites for the dual-lidar experiment. From 12 May until 7 June 2021, we installed two WindCube-100S scanning lidars, an automatic weather station (AWS), and a surface energy balance station (SEBS) at Vaksinen airport, Os, in western Norway, ca. 25 km south of Bergen. The same instrumentation was deployed from 14 July until 30 July 2022 for the second field campaign at Starmoen airport, Elverum, in eastern Norway, about 120 km northeast of Oslo. Figure 1 shows the mea-

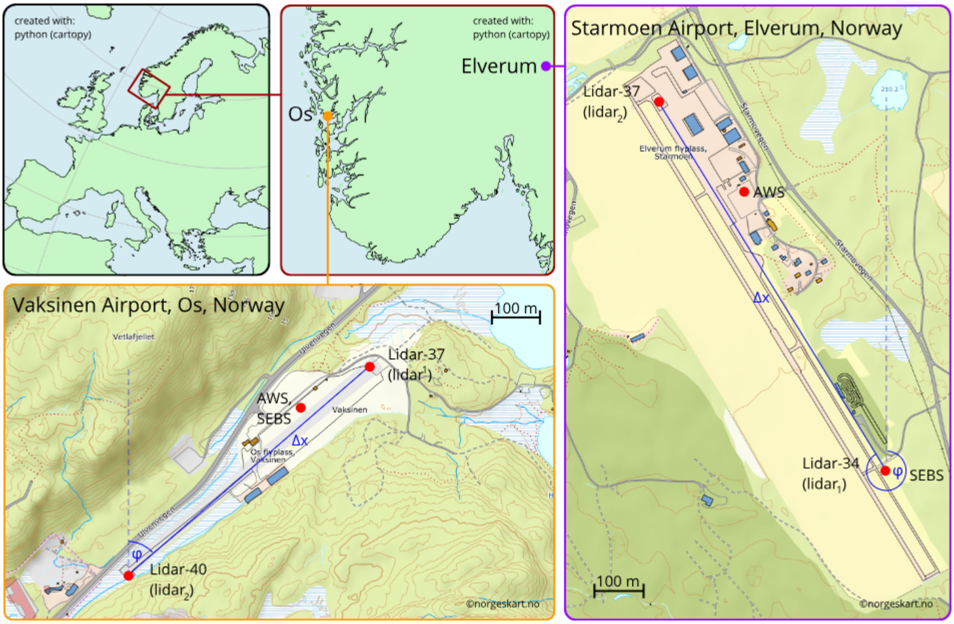

Figure 1. Location of the measurement sites and instrument setup. Top left: overview map of Europe. Top center: zoomed-in view of southern Norway with markers for the location of Os (orange) and Elverum (purple). Bottom left: overview of the measurement site at Vaksinen airport in Os with the locations of the utilized lidars, AWS, and SEBS indicated by red markers as well as distance, Δx, and angle, φ, relative to north between the lidars indicated in blue. Right: overview of the measurement site at Starmoen airport near Elverum with the locations of the utilized lidars, AWS, and SEBS indicated by red markers and Δx and φ indicated in blue.

Table 1. Coordinates (° N, ° E) of the instrumentation at Vaksinen airport and Starmoen airport. The numbering of the lidars corresponds to the respective serial numbers of the WindCube-100S series.

	Vaksinen	Starmoen
Lidar-34	Not installed	60.874353, 11.6793316
Lidar-37	60.1936435, 5.4242786	60.880778, 11.6703844
Lidar-40	60.1891728, 5.4166957	Not installed
AWS	60.1926322, 5.4216220	60.8787601, 11.6741224
SEBS	60.1925799, 5.4216013	60.8743419, 11.6794812

surement sites and the location of the instrumentation, and Table 1 documents the coordinates of each instrument.

2.2 The instrumentation

The AWS provides background information on the basic meteorological parameters of pressure, temperature, humidity, wind speed, wind direction, incoming shortwave radiation, and precipitation at 1 min temporal resolution. The SEBS measures the four components of the radiation balance, i.e., incoming and outgoing shortwave and longwave radiation, together with highly resolved (20 Hz) measurements of temperature, humidity, and three-dimensional wind speed, each variable at a single altitude above ground. In addition the SEBS also provided profile measurements of temperature, humidity and wind at 1, 2, and 4 m above the surface at a lower resolution (1 min). In this study, we utilize measurements from AWS and SEBS mainly to identify precipitation-free periods that favor convective conditions throughout the two campaigns and to estimate the surface heat flux (see Sect. 5.2) and flux Richardson number (see Sect. 5.3) as an indication of the presence of convection.

In both campaigns the two scanning lidars were installed with a relative distance, Δx (m), and angle, φ (°), relative to north to each other at opposing ends of the runway of the corresponding airfields (Fig. 1). The lidars observe radial velocity, v_r (m s^{-1}), which is the velocity of the wind projected to the line of sight (LOS) of the lidar beam. The scanning lidars used in the experiment can be programmed to point towards a direction corresponding to a certain azimuth angle, α (°), and an elevation angle, θ (°). For each combination of α and θ, v_r values are simultaneously obtained at several ranges, r (m), from the lidar.

Table 2. Dual-lidar setup specifications for the two sites at Vaksinen airport and Starmoen airport.

	Vaksinen	Starmoen
Δx (m)	669	863
φ (°)	40	326
r_{min} (m)	50	50
r_{max} (m)	3000	3146
Δr (m)	25	25
N_{gates}	119	259
r_{res} (m)	25	12

Table 3. Hourly returning schedule (* starting each hour at MM:SS) of the RHI scan configurations during the Vaksinen and Starmoen campaign.

Site	Return *	D_{run} (min)	v_{scan} ($^{\circ}\,\mathrm{s}^{-1}$)	T_{int} (s)	$\Delta\theta$ (°)	D_{scan} (s)
Vaksinen	10:00	10	1.0	0.5	0.5	150.0
	20:00	10	1.0	1.0	1.0	150.0
	30:00	10	4.0	0.5	2.0	37.5
Starmoen	00:00	50	2.0	0.5	1.0	80.0

Along the lidar beam, each v_{r} value is observed as a composite of the Doppler velocity of all particles, which contribute to the lidar's backscattering signal (e.g., aerosols) within the lidar range gate length, Δr (m). The strength of the particle backscatter is related to the signal-to-noise ratio, SNR (dB), which is also recorded by the lidar. By default, the distance between the range gates, which defines the range gate resolution, r_{res} (m), is equal to Δr. Yet, r_{res} can also be set manually, e.g., smaller than Δr, such that range gates overlap. The minimum range, r_{min} (m), needs to be at least $2 \cdot \Delta r$ and the maximum range, r_{max} (m), is dependent on the number of utilized range gates, N_{gates}, and r_{res}. Table 2 summarizes the lidar parameter specifications utilized during the two campaigns.

2.3 The lidar strategy

We utilized two lidar measurement strategies. In both campaigns, we sampled the three-dimensional wind profile using a Doppler beam swinging mode (DBS) with five consecutive beams: four beams, which are perpendicular at $\alpha = (0^{\circ}, 90^{\circ}, 180^{\circ}, 270^{\circ})$, each with $\theta = 75^{\circ}$. The fifth beam points upward with $\theta = 90^{\circ}$. The DBS is programmed to run for a duration, D_{run}, of 10 min within each hour. We retrieve an average of the wind profile over these 10 min, which we assume to be the representative profile for the corresponding hour.

The main strategy of the experiment aims to enable a retrieval of the plane-parallel horizontal and the vertical velocity components, u and w ($\mathrm{m\,s^{-1}}$), in a vertical cross-section above the runway of each airport. As displayed in Fig. 2, this is achieved by range height indicator (RHI) scanning patterns performed by each lidar. Here, the lidar points horizontally to the complementing lidar (lidar$_1$: $\alpha = \varphi$, lidar$_2$: $\alpha = \varphi + 180^{\circ}$, with $\theta = 0^{\circ}$ orientation in the direction of φ) and then performs a continuous scan by changing θ (lidar$_1$: from $\theta = 0$ to 150°, lidar$_2$: $\theta = 180$ to 30°). The accuracy of the horizontal (azimuth) alignment was ensured by a hard-target calibration of each lidar at the start of the campaigns. We utilize a retrieval to estimate u and w from overlapping RHI scans of the two lidars in the vertical cross-section above the runway. The retrieval combines v_{r} values of the two lidars with different polar coordinate systems and achieves u and w values on a Cartesian grid (see Fig. 2). We document further details of this retrieval method and its shortcomings in Sect. 3.

Convection is a dynamic process, which may rapidly modify u and w on short timescales and small spatial scales. It is therefore an important goal of this study to investigate the combination of temporal and spatial RHI scan resolution that accurately captures the development of the convective circulation. The combination of the following parameters determines the temporal and spatial resolution of a single RHI scan. The scan speed, v_{scan} ($^{\circ}\,\mathrm{s}^{-1}$), determines the duration, D_{scan} (s), of a single RHI scan, which spans a certain range of θ (i.e., 150° from $\theta = 30^{\circ}$ to $\theta = 180^{\circ}$). The product of v_{scan} and the integration time, T_{int} (s), of the Doppler velocities that contribute to a single v_{r} values determines the angular resolution, $\Delta\theta$ (°), of the RHI scan.

High angular (spatial) resolution can be achieved with a low v_{scan} at the cost of a long D_{scan} and hence a low temporal resolution when keeping the angular range and T_{int} constant. On the other hand, by decreasing T_{int}, the angular resolution can be increased without changing v_{scan} and consequently without sacrificing temporal resolution for covering the same angular range in a scan. However, short T_{int} can result in poor quality of the measured data due to low SNR.

During the two campaigns, we tested different scanning configurations with varying balance between temporal and spatial resolutions, as well as integration time. These configurations are summarized in Table 3.

A major goal of the Vaksinen campaign was to evaluate the ability of different scan configurations to accurately map convection. At Vaksinen airport, several scanning patterns with either high temporal or high spatial resolution were run in sequence within a 1 h return period: first the wind profile was observed with a DBS scan for 10 min. Then the three scan configurations introduced in Table 3 were subsequently scheduled for 10 min each. This was followed by a series of fixed, out-of-plane RHI and plan position indicator (PPI) scans for 20 min. These latter scan configurations of the experiment are, however, not relevant for this study and thus not further described.

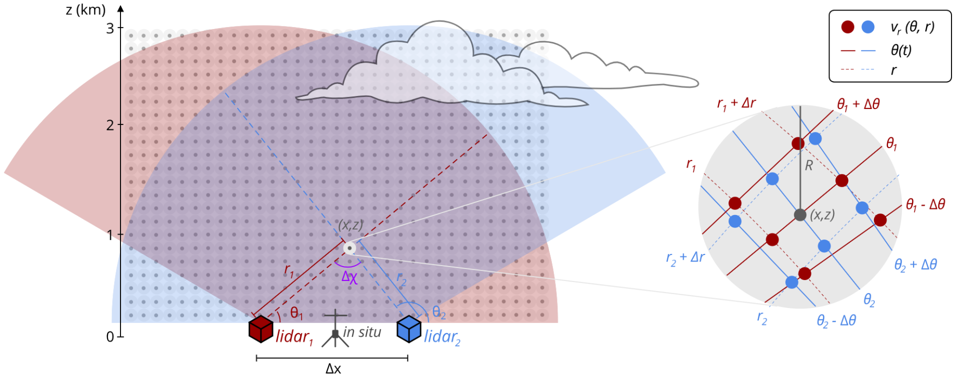

Figure 2. Vertical cross-section of the dual-lidar setup utilized during the campaigns at Vaksinen airport and Starmoen airport, respectively. The transparent red and blue surface areas represent the angular range covered by the RHI scans of the individual lidars, which are represented by the red and blue boxes. The dark grey dots represent a schematic of the Cartesian retrieval grid. A zoom in on to the polar grid of the two lidars and the corresponding positions of all v_r values used for the retrieval of u and w in an exemplary point (x, z) of the Cartesian grid is shown on the right-hand side of the figure.

At Starmoen airport, we aimed to study the evolution of convection more continuously than during the Vaksinen airport campaign, utilizing longer D_{run} and sampling with only one scan configuration throughout the campaign (see Table 3). The RHI scan configuration is scheduled for 50 min, followed by a 10 min DBS scan. This schedule is repeated by each of the two lidars with a return period of 60 min throughout the campaign. The scan configuration chosen here is a compromise between the extremes of temporal or spatial resolution utilized during the Vaksinen campaign.

2.4 The challenges

During both campaigns, we encountered various challenges that affected the availability and quality of the data. At the Vaksinen airport site, there were several power outages that disordered the schedule of lidar-37 (northeastern end of Vaksinen airport, see Fig. 1), demanding a manual fix on site. This led to a substantial loss of data during several convective days, as the failure was first detected after a site visit. Also, the data download from the internal computer of the lidars was very slow, which delayed full recovery of the data, processing, and the identification of further problems occurring during the campaign until after the recovery of the instrumentation from the field. Despite the challenges encountered, we were able to secure representative observations from both lidars simultaneously during 1 very convective day (28 May 2021), which will be evaluated and discussed in Sect. 6.

As a consequence of the challenges during the Vaksinen airport campaign, we developed an upgraded version of our lidar setup. During the Starmoen campaign, the data were not only stored on the internal computer of the lidars, but also transferred via “sftp” protocol to a Raspberry Pi 4 Model B[1]. The Raspberry Pi was integrated into a remote access system developed by the Geophysical Institute, University of Bergen, and solved the problem of the slow data download. The remote access system also includes an industrial router, which enabled real-time data upload and visualization of the lidar observations on a server provided by the Norwegian Research and Education Cloud (NREC[2]), as well as a time synchronization of the lidars independent from GPS. This enabled us to identify and already fix problems occurring during the campaign and ensured that the schedule of the lidar program was kept throughout the campaign. A future application of this remote access system includes, among others, remote control and programming of the lidar in the field.

Nonetheless, the period of installation at Starmoen airport was impacted by several precipitation events during the first half of the campaign, which almost completely depleted the aerosol content in the boundary layer. This strongly reduced the SNR obtained by the lidars and hence the reliability of the observed v_r. It required several convective days after the precipitation period for the SNR to increase such that sufficient data availability of v_r for processing and data analysis was achieved. After the precipitation period during the Starmoen campaign, mainly 1 convective day (29 July 2022) with weak synoptic wind and strong fluxes qualified for further detailed analysis (see Sect. 6).

---

[1] see https://www.raspberrypi.com (last access: 21 March 2022)
[2] see https://www.nrec.no (last access: 5 April 2022)

3 Retrieval of the two-dimensional wind field

To retrieve the u and w wind components for any point (x,z) in the lidar cross-section at discrete points in time, we combine pre-processed v_r fields (see Sect. 4) from both lidars. The temporal resolution of the retrieved cross-sections is the same as the temporal resolution of the utilized v_r fields. As we save the v_r fields once per 1 s or even once per 0.5 s (see T_int in Table 3), we can retrieve u and w fields at any lower resolution that fits the purpose of interest. The methodology to estimate u and w from independent v_r observations and the errors connected to the method are documented in the two subsections below.

3.1 Retrieval principle

At any position (x,z) within the vertical cross-section of the overlapping RHI scans, v_r is related to the instantaneous u and w components of the real wind projected to the θ-dependent LOS of the lidar beam,

$$v_\mathrm{r}(x,z) = u(x,z)\cdot\cos\theta + w(x,z)\cdot\sin\theta, \tag{1}$$

with (x,z) connected to θ and r by

$$\begin{pmatrix} x \\ z \end{pmatrix} = r\begin{pmatrix} \cos\theta \\ \sin\theta \end{pmatrix} + \begin{pmatrix} x_0 \\ z_0 \end{pmatrix}, \tag{2}$$

where x_0 and z_0 define the relative position of the lidar to the origin point $(0,0)$ of the Cartesian coordinate system of choice for the retrieval. We set the location of the origin point at the individual ground level of the two sites in the middle of the two lidars.

To solve Eq. (1) for u and w in the point (x,z), we need to construct an equation system utilizing at least two observations of v_r, each obtained with an independent θ. Since lidars do not operate on a Cartesian coordinate system (x,z) but on individual polar coordinate systems (θ,r), there are very few combinations of θ and r for the two lidars for which the v_r observations fall into exactly the same point (x,z) in space (see Fig. 2). Still, retrieving the u and w on a Cartesian instead of a polar retrieval grid is a common approach to merge the observations of two lidars (e.g., Stawiarski et al., 2013; Adler et al., 2020; Haid et al., 2020).

Here, instead of using only two independent v_r observations in a single point (x,z), we construct an equation system (based on Eq. 1), containing all valid v_r values (excluding "not a number" or NaN values) and their individual dependencies on r and θ, from the two lidars within a radius, R, around the Cartesian point (x,z) of interest (see Fig. 2).

$$\begin{pmatrix} v_{r1}(r_1,\theta_1) \\ v_{r2}(r_2,\theta_2) \\ \cdot \\ \cdot \\ v_{rn}(r_n,\theta_n) \end{pmatrix} = \begin{pmatrix} \cos\theta_1 & \sin\theta_1 \\ \cos\theta_2 & \sin\theta_2 \\ \cdot & \cdot \\ \cdot & \cdot \\ \cos\theta_n & \sin\theta_n \end{pmatrix} \begin{pmatrix} u \\ w \end{pmatrix} \tag{3}$$

The equation system can also be written in vector and matrix format.

$$\boldsymbol{v}_\mathrm{r} = \mathbf{N}\,\boldsymbol{v} \tag{4}$$

If more than two independent v_r observations are within R to construct the equation system, it is over-constrained. To solve the over-constrained equation system which results from using R, we apply a least-squares approach (see Lai et al., 1978; Cherukuru et al., 2015) using matrix inversion:

$$\hat{\boldsymbol{v}} = \left(\mathbf{N}^T\mathbf{N}\right)^{-1}\mathbf{N}^T\boldsymbol{v}_\mathrm{r}, \tag{5}$$

where $\hat{\boldsymbol{v}}$ is the best fit of $\boldsymbol{v}$ considering all utilized v_r observations. Note that u and w are only retrieved if there is at least one valid v_r value provided by each lidar within R; otherwise, u and w are set to NaN in the corresponding Cartesian grid point.

It is also possible to incorporate v_r observations within a temporal radius, T_r, around the point of interest in time into the over-constrained equation system discussed above (see Newsom et al., 2008). Yet, the usage of T_r rather represents a temporal average of the flow field and is not meaningful when using instantaneous RHI scans which result from the temporal interpolation (see Sect. 4.2).

3.2 Retrieval errors and uncertainties

There are several sources of errors and uncertainties, which need to be considered for dual-lidar retrievals. Many errors in the single-lidar observation are projected and amplified in the co-planar, dual-lidar retrieval, e.g., lidar-specific uncorrelated noise and systematic error, as well as imprecise azimuth adjustment or leveling during the lidar setup and calibration (see, e.g., Stawiarski et al., 2013).

We attempt to minimize or avoid the errors and error amplifications that are connected to the dual-lidar retrieval. One prominent error in the dual-lidar retrieval is the temporal under-sampling error: the observations of v_r of the two lidars may each correspond to a different state of u and w due to a difference in the time at which v_r was observed by each lidar. Utilizing v_r values which do not correspond to the same state of u and w in reality will yield retrieved u and w values that may correspond to neither of the wind fields sampled by the individual lidar. The magnitude of the temporal under-sampling error is proportional to the absolute velocity difference in the flow field at the two time steps the two individual lidar obtained v_r (Stawiarski et al., 2013).

$$\sigma_\mathrm{time}(\Delta t) \approx |v_{\mathrm{r}1}(t_1) - v_{\mathrm{r}2}(t_2)| \tag{6}$$

The time difference, $\Delta t = |t_2 - t_1|$, is dependent on the spatial location (x,z) in the dual-lidar cross-section. In Sect. 4.2 we introduce a processing procedure to minimize the temporal under-sampling error using instantaneous RHI cross-sections achieved from temporal interpolation instead of single scans.

A further reduction of this error can be related to the usage of R and over-constrained equation systems to retrieve u and w for each point on the Cartesian grid. Here, temporal errors caused by small spatial displacement (within R) between two scans are averaged out.

For certain conditions the equation system (see Eq. 4) is ill-posed. In the case that the angles θ_1 and θ_2 of the two intersecting lidar beams are both close to horizontal or close to vertical, the v_r observations are not really independent. This is the case for $\Delta\chi = |\theta_1 - \theta_2|$, which is either very small or very large (see Fig. 2). When the two lidars are both pointing horizontally, the horizontal component dominates the v_r observations of both lidars and the retrieval error of w is amplified. In this case $\Delta\chi$ is either large (beams point towards each other) or small (both beam point in the same direction horizontally). Mainly vertically pointing beams result in small $\Delta\chi$ and will amplify the retrieval error of u. Yet, with a sufficiently large Δx, which is the case for our setups, the point at which the retrieval error of u becomes important is located above the retrieval grid. The amplification of the retrieval error, depending on $\Delta\chi$, is defined by the factor σ_amp (see Stawiarski et al., 2013):

$$\sigma^i_\mathrm{amp} = \sigma_\mathrm{amp} \cdot \sigma^i = \frac{1}{\sin^2(\Delta\chi)} \cdot \sigma^i, \tag{7}$$

where σ^i is a placeholder for any single- or dual-lidar error (e.g., the temporal under-sampling error). We remove all retrieved values of w that correspond to $\Delta\chi > 150°$ and $\Delta\chi < 30°$ to avoid strongly amplified single- and dual-lidar errors in the retrieval, such as those errors discussed in the paragraphs above.

Utilizing an over-constrained equation system enables quantifying the uncertainty in the retrieved wind field. The least-squares retrieval yields the best fit and hence a single retrieved value $\hat{u}$ or $\hat{w}$. By projecting these retrieved $\hat{u}$ and $\hat{w}$ values back onto the LOS (see Eq. 1), which yields a single value $v_\mathrm{r}(\hat{u}, \hat{w})$ for each grid point (x, z), we can estimate the root mean square error, RMSE (m s^{-1}).

$$\mathrm{RMSE} = \sqrt{\frac{1}{N}\sum_{n=1}^{N} \left| v_\mathrm{r}(\theta_n, r_n) - v_\mathrm{r}\left(\hat{u}, \hat{v}\right)\right|^2} \tag{8}$$

The RMSE is estimated on the basis of all N points of v_r within each R. This metric is useful to identify regions where processes are averaged over the area covered by R on the discrete Cartesian retrieval grid or where the temporal interpolation (Sect. 4.2) is not able to accurately restore the dynamic behavior of the convective circulation.

4 Processing of dual-scanning lidar observations

Before combining the v_r values from the two lidars into the u and w wind components, the RHI scan data from individual instruments require processing. In particular, the data need to be filtered for noise and erroneous features. After filtering, we apply temporal gap filling using interpolation by replacing discarded data points, and achieve instantaneous RHI scans with an increased temporal resolution.

4.1 Radial velocity filtering

We apply v_r data filtering to all utilized lidar scanning patterns (RHI and DBS). In a first step, we remove all v_r observations with absolute values exceeding 30 m s^{-1}, as they are unrealistically high for convective conditions. Further, we have observed three types of problems with the data: individual data points with noise; larger irregular "streak" patterns in the RHI scans, which can be associated with range-folded ambiguities as described by Bonin and Brewer (2017); and irregular patterns, which result from interaction with obstacles. For the retrieval (Sect. 3) to work, it is critical to remove the areas with points that correspond to these erroneous features and large spatial patches of noise. We address these problems by using the Density-Based Spatial Clustering of Applications with Noise (DBSCAN) algorithm, which was previously used by Alcayaga (2020) to filter PPI scans of Doppler lidar observations. In contrast to conventional filters, this clustering algorithm does not apply a fixed threshold to either SNR or v_r. Instead, the DBSCAN algorithm detects clusters of dense data points characterized by both v_r and SNR. Therefore, it can distinguish between reasonable v_r observations and noise in the same SNR range. This allows for the recovery of reliable v_r values for SNR values even below −30 dB, which would be lost if the SNR threshold of −27 dB that is suggested by the lidar manufacturer (Leosphere) were applied.

We use the implementation of the DBSCAN algorithm in the "scipy" Python package (Virtanen et al., 2020) to identify clusters of data points in the SNR–v_r space. Figure 3 displays the application of the DBSCAN filter for one example RHI scan obtained during the Starmoen campaign on 29 July 2022 starting at 14:20 UTC.

Here, v_r is scattered against SNR and data points which are identified as reasonable by the DBSCAN filter (dense scatterers) are highlighted in blue, while data points identified as noise (rarefied scatterers) are displayed in grey. In addition, we highlighted scatterers in mint that correspond to features in the scan, though it should be noted that here these features fall into the same rarefied DBSCAN cluster as the noise.

The DBSCAN algorithm clusters scatterers as dense (cluster) or non-dense (noise) depending on a density radius, ϵ, and minimum number of samples, n_sample. Our criterion for choosing a combination of ϵ and n_sample was, apart from the noise, that only one main cluster was identified and any secondary cluster needed to be separated from that main cluster by at least 3ϵ. The same ϵ and n_sample need to fulfill this criterion for all scans of the same sample size and hence for all scans using the same scan configuration. To determine the

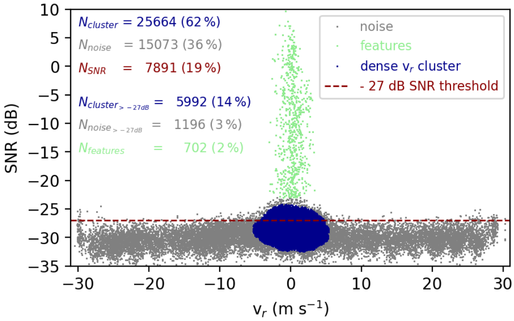

Figure 3. Scatter of v_r against SNR, with a DBSCAN-identified cluster of dense scatterers (valid v_r) marked in blue, rarefied scatterers (noise) marked in grey, and rarefied scatterers corresponding to features marked in mint. The number of points (and the percentage relative to all data) classified as noise (N_noise, grey), features (N_features, mint), and clusters of reasonable points (N_cluster, blue) are documented in the upper left corner. The dashed red line indicates the −27 dB SNR threshold. Values of v_r corresponding to SNR values below this line are discarded by the SNR filter. N_SNR (red) corresponds to the number of points (and percentage relative to all data) recovered by the SNR filter, while $N_{\mathrm{cluster}_{>-27\,\mathrm{dB}}}$ (blue) and $N_{\mathrm{noise}_{>-27\,\mathrm{dB}}}$ (grey) correspond to the number of scatterers (and percentage relative to all data) recovered by the SNR filter but attributed to the points corresponding to noise and reasonable values by the DBSCAN filter, respectively.

parameters for each scan configuration, we kept ϵ constant and adjusted n_sample according to the change in absolute sample size. For RHI scans the DBSCAN algorithm with corresponding ϵ and n_sample was applied to each cross-section individually, while for the DBS scans, the DBSCAN algorithm was applied to the 10 min time series of each beam direction individually. Specific to the number of points sampled in the RHI scan presented here, we apply $\epsilon = 0.6$ and $n_\mathrm{sample} = 150$.

For the example displayed in Fig. 3, the DBSCAN algorithm identifies a cluster of v_r values as reasonable, which makes up 62 % of the observed data points. The remaining 38 % of the data points are classified as noise (36 %) or features (2 %), such as range-folded ambiguities (Bonin and Brewer, 2017), obstacles, and clouds. The majority of noise identified by the DBSCAN algorithm (31 %) is evident just below SNR = −27 dB, where v_r fluctuates $\pm 30\,\mathrm{m\,s^{-1}}$. In order to remove noise from the v_r data the conventional SNR threshold is therefore reasonably set to −27 dB. However, when applying the SNR threshold filter to the RHI scan, only 19 % of the v_r values are kept and a large amount of data identified as reasonable by the DBSCAN filter (48 %) are discarded. Further, only 14 % of the data points are both above the SNR threshold and within the cluster identified as reasonable by the DBSCAN algorithm, while 5 % of the data points which are above the SNR threshold are classified as noise (3 %) or irregular erroneous features and clouds (2 %).

Figure 4 shows the RHI cross-sections of v_r values (Fig. 4a) and SNR values (Fig. 4b) that are scattered against each other in Fig. 3, as well as the filtered v_r values using the SNR threshold (Fig. 4c) and using the DBSCAN algorithm (Fig. 4d). This depiction allows us to investigate the ability of the SNR threshold filter as well as the DBSCAN filter to discard noise and erroneous features, while retaining valid data points. The situation captured on 29 July 2022 at Starmoen by this RHI scan is convective and rather complex, which is evident mainly from the convergence of the horizontal velocity close to the surface around the $x = -1$ km horizontal of distance mark, visible in the non-filtered v_r data (Fig. 4a). The obtained SNR is very low (below −27 dB) both close to lidar and at a larger range (Fig. 4b). For r beyond ≈ 2 km distance from the lidar the originally observed v_r values (Fig. 4a) are irregular and noisy, while they appear rather regular close to the lidar despite the comparable low SNR (Fig. 4b). Only for r between 0.8 and 1.8 km from the lidar is the SNR increased overall. Additionally, several features of partially irregular v_r values, which correspond to local, strongly increased SNR, are visible (Fig. 4b). We identify range-folded ambiguities around $(x, z) = (1.0, 0.5)$ and $(x, z) = (-3.0, 0.5)$ km, a physical obstacle which blocks the LOS around $(x, z) = (-1.2, 0.0)$ km, and a cloud around $(x, z) = (-2.0, 2.3)$ km. These features are also apparent in the v_r values (Fig. 4a) and highlighted in mint in the RHI cross-section with the DBSCAN filter applied (Fig. 4d).

The SNR threshold filter (Fig. 4c) removes a large number of v_r values within a 1 km radius around the lidar and at r larger than 2 km from the lidar. Yet, erroneous v_r values corresponding to range-folded ambiguities are not filtered out. On the basis of the remaining v_r data, the convective circulation is hardly recognizable. The RHI scan observed during the same time period from the complementary lidar experiences a similar extreme reduction of v_r values when applying the SNR threshold filter (not shown here). As a consequence the region of valid overlapping v_r is even more reduced and will yield an even less valuable retrieval of u and w after applying the SNR threshold filter.

The DBSCAN filter (Fig. 4d), on the other hand, successfully removes noise, which is clearly evident in the non-filtered v_r observations (Fig. 4a) at $r > 2$ km from the lidar. Reasonable v_r values with SNR < -27 dB, which follow the same radial velocity patterns as the surrounding non-noisy points that are above the −27 dB threshold, are not filtered close to the lidar or at larger distances. In contrast to the SNR threshold filter (Fig. 4c) the information about the convective flow field is retained by the DBSCAN filter (Fig. 4d). The small number of points attributed to noise above −27 dB by the DBSCAN algorithm (3 %) are distributed over the cross-section and therefore have no relevance for the retrieval performance. Here, a sufficient number of valid v_r values are within R for most Cartesian points covering the convective

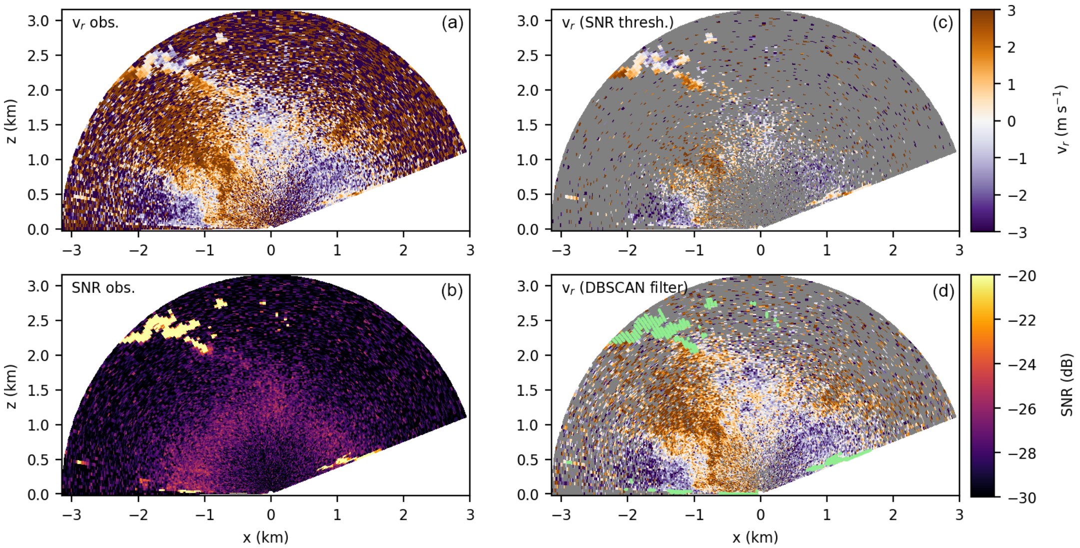

Figure 4. Sample RHI scan from the Starmoen campaign on 29 July 2022 at 14:20 UTC with **(a)** observed v_r, **(b)** observed SNR, **(c)** filtered v_r using an SNR threshold, and **(d)** filtered v_r using the DBSCAN clustering algorithm. Grey areas correspond to filtered values flagged as NaN by the **(c)** SNR threshold filter or the **(d)** DBSCAN filter. Features also flagged as NaN by the DBSCAN filter are highlighted in mint.

circulation. Further, most range-folded ambiguities and features caused by blocking of LOS by obstacles are removed from the data. Unfortunately, this also includes parts of the data points obtained within clouds, which is of interest for the convective circulation. Still, the gain of retained data points corresponding to the convective circulation (48 %) within the boundary layer outweighs the loss of data points within the cloud (< 2 %) at the edge of the circulation achieved by the DBSCAN filter.

The example presented in Figs. 3 and 4 corresponds to conditions with comparably low aerosol content due to preceding periods with precipitation during the Starmoen campaign. Considering the composite of relevant RHI scans throughout the convective day at Starmoen (29 July 2022) which is presented in this study, the DBSCAN filter discards 61 % (and retains 39 %) of data points, while the SNR filter discards 85 % (and retains only 15 %) of data points. The lower recovery rates compared to the presented example are mainly due to lower boundary layer depths at earlier hours during the day (see Sects. 5.1 and 6.1). During the Vaksinen campaign, we did not sample any precipitation event in the period prior to the convective day, which is presented as an example case in this study. As a consequence, aerosols could accumulate in the boundary layer, and SNR was comparably high. Filtering by DBSCAN (discarded: 38 %, retained: 62 %) and SNR threshold (discarded: 60 %, retained: 40 %) yielded comparably lower rates of removal for the evaluated convective day at Vaksinen (28 May 2021). Even lower and more similar removal rates are found for the DBSCAN filter (discarded: 19 %, retained: 81 %) and the SNR threshold filter (discarded: 23 %, retained: 77 %) on 28 May 2021 when considering only the filtered values within the boundary layer (for boundary layer depth estimation see Sect. 5.1). Here, the DBSCAN filter outperforms the SNR threshold filter, mainly by removing noise and range-folded ambiguities which are also present at SNR > -27 dB.

Due to the improved data quality and availability, we prepare the v_r data for further processing by applying the DBSCAN filter to each RHI scan (and DBS scan series) throughout the evaluated convective days of both campaigns. Since the DBSCAN algorithm is relatively costly in terms of computational power, we store the filtered data in hourly NetCDF files, along with the other relevant variables observed by the lidar. This dataset is utilized in the following processing step.

4.2 Temporal interpolation

Dependent on the scan configuration (Table 3), each individual RHI scan takes a few tens of seconds up to 2.5 min. Consequently, the RHI scans used for the reconstruction of the wind field between the two lidars are not instantaneous snapshots of the radial velocity field. Only the observations along the beam of a single θ correspond to the same time step within the same RHI scan. Even if the RHI scans of the two lidars are perfectly synchronized, only a very small number of spatially overlapping points in the cross-section (see Fig. 2 and Röhner and Träumner, 2013) are observed without any time lag between the two lidars. For any fixed point in the overlap of the lidar scans, the maximum possible time difference between observations by each lidar is bound by D_{scan}. If the time difference is considerably large, the convective wind field observed as v_{r} at a certain point in the cross-section by one lidar can strongly differ from the wind field observed by the complementing lidar. Such temporal deviation of the v_{r} observations in a given point propagates and is amplified as a temporal under-sampling error in the retrieval of u and w (see Sect. 3.2).

To reduce the impact of the temporally induced error, we test the usage of an instantaneous lidar cross-section, achieved by temporal interpolation. For that, we interpolate linearly between each $v_{\mathrm{r}}(r,\theta,t)$ and $v_{\mathrm{r}}(r,\theta,t+D_{\mathrm{scan}})$, located in the same position in space (r,θ) yet at the time of the next scan $(t+D_{\mathrm{scan}})$. The highest time resolution of the interpolated grid corresponds to one RHI cross-section every T_{scan} of the respective scan configuration (see Table 3). From an interpolated array of v_{r} values (with three dimensions: θ, r, t) we can now extract instantaneous cross-sections, where all v_{r} values correspond to one specific time stamp. Only values corresponding to one single θ are actually observed by the lidar in this scan, and the remaining values are a result of the interpolation. A big advantage of the temporal interpolation is that we can utilize cross-sections from the two lidars that correspond to the exact same t. Hence, when using temporal interpolation, perfect synchronization of the RHI scans of the two lidars is not required. The v_{r} values will still be most accurate around the θ that is observed at the time step to which the instantaneous scan is interpolated. Synchronization of the lidar scans mainly achieves a line of no time lag located along the vertical profile above the mid-point between the two lidars. Yet, convective eddies are not necessarily located directly in the middle of the lidars.

To demonstrate how the maximum possible error of the interpolated scan compares to the maximum possible error between non-interpolated, consecutive scans, we create an interpolated series. To achieve this, we interpolate between every second RHI scan obtained. Here, we actually create two interpolated series based on both the odd and even RHI scans to double the number of interpolated cross-sections. From both of these interpolated series we extract the v_{r} values that correspond to $\theta(t)$ of the RHI scans, which are not used to create an interpolated series. Thus, we can estimate the average difference between an interpolated and the control RHI scan to quantify the error in the interpolated series, e_{int}. It should be mentioned that e_{int} is conservative, as the real interpolation is performed for only the half-time-step of the presented validation method. Also, in contrast to an instantaneous cross-section, here all extracted v_{r} values from the interpolated series correspond to the maximum time lag within the cross-section, which is D_{scan}.

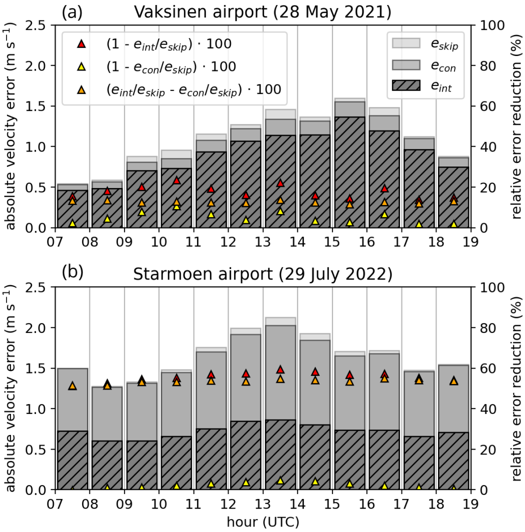

Figure 5. Maximum estimates of the temporal under-sampling errors for consecutive RHI scans (e_{con}) and for every second RHI scan (e_{skip}) as well as the temporal interpolation error (e_{int}) at **(a)** the Vaksinen site on 28 May 2021 between 07:00 and 19:00 UTC and at **(b)** the Starmoen site on 29 July 2022 between 07:00 and 19:00 UTC. For both sites, the error reduction of e_{con} and e_{int} relative to the largest expected error e_{skip} is also displayed with triangles on a secondary right-bound y axis.

In a next step, we want to investigate the difference of e_{int} compared to the conservative temporal under-sampling error of the corresponding RHI scan series. We expect the maximum temporal under-sampling error for points where v_{r} values are measured with the maximum possible time lag of D_{scan} between the data points of two synchronized RHI scans. The average difference between two consecutive scans therefore gives an estimate of the maximum expected temporal under-sampling error, e_{con}, of the RHI scan series. In addition to e_{con}, we also estimate the temporal under-sampling error, merged for odd and evenly skipped RHI scan series, e_{skip}, which is the RHI scan resolution ($\sim 2\cdot D_{\mathrm{scan}}$) we used to estimate the interpolated series on which e_{int} is based. Figure 5 shows time series of these three error estimates e_{skip}, e_{con}, and e_{int}, how much e_{int} decreases in comparison to e_{con}, and how both of these error estimates behave in comparison to e_{skip} for two cases at the Starmoen and the Vaksinen site. We only consider values of the RHI scans which are within the boundary layer and hence below the boundary layer depth; see Sect. 5.1.

For the case on 28 May 2021 at the Vaksinen site (Fig. 5), the error estimates correspond to the scan configuration with the highest temporal scan resolution ($D_{\mathrm{scan}}=37.5$ s). Unfortunately, the other two scan configurations (see Table 3) utilized during the Vaksinen campaign do not provide a sufficient number of RHI scans to estimate a representative estimate of e_{int}.

With enhanced convective activity during the daytime hours, all three error estimates on 28 May 2021 (Fig. 5a) generally increase from 07:00 until 16:00 UTC. Within the early hours of the day (07:00–09:00 UTC), the average total error between consecutive scans is low ($\sim 0.5\,\mathrm{m\,s^{-1}}$) and increases to $\sim 1.5\,\mathrm{m\,s^{-1}}$ at the peak of the convective activity (15:00–16:00 UTC). Over the course of the day, e_{con} improves by 2 %–10 % compared to e_{skip}, while e_{int} is consistently reduced by at least 10 % and up to 25 % compared to e_{skip}. The improvement of e_{skip} is approximately $\sim 15\,\%$ larger when using interpolation instead of a doubled time resolution throughout almost the whole convective day.

In comparison to the temporal error series displayed for the Vaksinen site (Fig. 5a), each RHI scan utilized to estimate the temporal error at the Starmoen site (Fig. 5b) takes approximately twice as long to complete ($D_{\mathrm{scan}} = 80\,\mathrm{s}$). Overall, temporal under-sampling errors estimated for the convective day at Starmoen (Fig. 5b) are larger than at Vaksinen (Fig. 5a). Also, all error estimates sampled on 29 July 2023 (Fig. 5b) reach their peak about 2 h earlier (between 13:00 and 14:00 UTC), exceeding $2\,\mathrm{m\,s^{-1}}$. Here, error reduction by simply doubling the temporal resolution of the RHI scans is negligible ($\leq 5\,\%$). Strikingly, temporal interpolation strongly reduces the temporal under-sampling errors. For each displayed hour, e_{int} corresponds to less than half of the amount estimated for e_{skip} and e_{con}.

The much stronger error reduction by temporal interpolation for the Starmoen compared to the Vaksinen case can be partially linked to the longer ($D_{\mathrm{run}} = 50\,\mathrm{min}$) and hence more continuous RHI series at Starmoen. The representation of individual convective structure dynamics potentially also benefits more from temporal interpolation for the Starmoen than for the Vaksinen case. Given that in both evaluated cases (Fig. 5a and b) the interpolation consistently reduces the temporal under-sampling errors (e_{skip} and e_{con}) and that it has a larger improving effect than simply increasing (here doubling) the time resolution, we utilize interpolated instantaneous RHI scan series for all further processing steps.

5 Convective boundary layer parameters

In addition to the retrieval of the two-dimensional velocity field $(\hat{u}, \hat{w})$, we estimate several boundary layer parameters based on complementary measurements from the lidars, the SEBS, and the AWS, but also from further processing the retrieved velocity field.

5.1 Boundary layer depth

We estimate the boundary layer depth on the basis of the derivative of unprocessed SNR with altitude. For both campaigns, the lidars are scheduled to obtain mainly RHI cross-sections. With Eq. (2) we can estimate the z coordinate corresponding to each $\mathrm{SNR}(\theta, r)$ value and collapse all SNR values of a RHI cross-section to a single profile. We further average the profile for altitude bins of 25 m. For the boundary layer depth estimate, we distinguish between clear-sky and cloud-topped boundary layers.

For clear sky, relatively increased SNR values are usually connected to an increased number of aerosol particles in the air. Convection usually enhances the transport of aerosols (Kunkel et al., 1977), and hence aerosol particles are usually more numerous in the convective boundary layer than in the free atmosphere aloft. Hence, at the border between the boundary layer and free atmosphere, a strong decrease in SNR is usually observed. The height at which we identify the strongest decrease in SNR with height is therefore estimated to be the “clear-sky” or “dry” boundary layer height (m a.s.l.). We define the clear-sky boundary layer depth as the distance between the surface and the clear-sky boundary layer height.

For atmospheric conditions in which convective clouds form, we expect the SNR to rapidly increase at the cloud base, as cloud droplets reflect the lidar beam even more strongly than aerosol particles. Usually the lidar beam is absorbed after it penetrates a few range gates into the cloud and SNR strongly decreases again. During convective conditions with clouds, we assume the convective cloud-base height to be the upper limit of the boundary layer. We identify the cloud-base height at the altitude, where SNR increases the most strongly with height. We define the cloud-topped boundary layer depth as the distance from the surface to the cloud-base height.

5.2 Turbulent surface heat fluxes

The eddy covariance instrumentation of the SEBS, utilized in both campaigns, provides measurements of the three-dimensional wind vector, (u, v, w) ($\mathrm{m\,s^{-1}}$), the sonic temperature, T_{s} (°C), and the specific humidity, q ($\mathrm{kg\,kg^{-1}}$), at 20 Hz time resolution. From the time series of w, T_{s}, and q, we extract the fluctuations w', T_{s}', and q' by removing the 30 min average from the measured time series. Then we estimate the 30 min averaged sensible heat flux, H_{s} (based on Stull, 1988):

$$H_{\mathrm{s}} = \rho_{\mathrm{air}} \cdot c_p \cdot \overline{w'T_{\mathrm{s}}'}, \tag{9}$$

with the heat capacity of air $c_p = 1003.5\,\mathrm{J\,kg^{-1}\,K^{-1}}$ and the covariance of w' and T_{s}' averaged over a 30 min interval. We further estimate the 30 min averaged latent heat flux, H_{e} (based on Stull, 1988):

$$H_{\mathrm{e}} = \rho_{\mathrm{air}} L_v \cdot \overline{w'q'}, \tag{10}$$

with the density of air, $\rho_{\mathrm{air}} \approx 1.25\,\mathrm{kg\,m^{-3}}$, and the latent heat of water, $L_{\mathrm{v}} = 2264.705 \times 10^3\,\mathrm{J\,kg^{-1}}$. The covariance of w' and q' is also averaged over the 30 min interval.

5.3 Flux Richardson number

In the unstably stratified boundary layer, the source of turbulence generation is either buoyancy or shear. The dimensionless ratio of these two terms is defined as the Richardson number. With our setup, the assumption of horizontal homogeneity, and neglecting subsidence, we can estimate the near-surface flux Richardson number, Ri_f (based on Stull, 1988):

$$Ri_\mathrm{f} = \frac{-\frac{g}{\overline{\theta}} \cdot \overline{w' T_\mathrm{s}'}}{|\overline{u'w'} \frac{\Delta \overline{u}}{\Delta z}| + |\overline{v'w'} \frac{\Delta \overline{v}}{\Delta z}|}, \tag{11}$$

where $g = 9.81\,\mathrm{m\,s^{-1}}$ is the Earth's gravitational acceleration constant and T_s', u', v', and w' are fluctuations relative to the 30 min average values $\overline{u}$, $\overline{v}$, $\overline{w}$, and $\overline{T_\mathrm{s}}$ of the series measured by the SEBS. The sonic anemometer was installed 3 m above the surface and $\overline{\theta}$ was estimated on the basis of $\overline{T_\mathrm{s}}$ utilizing the pressure, p (hPa), measured by the AWS. The 30 min average vertical gradients, $\frac{\Delta \overline{u}}{\Delta z}$ and $\frac{\Delta \overline{v}}{\Delta z}$, are estimated from the profile measurements of $\overline{u}$ and $\overline{v}$ (gradient between cup anemometers and wind vanes installed at 2 and 4 m).

Only for negative Ri_f is turbulence generated by buoyancy, while for positive Ri_f buoyancy suppresses turbulence. For $Ri_\mathrm{f} \approx -1$, production of turbulence is balanced between buoyancy and shear, while buoyancy dominates the turbulence generation for $Ri_\mathrm{f} < -1$.

5.4 Convective updraft location

Buoyancy is also the generating mechanism for the convective circulation, which represents the largest eddies in the boundary layer. Convective (buoyant) motion is initiated due to horizontal density anomalies (see Jeevanjee and Romps, 2015). Locally reduced density at the surface (e.g., by a local temperature increase) results in upward motion of air (buoyant updraft), which is compensated for by a horizontal flow towards the updraft region (horizontal convergence). Consequently, we can utilize the retrieved velocity fields of $u(x,z)$ and $w(x,z)$ to identify the presence and the location, x_up, of a convective updraft. Generally two conditions need to be met within the lowest hundreds of meters for the presence of a convective updraft at x_up: a sufficient updraft velocity $w(x) > 0.5\,\mathrm{m\,s^{-1}}$ and a negative horizontal divergence $\frac{\Delta u}{\Delta x}(x) < 0\,\mathrm{s^{-1}}$. As an additional condition, turbulence generation should not be suppressed by buoyancy ($Ri_\mathrm{f} < 0$) during the corresponding time.

6 Two convective case studies

We demonstrate the potential of dual-lidar observations and retrieval for studying convection on the basis of data collected during two convective days. Each day corresponds to one of the campaigns at Vaksinen and Starmoen airport. The cases represent a variety of scan configurations, surrounding terrain, and meteorological conditions. Considering the challenges during the two campaigns (see Sect. 2.4), the two days of choice (28 May 2021 and 29 July 2022) provide the most robust observations, namely those with the most favorable convective conditions and highest data availability during each of the campaigns. It should be noted that these two examples are a proof of concept for the potential of the dual-lidar approach to study convection. A generalization of the presented findings for a wide range of convective conditions will require longer observational periods.

6.1 Meteorological conditions and energy balance

Though obtained in May 2021 and July 2022 at different locations, the incoming shortwave radiation, $\mathrm{SW}_\downarrow$ ($\mathrm{W\,m^{-2}}$), is of similar magnitude for both evaluated days (clear sky: $\mathrm{SW}_{\downarrow,\mathrm{max}} \approx 750\,\mathrm{W\,m^{-2}}$, shown in Fig. 6). Both cases show a diurnal cycle in temperature, humidity, and wind, which is slightly lagged with respect to the $\mathrm{SW}_\downarrow$ series. Compared to the case shown for the Vaksinen site, the near-surface wind is slightly weaker and the diurnal temperature amplitude is larger at the Starmoen site. As a consequence, the turbulence generation during hours of net radiative forcing is mainly buoyancy-dominated ($Ri_\mathrm{f} < -1$) at Starmoen, while at Vaksinen turbulence generation is rather balanced between buoyancy and shear ($Ri_\mathrm{f} \approx -1$). Despite the different forcing mechanisms for turbulence generation, the sensible and latent turbulent surface heat fluxes are of comparable magnitude for both cases displayed in Fig. 6.

Throughout both days, we observe a net radiative forcing of up to $490\,\mathrm{W\,m^{-2}}$ at the Vaksinen site and up to $460\,\mathrm{W\,m^{-2}}$ at the Starmoen site (see Fig. 6). The latent and sensible heat fluxes make up ca. 55 % and ca. 60 % of the net radiation forcing at the Vaksinen and the Starmoen site, respectively. A maximum residuum of ca. $225\,\mathrm{W\,m^{-2}}$ at Vaksinen and $180\,\mathrm{W\,m^{-2}}$ at Starmoen remains around the period of peak net radiative forcing. The main part of this residuum is usually compensated for by the ground heat flux (not measured here), which can reach values of the order of a few hundred Watts per square meter ($\mathrm{W\,m^{-2}}$) (e.g., Arya, 2001). Still, large convective eddies, which are nearly stationary over the averaging period of the turbulent flux (30 min), may contribute substantially to the energy transport away from the surface. The contribution of such large eddies is not necessarily captured by the turbulent surface heat fluxes. With the dual-lidar setup, on the other hand, we can get a qualitative estimate of the larger-scale flow patterns and their evolution.

The wind speed and direction profiles reconstructed from the DBS scans and the boundary layer depth estimated from SNR profiles based on composites of all RHI scans already give a good overview of the predominating state of the circulation over the two chosen days (Fig. 6, two lower rows). Similar to the surface wind, wind speed is also increased throughout the whole profile at the Vaksinen site compared to the Starmoen site, in particular during the convective hours

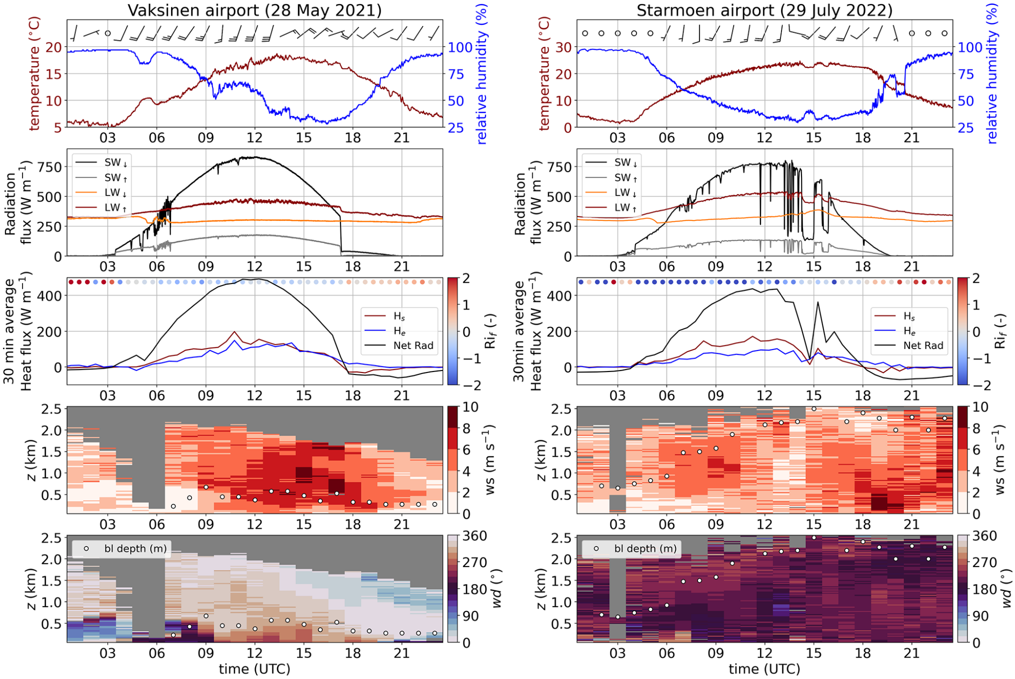

Figure 6. Diurnal cycle of temperature, humidity, and surface wind barbs (short feathers: $1\,\mathrm{m\,s^{-1}}$, long feathers: $2\,\mathrm{m\,s^{-1}}$) measured by AWS, incoming (↓) and outgoing (↑) longwave (LW) and shortwave (SW) radiation, net radiation, turbulent sensible (H_s) and latent heat (H_e) fluxes measured and estimated from SEBS measurements, temporal evolution of wind speed (ws) and wind direction (wd) profiles, and boundary layer depth (bl depth; m above the surface) from lidar observations during two convective days. Left panels: observations at Vaksinen airport (28 May 2021); right panels: observations at Starmoen airport (29 July 2022).

of the day (Fig. 6). Wind direction changes substantially both in time and with altitude at the Vaksinen site, turning from southerly to southwesterly (almost parallel to the airstrip) in the boundary layer during the convectively active hours. Above the boundary layer, wind direction turns towards north and later on towards east. At Starmoen, wind is mostly from south to southwesterly directions over the whole day and observed altitude range, which is almost perpendicular to the airstrip. The most striking difference between the two cases is the large difference in boundary layer depth. At the Vaksinen site the boundary layer is quite shallow and reaches only a few hundred meters of depth. At Starmoen, on the other hand, the boundary layer rises up to more than 2000 m over the course of the day, also yielding the possibility of comparably deeper convective circulation.

6.2 Dual-lidar approach for a clear-sky case of convection

We demonstrate the reconstruction of the flow field (u, w) in the cross-section between the two lidars from the temporally interpolated v_r fields (one snapshot) during the Vaksinen airport campaign (28 May 2021 between 15:00 and 16:00 UTC), which is displayed in Fig. 7. The interpolated v_r values in the RHI scans (Fig. 7a–f) correspond to the time step which is exactly at the middle of each individual scan configuration period.

Despite a time difference of 10 and 20 min between the different scan configurations, all retrieved fields of u and w indicate the presence of a convective updraft, triggered at around $x = 200$ (Fig. 7g–l). With the retrieved u and w fields and on the basis of the method introduced in Sect. 5.4, we estimated x_up, where the convective updrafts originate at the surface. Figure 8 visualizes the identification process applied to the three retrieved u and v fields which are presented in Fig. 7. Here, the height-averaged w (over the lowest 150 m) reaches a local maximum ($w > 0.5\,\mathrm{m\,s^{-1}}$) and u converges (reverses sign from positive to negative with increasing x: $\frac{\Delta u}{\Delta x}$) within the grey shaded area for the three tested scan configurations. This area is in fact located around the $x = 200$ mark (Fig. 8d–f).

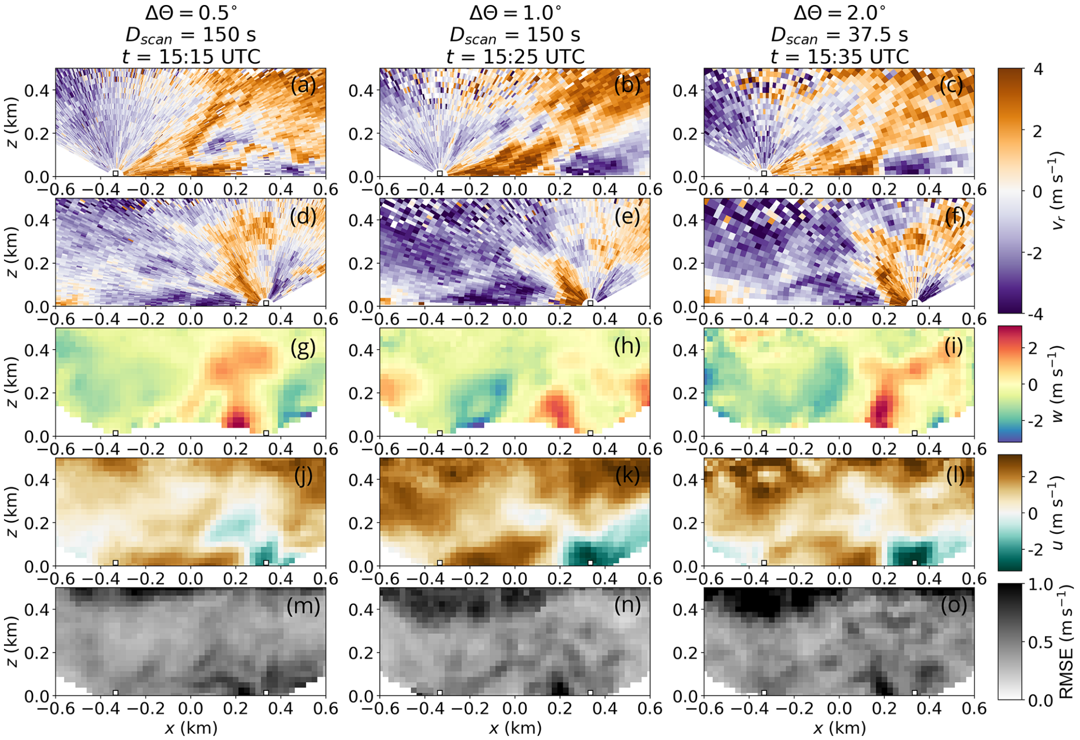

$\Delta\Theta = 0.5°$
D_{scan} = 150 s
t = 15:15 UTC

$\Delta\Theta = 1.0°$
D_{scan} = 150 s
t = 15:25 UTC

$\Delta\Theta = 2.0°$
D_{scan} = 37.5 s
t = 15:35 UTC

Figure 7. Filtered and temporally interpolated v_r observations, retrieval, and retrieval error obtained for 28 May 2021 between 15:00 and 16:00 UTC at Vaksinen airport. The location of the utilized lidars is indicated by white squares with a black border just above the surface, with lidar$_1$ in the negative and lidar$_2$ in the positive x domain in each of the panels. The three columns correspond to the three different scan configurations with configuration-specific $\Delta\theta$, D_scan, and t (instantaneous cross-section). Each row corresponds to one relevant variable. The first row **(a–c)** shows processed, instantaneous v_r fields from lidar-37 (here lidar$_1$). The second row **(d–f)** shows processed, instantaneous v_r fields from lidar-40 (here lidar$_2$). The third row **(g–i)** shows the retrieved w field. The fourth row **(j–l)** shows the retrieved u field, and the fifth row **(m–o)** shows the retrieval RMSE field.

For all three scan configurations the maximum w and minimum $\frac{\Delta u}{\Delta x}$ fall into almost the same point (x_up) at $x = 230$ m, $x = 200$ m, and $x = 200$ m. Given the meteorological background conditions (see Sect. 6.1 and Fig. 6), buoyancy contributes to the turbulence generation ($Ri_\mathrm{f} < 0$) and can be considered the main driver for the observed circulation patterns. Horizontal velocity divergence is expected at the upper edge of the convective updraft to compensate for the upward motion of air. A divergent behavior is, in fact, evident in all three retrieved u fields (Fig. 7j–l) but much weaker than the near-surface convergence. Similar to what was observed by Kunkel et al. (1977), the updraft is attached to the surface and has more of a plume-like character, while at higher altitudes "bubbles" of increased vertical velocities seem to detach.

The near-surface horizontal velocity convergence around $x = 200$ m is already well captured by the v_r fields obtained by lidar-37, which is located at $x = -335$ m (Fig. 7a–c). The lidars's beam is oriented almost horizontal relative to the near-surface flow field, relevant to the convective updraft and convergence region. Here, angular or spatial resolution does not matter, since even the lowest angular resolution of 2.0° (Fig. 7c) sufficiently captures all relevant features of the horizontal flow. Lidar-40 is located at $x = 335$ m, which is comparably close to the convective updraft region around $x = 200$ m, for all three scan configurations. The region of horizontal velocity convergence, which is not exactly located above lidar-40, is also evident in the horizontally pointing beams (Fig. 7d–f, j–l). Yet here, the updraft strongly contributes to the v_r signal of the vertically or close to vertically pointing beams (Fig. 7d–i).

Within the convectively active region, the RMSE is remarkably similar for all three scan configurations (Fig. 7m–o). It is increased close to the updraft region near the surface ($x = 200$, $z < 100$). The main cause of this increased

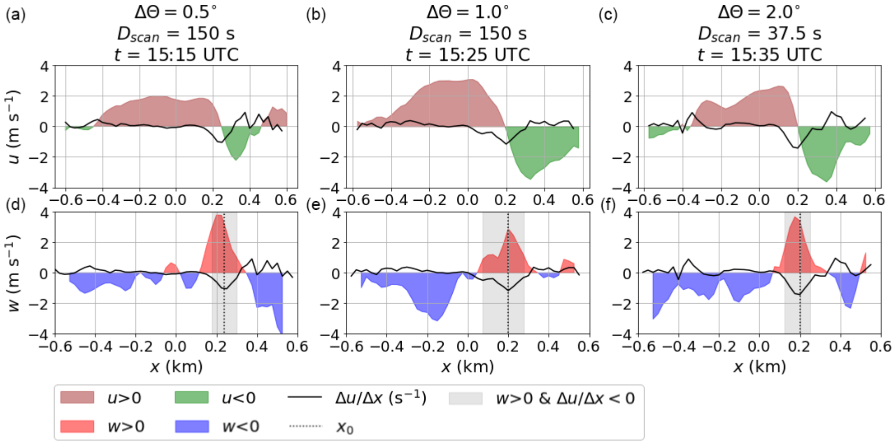

Figure 8. Averaged near-surface ($\leq$ 150 m) horizontal divergence. The first row **(a–c)** shows u and the second row **(d–f)** shows w estimates to visualize the identification process for the near-surface updraft location, x_0. The three columns correspond to the three different scan configurations with configuration-specific $\Delta\theta$, D_{scan}, and t (instantaneous cross-section).

RMSE is an erroneous estimate of the large w component in the near-surface region. The w contribution to the observed v_r is negligible, since here both lidars observe v_r with predominantly horizontally pointing beams (ill-posed in w). This issue was already addressed by removing any ill-posed w values from the retrieved field (see Sect. 3.2). Above the downdraft region, a larger area of increased RMSE is present for all three scan configurations (upper left corner of the displayed retrieval grid). Here SNR values are decreased (not shown); hence, fewer v_r values are available for the retrieval. The boundary layer depth is horizontally inhomogeneous and particularly increased above the updraft. Hence, the convective updraft directly drives the boundary layer deepening, while the downdraft entrains clear air from the free atmosphere, where uncertainty in the lidar retrieval rapidly increases. Due to its rapid transport of aerosols through the atmosphere, the convective updraft is consequently well suited to be observed with a Doppler lidar.

6.3 Development of a cloud-topped convective structure

During the Starmoen campaign, we captured a convective day with comparable temperature and humidity development, as well as radiation and turbulent fluxes (Fig. 6). The main differences to the convective day investigated from the Vaksinen campaign are the increased depth of the boundary layer and the formation of convective clouds in the afternoon. The presence of clouds at Starmoen airport on the day of interest is evident from the periods of strongly reduced values of SW$_\downarrow$ during the afternoon (see Fig. 6). From ca. 13:00 until 14:00 UTC, SW$_\downarrow$ rapidly fluctuates between diffuse (cloud-shadowed) and nearly clear-sky values, indicating the presence of nonstationary and rather small-scale clouds. From ca. 14:00 to 15:00 UTC, the pyranometer was continuously shadowed by a larger, more stationary cloud (see Fig. 9). At the time the photo in Fig. 9 was taken, the shadow of the cloud covered the entire airfield, though the lidars only capture a finite slice of this cloud within the scanned cross-section as a strong, local increase in SNR at the cloud base.

Figure 9. Cloud observed over Starmoen airport on 29 July 2022 at 14:23 UTC

We estimate the fields of u and w in the vertical cross-section between the lidar on the basis of instantaneous RHI scans (see Sect. 4.2) every 4 min from 14:04 until 14:32 UTC. These fields, as well as the corresponding streamlines and an indication of the cloud base as SNR contours (SNR > −10 dB), are displayed in Fig. 10.

The initial velocity fields and streamlines show only weak signs of convection. The velocity patterns indicate predominantly turbulent flow with small-scale fluctuations and no clear convective pattern (Fig. 10a–c). An indication of a cloud is visible above the weak updraft region, which is possibly a remnant of an earlier convective circulation. As time progresses, the velocity clusters intensify, dividing into updraft and downdraft regions (Fig. 10d). Also, the streamlines imply a clearer organization of the flow (Fig. 10f) with less impact of localized and small-scale turbulence indicating the onset of a new, emerging convective circulation. Here, the maximum updraft velocity, $w^{\uparrow}_{\max}$, reaches $2.1\,\mathrm{m\,s^{-1}}$. The updraft terminates just below the cloud base and spans the whole depth of the cloud-topped boundary layer.

The subsequent time steps show further intensification of the updraft and downdraft (Fig. 10g–l), where a converging horizontal velocity pattern in the lower levels focuses into the convective stream into a narrow core of maximum updraft velocity with plume-like characteristics ($x_{\mathrm{up}} = -0.6$), as also observed by Kunkel et al. (1977). Just below the cloud, a diverging horizontal velocity pattern (Fig. 10h, k) drives the widening of the convective updraft (Fig. 10g, j). Interestingly, the width of the convective stream (Fig. 10i, l) is conserved over the altitude range where horizontal convergence dominates. Here, the streamlines are tilted towards the left-hand side of the cross-section. At 14:12 UTC, $w^{\uparrow}_{\max} = 2.9\,\mathrm{m\,s^{-1}}$ reaches the maximum value of the displayed series and slightly declines to $w^{\uparrow}_{\max} = 2.8\,\mathrm{m\,s^{-1}}$ at 14:16 UTC. Here, the updraft cluster (Fig. 10j) is widened substantially in comparison to the preceding time step (Fig. 10g) and spans over nearly the entire width of the cross-section, which is now too narrow and would require Δx (see Table 2) to nearly double to document the complete convective circulation pattern.

The convective circulation further weakens, as entrainment of environmental air and drag forces counteract the effective buoyancy in the following time steps (Fig. 10m–x). The thin core of maximum velocity vanishes and the updraft loses its predominantly plume-like character. Here, the buoyant forcing of the convection begins to break down and only inertia maintains the circulation (see, e.g., Jeevanjee and Romps, 2016). In the last displayed time step (Fig. 10v–x), the cloud is still present, though with no further support from below. The cloud will eventually break down or be advected from the site over time. Here, the streamlines tilt toward the right-hand side of the lidar cross-section with increasing altitude, opposite to the tilt which we observed at the onset of the convective circulation. The boundary layer reached its maximum depth of the day during this hour. Afterwards, radiative forcing, turbulent heat fluxes, and turbulence generation by buoyancy decrease (Fig. 6) and convective activity ceases for that day.

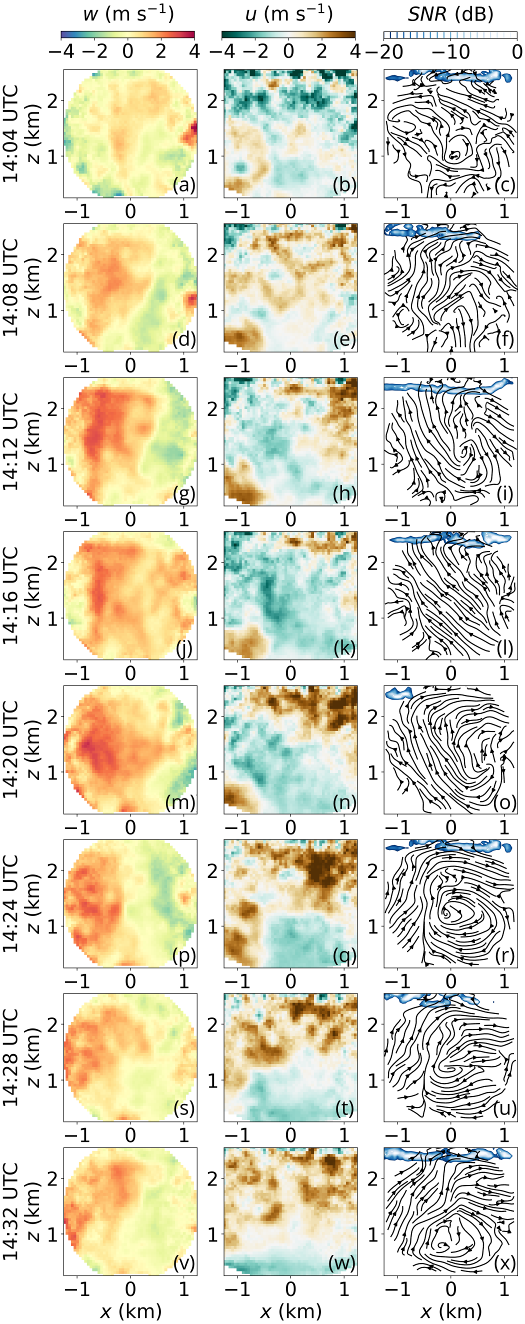

Figure 10. Temporal evolution of convection on 29 July 2022 at Starmoen airport. First column: retrieved w field. Second column: retrieved u field. Third column: streamlines and SNR (cloud backscatter).

7 Discussion

In the following we discuss the performance of the presented approach and its potential and limitations to sample convection in instantaneous cross-sections of high temporal and spatial resolution. We also discuss and summarize our experiences gained throughout the two presented case studies and interpret the local variability of the convective properties for the two selected sites, as well as the benefit of complementary meteorological observations.

7.1 Lidar setup

We tested the potential of a setup combining two scanning lidars to resolve and characterize atmospheric convection in a vertical plane. The setup will at best be able to retrieve the two-dimensional evolution of the three-dimensional convective flow. Yet, convective circulation is often rather symmetric around its vertical axis (updraft or downdraft) given calm background wind speed conditions (e.g., Emanuel, 1994). In the case of sufficient background wind, the convective structure will be tilted and the cross-section should ideally be oriented parallel to the wind direction to capture the vertical extent of the convective circulation. Furthermore, to interpret the absolute strength and width of the convective updraft or downdraft, the cross-section should pass through the core of the convective structure.

For our setup along the airport runways, we experienced a satisfying hit rate of representative convective circulation patterns during convective conditions indicated by Ri_f even though wind and surface conditions were not necessarily optimal. As the lidars are rather immobile, it is still beneficial to orient the lidars according to the dominant wind direction during convective conditions. To ensure that the setup frequently captures convection, it is also advantageous that the cross-section is placed over surfaces that are likely to trigger the release of thermal updrafts.

Reducing the errors and complications connected to the setup has a substantial impact on the performance of the dual-lidar retrieval. A thorough azimuth calibration of the utilized lidars following the instructions of the lidar manufacturer Leosphere[3] prevents unnecessary amplification of out-of-plane v_r errors in the retrieval (see Stawiarski et al., 2013). While synchronization of scan schedules is only of secondary importance (in contrast to Röhner and Träumner, 2013), time synchronization of the lidar-internal clocks is critical. Wrongly matched time stamps are generally hard to identify and correct, yielding amplified errors in v_r retrieval.

7.2 Retrieval and processing

We implement and apply a retrieval algorithm that follows a similar methodology as well-established retrievals for overlapping dual-lidar scans (e.g., Newsom et al., 2008; Cherukuru et al., 2015; Träumner et al., 2015; Haid et al., 2020). We find the best estimate of u and v by solving an over-constrained equation system for each Cartesian point containing several v_r values of both lidars. This reduces the impact of outliers and additionally yields a retrieval error estimate that serves as a measure of confidence for the retrieval in each point.

Generally, the dual-lidar retrieval is quite sensitive to erroneous v_r input, as also discussed by Stawiarski et al. (2013). We found that pre-processing the RHI scans before retrieval has a positive impact on the error reduction and hence on the performance of the dual-lidar approach. The error in v_r connected to noise and erroneous features can be up to an order of magnitude larger than actual values of v_r. As RHI scans are particularly prone to range-folded ambiguities (Bonin and Brewer, 2017), it is crucial to remove these before further processing.

For the lidar observations, the DBSCAN filter (adapted from Alcayaga, 2020) proves to be more effective and accurate than the conventional SNR threshold filter. Applying the DBSCAN filter strongly increases the performance of the dual-lidar retrieval for various conditions. Further processing, in the form of temporal interpolation of the RHI scans, additionally reduces the error compared to using the obtained RHI scans, where θ is dependent on t. From the interpolated scan series, instantaneous scans can be extracted, which reduces the necessity of exact scan schedule synchronization. Also, the interpolation has a larger impact on the temporal error reduction than doubling the temporal resolution of the scans. Since temporal interpolation still has a “blurring” effect on the retrieval, similar to using a temporal radius (see Newsom et al., 2008), it is still beneficial to use a high sampling rate for the scans as the base for the interpolation.

The retrieval based on the processed v_r sections yields a promising representation of the convective circulation for two convective cases. In both cases, convection is well resolved and spans the entire depth of the boundary layer. Consequently, convection contributes substantially to the overturning of heat, moisture, momentum, and aerosols in the convective boundary layer. Convection also contributes to boundary layer deepening or is at least responsible for the maintenance of the boundary layer depth. In particular, the convective updraft and clear evidence of horizontal velocity convergence in the lower part of the convective circulation are captured. This also allows identifying secondary convective parameters, e.g., the origin of the updraft air mass close to the surface, the strength and the size of the updraft, and the horizontal structure of the boundary layer.

---

[3] WindCube Scan software suite User Manual Version 20.f, Vaisala France, Tech Park, 6A rue René Razel 91 400, Saclay, France, 2022.

7.3 Spatial and temporal resolution

We utilize several scan configurations with various temporal and spatial resolutions. During the first campaign at the Vaksinen site we even tested three different scan configurations. The comparison of the different scanning patterns proved to be challenging, as we cannot be sure whether the differences in observed data are due to changes in the flow conditions or changes in the scan configuration. In particular, the 10 min scanning interval turned out to be too short for the scan configurations with long D_{scan} (150 s) and did not achieve representative error statistics. To sufficiently compare the scan resolutions, simultaneous observations by an additional lidar would be required. However, we found a solution by artificially decreasing the highest obtained temporal resolution, yielding a representative indication of the impact of the temporal resolution on the error.

It was also not easy to find continuity between the consecutive series of changing scan configurations each 10 min at the Vaksinen site, as the temporal interpolation is only able to produce an entire instantaneous RHI scan after one complete scan. We can only sufficiently resolve the full temporal development of a convective circulation for a continuously sampled series with constant temporal and spatial resolution. As observed for our cloud-topped case, the development of a convective circulation can have a life cycle of the order of several tens of minutes. But there is also an indication for longer-lasting convective patterns for the smaller convective scales obtained at the Vaksinen site.

Still, for the two evaluated cases, all convection relevant scales are well represented, even by the lowest spatial resolution tested within the retrieval grid, which is still in close vicinity of the lidars. It is remarkable that even in the shallow boundary layer case observed at the Vaksinen site, where only smaller-scale convection dominates, the lowest angular resolution is sufficient to resolve the characteristic features of the convective circulation. It is therefore reasonable to use high temporal resolution, even at the cost of spatial resolution or, if the aerosol concentration allows, at the cost of T_{scan}.

We face a bigger problem to capture the entirety of very large-scale convection that exceeds the boundaries of the retrieval grid in the cloud-topped case. Also, the retrieval becomes less reliable above the cloud base, as the lidar beams can only penetrate a few range gates into the cloud and the data availability drops rapidly. The dual-lidar retrieval is therefore mostly relevant for the dry part of the convective circulation and distance between the lidars should be increased compared to the setup at Starmoen to also capture the largest convective structures.

7.4 Local variability of convective properties

The dual-lidar retrieval complements valuable insights from the surface-based measurements by quantifying the substantial differences in the deepening of the boundary layer by the convective circulation for the case at Vaksinen compared to Starmoen. One potential explanation is the different geographic setting of the locations. The Vaksinen airport is located in a local valley with rather steep topography of approximately 300 m height. This topography potentially enhances the accumulation of cold air in the valley and the development of a nocturnal low-level temperature inversion. In addition, Vaksinen airport is located relatively close to the North Sea, which is a large body of comparably low temperature in May. Cold-air advection from the sea creates an internal boundary layer (Garratt, 1990), which can also contribute to the maintenance of a strong, low-altitude temperature inversion. This inversion is hard to penetrate even for strong updrafts, as observed at the Vaksinen site.

The Starmoen site is much flatter and located far away from any water body of comparable size, and the case features a deeper residual layer from the preceding day. As energy input near the surface and turbulent fluxes increase, convection continuously deepens the boundary layer. The strength of the convective updraft is not stronger compared to the one observed at the Vaksinen site, indicating that there is a weaker inversion. The potential of a deeper boundary layer is indicated, but it is not possible to quantify a weaker inversion without complementary temperature profiles.

7.5 Complementary meteorological observations

With the DBS scan included in the lidar schedules for 10 min each hour, we are able to gain an estimate of the mean profile of the three-dimensional wind. This profile indicates how parallel the flow is towards the evaluated dual-lidar cross-section. Yet, from the dual-lidar retrieval we can clearly observe that the flow during convective conditions is already very complex and nonhomogeneous on small horizontally scales, which is a requirement for an accurate DBS retrieval. As a consequence, the DBS retrieval may not sufficiently capture the profile, in particular with increasing separation of beams with height. Another problem of the DBS scan is that it introduces a discontinuity in the retrieved dual-lidar cross-section time series. In the worst case, the DBS scan is scheduled during a crucial period in the evolution of the convective circulation. As the quality of the DBS retrieval is uncertain, an alternative solution to sample the profile of the three-dimensional wind, which does not interrupt the continuity of the overlapping RHI scans, would be an improvement. A third lidar that scans perpendicular to the dual-lidar setup, creating a “virtual tower” (see Calhoun et al., 2006), could achieve this, for example.

The complementary ground-based measurements, such as those used here, are beneficial to the setup. They can enhance the process of identifying relevant periods for convection and give some indication of the strength and depth of the convection (e.g., Ri_{f} or a parameter such as the convective velocity scale $w_* \sim \overline{w'\theta'}$ as discussed by Träumner et al., 2011). However, to learn more about the character and physics of the convective boundary layer and evolution of convective circulation (i.e., the impact of drag or moisture on the vertical acceleration), more sophisticated measurements are needed. Background profiles of temperature, humidity, and wind as well as profiles simultaneously measured within the convective updraft to complement the flow field estimates of the dual-lidar approach could significantly improve our understanding of convection, e.g., when evaluated in an empirical model such as introduced by Pálenik et al. (2021). The gLidar project actually aims to achieve such collocated observations.

8 Conclusions and outlook

We presented a dual-lidar setup and retrieval combined with an advanced filtering approach and temporal interpolation to sample and characterize the dynamic properties of atmospheric convection. We demonstrated that our dual-lidar setup and retrieval approach capture the flow field of convective structures projected onto a two-dimensional plane for a clear-sky and a cloud-topped case at two independent sites.

All tested angular resolutions yielded sufficient spatial resolution to resolve the details of the convective circulation, allowing us to prioritize increased temporal resolution. To ensure that the setup captures at least one wavelength of the convective circulation at any point in time, the distance between the two lidars should be increased compared to the presented setups. Utilizing an advanced filter successfully removes erroneous features and noise, yielding spatial continuity in the dual-lidar retrieval. Temporal interpolation further reduces errors that would be amplified in the dual-lidar retrieval and yields an increased temporal resolution. These two processing techniques simultaneously increase data availability while significantly reducing errors compared to conventionally used methods. In particular, these processing techniques enable the estimate of secondary convective parameters, such as the origin, depth, width, and strength of the convective updrafts that contribute to the transport of heat, moisture, momentum, and aerosols, as well as boundary layer deepening or are at least responsible for the maintenance of the boundary layer depth.

Overall, our study presents the potential of a dual-lidar setup as an observational tool to probe the convective flow field. A long-term installation of the setup could provide a sufficient observational basis to validate the representation of convection in LESs, which is used to guide parameterization schemes in weather and climate models. In combination with remote access solutions and processing capabilities, nowcasting of flow conditions, for example for takeoff and landing risk assessments at airports, is feasible. Finally, combining the proposed dual-lidar approach with the observation of additional profiles of temperature and humidity inside and outside the convective updraft offers the potential to gain a deeper understanding of the dynamic processes inherent to convection.

Code and data availability. All code as well as raw and processed data can be provided by the corresponding authors upon request.

Author contributions. CD, JP, TS, and JR developed the instrument setup and planned the campaign. CD and JP developed the retrieval and pre-processing code. CD analyzed the data and wrote the paper draft. JP, TS, and JR reviewed and edited the paper.

Competing interests. The contact author has declared that none of the authors has any competing interests.

Acknowledgements. The authors would like to thank Os Aero Klubb and the Ole Reistad Center, the Norwegian Air Sports Federation's national center for gliding, for the possibility to install our instrumentation and for their logistical support and hospitality during the campaigns. We would further like to thank Stephan Krahl and the students of field course in meteorology at the Geophysical Institute, University of Bergen (GEOF-322, 2021), for their help with the instrument setup at Vaksinen airport, as well as Tom Remond and Enora Cariou for the setup of the instrumentation at Starmoen airport. Special thanks go to our engineering staff: Anak Bhandari for his work and assistance in campaign planning and realization and Tor Olav Kristensen for the design and assistance in building the remote access solution for the lidar systems.

Financial support. The three lidars used in this study are part of the National Norwegian Research Infrastructure OBLO (Offshore Boundary Layer Observatory) funded by the Research Council of Norway (RCN) (project number: 227777). The experimental work was supported by funding from the Faculty of Mathematics and Natural Sciences at the University of Bergen (Fellesfond for geofysisk forskning). The campaign at Elverum was facilitated by the research school on changing climates in the coupled Earth system (CHESS) funded by RCN (project number: 245854).

Review statement. This paper was edited by Ad Stoffelen and reviewed by two anonymous referees.

References

Adler, B., Kalthoff, N., and Kiseleva, O.: Detection of structures in the horizontal wind field over complex terrain using coplanar Doppler lidar scans, Meteorol. Z., 29, 467–481, https://doi.org/10.1127/metz/2020/1031, 2020.

Adler, B., Gohm, A., Kalthoff, N., Babić, N., Corsmeier, U., Lehner, M., Rotach, M. W., Haid, M., Markmann, P., Gast, E., Tsaknakis, G., and Georgoussis, G.: CROSSINN: A Field Experiment to Study the Three-Dimensional Flow Structure in the Inn Valley, Austria, B. Am. Meteorol. Soc., 102, E38–E60, https://doi.org/10.1175/BAMS-D-19-0283.1, 2021.

Alcayaga, L.: Filtering of pulsed lidar data using spatial information and a clustering algorithm, Atmos. Meas. Tech., 13, 6237–6254, https://doi.org/10.5194/amt-13-6237-2020, 2020.

Arya, S. P.: Introduction to Micrometeorology, 2nd edn., Elsevier, San Diego, CA, ISBN 0120593548, 2001.

Bonin, T. A. and Brewer, A. W.: Detection of Range-Folded Returns in Doppler Lidar Observations, IEEE Geosci. Remote S., 14, 514–518, https://doi.org/10.1109/LGRS.2017.2652360, 2017.

Brown, A. R., Cederwall, R. T., Chlond, A., Duynkerke, P. G., Golaz, J.-C., Khairoutdinov, M., Lewellen, D. C., Lock, A. P., MacVean, M. K., Moeng, C.-H., Neggers, R. A. J., Siebesma, A. P., and Stevens, B.: Large-eddy simulation of the diurnal cycle of shallow cumulus convection over land, Q. J. Roy. Meteor. Soc., 128, 1075–1093, https://doi.org/10.1256/003590002320373210, 2002.

Calhoun, R., Heap, R., Princevac, M., Newsom, R., Fernando, H., and Ligon, D.: Virtual Towers Using Coherent Doppler Lidar during the Joint Urban 2003 Dispersion Experiment, J. Appl. Meteorol. Clim., 45, 1116–1126, https://doi.org/10.1175/JAM2391.1, 2006.

Cherukuru, N. W., Calhoun, R., Lehner, M., Hoch, S. W., and Whiteman, C. D.: Instrument configuration for dual-Doppler lidar coplanar scans: METCRAX II, J. Appl. Remote Sens., 9, 096090, https://doi.org/10.1117/1.JRS.9.096090, 2015.

Duscha, C., Barrell, C., Renfrew, I. A., Brooks, I. M., Sodemann, H., and Reuder, J.: A Ship-Based Characterization of Coherent Boundary-Layer Structures Over the Lifecycle of a Marine Cold-Air Outbreak, Bound.-Lay. Meteorol., 183, 355–380, https://doi.org/10.1007/s10546-022-00692-y, 2022.

Emanuel, K. A.: Atmospheric convection, Oxford University Press, New York, ISBN 9780195066302, 1994.

Garratt, J. R.: The internal boundary layer – A review, Bound.-Lay. Meteorol., 50, 171–203, https://doi.org/10.1007/BF00120524, 1990.

Geerts, B., Raymond, D. J., Grubišić, V., Davis, C. A., Barth, M. C., Detwiler, A., Klein, P. M., Lee, W.-C., Markowski, P. M., Mullendore, G. L., and Moore, J. A.: Recommendations for In Situ and Remote Sensing Capabilities in Atmospheric Convection and Turbulence, B. Am. Meteorol. Soc., 99, 2463–2470, https://doi.org/10.1175/BAMS-D-17-0310.1, 2018.

Haid, M., Gohm, A., Umek, L., Ward, H. C., Muschinski, T., Lehner, L., and Rotach, M. W.: Foehn–cold pool interactions in the Inn Valley during PIANO IOP2, Q. J. Roy. Meteor. Soc., 146, 1232–1263, https://doi.org/10.1002/qj.3735, 2020.

Iwai, H., Ishii, S., Tsunematsu, N., Mizutani, K., Murayama, Y., Itabe, T., Yamada, I., Matayoshi, N., Matsushima, D., Weiming, S., Yamazaki, T., and Iwasaki, T.: Dual-Doppler lidar observation of horizontal convective rolls and near-surface streaks, Geophys. Res. Lett., 35, L14808, https://doi.org/10.1029/2008GL034571, 2008.

Jeevanjee, N. and Romps, D. M.: Effective Buoyancy, Inertial Pressure, and the Mechanical Generation of Boundary Layer Mass Flux by Cold Pools, J. Atmos. Sci., 72, 3199–3213, https://doi.org/10.1175/JAS-D-14-0349.1, 2015.

Jeevanjee, N. and Romps, D. M.: Effective buoyancy at the surface and aloft, Q. J. Roy. Meteor. Soc., 142, 811–820, https://doi.org/10.1002/qj.2683, 2016.

Kunkel, K. E., Eloranta, E. W., and Shipley, S. T.: Lidar Observations of the Convective Boundary Layer, J. Appl. Meteorol. Clim., 16, 1306–1311, https://doi.org/10.1175/1520-0450(1977)016<1306:LOOTCB>2.0.CO;2, 1977.

Lai, T. L., Robbins, H., and Wei, C. Z.: Strong consistency of least squares estimates in multiple regression, P. Natl. Acad. Sci. USA, 75, 3034–3036, https://doi.org/10.1073/pnas.75.7.3034, 1978.

Newsom, R., Calhoun, R., and Ligon, D.: Linearly Organized Turbulence Structures Observed Over a Suburban Area by Dual-Doppler Lidar, Bound.-Lay. Meteorol., 127, 111–130, https://doi.org/10.1007/s10546-007-9243-0, 2008.

Newsom, R. K., Ligon, D., Calhoun, R., Heap, R., Cregan, E., and Princevac, M.: Retrieval of microscale wind and temperature fields from single- and dual-Doppler lidar data, J. Appl. Meteorol. Clim., 44, 1324–1345, https://doi.org/10.1175/JAM2280.1, 2005.

Pálenik, J.: gLidar project website, https://glidar-project.github.io/ (last access: 25 January 2023), 2022.

Pálenik, J., Spengler, T., and Hauser, H.: IsoTrotter: Visually Guided Empirical Modelling of Atmospheric Convection, IEEE Transactions on Visualization and Computer Graphics, 27, 775–784, https://doi.org/10.1109/TVCG.2020.3030389, 24 August 2021.

Prein, A. F., Rasmussen, R., and Stephens, G.: Challenges and Advances in Convection-Permitting Climate Modeling, B. Am. Meteorol. Soc., 98, 1027–1030, https://doi.org/10.1175/BAMS-D-16-0263.1, 2017.

Röhner, L. and Träumner, K.: Aspects of Convective Boundary Layer Turbulence Measured by a Dual-Doppler Lidar System, J. Atmos. Ocean. Tech., 30, 2132–2142, https://doi.org/10.1175/JTECH-D-12-00193.1, 2013.

Siebesma, A. P., Soares, P. M. M., and Teixeira, J.: A Combined Eddy-Diffusivity Mass-Flux Approach for the Convective Boundary Layer, J. Atmos. Sci., 64, 1230–1248, https://doi.org/10.1175/JAS3888.1, 2007.

Stawiarski, C., Träumner, K., Knigge, C., and Calhoun, R.: Scopes and Challenges of Dual-Doppler Lidar Wind Measurements – An Error Analysis, J. Atmos. Ocean. Tech., 30, 2044–2062, https://doi.org/10.1175/JTECH-D-12-00244.1, 2013.

Stull, R. B.: An Introduction to Boundary Layer Meteorology, Springer, Dordrecht, https://doi.org/10.1007/978-94-009-3027-8, ISBN 978-90-277-2769-5, 1988.

Träumner, K., Kottmeier, C., Corsmeier, U., and Wieser, A.: Convective boundary-layer entrainment: Short review and progress using Doppler lidar, Bound.-Lay. Meteorol., 141, 369–391, https://doi.org/10.1007/s10546-011-9657-6, 2011.

Träumner, K., Damian, T., Stawiarski, C., and Wieser, A.: Turbulent Structures and Coherence in the Atmospheric Surface Layer, Bound.-Lay. Meteorol., 154, 1–25, https://doi.org/10.1007/s10546-014-9967-6, 2015.

Virtanen, P., Gommers, R., Oliphant, T. E., Haberland, M., Reddy, T., Cournapeau, D., Burovski, E., Peterson, P., Weckesser, W., Bright, J., van der Walt, S. J., Brett, M., Wilson, J., Millman, K. J., Mayorov, N., Nelson, A. R. J., Jones, E., Kern, R., Larson, E., Carey, C. J., Polat, İ., Feng, Y., Moore, E. W., VanderPlas, J., Laxalde, D., Perktold, J., Cimrman, R., Henriksen, I., Quintero, E. A., Harris, C. R., Archibald, A. M., Ribeiro, A. H., Pedregosa, F., van Mulbregt, P., and SciPy 1.0 Contributors: SciPy 1.0: Fundamental Algorithms for Scientific Computing in Python, Nat. Methods, 17, 261–272, https://doi.org/10.1038/s41592-019-0686-2, 2020.

Werner, C.: Doppler wind lidar, in: Lidar, Springer, New York, NY, 325–354, https://doi.org/10.1007/0-387-25101-4_12, 2005.

Whiteman, C. D., Lehner, M., Hoch, S. W., Adler, B., Kalthoff, N., Vogt, R., Feigenwinter, I., Haiden, T., and Hills, M. O. G.: The Nocturnal Evolution of Atmospheric Structure in a Basin as a Larger-Scale Katabatic Flow Is Lifted over Its Rim, J. Appl. Meteorol. Clim., 57, 969–989, https://doi.org/10.1175/JAMC-D-17-0156.1, 2018.

Wildmann, N., Kigle, S., and Gerz, T.: Coplanar lidar measurement of a single wind energy converter wake in distinct atmospheric stability regimes at the Perdigão 2017 experiment, J. Phys. Conf. Ser., 1037, 052006, https://doi.org/10.1088/1742-6596/1037/5/052006, 2018.

A Alternative motion correction approach

The equation that needs to be solved to compensate the radial velocities from motion impact and retrieved the three dimensional wind vector:

$$v_r = u\, sin(\alpha)\, sin(\theta_z)\; +\; v\, cos(\alpha)\, sin(\theta_z)\; +\; cos(\theta_z) \tag{A.1}$$

Completely define the rotation matrix already (the equation system), such that each single beam corresponds to the right angle, which changes throughout the scanning cycle.

$$\begin{pmatrix} v_{rx}(t_1) \\ v_{ry}(t_2) \\ v_{rz}(t_3) \\ v'_{rz}(t_4) \end{pmatrix} = \begin{pmatrix} r_{xx} & r_{xy} & r_{xz} \\ r_{yx} & r_{yy} & r_{yz} \\ r_{z_1x} & r_{z_1y} & r_{zz} \\ r'_{zx} & r'_{zy} & r'_{zz} \end{pmatrix} \begin{pmatrix} \overline{u_x}_{[t_1,t_5]} \\ \overline{u_y}_{[t_1,t_5]} \\ \overline{u_z}_{[t_1,t_5]} \end{pmatrix}$$

Beams pointing in x-direction v_{rx}

The x-component of the beam pointing in x-direction (r_{xx}) results from addition of φ to θ_z (adjusted zenith angle in x-direction):

$r_{xx} = sin(\theta_z + \varphi)$

The y-component of the beam pointing in x-direction (r_{xy}) results from rotation of beam tilted by $(\theta_z + \varphi)$ around the y-axis (by ϕ):

$r_{xy} = cos(\theta_z + \varphi)\ sin\phi$

The z-component of the beam pointing in x-direction (r_{xz}) results from rotation of beam tilted by $(\theta_z + \varphi)$ around the y-axis (by ϕ):

$r_{xz} = cos(\theta_z + \varphi)\ cos\phi$

Then rotation around the z-axis is applied:

$r_{xx} = sin(\theta_z + \varphi)\ cos\psi - cos(\theta_z + \varphi)\ sin\phi\ sin\psi$
$r_{xy} = sin(\theta_z + \varphi)\ sin\psi + cos(\theta_z + \varphi)\ sin\phi\ cos\psi$
$r_{xz} = cos(\theta_z + \varphi)\ cos\phi$

Beams pointing in y-direction v_{ry}

The x-component of the beam pointing in x-direction (r_{yx}) results from rotation of beam tilted by $(\theta_z + \phi)$ around the x-axis (by φ):

$r_{yx} = cos(\theta_z + \phi)\ sin\varphi$

The y-component of the beam pointing in y-direction (r_{yy}) results from addition of ϕ to θ_z (adjusted zenith angle in x-direction):

$r_{yy} = sin(\theta_z + \phi)$

The z-component of the beam pointing in y-direction (r_{yz}) results from rotation of beam tilted by $(\theta_z + \phi)$ around the y-axis (by φ):

$r_{yz} = cos(\theta_z + \phi)\ cos\varphi$

Then rotation around the z-axis is applied:

$r_{yx} = cos(\theta_z + \phi)\ sin\varphi\ cos\psi - sin(\theta_z + \phi)\ sin\psi$
$r_{yy} = cos(\theta_z + \phi)\ sin\varphi\ sin\psi + sin(\theta_z + \phi)\ cos\psi$
$r_{yz} = cos(\theta_z + \phi)\ cos\varphi$

Beams pointing vertically/ in z-direction v_{rz} and v'_{rz}

Here two cases are considered:

1. $|\varphi| > |\phi|$ with
   $r_{zx} = sin\varphi$
   $r_{zy} = sin\phi\ cos\varphi$
   $r_{zz} = cos\phi\ cos\varphi$

   Then rotation around the z-axis is applied:

   $r_{zx} = sin\varphi\ cos\psi - sin\phi\ cos\varphi\ sin\psi$
   $r_{zy} = sin\varphi\ sin\psi + sin\phi\ cos\varphi\ cos\psi$
   $r_{zz} = cos\phi\ cos\varphi$

2. $|\phi| > |\varphi|$ with
   $r'_{zx} = sin\varphi\ cos\phi$
   $r'_{zy} = sin\phi$
   $r'_{zz} = cos\phi\ cos\varphi$

   Then rotation around the z-axis is applied:

   $r'_{zx} = sin\varphi\ cos\phi\ cos\psi - sin\phi\ sin\psi$
   $r'_{zy} = sin\varphi\ cos\phi\ sin\psi + sin\phi\ cos\psi$
   $r'_{zz} = cos\phi\ cos\varphi$

Graphic design: Communication Division, UIB / Print: Skipnes Kommunikasjon AS

uib.no

ISBN: 9788230843154 (print)
9788230847817 (PDF)